CASCADES ATMOSPHERIC WATER RESOURCES PROGRAM

VOLUME II

Prepared for

U.S. DEPARTMENT OF THE INTERIOR
BUREAU OF RECLAMATION
DIVISION OF ATMOSPHERIC WATER RESOURCES MANAGEMENT
DENVER, COLORADO
UNDER CONTRACT NO. 14-06-D-6999

STATE OF WASHINGTON
DANIEL J. EVANS
GOVERNOR

DEPARTMENT OF ECOLOGY
JOHN A. BIGGS
DIRECTOR

FINAL REPORT
JULY 1, 1970 - JUNE 30, 1975

MS-230 (8-70)
Bureau of Reclamation

TECHNICAL REPORT STANDARD TITLE PAGE

1. REPORT NO.
VII

2. GOVERNMENT ACCESSION NO.

3. RECIPIENT'S CATALOG NO.

4. TITLE AND SUBTITLE
Cascade Atmospheric Water Resources Program

5. REPORT DATE
May 1, 1975

6. PERFORMING ORGANIZATION CODE

7. AUTHOR(S) Peter V. Hobbs, L.F. Radke, J.D. Locatelli, D.G. Atkinson, C.E. Robertson, R.R. Weiss, F.M. Turner and R.R. Brown

8. PERFORMING ORGANIZATION REPORT NO.
VII (same as Item 1)

9. PERFORMING ORGANIZATION NAME AND ADDRESS
Department of Ecology
State of Washington
Olympia, WA 98504

10. WORK UNIT NO.

11. CONTRACT OR GRANT NO.
14-06-D-6999

12. SPONSORING AGENCY NAME AND ADDRESS
Engineering and Research Center
Bureau of Reclamation
Division of Atmospheric Water Resource Mgm't
Denver, CO 80225

13. TYPE OF REPORT AND PERIOD COVERED
Final
Volume 2 of 3

14. SPONSORING AGENCY CODE

15. SUPPLEMENTARY NOTES This document is a report on research conducted by the Cloud Physics Group, Atmospheric Sciences Dept., University of Washington, directed by Professor Peter V. Hobbs, and under subcontract to the State of Washington, Department of Ecology.

16. ABSTRACT

This report describes the detailed theoretical and field investigations of winter cloud and precipitation systems over the Cascade Mountains of Washington State carried out during 1971-72. Highlights of the report include a description of further developments of our theoretical model for orographic clouds and precipitation, presentation of the results of an extensive set of measurements on the concentrations of ice particles in natural clouds, a discussion of the factors which affect the aggregation of ice particles, a description of five case studies (two described in detail) of the effects of artificial seeding on clouds and precipitation, and a preliminary evaluation of the reliability of artificial seeding for the controlled redistribution of snowfall in the Cascade Mountains.

17. KEY WORDS AND DOCUMENT ANALYSIS

a. DESCRIPTORS-- artificial seeding, Cascade Mountains, orographic clouds, precipitation, snowfall, weather modification

b. IDENTIFIERS-- Cascade Mountains - State of Washington

c. COSATI Field/Group

18. DISTRIBUTION STATEMENT
Available from the National Technical Information Service, Operations Division, Springfield, Virginia 22151.

19. SECURITY CLASS (THIS REPORT)
UNCLASSIFIED

20. SECURITY CLASS (THIS PAGE)
UNCLASSIFIED

21. NO. OF PAGES
293

22. PRICE
$3.00

TABLE OF CONTENTS

PREFACE

Section 1 of this report reviews briefly the airborne, ground and radar facilities used in the Cascade Project, with emphasis on new developments and modifications made during the past year.

In the second section of the report the "detailed" and "simple" theoretical models for orographic cloud and precipitation processes developed for the Cascade Project are described. In the "detailed" model both the airflow and microphysics are modelled. The airflow model is based on equations for steady, two-dimensional, laminar, inviscid flow and includes the effects of latent heat release. Approximate solutions to the linearized equations are obtained for stable stratified conditions, and a terrain consisting of broad ridges (width $>$ 25 km), through an iterative transform technique which allows the non-linear boundary conditions to be satisfied. The model indicates that the dynamical effects of latent heat are significant in some cases but are generally secondary to the barrier effect of the terrain. The airflow model can be used to predict horizontal and vertical components of the wind, temperature and the mass of water vapor condensed when air flows over a mountain. The growth of solid precipitation particles in the orographic clouds by deposition from the vapor phase, riming and aggregation are considered. The latter process is treated in some detail in this report. The model is used to investigate the effects of the microstructure of clouds on the growth and fallout of solid precipitation over the Cascade Mountains under various conditions. It is shown that under certain circumstances increases in the concentration of ice particles in the clouds from 1 to 100 liter^{-1} (produced, for example, by artificial seeding) can cause snowfall to be carried farther downwind so that it is deposited on the eastern rather than the western slopes of the Cascade Mountains. The "simple" model, which has been used operationally in the Cascade Project, uses rawinsonde and surface observations of snow crystal types to construct the trajectories of various snow particles without regard to vertical air motions. The predictions of this model are compared to those of the "detailed" model.

Conclusions based on the research flights made during 1971-72 are described in Section 3. Distributions of cloud liquid water and ice particles across the Cascade Mountains are presented. Ice particle concentrations in the clouds are regularly many orders of magnitude greater than would be predicted from ice nucleus measurements. These anomalously high concentrations are exhibited to a greater degree in altostratus, stratocumulus and cirrostratus than in cumulus clouds, and appear to be a feature of "old" rather than "young" clouds. A best-fit line to the experimental results shows that the ratio $R(\Delta T)$ of the maximum sustained ice particle concentration to the normally assumed ice nucleus concentration to temperature $\Delta T^{o}C$ below $0^{o}C$ is given by

$$R(\Delta T) = 5.89 \times 10^6 \exp(-0.4\Delta T)$$

Data on the relationship between the occurrence of ice crystal aggregates in clouds, temperature and concentrations of ice particles are described. The probability of aggregates forming (and their sizes) generally decreases with decreasing temperature but there is a local peak in the dendritic growth region. At temperatures below -15°C, and with ice particle concentrations less than 0.1 cm^{-3}, aggregates appear unlikely to form. For temperatures above -5°C, and particle concentrations in excess of 1 cm^{-3}, there is more than a 50 per cent probability of finding aggregates in clouds.

Section 4 is concerned with the ground data, particularly the types of snow particles, collected in the Cascade Project in 1971-72. Statistics on the types, sizes and degrees of riming of the ice particles are given. Particular attention is paid to aggregates and double crystals with a common drop center. A case study is described of the effects of a frontal passage on snow crystal types and precipitation rates in the Cascade Mountains; the results show that passage of a warm front causes a lowering of the diffusional growth layer of ice crystals and a change from unrimed cold-type to rimed warm-type crystals. The results of ice nucleus measurements with Millipore filters in the Cascade Mountains are presented. Ice nuclei were most numerous when artificial seeding with AgI was being carried out from the aircraft, when the winds were westerly, when ground temperatures were below 0°C, and when there was no precipitation.

Artificial seeding of clouds over the Cascade Mountains was carried on twenty-three occasions during 1971-72 to see what extent and with what accuracy snowfall could be modified and redistributed within a small target area on the ground in the manner predicted by our theoretical models. Evaluation was carried out through a series of comprehensive airborne, ground and radar observations. In Section 5 of this report, five case studies are described in which it appeared that significant modifications to clouds and precipitation were produced in the target area by artificial seeding. For example, in one case clouds upwind and west of the Cascade Divide were glaciated by artificial seeding, subsequently the crystal habits and degrees of riming of snow particles reaching the ground in the target area were markedly modified and the snowfall rate decreased at the divide and simultaneously increased 20 km east of the divide during the predicted period-of-effect of seeding.

In the last section of the report an overall evaluation is given of the observed effects of artificial seeding in the 1971-72 Cascade Project. Artificial seeding produced observable or measurable effects on clouds on 80 per cent of occasions, with changes in the habits or concentrations of ice crystals being the most reliable criterion. Artificial seeding produced the largest increases in the concentrations of ice particles in clouds when the concentrations were low. When natural ice particle concentrations exceeded 2000 liter^{-1}, artificial seeding did not produce detectable effects. On six occasions when artificial seeding was carried out "good" effects attributable to the seeding were detected in the small target area on the ground, on four occasions the effects were "fair" and on ten occasions they were "poor". In the six "good" cases the precipitation was predominently orographic rather than cyclonic.

SECTION 1

OBSERVATIONAL TECHNIQUES

1.1 The B-23 Aircraft

A detailed description of the B-23 cloud physics research aircraft and its instrumentation has been given by Hobbs *et al.*, (1971) and will not be repeated here. However, several modifications and improvements were made to this facility during the 1971-72 season and these are described below.

1.1.1. Instrumentation

To provide on-board, real-time measurements of the distribution of cloud droplet sizes up to about 30 μm in radius, we have adopted and built NCAR's version of the Keily electrostatic cloud droplet probe (Abbott *et al.*, 1972). This probe is mated to a modified 256-channel pulse height analyzer which generates histograms of the number concentration of cloud droplets in various size intervals. Examples of some data are shown in Figs. 1.1. - 1.3. Preliminary trials indicate that further modifications to this device will be necessary if droplets less than about 8 μm in radius are to be measured, since signals produced by these small droplets are obscured by acoustically induced electrical noise.

The RCA 5cm weather radar was modified by the installation of modern receiver crystals which resulted in significantly improved performance. Also, a variable persistence storage oscilloscope was installed as a monitor for this radar near the newly installed viewing dome (see below).

In an attempt to obtain measurements of vertical air motions, we have installed on the B-23 a glider variometer (Ball Engineering Co., Model 101-D). This provides measurements of the vertical velocities of the aircraft which are independent of the motions produced by the pilot's stick. However, it does not compensate for changes in the power of the engines. The system is still under test but we hope to be able to resolve vertical air motions of 0.1 m s^{-1}.

The two electric field mills on the aircraft have been carefully rebuilt and modified aerodynamically in order to withstand severe icing conditions. This has significantly increased their reliability.

An on-board analog computer is under development for providing a read-out of the wind speed and direction at flight level. This computer combines

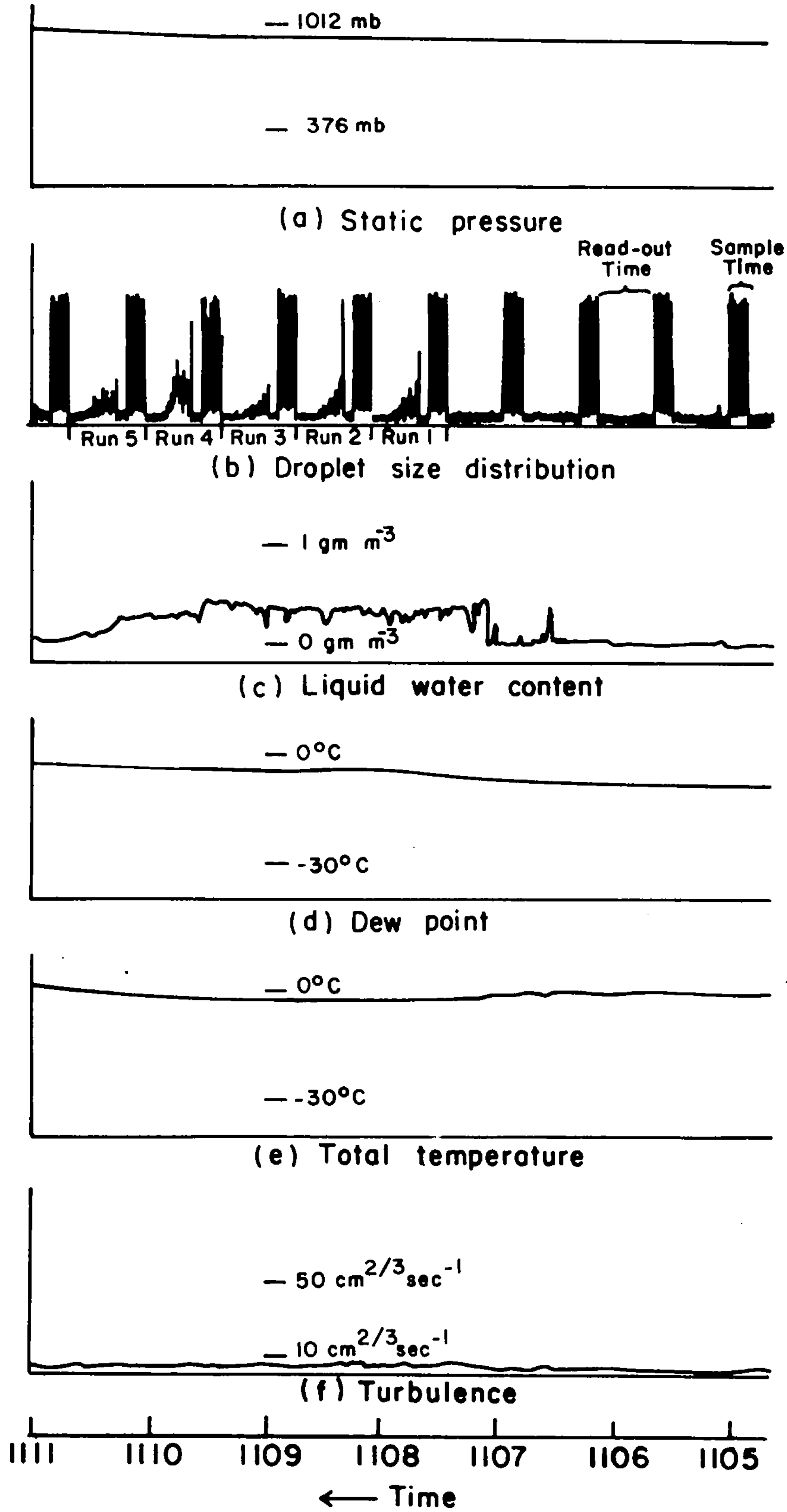

Fig. 1.1 Measurement of static pressure, droplet size distributions (Keily probe), liquid water content (Johnson-Williams), dew point, total temperature and air turbulence as aircraft descended through a layer of stratocumulus cloud (Flight 154, December 14, 1972). A segment of (b) and (c) are shown on an expanded scale in Fig. 1.2.

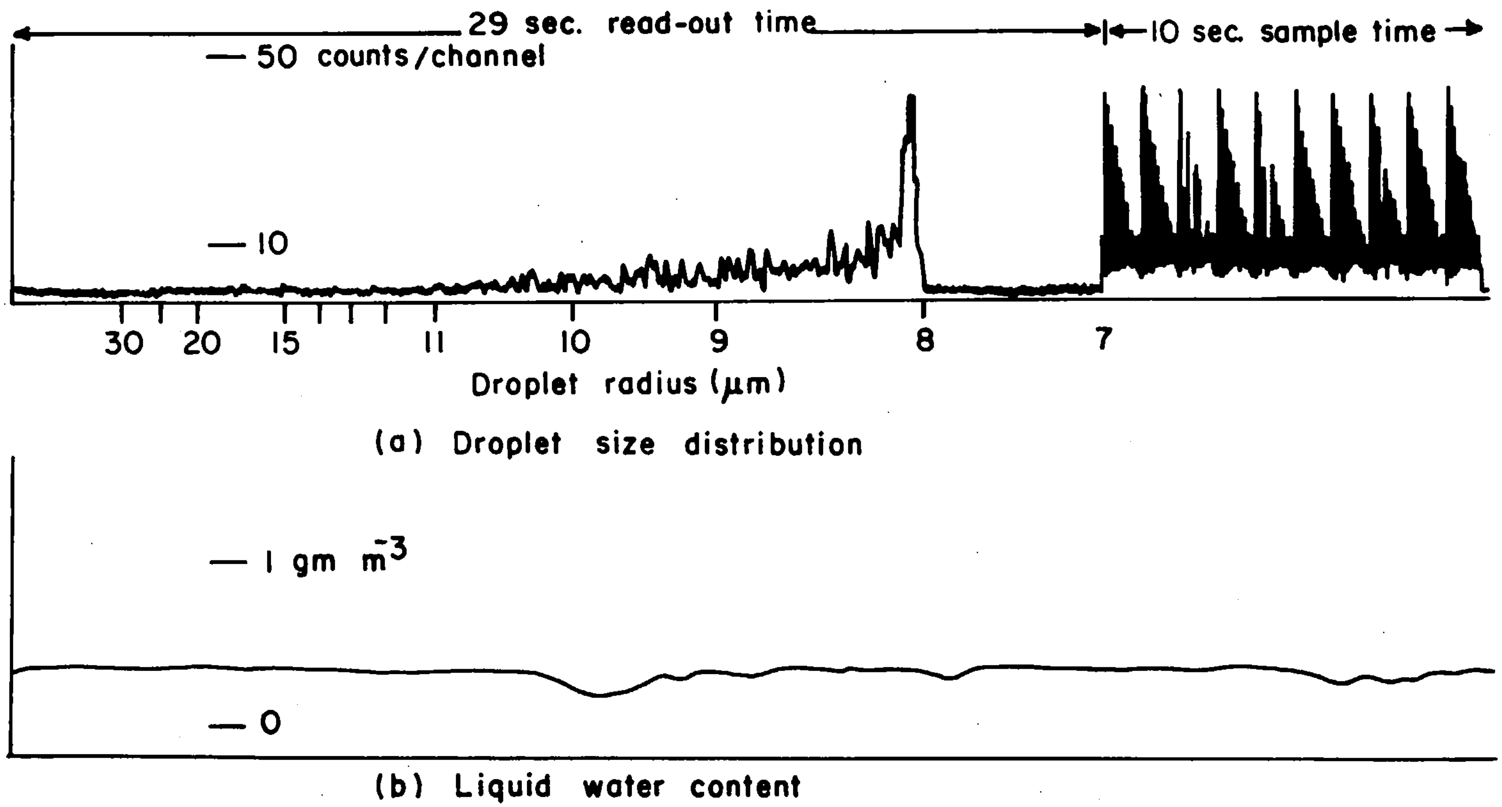

Fig. 1.2 Portion of the data shown in Fig. 1.1 on an expanded time scale.

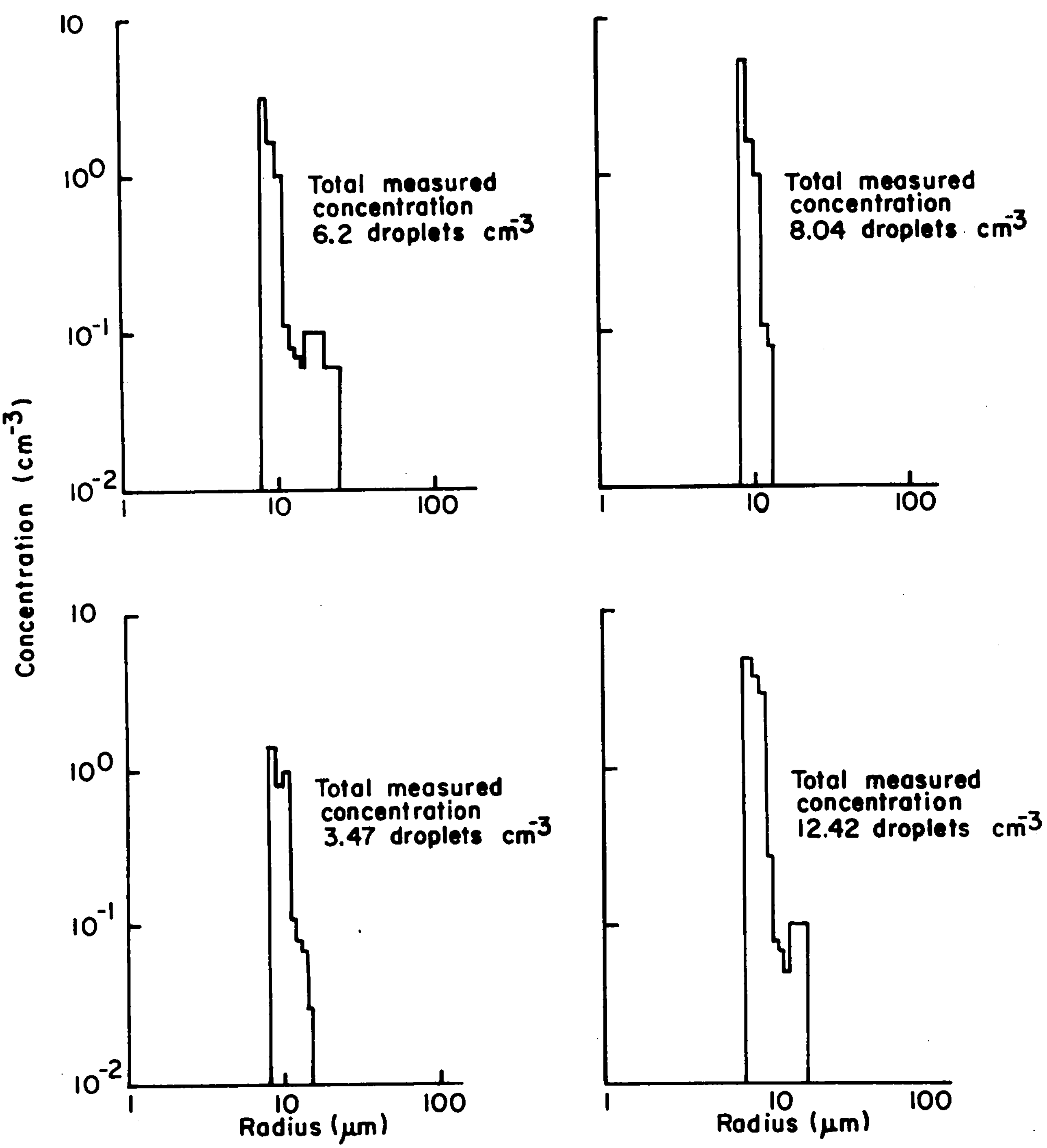

Fig. 1.3 Drop size distributions deduced from Runs 1 - 4 shown in Fig. 1.1. Droplets with radius less than 8μm were not counted. Note the tendency toward a bimodal distribution.

information from the in-house built aircraft position plotter, the true airspeed computer and the magnetic slaved gyrocompass to give the wind speed and direction.

1.1.2 Rearrangement of Personnel and Equipment

Improvements in the reliability of the on-board instrumentation made it possible to carry out many of our research flights with a three-man crew (plus pilot and copilot) rather than the four or five man crew used in 1970-71. This involved the following reorganization of men and equipment within the aircraft. The controls for the continuous particle sampler and the metal foil impactor were moved from their previous position near the center of the cabin to just in front of seat 3 in the forward part of the cabin (see Fig. 1.2 in Hobbs et al., 1971). This allowed the work of Instrumentation Monitor and Observer to be carried out by one person located in seat 3.

The work required of the Instrumentation Engineer was reduced by triggering the automatic calibration and control systems for the instruments measuring the state parameters with the push of a single button. This system provides accurate set-point and span calibration of about 90 per cent of the electronic instruments on board the aircraft through sequential substitution of precision resistors or voltage differences immediately behind the sensing heads.

The task of the Flight Director was also eased by the addition of a hemispherical transparent dome located in the roof of the fuselage just forward of the vertical stabilizer. This position allows good visibility in all directions (except vertically downward). In this position the Flight Director can also view the monitor of the aircraft's 5 cm weather radar and he can communicate with the pilot through an intercom system.

1.1.3 Operational Procedures

The aircraft operated out of Boeing Field in Seattle and on "storm days" it followed a similar flight plan to that used in 1970-71, namely, first a flight along the V-2 airway from Seattle to Ellensburg, which crosses the Cascade Mountains, and then back again to the western side of the Cascades. Detailed in-cloud measurements were obtained over the western and eastern slopes of the Cascade Mountains in the vicinity of Snoqualmie Pass. If these measurements, and those made at the ground, indicated that a potential existed for the artificial modification of snowfall at the ground in the Snoqualmie Pass area, in situ or ejection silver iodide pyrotechnic units or dry ice were dispersed from the aircraft for a period of one hour or so over an area determined by our operational numerical model (see Hobbs et al., 1971). Following completion of this operation, the aircraft was used to evaluate the effects of the artificial seeding on the clouds.

1.2 Pulsed Doppler Radar

In 1971-72 the vertically pointing CW Doppler radar used in the previous year was expanded to include an incoherent search capability and vertically pointing pulsed Doppler of limited range. This radar was located at Hyak (Fig. 1.4).

The pulsed Doppler system was interfaced with the incoherent military tracking radar described by Hobbs et al. (1971) so that a common antenna and receiver hardware could be used. Since the pulsed Doppler power was not sufficient to fire the transmit receiver switches in the incoherent radar duplexer, a separate antenna was used for the pulsed Doppler transmissions. A block diagram of the radar system is shown in Fig. 1.5. The characteristics of the incoherent radar were: peak power 30 kW, wavelength 3.2 cm, beam width 2.8°, pulse repetition rate 4 kHz, pulse duration 0.25 microseconds, single range gate position 300 to 25,000 meters. The parameters of the pulsed Doppler radar which were different from the incoherent radar were: peak power 20 W, pulse repetition rate 40 kHz. The incoherent and pulsed Doppler systems could be operated simultaneously when the pulsed repetition rates were harmonically related, but the incoherent radar was then restricted to vertical observations.

Significant progress was made in 1971-72 in developing a data processing system for the Doppler radar. Earlier observations of spectra from CW radar returns and later pulsed Doppler returns showed the variability in the raw spectra representing the fall velocities of hydrometeors. These spectra had a phase flicker with a time constant of about 16×10^{-3} seconds due to the shuffling of the scatterers in and out of the radar beam. A slower variation occurred over a period of minutes which was presumably due to meteorological factors. Proper reduction of this type of data entails identifying internal variables which are independent of the randomness of the signals. As a first step in this direction, electronic systems were developed for transposing the raw spectra onto digital tape. The data could then be analyzed with a large digital computer using standard Fortran programs.

The data processing system is shown in block form in Fig. 1.6. The magnetic tape recorded by the radar is played back into a HP 302A analog wave

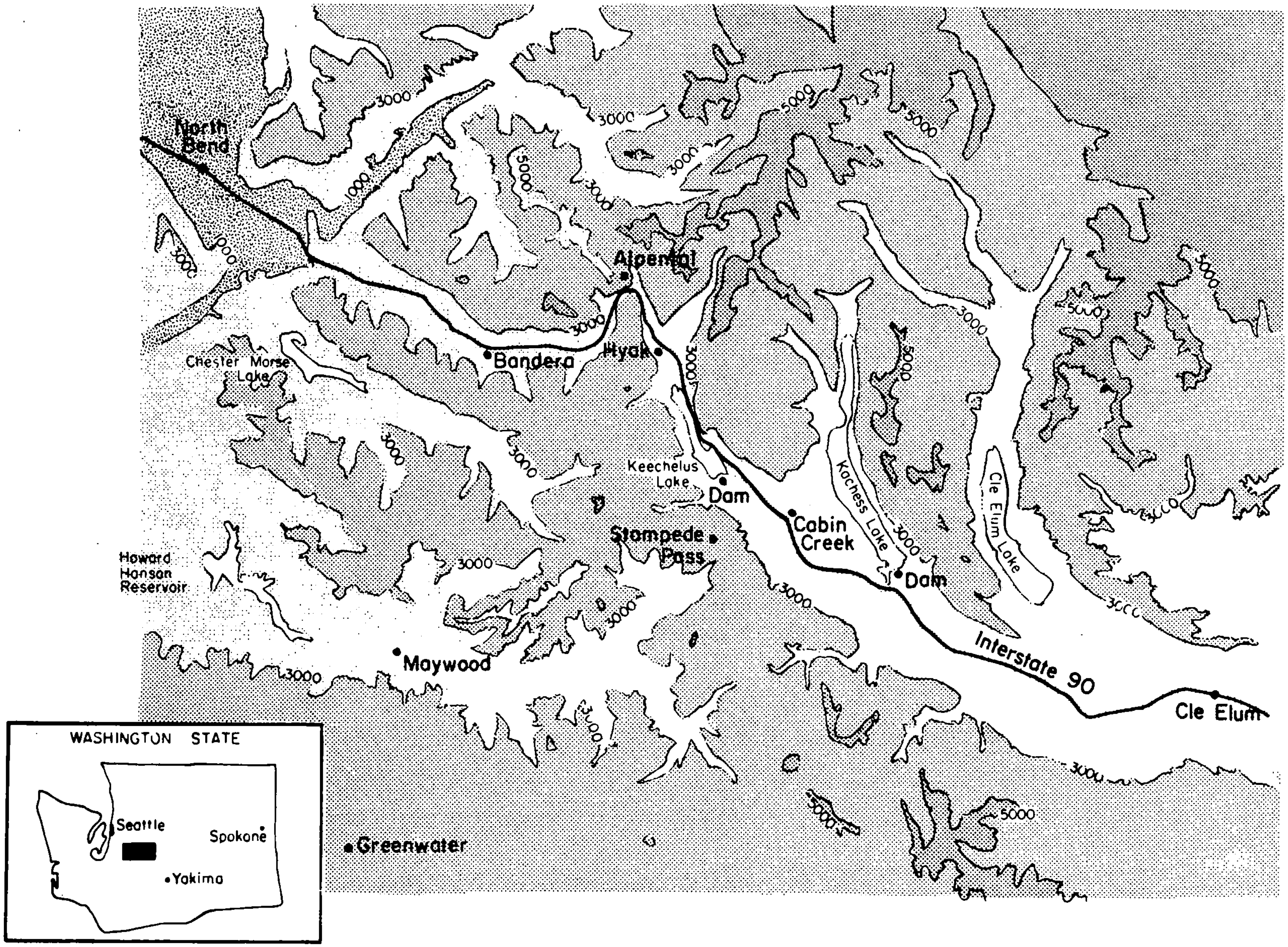

Fig. 1.4 Region of the Cascade Mountains in which ground measurements were made.

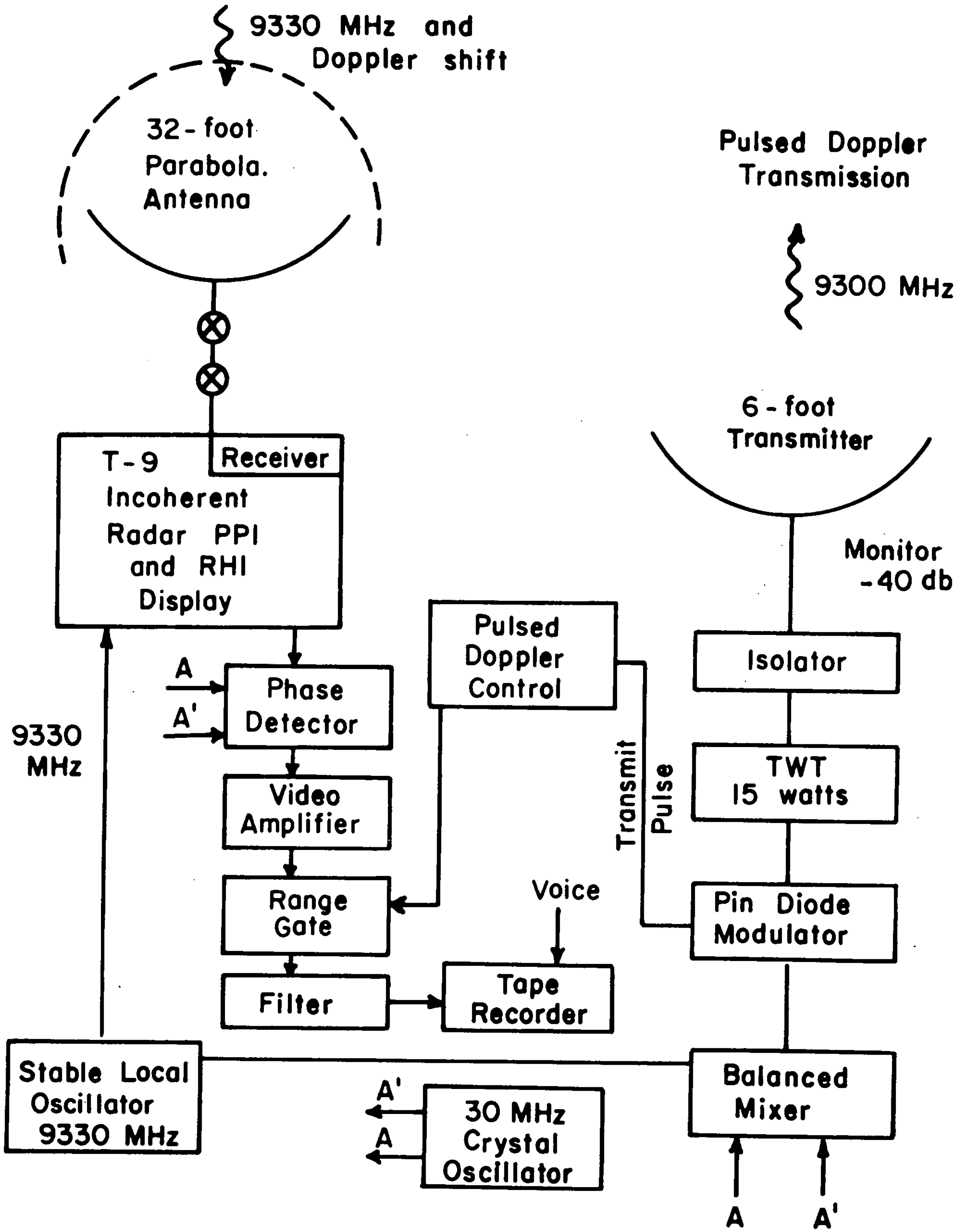

Fig. 1.5 Block diagram of pulsed Doppler radar.

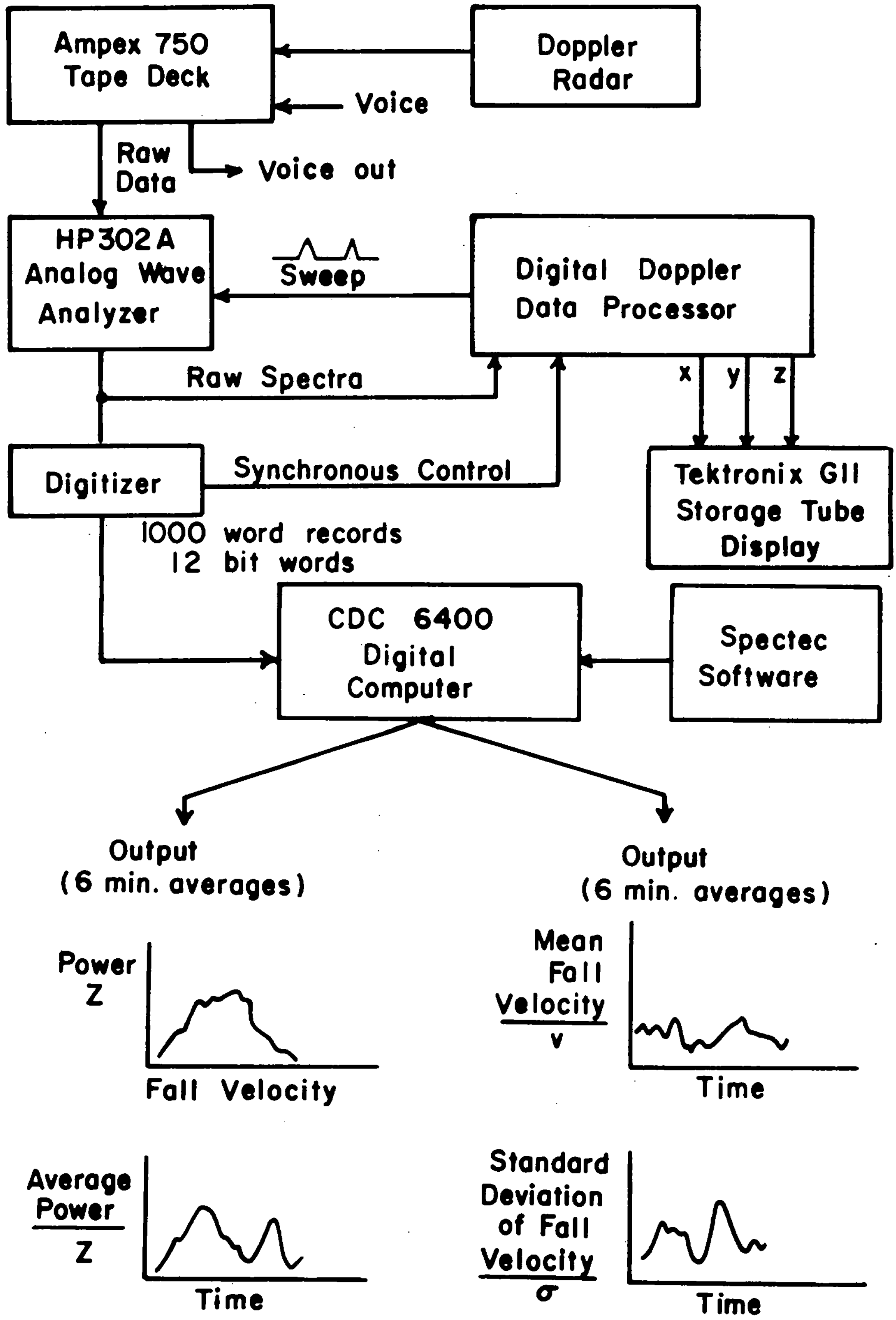

Fig. 1.6 Data processing system for Doppler radar.

analyzer which has been modified to sweep electronically. The HP 302A is a very sharply tuned variable filter of 7Hz bandwidth. This filter is swept electronically over 500 Hz in 5 seconds with less than 3 ms flyback time. Thus if a 100 Hz signal from hydrometeors were present at the input the analyzer would register output while it swept from 96.5 to 103.5 Hz for a dwell time of 70 ms. The analyzer would record amplitude changes that occurred slower than 5 seconds and thus would record the slow meteorological changes while ignoring the fast phase flicker due to the scatterers shuffling in and out of the beam.

A second track is used for voice to record time, range gate position, crystal type and any other related information. The digitizer supplies the time base which is fed to the digital Doppler data processor. Using the triggers supplied the 3DP provides a calibrated sweep voltage to the HP 302 and Tektronics 611 storage tube. In addition an intensity modulation and stepping action from the 3DP allows ten spectra to be displayed sequentially and stored on the tube for convenient viewing. Erasing on the storage tube is done manually allowing the operator to superimpose every tenth spectra.

The output of the HP 302A is digitized in 1000 word records on magnetic tape which is compatible with the CDC 6400 digital computer. When the raw spectra are in the computer they are analyzed with the program SPECTEC. A block diagram of SPECTEC is shown in Fig. 1.7. The first step, that of word conversion, is required because the CDC words are 60 bits and the radar digitizer has 12 bit words. As the CDC reads the tape the 12 bit words are packed, 5 at a time, into the 60 bit words of the CDC. Thus the original 1000 word record now becomes 200 CDC words. The step of "masking" involves the unpacking of these words into 1000 CDC words with the original data in the 12 least significant bits of the 60 bit CDC words. These data words are now stored in an array and arranged in 100 word blocks to recreate the raw spectra in the CDC. A continuous plot of smoothed spectra against velocity is supplied by the main program. The raw spectra are summed and averaged to give plots of power against velocity permuted in time. The second branch constitutes a summary operation. The subroutine RSPR operates on the data to compute average power, average veloctiy and smoothed variance for each spectrum. These values are averaged with smoothing constants chosen by the operator and stored until the data operation is complete. Once the power, velocity and variance computations are done, the computer plots these variables as functions of time.

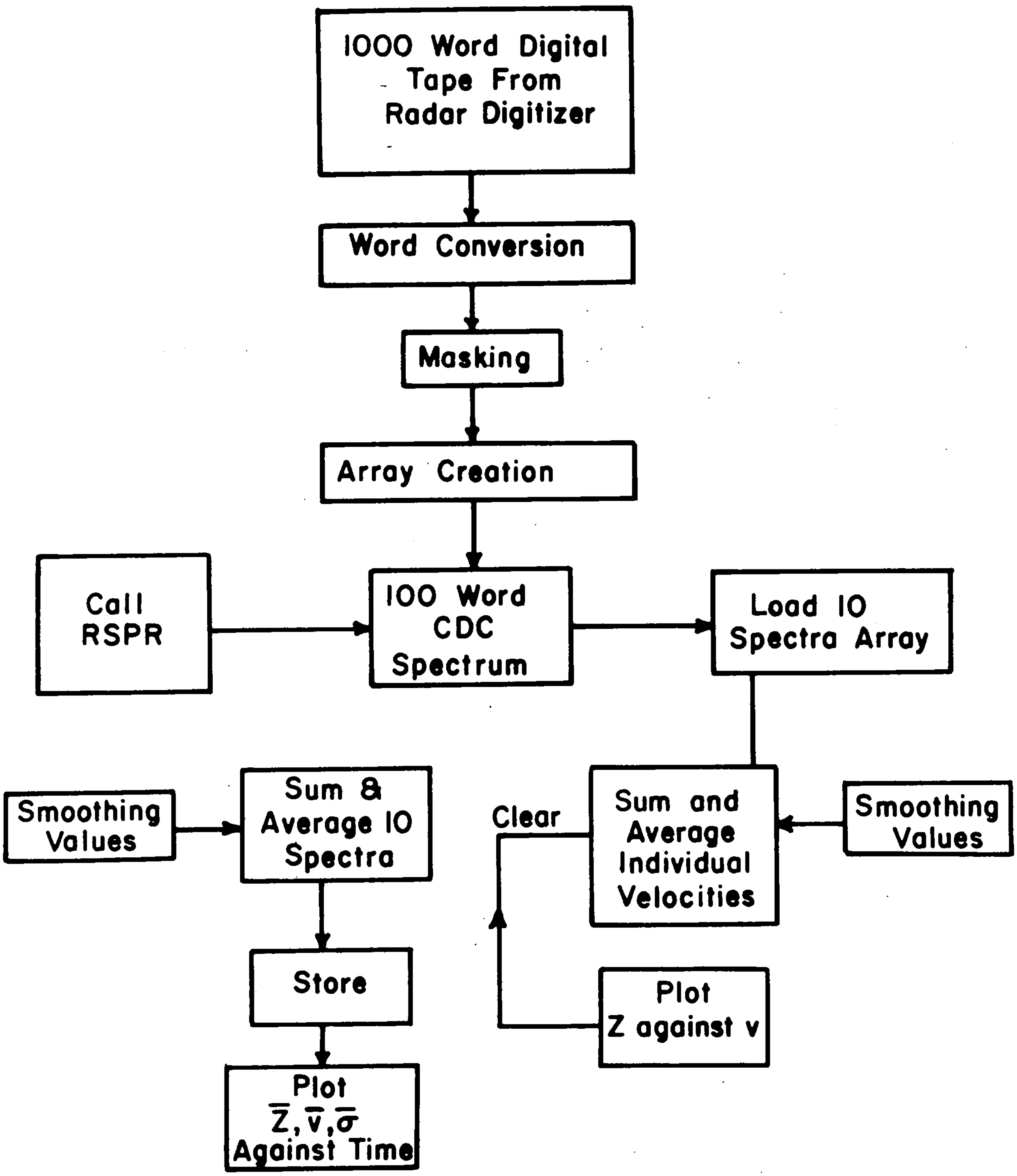

Fig. 1.7 Digital program "Spectec".

Data collected with the Doppler radar in 1971-72 are mentioned only briefly in this report since far superior data were collected in 1972-73 which will be described in the next report on the Cascade Project.

1.3 Ground Instrumentation and Procedures

The network of ground stations and the types of measurements made were essentially the same in 1971-72 as in 1970-71 (for a detailed description of the latter see Hobbs et al., 1971). The few changes which were made are described below.

1.3.1. Network of Stations

The network of ground stations used in the 1971-72 season is shown in Fig. 1.4. and the measurements made at each station are listed in Table 1.1. The major changes from 1970-71 were the elimination of the weighing bucket precipitation gauge at Denny Creek (due to highway construction), the elimination of specialized measurements at Stampede Pass (although regular observations made by the National Weather Service were still available), and the addition of a weighing bucket precipitation gauge at Maywood which is located about 17 miles southwest of Snoqualmie Pass.

1.3.2. Precipitation Gauges

Weighing bucket precipitation gauges remained the backbone of our network of precipitation gauges. However, the success of the heated tipping bucket in 1970-71 led to the use of five of these gauges during 1971-72. Each of these gauges was calibrated prior to being placed in the field and again half way through the winter season. No significant drifts in the readings were noted on recalibration. The high-resolution tipping bucket used during 1970-71 was not used in 1971-72. All gauges used in 1971-72 had the same resolution which, on average, was 4.2×10^{-2} mm of water per tip. The time at which each tip occurred was recorded at Alpental base but at the other stations the number of tips which occurred in every 5-minute interval was recorded.

Due to the failure of the E. Bollay Associates' (now a division of EG&G) optical snow rate sensor to reliably measure the snowfall rates of rimed crystals (see Hobbs et al., 1971), only three of these instruments were used during 1971-72 and these were located at manned stations where they could be frequently calibrated.

1.3.3. Ice Nucleus Concentrations

A modified NCAR ice nucleus counter was located at Keechelus Dam and was run continuously at -20°C on some of the storm days. Millipore filters

TABLE 1.1

MEASUREMENTS MADE AT GROUND STATIONS

	North Bend	Bandera	Alpental		Hyak†	Keechelus Dam†	Cabin Creek	Kachess Dam	Maywood	Greenwater†	Univ. of Washington (Contol Center)†
			Bottom†	Top†							
Weighing Bucket Precipitation Gauge	✓	✓	✓		✓	✓	✓	✓	✓		
Heated Tipping Bucket Precipitation Gauge			✓		✓	✓		✓			✓
Optical Snow Rate Sensor (Bollay/EG & G)			✓		✓	✓					
Snow Crystal Replicas			✓	✓	✓	✓					
Snow Samples for Concentrations of Freezing Nuclei & Silver			✓		✓	✓					
Ice Nucleus Counter (NCAR)						✓					
Millipore Filters						✓					
Thermograph	✓		✓		✓	✓					✓
Microbarograph	✓		✓					✓			✓
Wind Speed and Direction	✓					✓					✓
Radio Communication			✓	✓	✓	✓				✓	✓
Rawinsonde Unit										✓	
Radar (Doppler, PPI, RHI, A-scan)					✓						

†Manned station

(Millipore Corp., Bedford, Mass. Type HAWG, 0.47 μm pores, 47 mm diameter) were exposed at Keechelus Dam from about 1200 to 1300 hours on storm days. Snow samples collected at the ground stations were melted and refrozen to determine the concentrations of freezing nuclei in them as described by Hobbs et al. (1971).

1.3.4. Operational Procedures

"Storm days" were defined in the same manner as for 1970-71, namely, those days for which the National Weather Service forecaster in Seattle predicted by 1600 hours on the preceding day that snow was likely to fall in the Cascade Mountains during daylight hours.

Ground crews were on-station by 1000 hours on "storm days" and continued taking observations until late afternoon. During this period, snow samples were collected and replicas taken every 15 minutes. When an observer was located at the top of the ski lift at Alpental, replicas were taken at this station every 10 minutes between about 1100 to 1530 hours.

SECTION 2

THEORETICAL STUDIES

2.1 Introduction

Two theoretical models have been developed in connection with the Cascade Project. The first of these is a "simple" model which is used in real-time to predict the location where artificial seeding should be carried out in order to affect precipitation on the ground in the Cascade Mountains. This is described in §2.3. The other model is more detailed and has as its ultimate objective the theoretical description of the flow of air across a mountain range, the development of orographic clouds, the fallout of solid precipitation within this airflow, and the prediction of the effects of artificial seeding on the distribution of the snowfall under various conditions. The status of this model as of December 1971 was described by Hobbs et al. (1971). Since then the model has been extended as described below in §2.2.

2.2 "Detailed" Theoretical Model

2.2.1. Airflow†

The problem of a steady, two-dimensional, stably stratified flow of air over a mountain has been considered by several workers, although generally the effects of the release of the latent heat of condensation associated with the formation of clouds has been neglected. The airflow model which has been developed for the Cascade Project is based on Scorer's (1949) work, however, latent effects have been considered and a method for applying boundary conditions at actual interfaces in order to treat transitions between unsaturated and saturated conditions on a streamline has been developed.

It may be shown (e.g. Hobbs et al., 1971) that the two-dimensional flow of dry air (in the x-direction) over a ridge lying normal to the flow is described by the equation

$$\frac{\rho_o}{\rho}\eta - \frac{\beta}{u_o}\left(g\zeta + \frac{q^2}{2}\right) = C \qquad (2.1)$$

†This section is based on a paper entitled "A Theoretical Study of the Flow of Air and Fallout of Solid Precipitation Over Mountainous Terrain: Part I. Airflow Model" by A. B. Fraser, R. C. Easter and P. V. Hobbs. J. Atmos. Sci., 30: 813-823, 1973.

where, ρ is the density of the air, ρ_o the density well upstream ($x = -\infty$), η the vorticity, β the upstream stability [defined as $\frac{d}{dz_o}$ (ln Θ) where Θ is the potential temperature and z_o the vertical coordinate at $x = -\infty$], u_o the horizontal speed of the air at $x = -\infty$, g the acceleration due to gravity, ζ the vertical displacement of a streamline ($= z-z_o$), q^2 the sum of the squares of the horizontal and vertical wind speeds, and C a constant. Under suitable conditions eqn. (2.1) reduces to

$$\nabla^2\zeta + \frac{g\beta}{u_o^2}\zeta + K_d \qquad (2.2)$$

where, K_d is a constant on a streamline.

For the flow of moist air over a ridge, the corresponding equation to eqn. (2.1) is

$$\frac{\rho_o}{\rho}\eta - \frac{\beta_E}{u_o}\left(\frac{q^2}{2} + gb\zeta\right) = K \qquad (2.3)$$

where, $\beta_E = \frac{d}{dz_o}(\ln \Theta_E)$, Θ_E is the equivalent potential temperature, K a constant on a streamline, and

$$b = 1 - \frac{1-\gamma_m/\gamma_d}{1-c_pT_o/\varepsilon L} \qquad (2.4)$$

where, γ_m and γ_d are the moist and dry adiabatic lapse rates, c_p the specific heat of dry air at constant pressure, T_o the air temperature at $x = -\infty$, $\varepsilon = R/R_v$, R and R_v are the gas constants for dry air and water vapor, and L is the latent heat of condensation. A solution of eqn. (2.3) is of the form

$$\nabla^2\zeta + \frac{gb\beta_E}{u_o^2}\zeta + K_w \qquad (2.5)$$

where K_w is a constant on a streamline.

Eqns. (2.3) and (2.5) contain constants which must be evaluated. Since both ζ and $\nabla^2\zeta$ approach zero as $x \to -\infty$, if a streamline is saturated as $x \to -\infty$, $K_w = 0$ in eqn. (2.5). Similarly, if a streamline is unsaturated as $x \to -\infty$, $K_d = 0$ in eqn. (2.2). If there is a transition from unsaturated to saturated conditions along a streamline, which occurs at z_s and $\zeta_s = z_s - z_o$, both ζ and $\nabla^2\zeta$ must be continuous at this point, therefore, at z_s we have

$$\frac{g}{u_o^2} (\beta - b\beta_E)\, \zeta_s = K_d - K_w \tag{2.6}$$

which gives K_d or K_w (whichever is non-zero) in terms of ζ_s. Some methods of solution and output from the airflow model were given by Hobbs et al. (1971). More sophisticated results have been obtained in the past year and these are described below.

It can be seen from eqns. (2.2) and (2.5) that provided there are no transitions between unsaturated and saturated conditions on a streamline, the streamline displacement function ζ obeys the equation

$$\nabla^2\zeta + \mu^2\zeta = 0 \tag{2.7}$$

where

$$\mu^2 = \mu_d^2 = \frac{g\beta}{u_o^2} \tag{2.8}$$

for unsaturated air, and

$$\mu^2 = \mu_w^2 = \frac{gb\beta_E}{u_o^2} \tag{2.9}$$

for saturated air. μ is termed the critical wave number of the flow. If μ is constant throughout the region of interest, solutions to eqn. (2.7) are readily obtained. However, μ is rarely constant in the atmosphere. Therefore, we approximate the variation of μ by dividing the atmosphere into layers in which μ is taken as constant.

Solutions to eqn. (2.7) may now be obtained using a transform technique (Queney, 1947, 1948; Scorer, 1949). The profile g(x) of the mountains is considered to be of the form

$$g(x) = \sum_{\ell=1}^{m} \frac{a_\ell}{\left[1 + \left(x-b_\ell\right)/c_\ell\right]^2} \tag{2.10}$$

where, a_ℓ, b_ℓ and c_ℓ are coefficients.

We will restrict ourselves to the case

$$\mu c_\ell >> 1 \quad (\mu \neq 0) \tag{2.11}$$

which corresponds to broad mountains (which is a good assumption for the Cascades). In this case, the terrain is not conducive to the formation of large-amplitude lee waves.

The atmosphere is divided into N layers in each of which μ is taken as constant, the first layer is adjacent to the surface and the N^{th} layer is on top. In each layer the solution to eqn. (2.7) is of the form

$$\zeta_j (x,z) = \mathcal{R}e \int_0^\infty dk \exp(ikx) \left[A_j \exp(i\lambda_j z) + B_j \exp(-i\lambda_j z)\right] \tag{2.12}$$

where,

$$\lambda_j^2 = \mu_j^2 - k^2 \tag{2.13}$$

The values of the coefficients A_j and B_j in eqn. (2.12), which are functions of K, are fixed by the 2N boundary conditions. These conditions are the radiative condition in the top layer, the continuity of ζ and $\frac{\partial \zeta}{\partial z}$ at the (N-1) interfaces between layers, and the $z_o = 0$ streamline which follows the profile of the ground. Let the boundary between the (j-1) and j layers be described by

$$z = h_j(x) \tag{2.14}$$

so that $h_1(x) = g(x)$. Since, in general, the h_j's are unknown functions, the usual procedure is to apply the boundary conditions at $h_j(-\infty)$. However, we show below that it is possible to apply the boundary conditions at $h_j(x)$ by using an iterative procedure which results in greater accuracy, particularly close to the ground.

Let us assume initially that h_j's are known. Then A_j and B_j can be found from the boundary conditions and the integral in eqn. (2.12) evaluated. The broad mountain assumption makes this evaluation quite simple. Each A_j and B_j is multiplied by the factor

$$\sum_{\ell=1}^{m} a_\ell c_\ell \exp\left[ik(x-b_\ell) - kc_\ell\right] \qquad (2.15)$$

which arises from the boundary condition applied at the ground. The $\exp(-kc_\ell)$ factor allows λ_j to be approximated by μ_j in the expressions for the A's and B's. (Essentially, we have replaced λ_j by the zero and first order terms in its Taylor's series in k about k = 0. This procedure also works for a layer of neutral stability with $\mu_i = 0$.)

The h_j's, however, are not known but are solutions to the equations

$$\zeta_j\left[x,\ h_j(x)\right] - h_j(x) + h_j(-\infty) = 0 \qquad (2.16)$$

For a fixed x, the $\zeta_j|x,\ h_j(x)|$ are rather complicated functions of all the h_j's, and the h_j's are roots to eqn. (2.16). These roots can be obtained using an iterative technique known as the "regula falsi algorithm" (see Ostrowski, 1960). The h_j's and ζ_j are then calculated for a specified set of x-values. The h_j's are first calculated at the most upwind x-positions where the surface height is still small and $|h_j(x) - h_j(-\infty)| \ll h_j(-\infty)$. One then moves downwind one x-position at a time. Extrapolation of the upwind h_j generally gives a good first approximation for the downwind h_j, and the method converges rather quickly to the solutions.

Applying the boundary conditions in the above fashion has the one disadvantage that the ζ_j's given by eqn. (2.12) are no longer exact solutions to eqn. (2.7) because the A_j and B_j now have an x-dependence. However, the error arising from the use of the non-constant h_j's is probably not much larger than the error inherent in the broad-mountain assumption. (This conclusion was arrived at by comparing the values of $\nabla^2\zeta_j + \mu_j^2\ \zeta_j$ using constant and variable h_j's for several cases.) The advantage of applying the boundary conditions correctly would seem to outweigh this slight disadvantage.

We turn now to a consideration of the transition between saturated and unsaturated conditions along a streamline. When the air is unsaturated as $x \to -\infty$, we have

$$\nabla^2\zeta + \mu_d^2\ \zeta = 0 \qquad (2.17)$$

in the unsaturated region, and

$$\nabla^2\zeta + \mu_w^2\,\zeta = \left(\mu_w^2 - \mu_d^2\right)\,\zeta_s \tag{2.18}$$

in the saturated region, where ζ_s is a function of z_o. Let us assume

$$\zeta_s = \varepsilon_1 z_o + \varepsilon_2 \tag{2.19}$$

This expression for ζ_s should not be too restrictive since the atmosphere is divided into several layers. Then, for saturated air, we have

$$\nabla^2\zeta + \left[\mu_w^2 + \varepsilon_1\left(\mu_w^2 - \mu_d^2\right)\right]\zeta = \left(\mu_w^2 - \mu_d^2\right)\left(\varepsilon_1 z + \varepsilon_2\right) \tag{2.20}$$

In a layer where μ_d and μ_w are constant, for unsaturated air

$$\zeta(x,z) = \mathcal{R}e\int_o^\infty dk\,\exp(ikx)\left[A\exp(i\lambda_d z) + B\exp(-i\lambda_d z)\right] \tag{2.21}$$

where,

$$\lambda_d = \left(\mu_d^2 - k^2\right)^{1/2} \tag{2.22}$$

and for unsaturated air

$$\zeta(x,z) = \mathcal{R}e\int_o^\infty dk\,\exp(ikx)\left[A'\exp(i\lambda^* z) + B'\exp(-i\lambda^* z) - \alpha(\varepsilon_1 z + \varepsilon_2)\delta(k)\right] \tag{2.23}$$

where,

$$\lambda^* = \left(\mu^{*2} - k^2\right)^{1/2} \tag{2.24}$$

$$\mu^{*2} = \mu_w^2 + \varepsilon_1\left(\mu_w^2 - \mu_d^2\right) \tag{2.25}$$

and

$$\alpha = \left(\mu_d^2 - \mu_w^2\right)\Big/\mu^{*2} \tag{2.26}$$

and $\delta(k)$ is defined so that

$$\int_0^k dk' \;\; \delta(k') = \begin{cases} 1 \text{ for } k>0 \\ 0 \text{ for } k\leq 0 \end{cases} \tag{2.27}$$

ζ and $\partial\zeta/_{dz}$ are continuous at z_s and

$$z_s = \zeta_s + z_o = (\varepsilon_1 + 1)z_o + \varepsilon_2 \tag{2.28}$$

We will restrict ourselves to the case $\varepsilon_1 = -1$, which corresponds to the layer having a horizontal cloud base. Then $\mu^* = \mu_d$ and $\lambda^* = \lambda_d$ and

$$A' = A - \frac{\alpha \; \delta(k)}{2i \; \mu_d} \quad \exp(-i\mu_d \; \varepsilon_2) \tag{2.29}$$

$$B' = B + \frac{\alpha \; \delta(k)}{2i \; \mu_d} \quad \exp(i\mu_d \; \varepsilon_2) \tag{2.30}$$

Solutions can now be obtained as described previously for the case where there are no transitions between unsaturated and saturated conditions. The boundary conditions are applied at layer boundaries, but it must be noted whether the air is saturated or unsaturated in each layer at the boundaries. When the 2N linear equations are solved for the A_j and B_j's, each separate term in an expression for an A_j or B_j will be multiplied by the factor given by eqn. (2.15) or by $\delta(k)$. Thus, the evaluation of eqns. (2.21) and (2.23) is similar to the evaluation of eqn. (2.12) except for the trivial integration of terms multiplied by $\delta(k)$.

We turn now to some of the results obtained from the airflow model described above. The inclusion of the effects of moisture in the airflow model results in air which is less stable than when moisture is neglected since $b\beta_E < \beta$. However, the effects of the lessened stability on the airflow depends on all of the flow parameters. Consequently, the inclusion of moisture has, in some situations, a marked effect and, in others, very little effect on the airflow.

As a first example, we consider a case in which we divide the atmosphere into three layers separated by the streamlines $z_o = 1.6$ km and $z_o = 2.9$ km. The top and botton layers are dry with $\mu_d = 0.59 \text{ km}^{-1}$ and 0.45 km^{-1}, respectively. The middle layer is always saturated with $\mu_w = 0$. (These conditions were taken from an actual sounding.) We will define $h_w(x)$ as the height at x of the streamline defined by $z_o = 2.9$ km as calculated for this flow (this streamline defines the cloud top). A parallel calculation in which moisture effects were ignored was made. In this case the middle layer was dry with $\mu_d = 0.71\ km^{-1}$ (this is the appropriate value of μ_d for the previous μ_w). We define $h_d(x)$ as the height at x of the streamline defined by $z_o = 2.9$ km for this flow. Fig. 2.1 shows $h_w(x) - h_w(-\infty)$ and $h_w(x) - h_d(x)$. It can be seen that in this case neglect of the dynamical effects of the moisture would result in a considerable error in the streamlines in some regions of the flow.

We consider next calculations based on a two-layer model, with the boundary streamline between the layers being located at $z_o = 1.0$ km well upwind of the mountain. If both layers are dry, with $\mu_d = 0.8\ km^{-1}$ in the top layer and $\mu_d = 0.6\ km^{-1}$ in the lower layer, the model predicts streamlines as shown in Fig. 2.2. As an alternative, we may assume that the lower layer becomes saturated above the 1.1 km level with $\mu_w = 0$. The differences between the streamlines for these two cases are shown in Fig. 2.3, where $h_d(x)$ is the height at x of the streamline defined by $z_o = 1.0$ km for the first case and $h_w(x)$ the corresponding height for the second case. It can be seen that the inclusion of a transition from unsaturated to saturated conditions has little effect on the airflow. The region in which the air becomes saturated (i.e. a cloud forms) in the second case is indicated in Fig. 2.2.

In combining the airflow model described in this paper with the microphysical model described below we generally divide the atmosphere into three layers, however, there is no restriction on the number of layers into which the atmosphere may be divided in the airflow model. Also, since we have shown above that the airflow is not very sensitive to transitions between saturated and unsaturated air, such transitions are generally neglected. In the case of airflow over the Cascade Mountains, layers of cloudy air often exist far upwind. These layers are assumed to remain saturated throughout their passage over the mountain. This assumption might be incorrect in the downflow on the leeward side of the mountain, but we are primarily concerned with the upwind flow.

A serious difficulty encountered in a two-dimensional model of airflow over a mountain is the inability to describe the motion of air which fails to pass over the mountain. This is referred to as <u>blocking</u>. When the critical

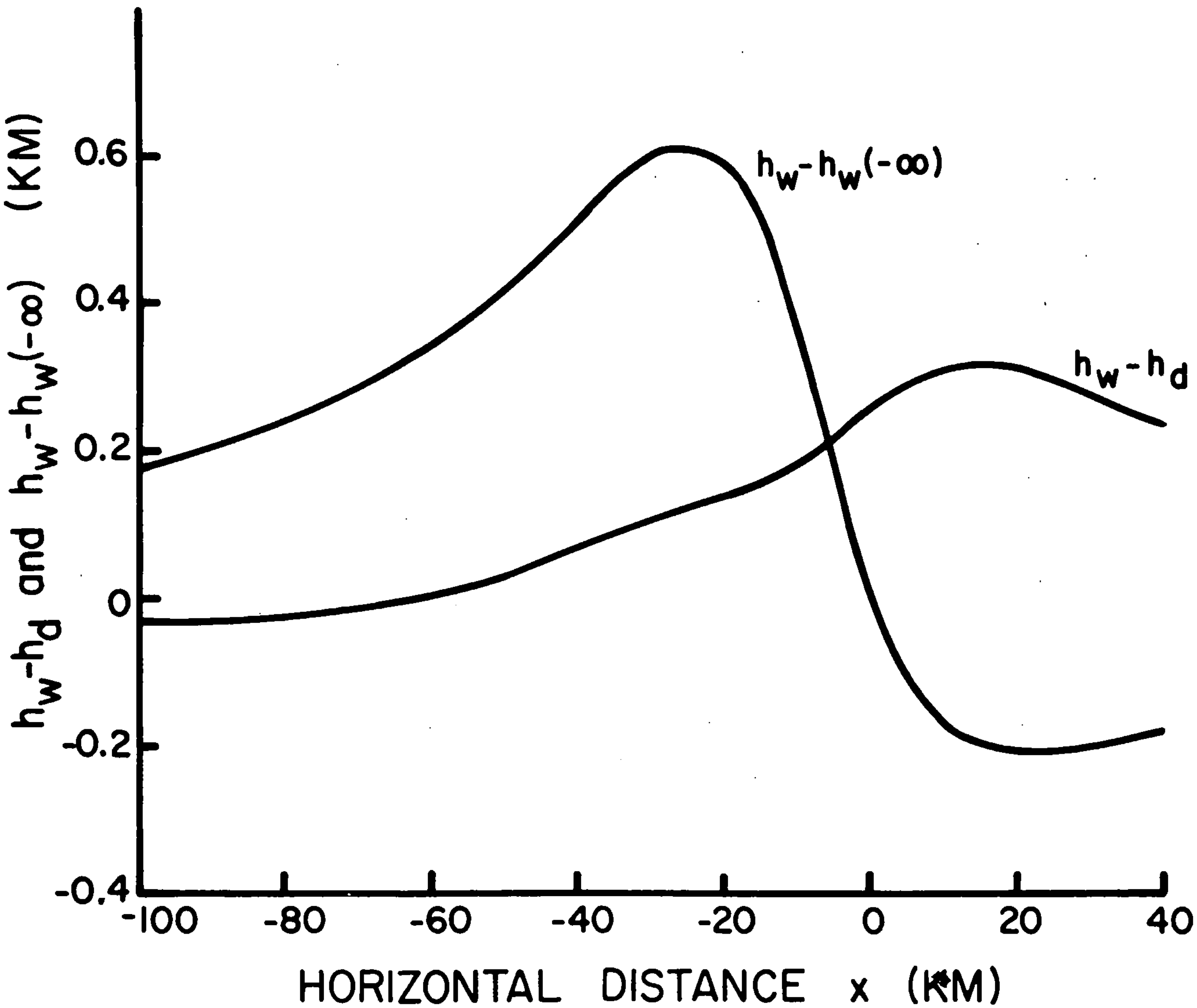

Fig. 2.1 Comparison of three-layer calculation with and without saturated middle layer. The curve marked h_w - h_w $(-\infty)$ gives the vertical displacement of a streamline as it moves across a smoothed profile of the Cascade Mountains, the summit of which is located at x = -12 km, when a saturated middle layer is included. The curve marked h_w - h_d gives the difference in height at x between corresponding streamlines with and without the saturated middle layer.

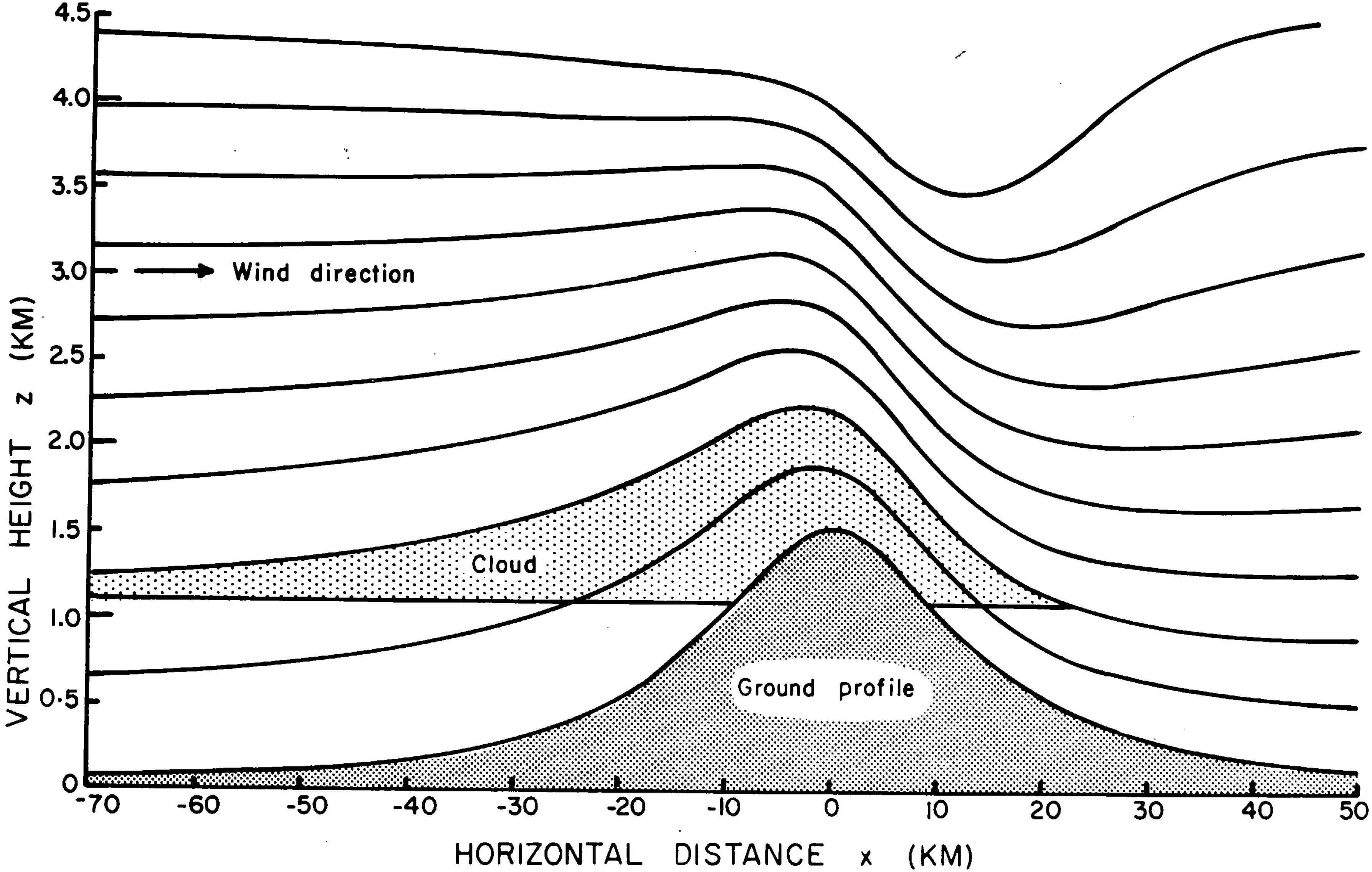

Fig. 2.2 Calculated streamlines over an arbitrary mountain for two-layer model without unsaturated-saturated transition. Location of cloud for case with transition is also indicated.

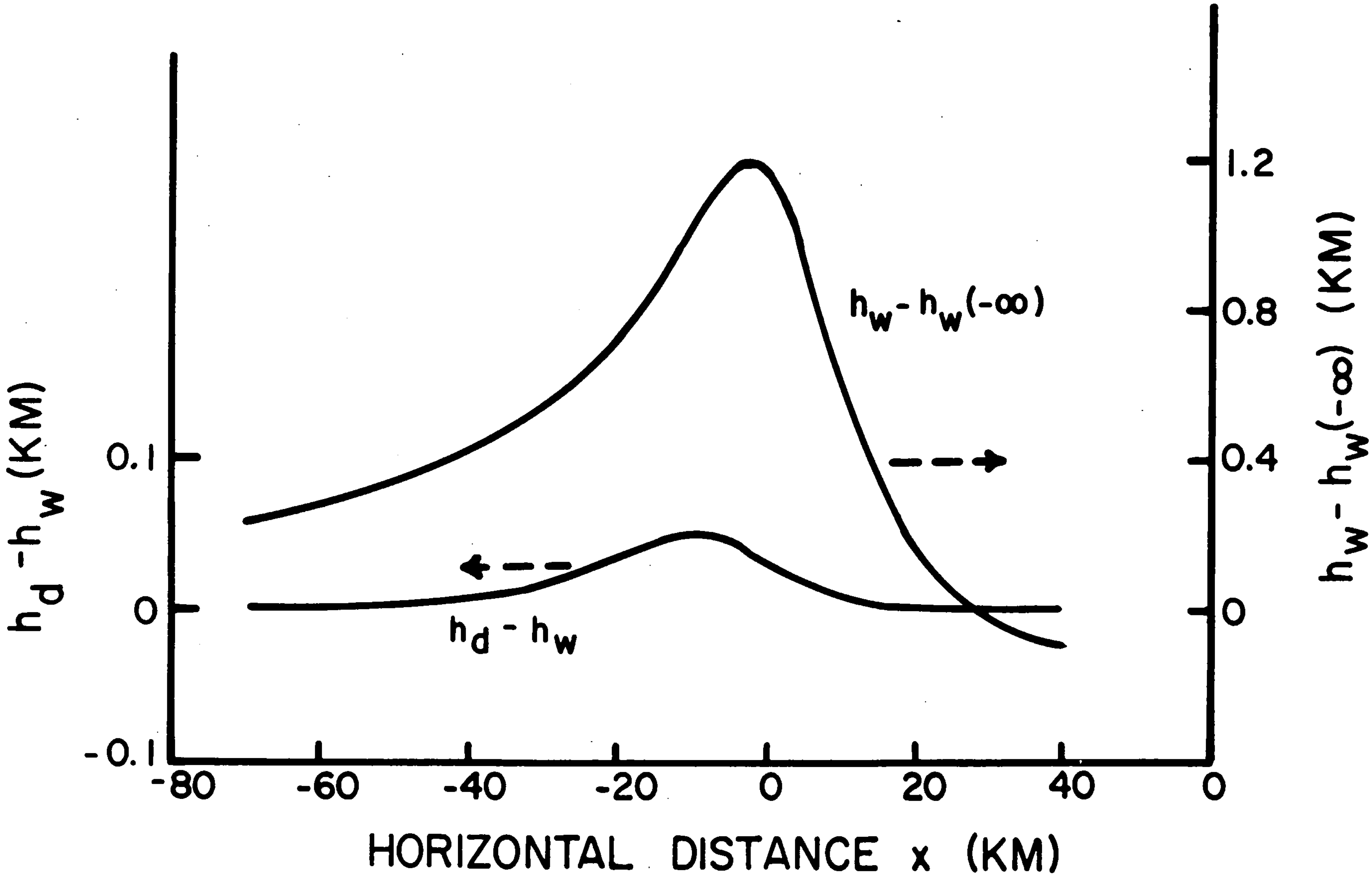

Fig. 2.3 Comparison of two-layer calculations for mountain shown in Fig. 2.2 with and without transition between saturated and unsaturated conditions. (Symbols are same as in Fig. 2.1).

wave number becomes large (a condition associated with high stabilities and low wind speeds) the model may predict individual streamlines with multiple solutions in the vertical. At certain levels, the streamlines may bend backwards into the wind or closed circulation patterns may form. While this may be a realistic result in the lee of a mountain, it is probably not so above or upwind of the mountain. Instead, it is probably indicative of a blocking situation in which the air moves out laterally along the windward side of the mountain in some three-dimensional pattern. Blocking is simulated in our model by introducing an artificial profile for the mountain which is higher in elevation than the actual profile (see Hobbs et al., 1971).

2.2.2 Microphysics†

Hobbs et al. (1971) considered the growth of ice particles in orographic clouds due to diffusion from the vapor phase and riming and, combining these results with the airflow model, they determined the trajectories of precipitation particles as they grow and fallout over the Cascade Mountains under various conditions. This model has since been extended in several ways, in particular the growth of crystals by aggregation has now been included. This recent work is described below.

The rate of increase in mass M of an ice particle is given by

$$\frac{dM}{dt} = \left(\frac{dM}{dt}\right)_{riming} + \left(\frac{dM}{dt}\right)_{deposition} + \left(\frac{dM}{dt}\right)_{aggregation} \qquad (2.31)$$

Equations for the rate of increase by riming and by deposition have been discussed by Hobbs et al. (1971) and will not be repeated here.

The growth of an ice crystal by aggregation with other ice particles can be approximated by the continuous growth equation:

$$\left(\frac{dM}{dt}\right)_{aggregation} = \pi r^2 \left(V_c - V_a\right) E_a X \qquad (2.32)$$

where, r is the effective radius of the crystal at time t, V_c and V_a the fall speeds of the crystal and ambient ice particles being collected, respectively, E_a the collection efficiency and X the ice content due to the ambient crystals.

†This section is based on a paper entitled "A Theoretial Study of the Flow of Air and Fallout of Solid Precipitation Over Mountainous Terrain: Part II. Microphysics" by P.V. Hobbs, R.C. Easter and A.B. Fraser. J. Atmos. Sci., 30:801-812, 1973.

The collection efficiency E_a may be written as

$$E_a = C_a S_a \tag{2.33}$$

where, C_a is the collision efficiency of an aggregate with the ambient ice particles and S_a the probability that an ice particle adheres to the aggregate after collision (which we call the sticking probability). In our calculations we assume that C_a = 0.5 or 1.0 (both values tried) for $V_c > V_a$, and $C_a = 0$ for $V_c < V_a$. Since aggregation is observed to be strongly dependent on temperature, a temperature-dependent sticking probability is used. Two types of sticking probability are used and these are shown in Fig. 2.4. Type I was obtained by fitting a polynomial to field data on the average size of ice crystal aggregates as a function of temperature (Hobbs, 1973) and then normalizing the maximum size to unity. Type II assumes a sticking probability of unity from 0 to -15°C and zero below -15°C.

The mass of an ice particle at a given time as it grows in a cloud may be computed from eqn. (2.31). However, in order to determine the trajectory of the particle in a given airflow the fall speed of the particle must be determined. This is achieved through equations of the form

$$M = ar^b \tag{2.34}$$

and,

$$V_c = cr^d \tag{2.35}$$

where M is the mass of the ice particle in gm, r the radius in cm of the enscribed sphere for the particle, and a, b, c, d constants for a given type of ice particle over a certain range of sizes.

The values used by Hobbs et al. (1971) for a, b, c and d in eqns. (2.34) and (2.35) were based on the best measurements available at the time. Recently we have obtained detailed measurements of the masses and fall speeds of different types of ice particles which fall over the Cascade Mountains (Locatelli and Hobbs: to be published) and by combining these measurements with those of other workers we are now able to improve on our previous estimates. The values now used are described below.

We divide ice particles into four general types which allow consideration of degree of riming and aggregation. They are: unrimed plate-like crystals, lightly to moderately rimed plate-like crystals, graupel, and aggregates of

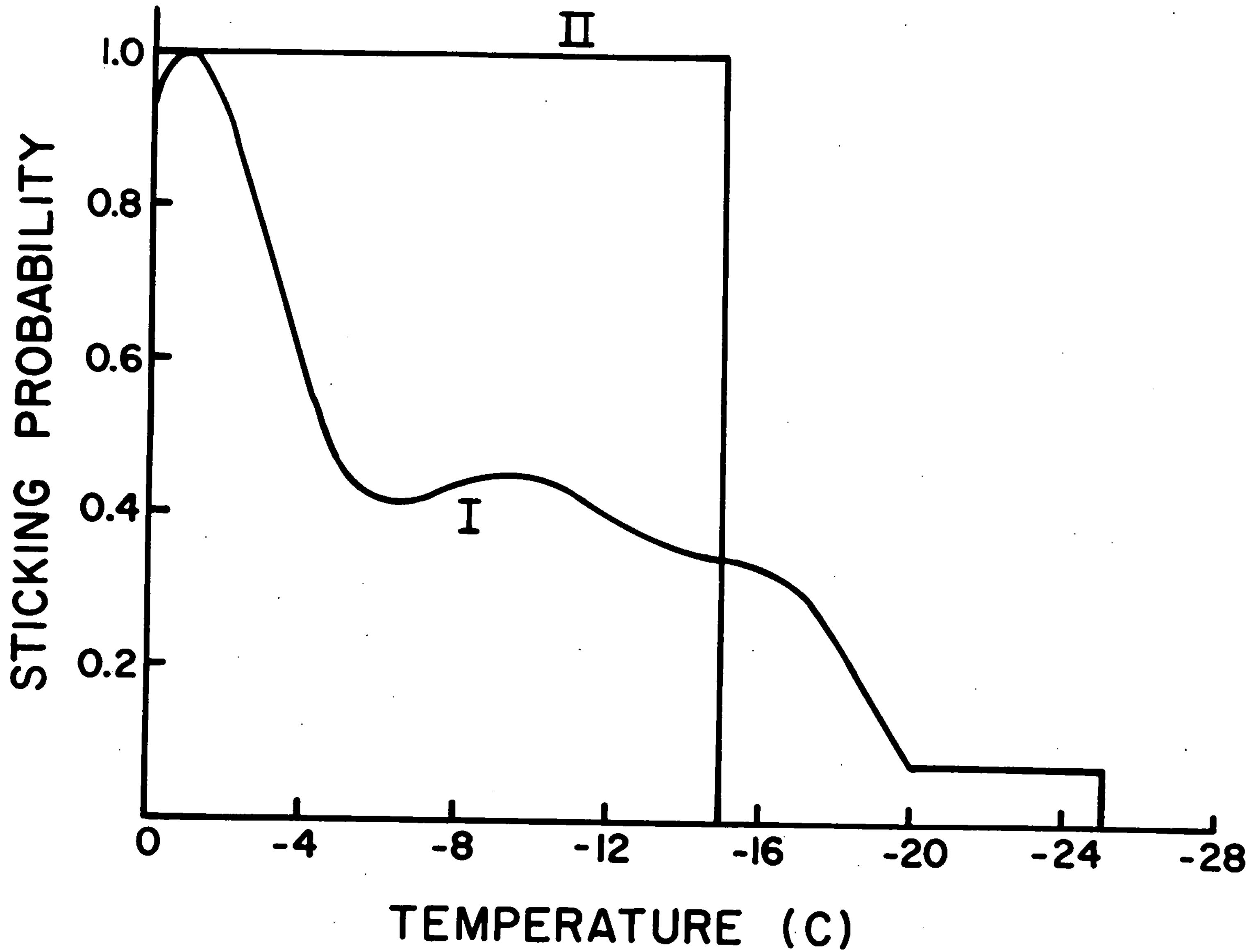

Fig. 2.4 Two types of temperature-dependent sticking probabilities for ice particles used in calculations. Type I is based on field observations by Hobbs (1973).

unrimed dendrites. Variations of crystal habit with temperature are not considered since their effects on the mass and fall speed of a particle appear to be less important than riming and aggregation.

Unrimed plate-like crystals are divided into the following three size ranges: (i) Those which fall with Reynold's number less than 0.1 ($r < 3.5 \times 10^{-3}$ cm), have a density of 0.35 gm cm^{-3}, and an axial ratio (length of c-axis/length of an a-axis) of 5.15 (Auer and Veal, 1970). The terminal velocity of these crystals is computed from the equation for Stokes' flow. (ii) For large (planar-dendritic) crystals with $r > 0.05$ cm, the mass is related to the size by eqn. (2.34) with $a = 1.51 \times 10^{-3}$ and $b = 2$ (Nakaya and Terada, 1935). The velocity is determined from eqn. (2.35) using values for c and d based on an average of the results of Nakaya and Terada and Brown (1970), namely, $c = 76.9$ and $d = 0.32$. (iii) For planar dendritic crystals with 3.5×10^{-3} cm $< r <$ 0.05 cm, the mass-size relation is the same as for crystals of this type with $r > 0.05$ cm. The velocities are obtained by interpolating logarithmically between the values at $r = 3.5 \times 10^{-3}$ and $r = 0.05$ cm.

For lightly to moderately rimed crystals, the mass-size relationship given by Nakaya and Terada is used for $r > 0.013$ cm, and the terminal fall speed-size relationship found by Langleben (1954) is used for $r > 0.032$ cm. However, for smaller crystal sizes the above formulae would predict that a lightly rimed plate has a greater mass and a greater terminal fall speed than a graupel particle with the same values of r. Since this seems unrealistic, the values of a, b, c and d appropriate to graupel particles are used for the smaller lightly rimed plates.

Our measurements of the dependences of the masses and fall speeds of graupel particles on r are fitted by eqns. (2.34) and (2.35) with $a = 0.23$, $b = 2.7$, $c = 7.18 \times 10^{4}$, and $d = 1.7$. This mass-size relationship is used for all sizes of graupel particles. However, for $r < 0.05$ cm, the fall speed of graupel particles is assumed to be the same as that of a sphere with mass given by eqn. (2.34) with values of a and b as above.

The dependence on r of the masses and fall speeds of aggregates of unrimed dendrites over the size range $0.025 < r < 0.7$ cm have also been measured by Locatelli and Hobbs. The results can be fitted by eqns. (2.34) and (2.35) with $a = 7.6 \times 10^{-3}$, $b = 2$, $c = 117$, and $d = 0.206$. The experimental results are extrapolated to larger or smaller aggregates of unrimed dendrites when necessary.

A summary of the relationships between sizes, masses and fall speeds of the different ice particles used in our model is contained in Table 2.1.

In those numerical calculations in which growth by deposition and riming are compared, only unrimed crystals and graupel particles are considered. In this case, ice particles grow either by deposition alone or they are converted to graupel and grow predominantly by riming. This is a good assumption in the context of the present model since at small sizes we treat rimed crystals and graupel identically.

In comparing growth by aggregation with growth by riming, all four particle types listed in Table 2.1 are allowed. An ice particle is placed into one of the four categories depending on the percentages of its mass which have been accrued by riming (R^*) and by aggregation (A^*). Two methods of classification were used and these are shown in Table 2.2. However, since both methods produced quite similar results, only the results obtained using the first method are presented below.

In calculating the trajectories of the solid precipitation particles, the horizontal and vertical coordinates and the mass of the ice particle are computed at small time increments (50 sec) along the path of the trajectory. The wind, temperature, pressure and condensation-product at the position of the particle are calculated, and these values are assumed constant over the next time increment. For the initial time steps, when the ice particle is growing only by deposition, the position and mass of the particle after each increment in time can be determined from a simple analytic solution to the growth and motion equations. After the particle becomes large enough to grow by riming or aggregation, the equations for the vertical height (z) and mass (M) of a particle are solved numerically. When growth by aggregation is not considered, a simple Eulerian method is used to calculate z and M. In comparing growth by aggregation and riming, a fourth-order Runge-Kutta scheme is used to calculate z and M and also the masses acquired through riming and aggregation. The equation for M is given by eqn. (2.31) and that for z is

$$\frac{dz}{dt} = w - V_c \qquad (2.36)$$

TABLE 2.1

RELATIONSHIPS BETWEEN SIZES, MASSES, AND FALL SPEEDS

OF ICE PARTICLES USED IN THE MODEL

(See text for sources of data.)

Crystal Types	Crystal Radius r (cm)	Crystal Mass M (gm)	Crystal Terminal Velocity V_c (cm sec^{-1})
Unrimed planar crystals	$r<0.0035$	$M = 0.430\ r^3$	$V_c = 1.65 \times 10^5\ r^2$
	$0.0035<r<0.05$	$M = 1.51 \times 10^{-3}\ r^2$	$V_c = 608\ r^{1.01}$
	$0.05 < r$		$V_c = 76.9\ r^{0.32}$
Lightly to moderately rimed planar crystals	$r<0.0073$	$M = 0.23\ r^{2.7}$	$V_c = 7.18 \times 10^4\ r^{1.7}$
	$0.0073<r<0.013$	"	$V_c = 2.54 \times 10^3\ r^{1.02}$
	$0.013<r<0.032$	$M = 0.0108\ r^2$	"
	$0.032<r$	"	$V_c = 210\ r^{0.2}$
Graupel	$r<0.0073$	$M = 0.23\ r^{2.7}$	$V_c = 7.18 \times 10^4\ r^{1.7}$
	$0.0073<r<0.050$	"	$V_c = 2.54 \times 10^3\ r^{1.02}$
	$0.050<r$	"	$V_c = 790\ r^{0.63}$
Aggregates of unrimed dendrites	————	$M = 7.6 \times 10^{-3}\ r^2$	$V_c = 117\ r^{0.206}$

TABLE 2.2

METHODS USED FOR CLASSIFYING ICE PARTICLES. A^* AND R^* ARE THE PERCENTAGES OF THE MASS OF THE PARTICLE ACCRUED BY AGGREGATION AND RIMING, RESPECTIVELY

Particle Type	Method I	Method II
Unrimed planar crystal	$A^* < 50$, $R^* < 10$	$A^* < 50$, $R^* < 25$
Lightly to moderately rimed planar crystal	$A^* < 50$, $10 < R^* < 50$	$A^* < 50$, $25 < R^* < 75$
Graupel	$A^* < 50$, $R^* > 50$	$A^* < 50$, $R^* > 75$
Aggregates of unrimed dendrites	$A^* > 50$	$A^* > 50$

2.2.3. Results

(a) Comparison of Growth by Riming and Deposition

Examples of the trajectories of ice particles grown by riming and deposition and by deposition alone as they fall out over the Cascade Mountains are shown in Figs. 2.5 - 2.7. The airflow model described in §2.2.1 was used to predict the horizontal and vertical winds for these results. The vertical distributions of temperature and wind speed used in these calculations are shown in Fig. 2.8. These distributions were taken as input data for the airflow model along vertical lines located at x = -30 km in Figs. 2.5 and 2.7 and at x = -70 km in Fig. 2.6. In Figs. 2.5 - 2.7 the Cascade crest is located at x = -15 km. The terrain of the Cascades falls away to a broad valley east of the crest (Figs. 2.5 and 2.7) but northeast of the crest there exists another range of mountains (Fig. 2.6).

Fig. 2.5 shows six trajectories in a westerly flow. At each of the two starting positions (A and B) three trajectories originate which correspond to specified ice particle concentrations (N_o) of 1, 25 and 100 per liter. The number shown at the end of each trajectory is the product of the ice particle concentration (per liter of air) and the mass (in mg) of an ice particle at the ground. It therefore represents the total mass of precipitation which reaches the ground at the indicated point which originated in one liter of air at the beginning of the trajectory.

It can be seen from Fig. 2.5 that as the concentration of ice particles is increased, the particles tend to be carried further downwind and the amount of precipitation reaching the ground increases. Thus, when the concentration of ice particles is increased from 1 to 100 per liter, the solid precipitation particles are carried over the crest of the Cascade Mountains and reach the ground about 70 km further east; the mass of precipitate reaching the ground, which originates from the same unit volume at A, increases from 0.089 to 0.57 mg. This is because at a concentration of 1 ice particle per liter, growth is mainly by riming so the particles become densely rimed and attain relatively large fall speeds. At high concentrations of ice particles, on the other hand, diffusional growth generally dominates and less dense ice particles with smaller fall speeds are formed. The trajectories originating at B pass through a region of strong updraught where the critical concentration (N_c) of ice particles is greater than 25 per liter. Consequently, the trajectories for 1 and 25 particles per liter are identical.

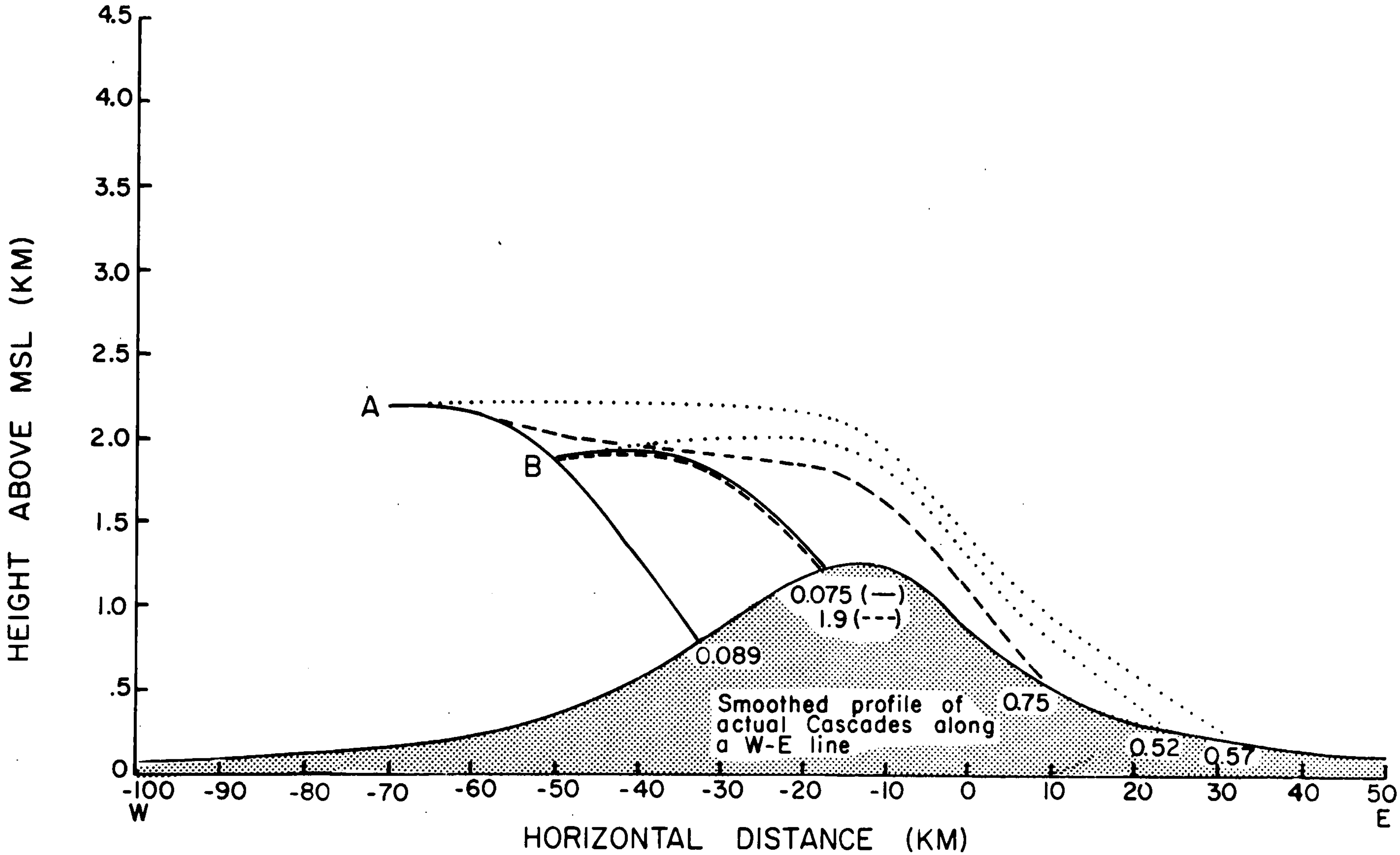

Fig. 2.5 Calculated trajectories for precipitation particles growing by deposition and riming over the Cascade Mountains in a westerly airstream for the following specified concentrations of ice particles: 1 per liter (———), 25 per liter (- - -), 100 per liter (•••). The number at the end point of each trajectory is the total mass (in mg) of precipitation which reaches the ground at that point originating in a volume of 1 liter at the starting point of the trajectory.

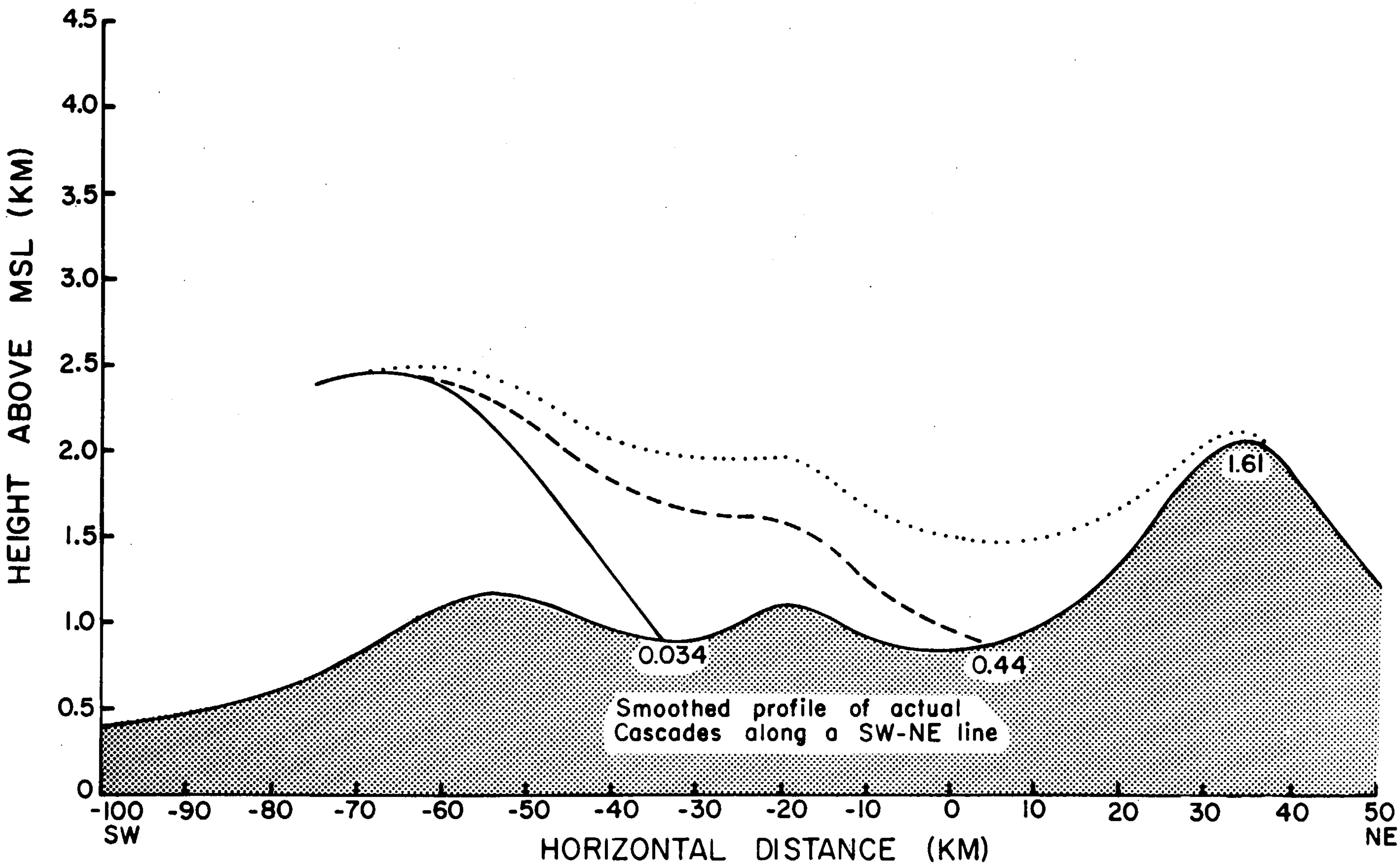

Fig. 2.6 Calculated trajectories for precipitation particles growing by deposition and riming over the Cascade Mountains in a southwesterly airstream for the following specified concentrations of ice particles: 1 per liter (——), 25 per liter (– – –), 100 per liter (• • • •). The number at the end of each trajectory is the total mass (in mg) of precipitation which reaches the ground at that point originating in a volume of 1 liter at the starting point of the trajectory.

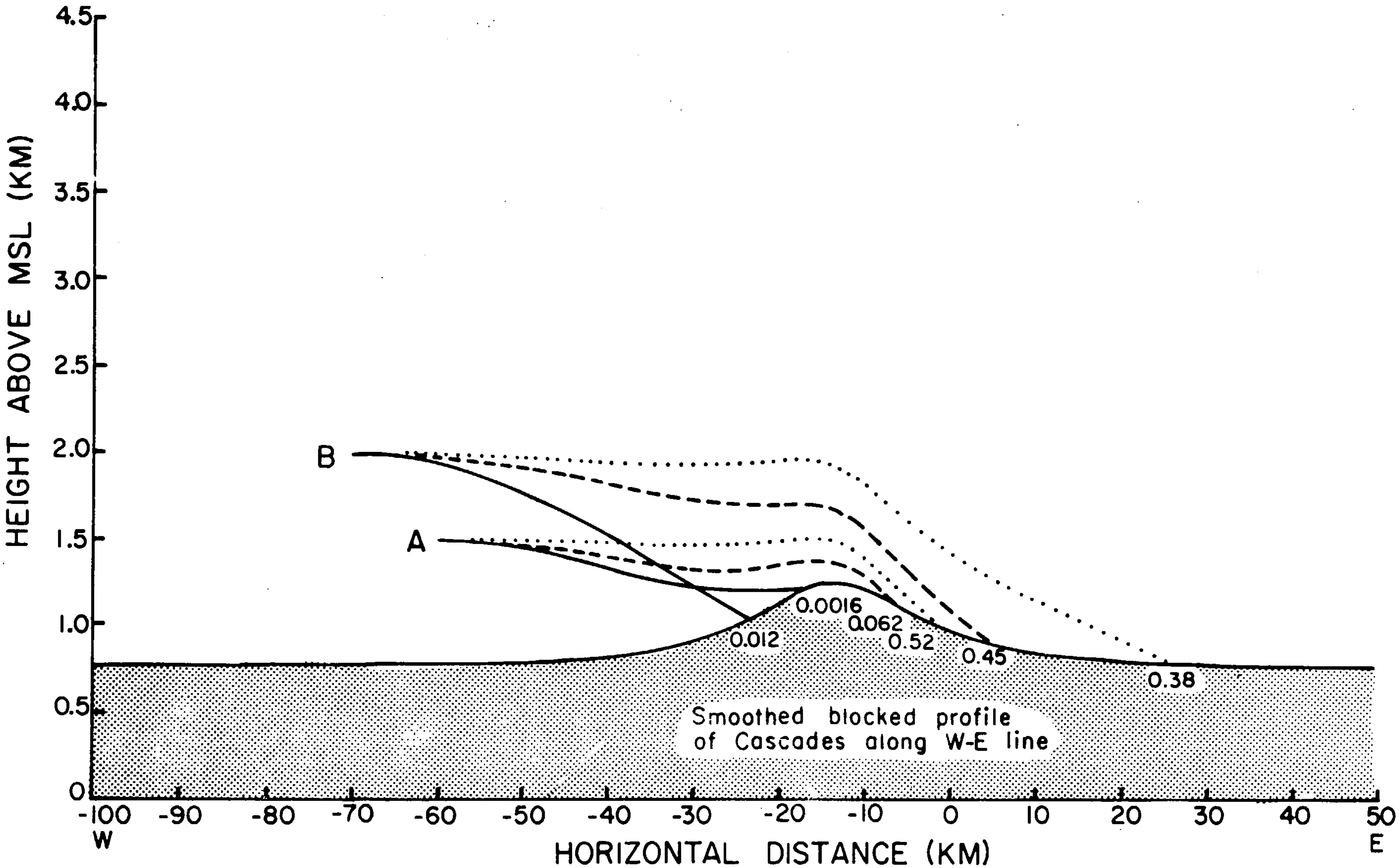

Fig. 2.7 Calculated trajectories for precipitation particles growing by deposition and riming over the Cascade Mountains in a westerly airstream with simulated blocking. Specified concentrations of ice particles are 1 per liter (——), 25 per liter (– – –), 100 per liter (• • •). The number at the end point of each trajectory is the total mass (in mg) of precipitation which reaches the ground at that point originating in one liter at the starting point of the trajectory.

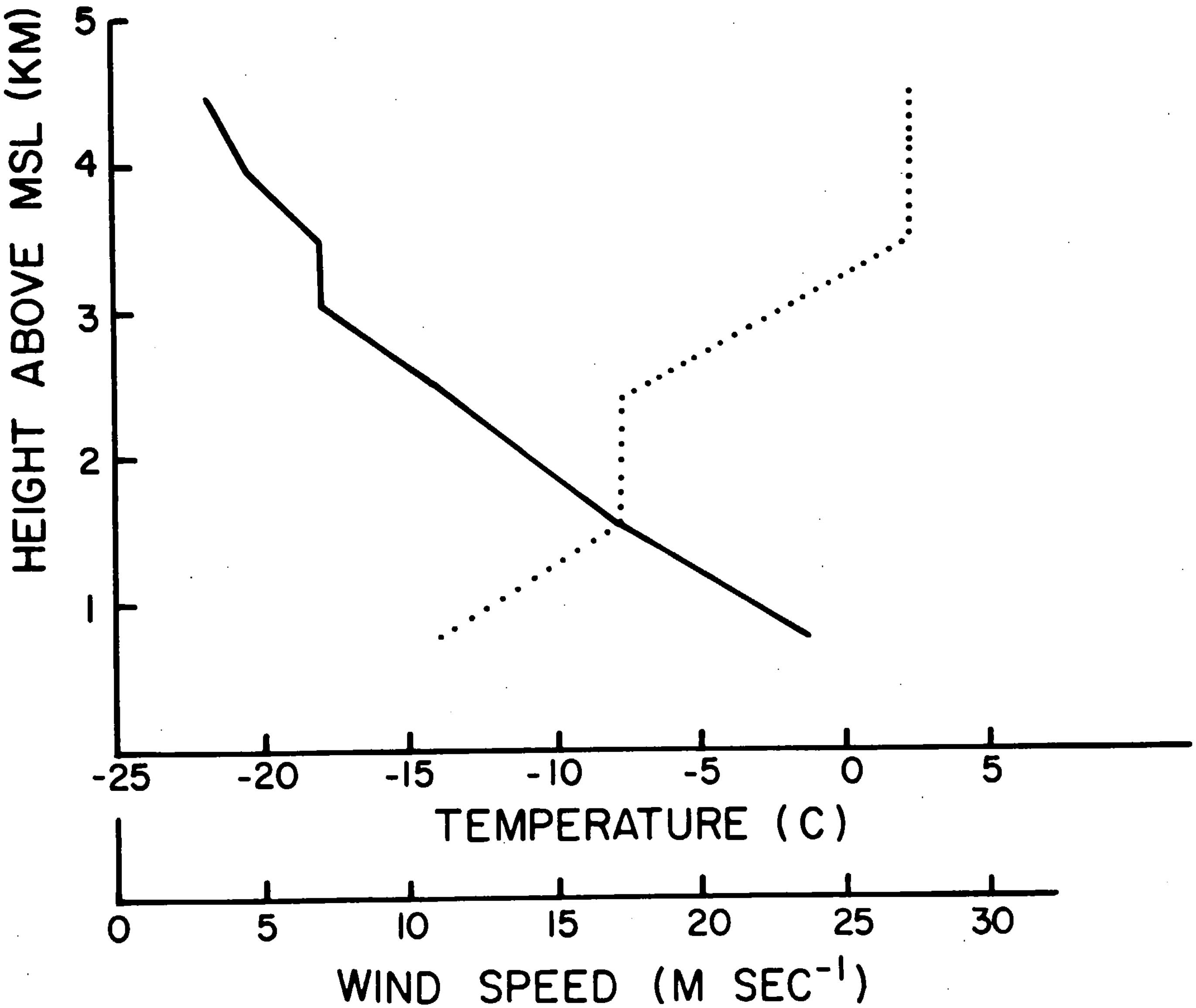

Fig. 2.8 Vertical profiles of temperature (——) and wind (•••) used for results shown in Figs. 2.5, 2.6, and 2.7.

It should be noted that when N_o and N_c are comparable, neglect of the depletion of cloud water by riming and diffusional growth are serious. Ignoring the possibility of aggregation, the cases where $N_o << N_c$, or vice versa, are treated most realistically by the model.

Fig. 2.6 shows three trajectories in a southwesterly airflow over the Cascade Mountains. Again the trajectories lengthen with increasing concentration of ice particles. The effect of the additional mountain ridge to the northeast of the crest is to produce a second region of updraughts in which further growth of the ice particles occurs under glaciated conditions. Thus the final mass of the precipitated ice particles is somewhat greater than for the corresponding trajectory in Fig. 2.5.

Fig. 2.7 shows several trajectories in a westerly flow with simulated blocking. The effect of blocking is to reduce the vertical displacement of the streamlines and therefore reduce the liquid water content. Consequently, growth by riming is considerably slower and the final masses of particles grown at 1 per liter are much less than when blocking is not simulated. It should be noted that when blocking is simulated the trajectories of the ice particles are terminated at the modified profile of the mountains since winds below this level are not computed.

The above results indicate that for ice particles growing only by deposition and riming the points at which solid precipitation reaches the ground are shifted downwind as the concentration of ice particles is increased. However, since it is observed that aggregation plays an important role in the growth of ice particles in clouds, we now attempt to estimate the effect of aggregation on the trajectories of the particles.

(b) Comparison of Growth by Riming and Aggregation

Two different airflows are used to obtain the results described below. The temperature soundings for these two cases are shown in Fig. 2.9 where the two airflows are referred to as "warm" and "cold" flows. The calculated adiabatic condensation-products for these two flows are shown in Figs. 2.10 and 2.11.

The results indicate that aggregation is a more efficient growth process than riming. It should be noted, however, that the model compares the effects of equal mass concentrations of water droplets and ice particles in a cloud. A typical example is presented in Fig. 2.12 which shows the effect of the extent of the ice layer on ice particle growth. These growth curves were computed for the "warm" flow shown in Fig. 2.9, and all of the particles originated at x = -50 km and at a height of 3 km (see Fig. 2.10). The top

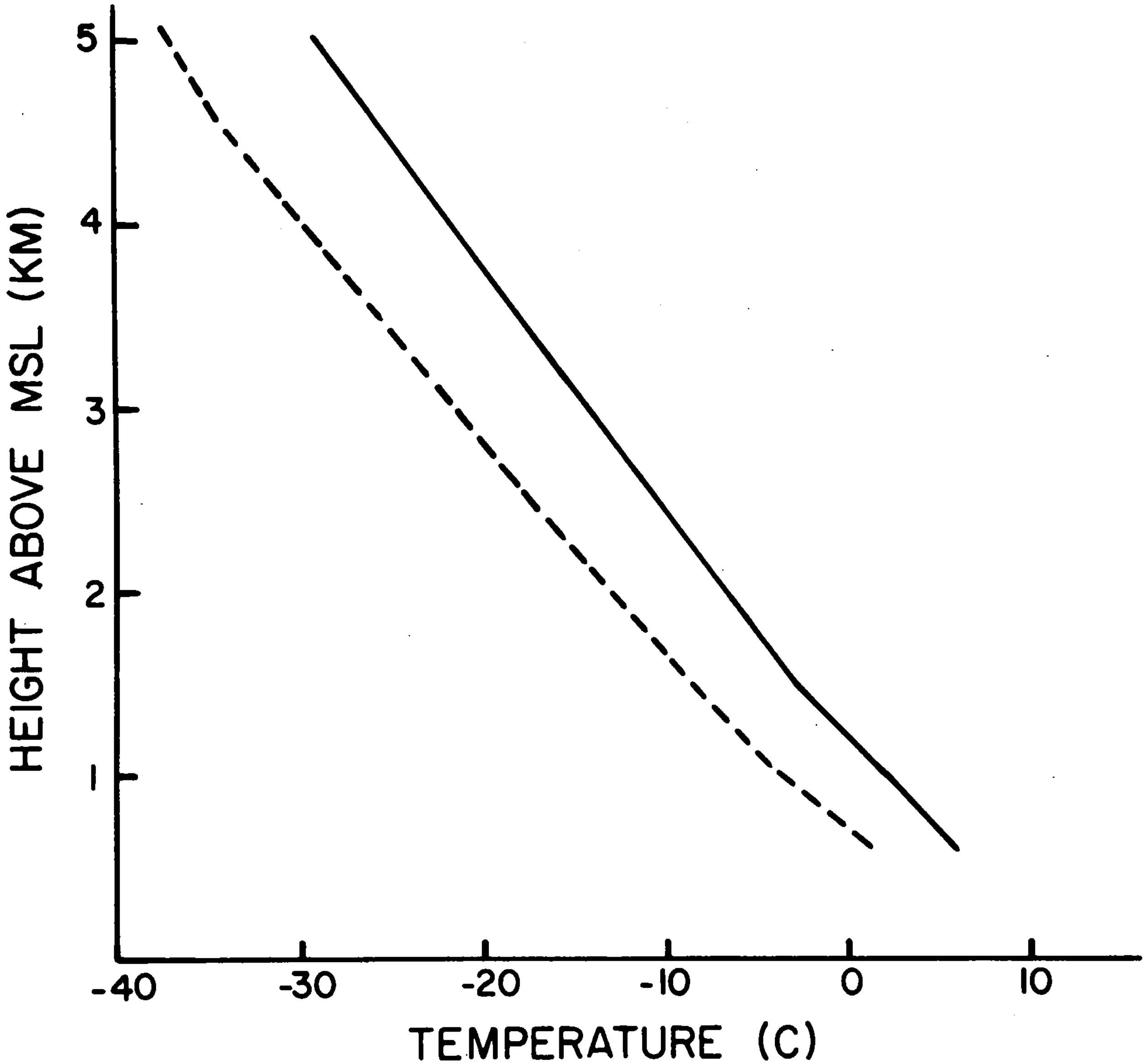

Fig. 2.9 Temperature soundings for airflows. "Warm" flow (——), "cold" flow (- - -).

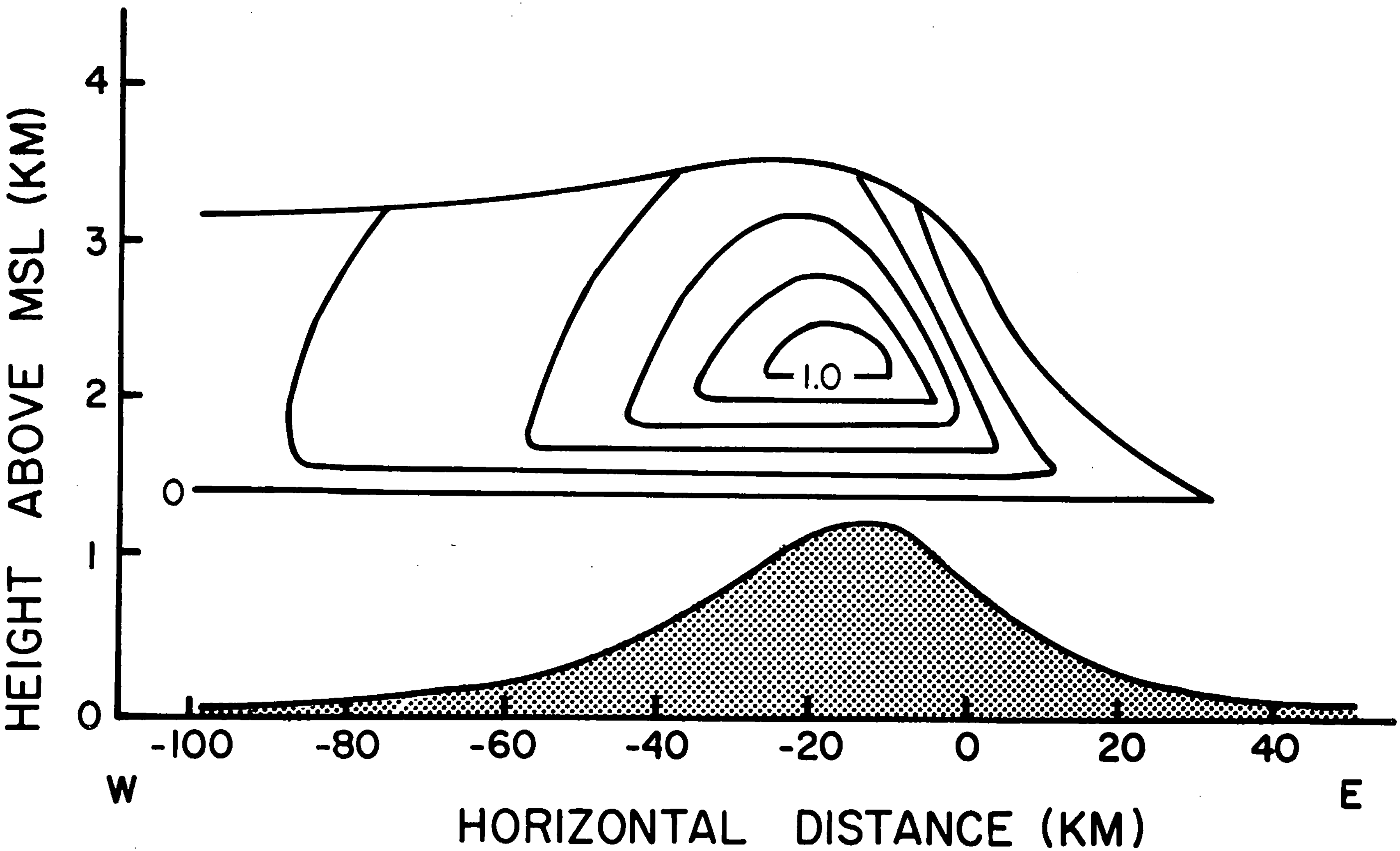

Fig. 2.10 Isopleths of adiabatic condensate content (at 0.2 gm kg^{-1} intervals) calculated from the airflow model for "warm" flow shown in Fig. 2.9. The shaded area indicates the smoothed profile of actual Cascades along a W-E line.

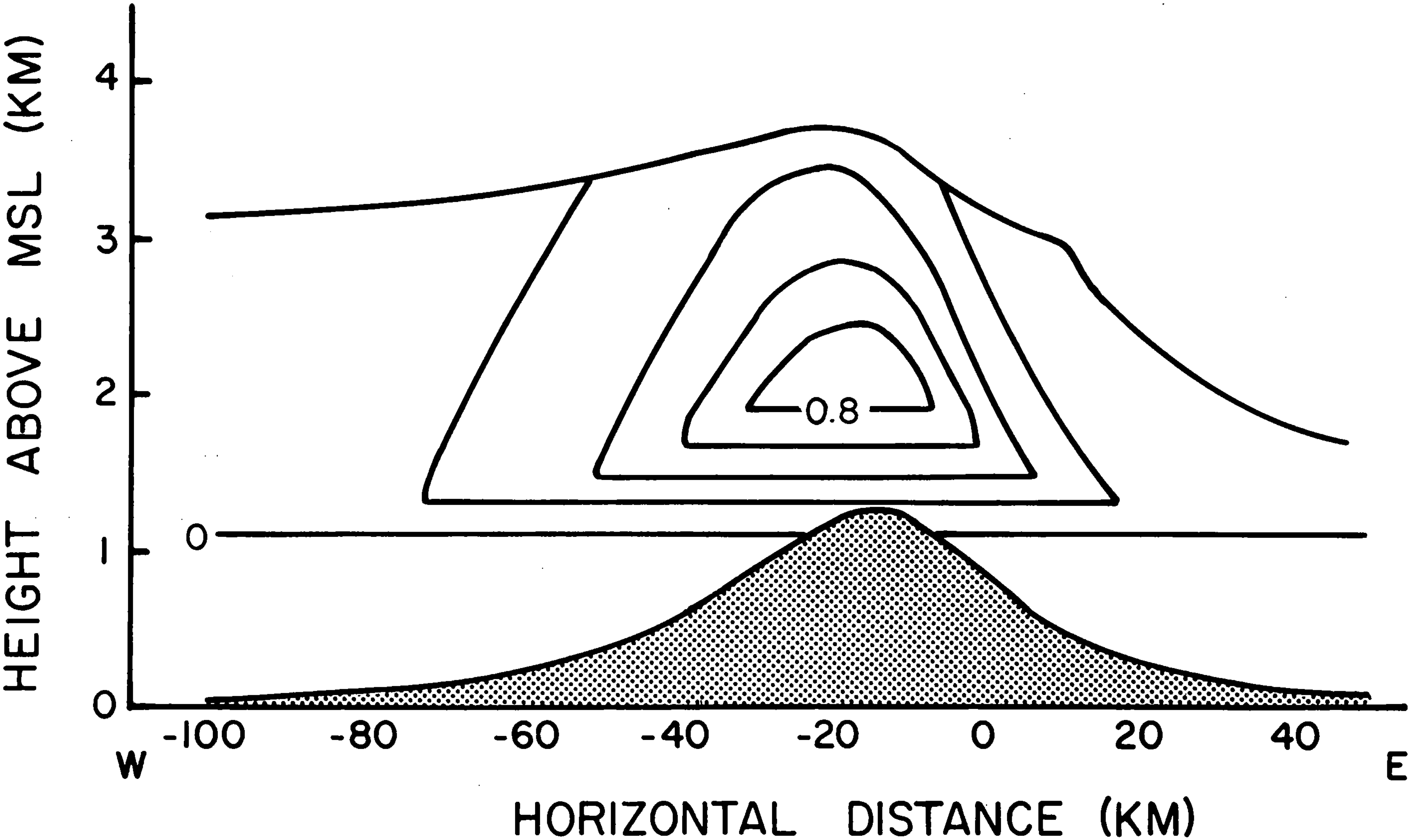

Fig. 2.11 Isopleths of adiabatic condensate content (at 0.2 gm kg^{-1} intervals) calculated from the airflow model for the "cold" flow shown in Fig. 2.9. Shaded area indicates smoothed profile of actual Cascades along a W-E line.

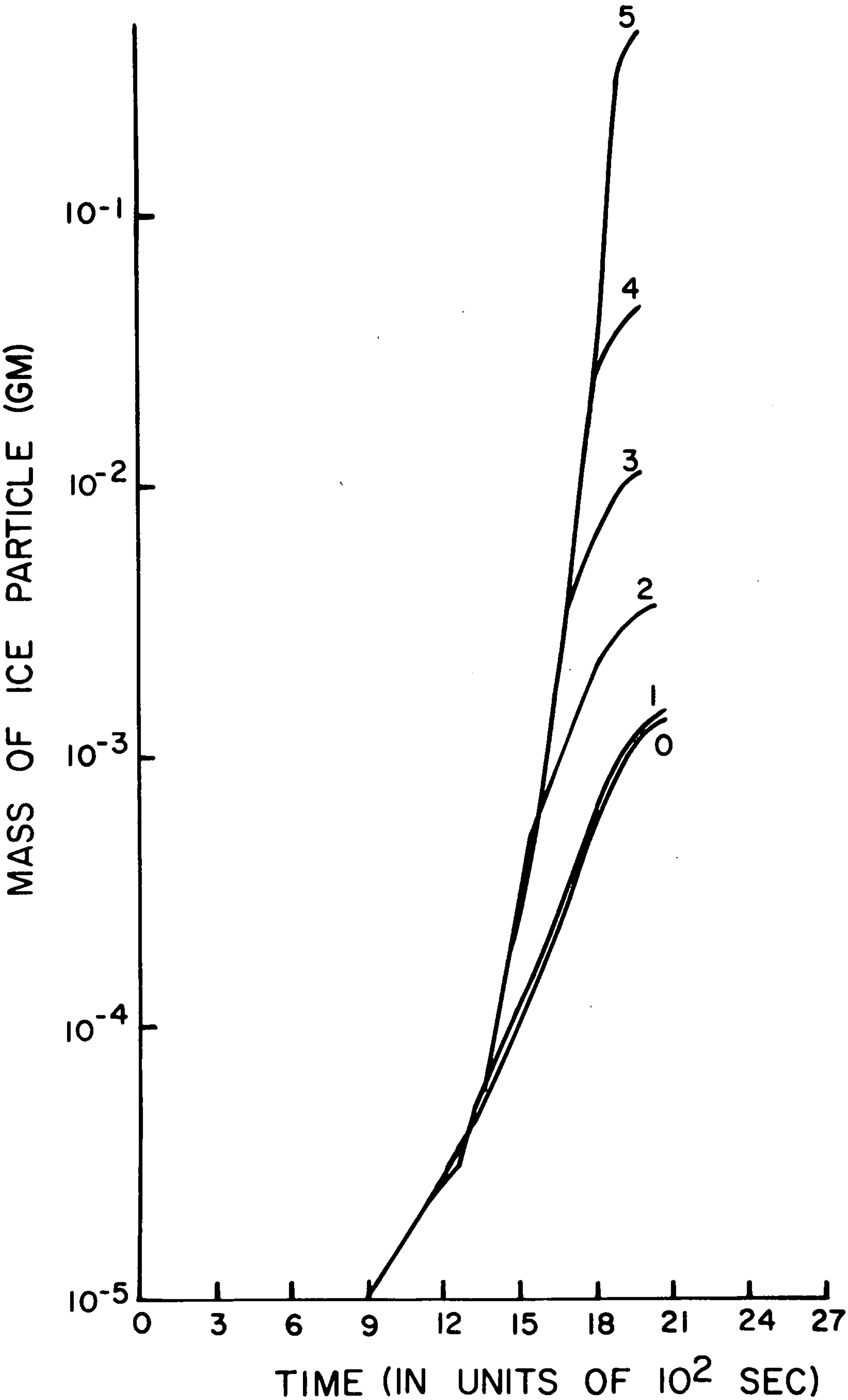

Fig. 2.12 Effect of depth of ice layer on ice particle growth. Number on each curve gives the vertical extent of the ice layer in degrees C. The results are for "warm" flow (Fig. 2.9), the sticking probability is assumed to be Type II (Fig. 2.4) and $E_r = C_a = 0.5$.

of the ice layer was the -11°C level (a height of about 2.75 km), and the vertical extent of the layer was varied at 1°C intervals. (Thus, the ice layers were in the regions -10 to -11°C, -9 to -11°C, etc.) The ambient ice particles were unrimed planar crystals 0.02 cm in radius, the riming collection efficiency and the aggregation collision efficiency were taken as 0.5, and sticking probability Type I (Fig. 2.4) was used (so that the riming and aggregation collision efficiencies were equal). It can be seen that the ice layer encompassing a temperature range of 1°C has little effect on the growth, since in this case the aggregation which occurs is not sufficient to change the particle from the graupel to the aggregate category (see Table 2.2). However, as the extent of the ice layer is increased the ice particle growth rate increases dramatically. The first order discontinuities in the curves are due to the switching from aggregates to graupel, or to lightly-rimed planar crystals, after the particles pass back into the water cloud region. The growth rates gradually decrease near the end of each trajectory as the particles approach the cloud base with its lower adiabatic condensate content.

The sticking effect of aggregation on the growth rate is readily explained as follows. If we neglect the small fall velocities of the collected particles (i.e. cloud droplets or ambient ice particles), then for both riming and aggregation growth we have

$$\frac{dM}{dz} = \frac{dM}{dt}\Big/V_c = \pi r^2 EX \qquad (2.37)$$

where $\frac{dM}{dz}$ is taken in a reference frame moving with the wind, and we have assumed a circular cross-section for the growing ice particles. Thus, for equal collection efficiencies and equal mass concentrations of collected particles for both riming and aggregation, we have

$$\frac{dM}{dz} \sim r^2 \sim M^f \qquad (2.38)$$

where $f = \frac{2}{b}$. The growth of an ice particle in a layer of specified vertical thickness can be extremely sensitive to the magnitude of f. If an ice particle grows predominantly by riming and is converted to graupel, then f = 0.72; while if an ice particle grows by the aggregation of dendritic crystals f = 1.0. Thus, under the assumptions mentioned above, growth by aggregation can be much greater than growth by riming.

For the cases shown in Fig. 2.12, a typical mass concentration of ambient particles in the ice layer was 0.6 gm kg^{-1}. For an unrimed planar-crystal 0.02 cm in radius, this corresponds to a concentration of about 1000 per liter.

The results are somewhat modified when a temperature-dependent aggregation collection efficiency is used. Specifically, at low temperatures if E_a is much smaller than E_d, the increase in mass of an ice particle by aggregation in an ice layer of limited extent may be less than its mass increase would have been by riming. This is illustrated in Fig. 2.13 which shows the final masses of ice particles, originating at x = -60 km and z = 3.0 km in Fig. 2.11, for the case of "cold" flow. The top of the ice layer was at -21°C, its thickness was varied at 1°C intervals, and the ambient ice particles were unrimed planar-crystals 0.02 cm in radius. The aggregation collision efficiency was taken as 1.0 and the Type I sticking probability (Fig. 2.4) was used.

The model results indicate that aggregation does not have a significant effect on the length of the ice particle trajectories. Fig. 2.14 shows the ratio of the horizontal displacement of an ice particle when an ice layer is present to the horizontal displacement in the absence of an ice layer based on the results shown in Figs. 2.12 and 2.13. For the "warm" flow, which has the larger sticking probability, aggregation tends to slightly shorten the trajectories since the ice particles become more massive and fall faster. For the "cold" flow, with the lower sticking probability, the trajectories are lengthened somewhat since initially the particle grows slower in the aggregation layer than it would by riming and it therefore undergoes further horizontal displacement. However, in neither case is the effect large enough to be significant.

(c) Distribution of Precipitation

Our model is unable to produce absolute precipitation rates. However, the masses of the ice particles at the points where their trajectories reach the ground provide some information about the distribution of precipitation over the mountain. In particular, comparison of this information for different conditions should demonstrate the qualitative effects of the environmental conditions on the distribution of precipitation.

Fig. 2.15 shows three such plots which were computed for the "warm" flow. All of the ice particles considered originated between values of 2.0 and 3.0 km. In one case the cloud consisted entirely of water, while for the other two cases the water-ice distribution shown in Fig. 2.16 was used. The ambient

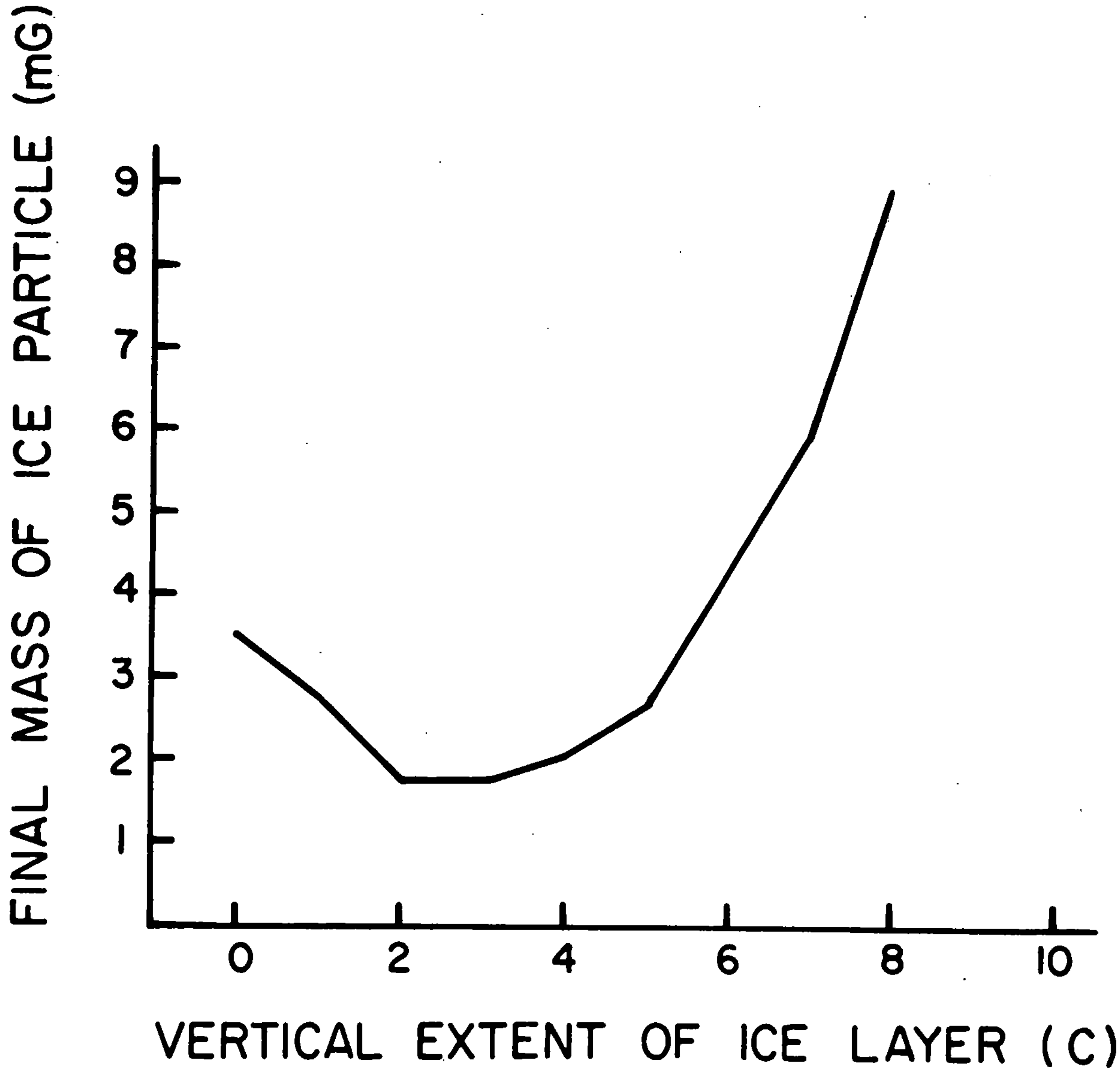

Fig. 2.13 Effects of the depth of an ice layer on ice particle growth at low temperatures with a temperature-dependent aggregation collection efficiency. The results are for Type I sticking probability (Fig. 2.4), $C_a = 1$ and "cold" flow (Fig. 2.9).

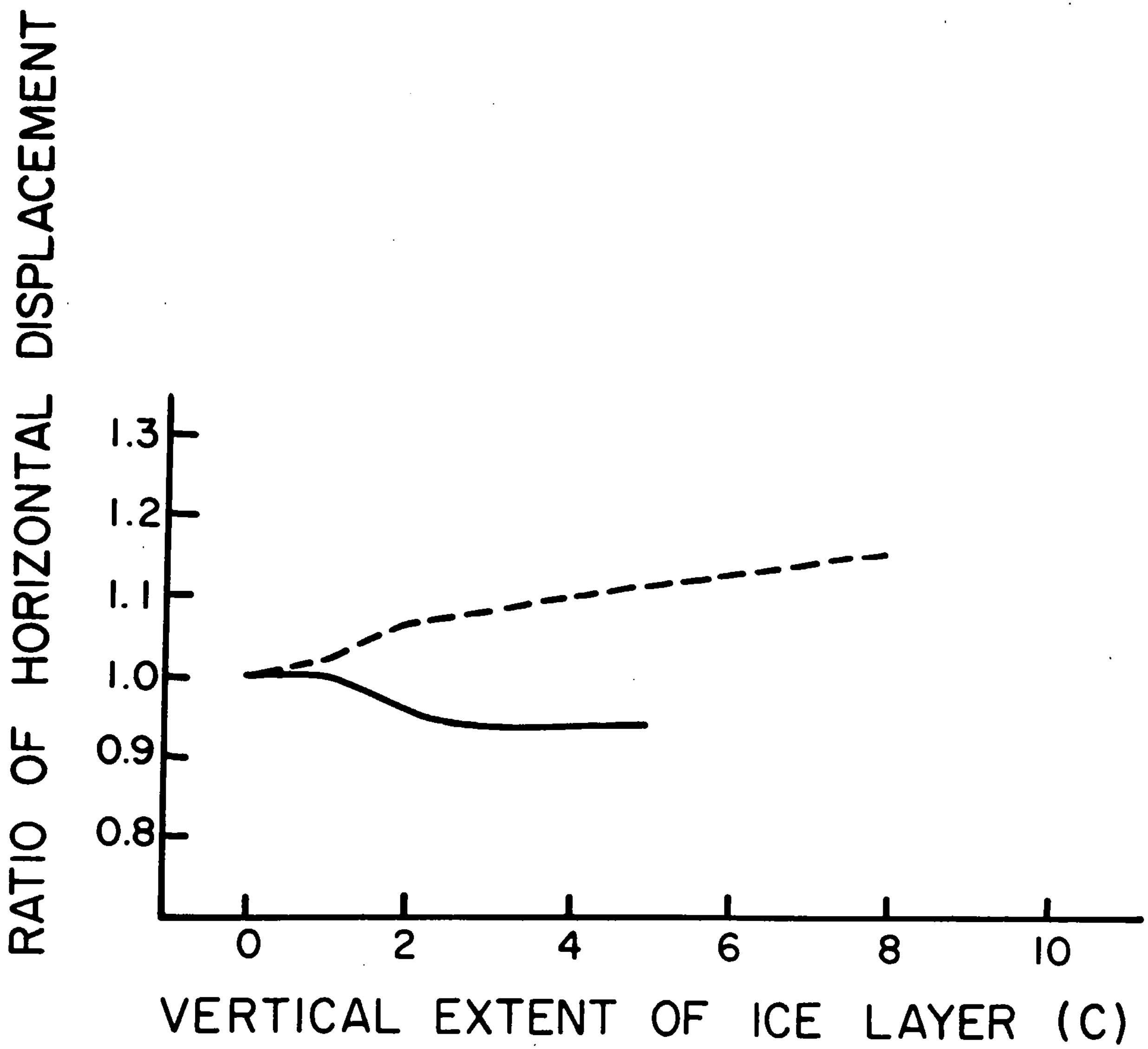

Fig. 2.14 Ratio of the horizontal displacement of an ice particle in the presence of an ice layer in which aggregation occurs to the horizontal displacement in the absence of the ice layer. "Cold" flow, top of ice layer at -21 C (----), "warm" flow, top of ice layer at -15 C (———).

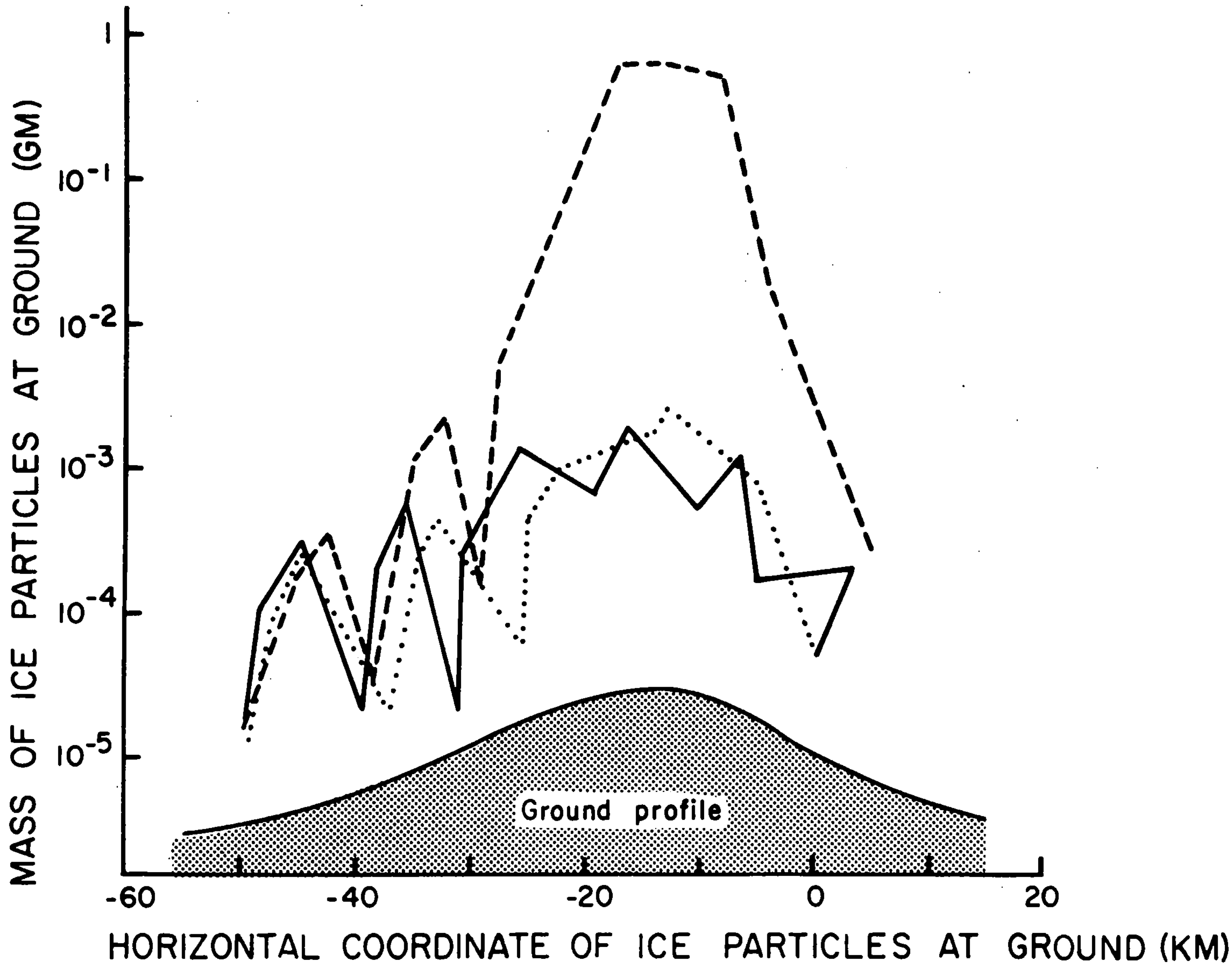

Fig. 2.15 Comparison of distributions of precipitation for a cloud without an aggregation ice layer (———), for a cloud containing an ice layer as shown in Fig. 2.16 a sticking probability of Type II and $C_a = 0.5$ (- - - -), and a cloud containing an ice layer as shown in Fig. 2.16 a sticking probability of Type I and $C_a = 0.5$ (·····).

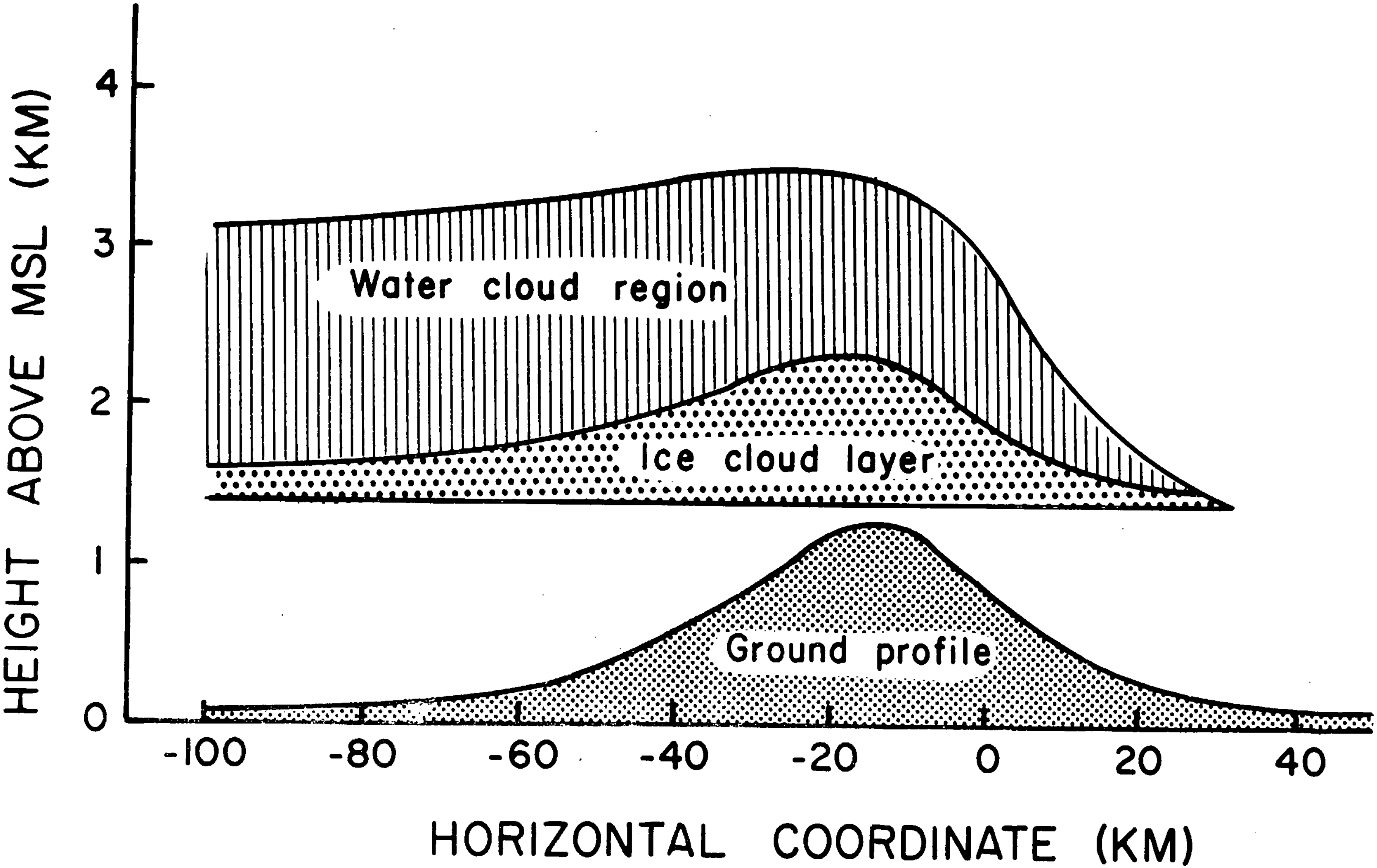

Fig. 2.16 Distribution of water and ice used in obtaining results shown in Fig. 2.15.

The destabilization can be extremely important for situations in which blocking exists. Under stable conditions the latent heating effects appear to be secondary to the barrier effect of the mountain. However, they should be considered in applications to orographic precipitation studies where the vertical displacements of the streamlines are of great importance in the production of liquid water.

The airflow model, within its limitation, is easily adaptable to a variety of terrains and atmospheric conditions. Moreover, the relatively fast and simple computational technique allows the airflow model to be used readily in conjunction with the modeling of microphysical processes in orographic clouds.

Using the airflow model equations we have derived for the horizontal and vertical components of the wind, the temperature, and the mass of water vapor condensed as air flows over a ridge (Hobbs et al., 1971). The input data required for these computations is a sounding well upwind of the ridge of wind, temperature and humidity. The growth of solid precipitation particles in the orographic clouds by deposition from the vapor phase, riming and aggregation have been computed. In the latter case, a temperature-dependent sticking probability, based on field measurements, was used. The trajectories of solid precipitation particles may be computed from the deduced magnitudes and directions of the wind across the ridge and the terminal fall speeds of the particles. For the latter purpose, solid precipitation particles have been divided into four general types which allow consideration of the degrees of riming and aggregation. The relationships between the masses, fall speeds and dimensions of different particles are based on direct measurements.

The model has been applied to the case of orographic clouds over the Cascade Mountains in order to investigate the effects of different cloud microstructures on the growth and fallout of solid precipitation. It has been shown that if aggregation is unimportant and the concentration of ice crystals is increased from 1 to 100 per liter, growth by riming is replaced by growth by deposition and the precipitation particles are carried further downwind and, in some cases, across the Cascade crest. These results suggest that the glaciation of supercooled, orographic clouds upwind of the crest, by overseeding with artificial ice nuclei or dry ice, should result in a redistribution of snowfall on the ground with a shift in some of the snowfall from the windward to the leeward slopes.

When the concentration of ice particles in the air is high, aggregation may play an important role in the growth of precipitation particles. Model calculations show that if the layer in which aggregation occurs is sufficiently thick, at temperatures above about -11°C, and crystals are present in concentrations on the order of 1000 per liter, growth by aggregation can be more rapid than growth by riming. However, even in this case, the aggregated crystals do not follow significantly different trajectories from unaggregated crystals although the precipitation rates may be higher in the former case.

2.3 "Simple" Model

While an important goal of the Cascade Project is to use our field measurements as input data in the "detailed" theoretical model described above, most of the decision making and targeting of precipitation affected by artificial seeding in our field investigations have been made using a "simple" model.

The "simple" model uses rawinsonde data and surface observations of snow crystal types to construct backward trajectories of rimed and unrimed snow crystals. The model is based upon experimental observations which indicate that specific crystal types (e.g., dendrites, needles, etc.) grow by diffusion only in particular temperature regimes, which are termed the "diffusion growth layers" for the crystals. Thus if, for example, a dendrite is sampled at the surface, the observer can be quite confident that the crystal grew by diffusion of vapor at temperatures between -12 and -17°C. When the dendritic crystal falls into a region with temperatures higher than -12°C, the operational model assumes that all additional mass increases can be attributed solely to riming. Diffusive growth of the ice crystals is not considered in the computations. The computer program simply identifies the level where diffusive growth is assumed to stop and then calculates trajectories from the surface to that height. Thus only a segment of the entire trajectory is actually calculated.

Fall velocities of the ice crystals are assumed to be constant if the crystals are unrimed. If riming is occurring, the fall velocities of the rimed crystals are assumed to increase linearly from the unrimed value at the base of the "diffusion growth layer" to twice the unrimed fall speed at the surface. Effects of topography are ignored in the computations and ice crystals are assumed to be displaced horizontally by the wind.

The atmosphere through which the crystals fall is divided into layers 250 meters thick and, except for those layers near the surface, the layers are assigned an average wind speed and direction as determined from rawinsonde input data. Near the surface an attempt is made to crudely approximate the channeling of the airflow which the local orographic features appear to produce. The wind velocity at points above the target is obtained by linearly averaging the surface velocity at the target (height ≈ 900 meters) and the 850 mb (height ≈ 1500 meters) velocity. Above 850 mb, the rawinsonde winds are assumed to be representative of the winds along the trajectory of the ice crystal.

The size of the observed surface crystals is implicitly incorporated into the calculations. Estimates of reasonable minimum and maximum fall velocities have been associated with each crystal type in an attempt to bracket all likely fall velocities. Trajectories are calculated based upon each of these extreme fall velocities, and it is assumed that the trajectories of the observed crystals will be bracketed by these computed extreme paths.

The model has the capability to compute trajectories for several different crystal types. Table 2.3 lists the crystal types that are presently included, the maximum temperature at which diffusive growth occurs, and the range of fall velocities associated with each crystal type.

On a typical operational day, raw rawinsonde data, surface observations of crystal type, and the surface wind at the target are fed into the computer. Output data include the coordinates of trajectory paths for rimed and unrimed snow crystals, the height of the trajectory at each coordinate, and fall time from the coordinate height to the surface. The selection of a seeding position is based upon the temperature where the seeding agent is effective and nearness to the target. Generally about 40 minutes is required to receive the raw rawinsonde data by telephone, punch the data on paper tape, compute the trajectories, and radio the seeding coordinates to the B-23 research aircraft which is flying near the target area.

The flow of information for the operational model is shown as a flow chart in Fig. 2.18. It should be noted that the programming of both input and output is done in such a straight forward manner that the program can be run by non-scientific staff.

2.4 Comparison of the Two Models

Before comparing results from the "detailed" and "simple" models the basic differences between them should be emphasized. In the "detailed"

TABLE 2.3

CRYSTAL CHARACTERISTICS INCORPORATED INTO THE "SIMPLE" MODEL

Crystal Type	Temperature at Base of Crystal Growth Layer (°C)	Minimum Fall Velocity (m sec^{-1})	Maximum Fall Velocity (m sec^{-1})(†)
Sectors	-12	0.25	0.50
Dendrites	-12	0.25	1.0
Stellars	-12	0.25	1.0
Plates	(‡)	0.25	0.8
Sheaths/Needles	- 4	0.25	1.0
Bullets	-20	0.50	1.0
Columns	- 5	0.50	1.5
Sideplanes	-20	0.25	0.50
Assemblages of Plates	-18	0.25	0.50
Assemblages of Sectors	-18	0.25	0.50
Graupel	-20	(§)	(*)
Aggregates	-20	0.50	2.0

(†) The minimum rimed fall speed is at the base of the crystal growth layer. The rimed fall speed increases linearly to twice the initial value at the surface.

(‡) Program asks for temperature. Plates can grow in three different temperature regimes; 0 to -3°C, -8 to 12°C and -16 to -25°C.

(§) Based upon graupel diameter; program requests size.

(*) Only one fall velocity is used for graupel.

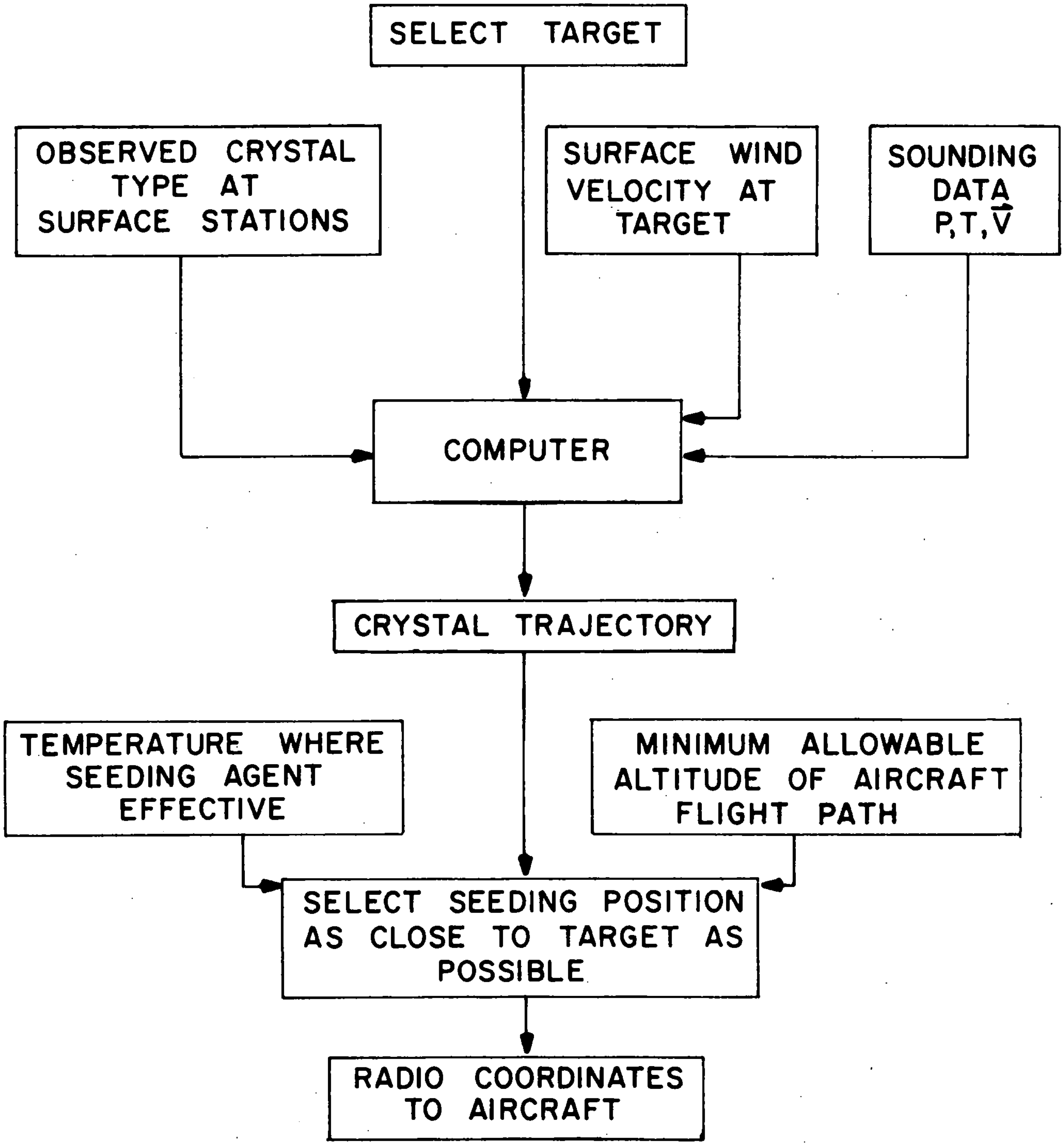

Fig. 2.18 Chart showing input and output data for the Cascade Operational Model.

model, the trajectories of solid precipitation particles are calculated from the points at which they are nucleated to the ground. The particles are allowed to grow continuously while they are in cloud by deposition, riming or aggregation, or a combination of these processes, depending on the cloud conditions. Also, the effects of vertical air motions, produced by the orographic flow, on the motions of the particles are included in the model. In the "simple" model the trajectories of the precipitation particles are calculated only below the base of their "diffusional growth layer." When growth by riming is considered, the fall speed of the particles is increased linearly between the base of the "diffusional growth layer" and the ground so that the fall speed doubles over the course of the trajectory. When growth by riming is not considered, the fall speed of the particle is maintained constant over its trajectory at a value appropriate to the nature of the particle.

The trajectories of particles over the Cascade Mountains predicted by the two models are compared in Figs. 2.19 - 2.23. In the case of unrimed crystals (Fig. 2.19), the "detailed" model predicts that the particles attain a fall speed of 30-40 cm sec^{-1} rather quickly, therefore, the effect of updrafts is not too great (except for the lower trajectory where the crystal originates in the strongest updrafts). Consequently, the trajectories predicted by the "detailed" model lie for the most part between the trajectories for particles with steady fall speeds of 25-30 cm sec^{-1} predicted by the "simple" model. For rimed crystals (Fig. 2.20), the "detailed" model predicts that the particles reach appreciable fall speeds ($\approx$ 40 cm sec^{-1}) faster than unrimed crystals. Thus, the updrafts are not too important in this case either.

The "detailed" model generally predicts an upward flow of air to the west of the Cascade crest and somewhat stronger downward flow to the east. Therefore, particles with a high fall speed are influenced mainly by the downward flow in the "detailed" model and have shorter trajectories than those predicted by the "simpler" model (Fig. 2.21). Particles with low fall speeds originate further west and are first influenced by the updrafts, therefore, the "detailed" model produces longer trajectories than the "simple" model (Figs. 2.22 and 2.23).

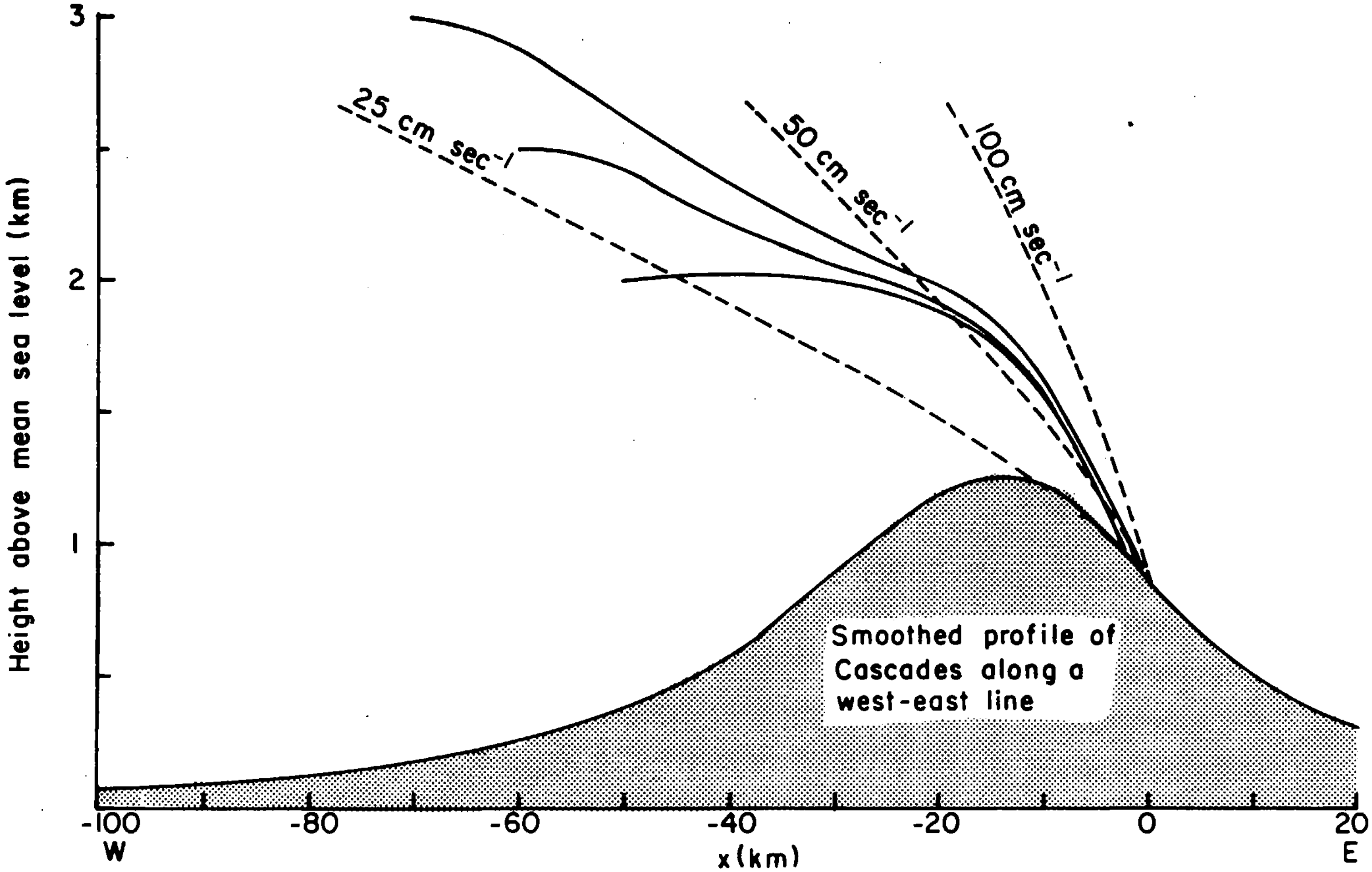

Fig. 2. 19 Comparison of trajectories of unrimed crystals predicted by the "detailed" theoretical model (————) and the "simple" model (– – – –). The constant fall speeds assumed in the "simple" model are shown on each curve.

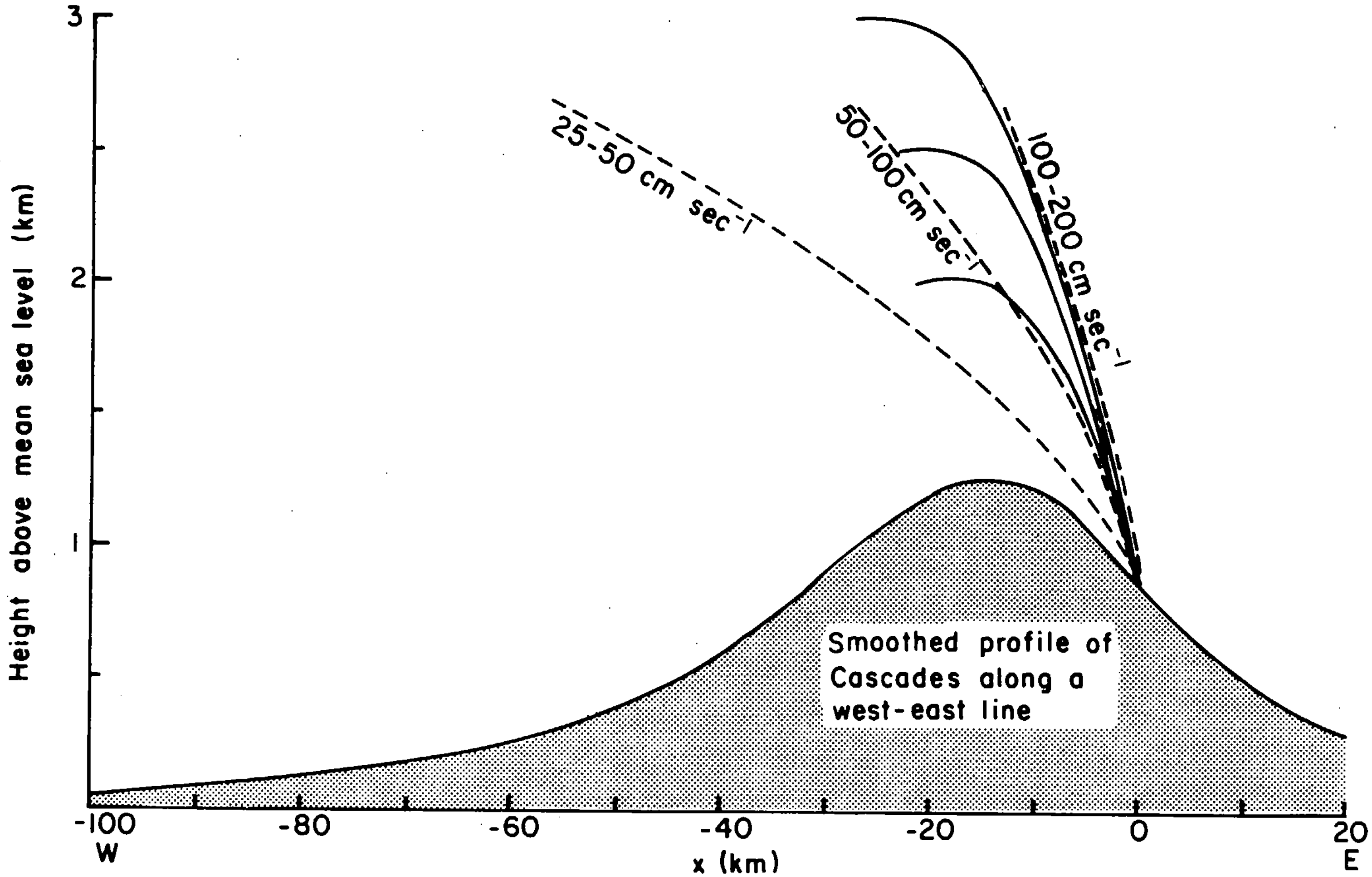

Fig. 2.20 Comparison of trajectories of rimed crystals predicted by the "detailed" theoretical model (———) and the "simple" model (- - - -). In the "simple" model the fall speed increases from the base of the "diffusional growth layer" to the ground in a linear manner between the values indicated on the curves.

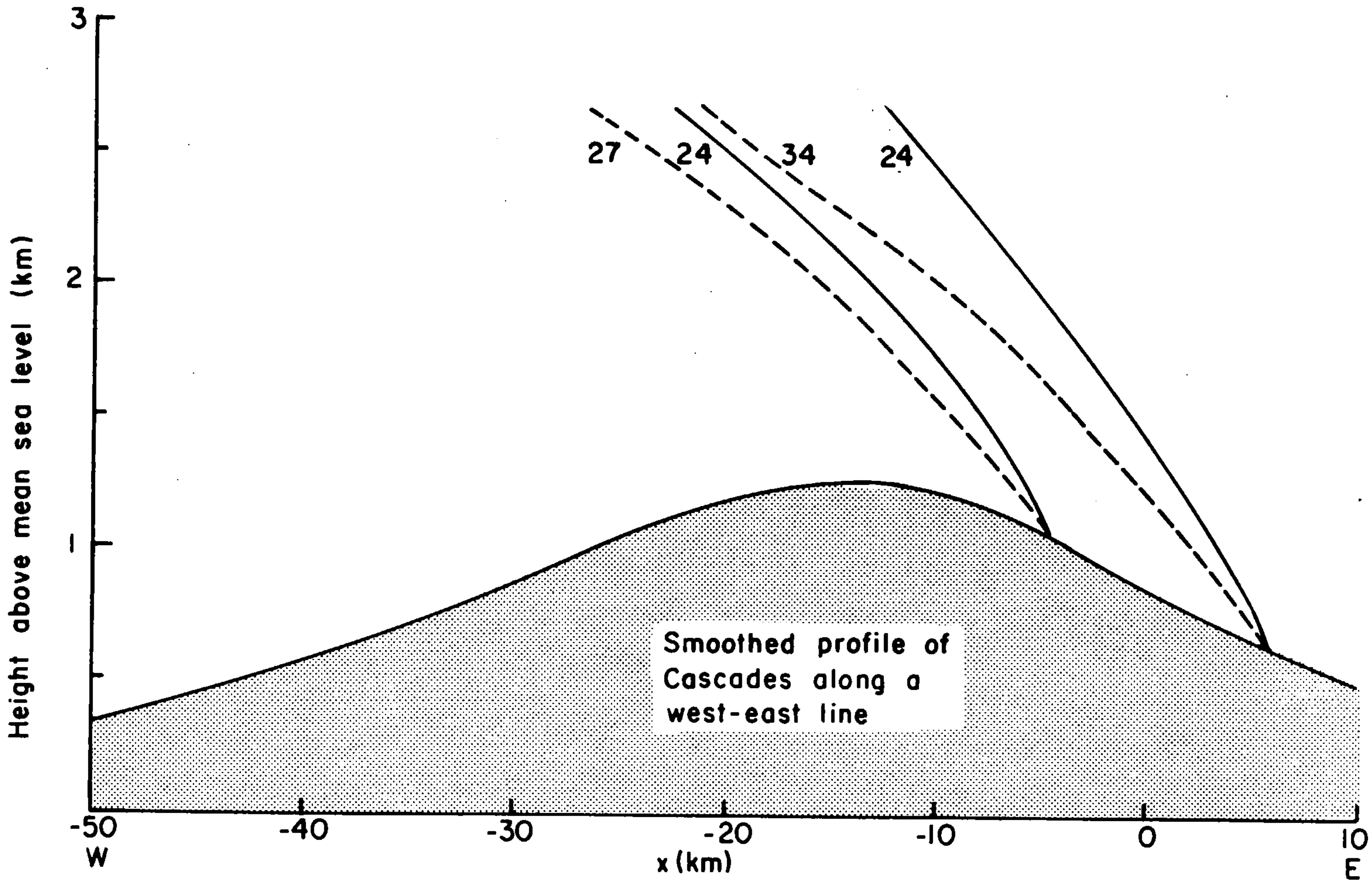

Fig. 2.21 Comparison of trajectories of crystals predicted by the "detailed" (———) and "simple" (– – – –) models. In the "simple" model the fall speed is assumed constant at 1 m sec^{-1} The number by each curve is the total time in minutes for the crystal to reach the ground.

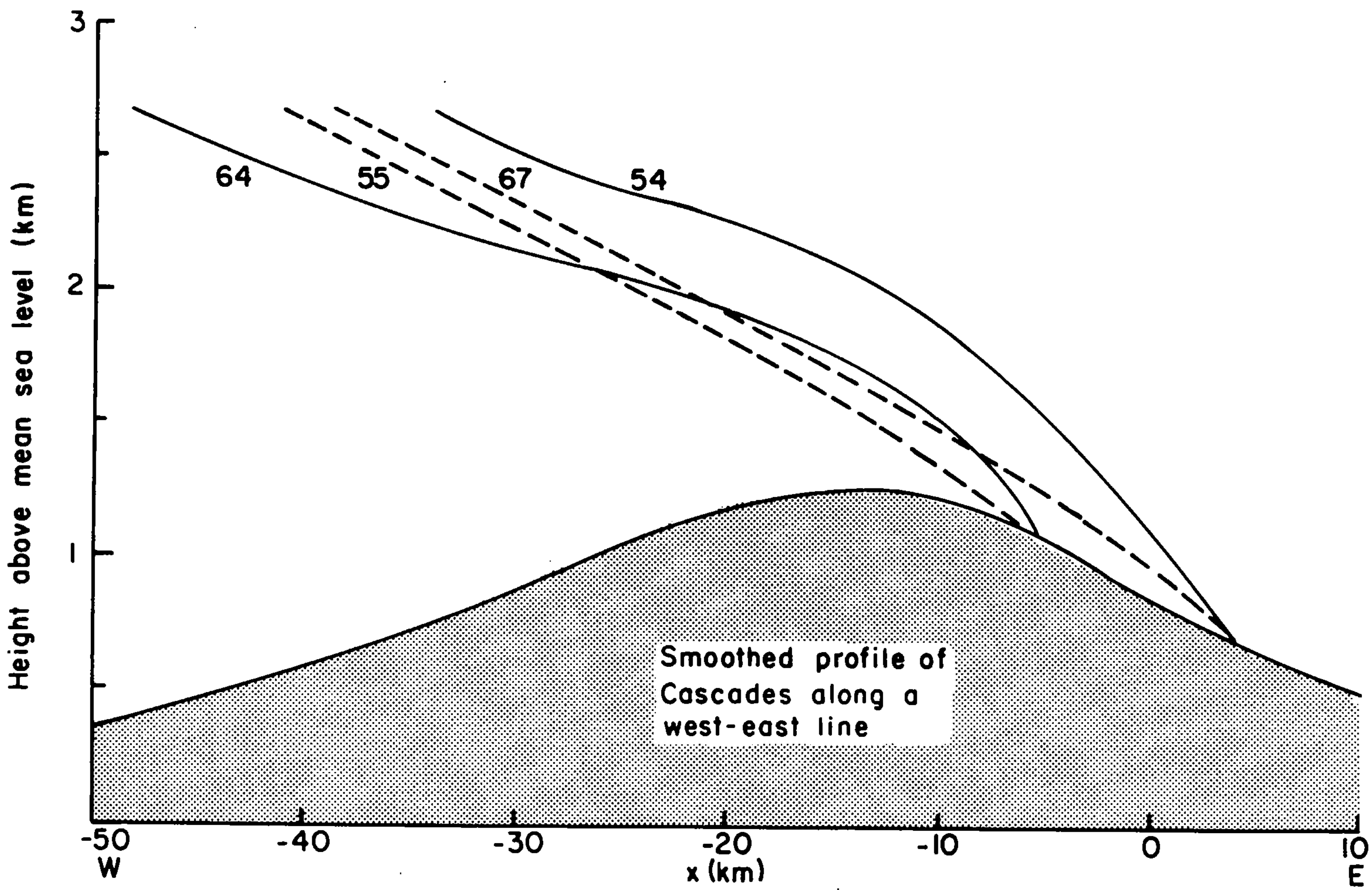

Fig. 2.22 Comparison of trajectories of crystals predicted by the "detailed" (———) and "simple" (– – – –) models. In the "simple" model the fall speed is assumed constant at 0.50 m sec^{-1}. The number by each curve is the total time in minutes for the crystal to reach the ground.

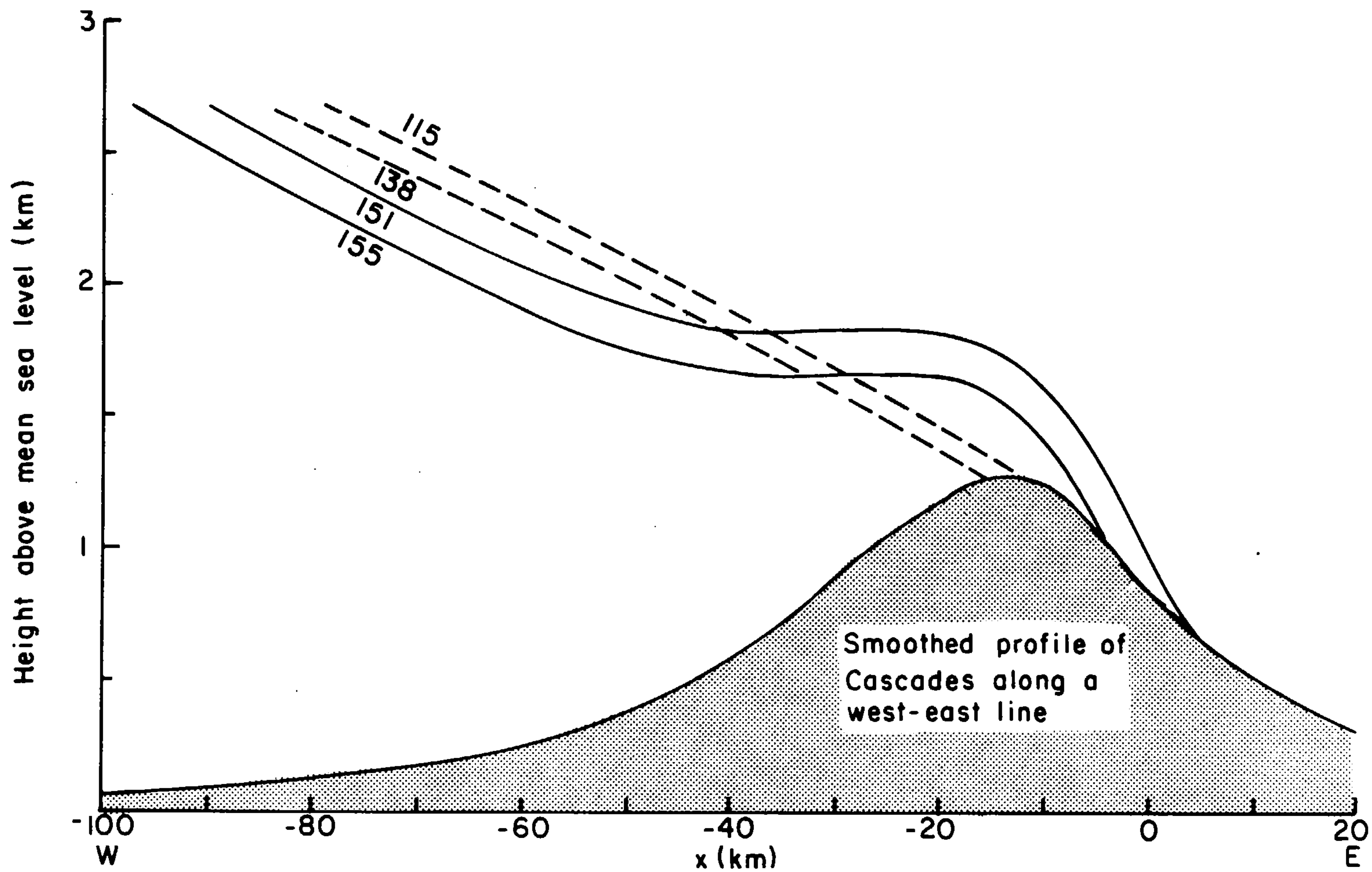

Fig. 2.23 Comparison of trajectories of crystals predicted by the "detailed" (———) and simple" (— — — —) models. In the "simple" model the fall speed is assumed constant at 0.25 m sec^{-1} in each case. The number by each curve is the total time in minutes for the crystal to reach the ground.

SECTION 3

AIRBORNE OBSERVATIONS

In this section we summarize some of the general results obtained from airborne observations and measurements in clouds over the Cascade Mountains during the winter of 1971-72. These results form an extension of the discussion given on pages 92-100 of Hobbs *et al.* (1971)[†] which described results obtained in 1970-71. Aircraft observations and measurements obtained in 1971-72 which are related to artificial seeding effects are described in §5 and §6 of this report.

3.1 General Results on Cloud Composition over the Cascade Mountains

3.1.1 Flight Procedures

On "storm days" it was a standard procedure for the B-23 research aircraft to take off from Seattle and then traverse the Cascade Mountains along the V-2 airway, which links Seattle to Ellensburg and crosses the Cascades about 10 nautical miles south of the Snoqualmie Pass area where our ground stations are located. The heading of the V-2 airway (108° true) is perpendicular to the main crest line of the Cascade Range. The crest is situated 41 nautical miles from Seattle on the V-2 airway and 35 nautical miles from Seattle in the vicinity of the ground stations. Replicas of cloud particles were obtained from the aircraft using the continuous particle sampler (CPS). All CPS runs are plotted according to their distance from Seattle measured parallel to the V-2 airway. Data collected more than 20 nautical miles from the airway or in seeded air are omitted from the results described in this section. Since all CPS runs were made in cloud, the data represent in-cloud averages. Some results on ice particle concentrations measured with the University of Washington ice particle counter (see §1.3.4 in Res. Rpt. VI) are also presented below.

3.1.2 Distribution of Liquid Water

The cloud liquid water content over the Cascade Mountains, measured by the Johnson-Williams hot wire liquid water meter, corresponding to each CPS run was plotted against altitude and temperature. Smooth curves through all the results obtained in 1971-72 are shown in Figs. 3.1 and 3.2. It can be

[†]Hereafter this publication is referred to as Res. Rpt. VI.

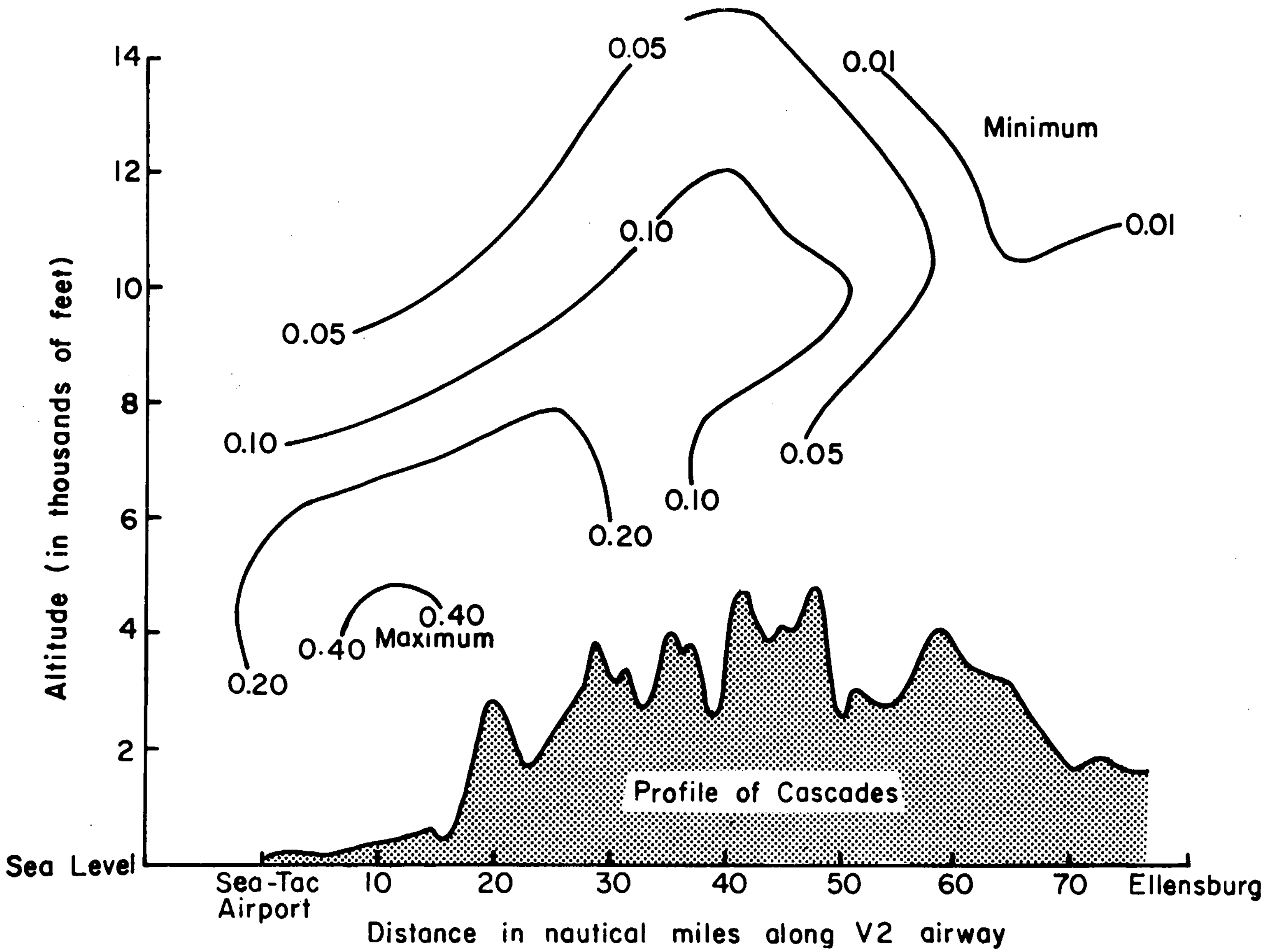

Fig. 3.1 Distribution of average liquid water content (in g m^{-3}) in clouds over the Cascade Mountains against altitude. Results are based on all data collected with Johnson-Williams liquid water meter during the 1971-72 winter season in which there was a westerly component to the wind (22 flights).

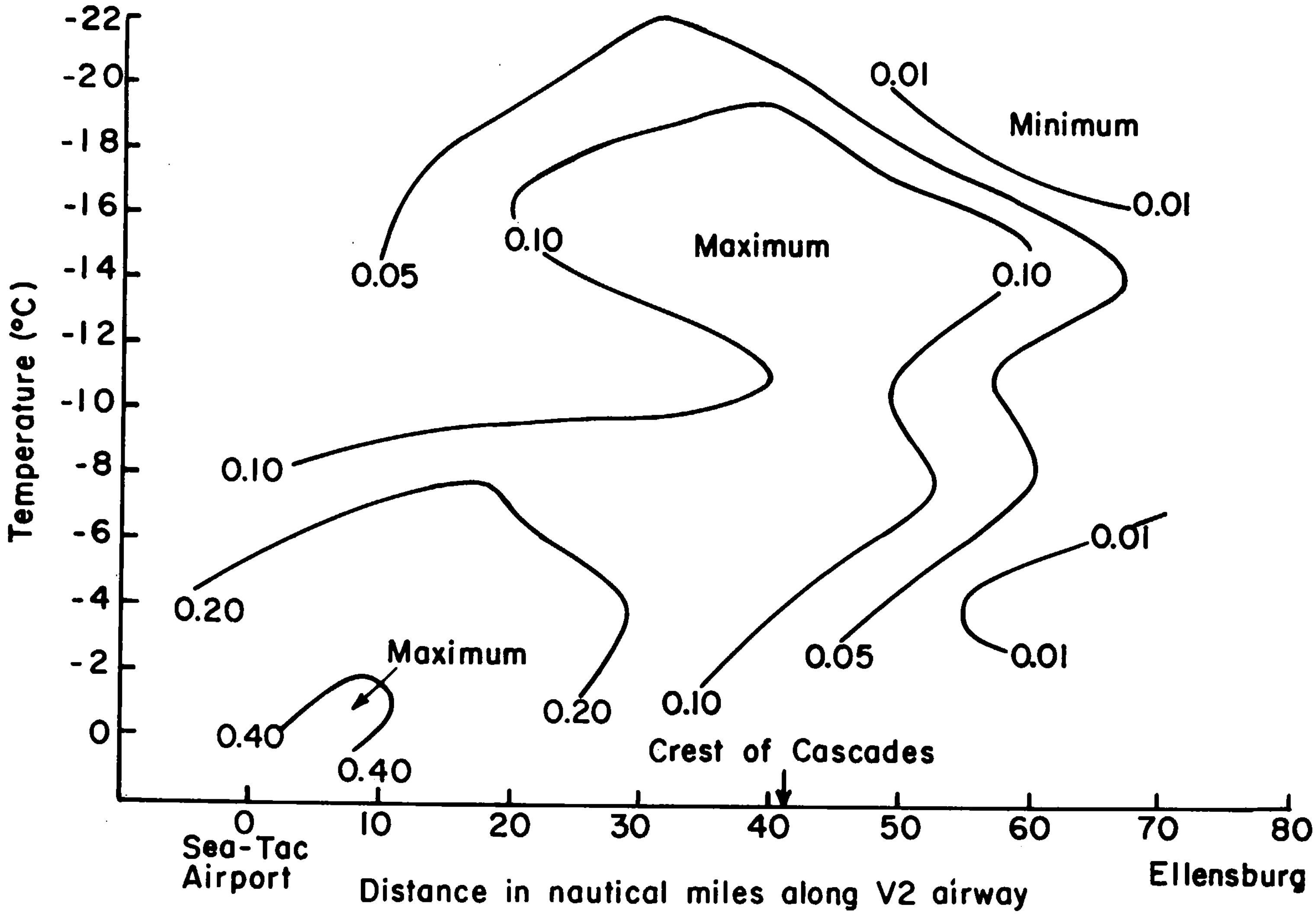

Fig. 3.2 Distribution of average liquid water content (in g m^{-3}) in clouds over the Cascade Mountains against temperature. Results are based on all data collected with the Johnson-Williams liquid water meter during the 1971-72 winter season in which there was a westerly component to the wind (22 flights).

seen from Fig. 3.1 that the liquid water contents along a series of vertical lines are pushed to higher levels in the atmosphere as the crest of the Cascades is approached from the west. This result is predicted by our theoretical model (e.g., it can be seen in Fig. 2.2 that the vertical height at which the streamlines reach their steepest slope increases as the crest of the mountain is approached).

Measurements obtained in pre-frontal and post-frontal situations were considered separately but the distributions of liquid water over the Cascade Mountains were similar in both cases. Higher liquid water contents might be expected in the more convective post-frontal situations (Fig. 3.3a), but the warmer and moister air associated with most of the pre-frontal situations studied probably compensated for the lower convective activity.

The results shown in Figs. 3.1 and 3.2 confirm the general features found in the 1970-71 data (see Figs. 4.1 and 4.2 in Res. Rpt. VI). However, a comparison of Fig. 3.1 with the results predicted by the theoretical model, shown in Figs. 2.10 and 2.11, shows that the measured liquid water contents achieve maximum values lower down and farther to the west of the Cascade crest than the model predicts, also the peak values are only about one-half those predicted. These differences are no doubt due to the fact that the model does not allow for the depletion of cloud water by precipitation.

3.1.3 Distribution of Ice

(a) Measurements with Continuous Particle Sampler

Smoothed isopleths for the concentrations of ice particles in clouds over the Cascade Mountains, based on all of the CPS data collected in the 1971-72 winter season, are shown in Figs. 3.4 and 3.5. The peak in the concentration of ice particles occurs much farther east than does the peak in liquid water content. Also, while the liquid water content decreases rapidly east of the Cascade crest, high concentrations of ice particles are observed over the eastern slopes. These can often be seen as a haze of ice crystals blowing out of the cap of the orographic clouds over the crest (Fig. 3.3b).

(b) Measurements with Optical Ice Particle Counter

Concentrations of ice particles were also measured with the University of Washington's optical ice particle counter. This airborne instrument detects and counts some plate-like ice crystals with maximum dimensions down to about 100 μm. It also detects aggregates and graupel but is somewhat less sensitive to columnar ice crystals. Although heavily rimed crystals and graupel are detected, the minimum size which these particles must have to be

(a)

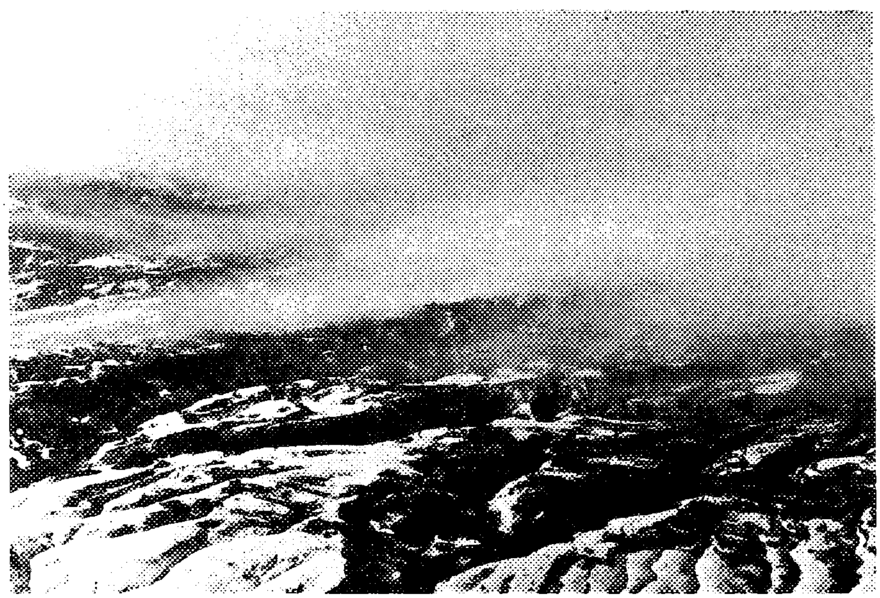

(b)

Fig. 3.3 (a) Orographic layer clouds with embedded cumulus over western (upwind) slopes of the Cascade Mountains in a post-frontal situation.

(b) Snow and ice crystals blowing out of clouds over the eastern (leeward) slopes of the Cascade Mountains.

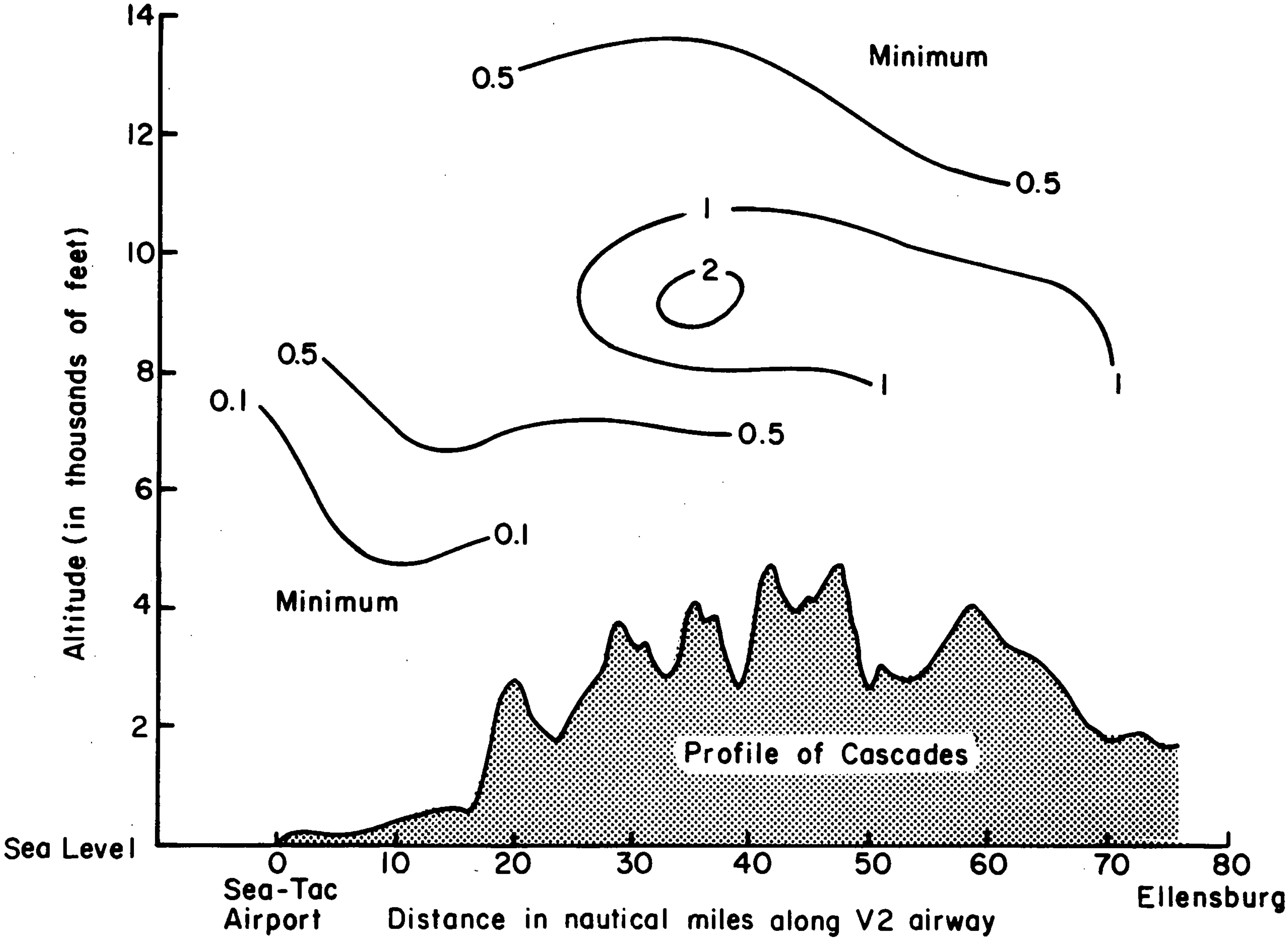

Fig. 3.4 Distribution of average concentrations of ice particles (cm^{-3}) in clouds over the Cascade Mountains against altitude. Results are based on all data collected with the continuous particle sampler during the 1971-72 winter season in which there was a westerly component to the wind (22 flights).

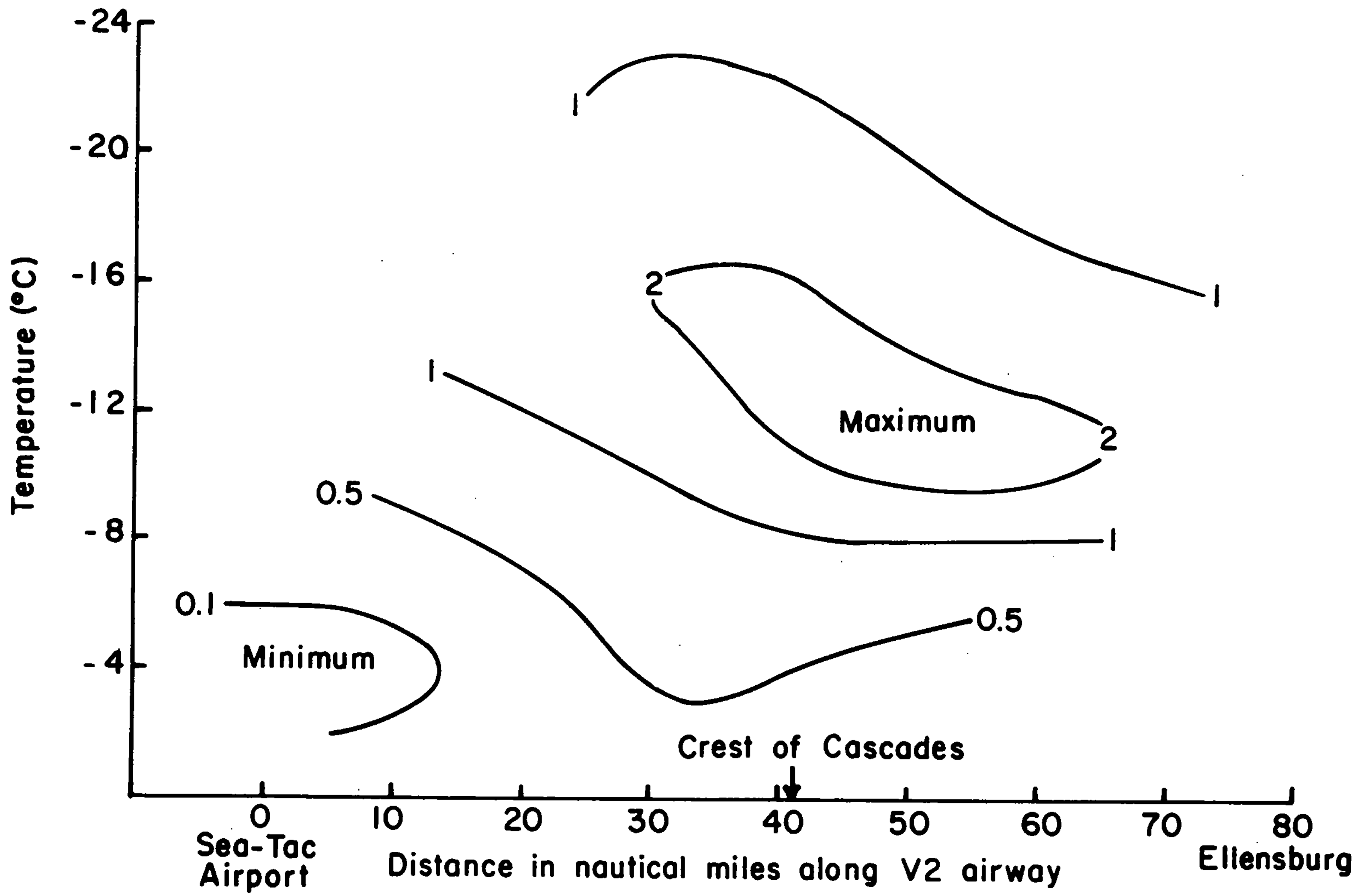

Fig. 3.5 Distribution of average concentration of ice particles (cm^{-3}) in clouds over the Cascade Mountains against temperature. Results are based on all data collected with the continuous particle sampler during the 1971-72 winter season in which there was a westerly component to the wind (22 flights).

detected is larger than for unrimed particles. As the size of the ice particles increases the percentage detected also increases, but the exact fraction of ice particles of any given size and type which are counted has not yet been determined. The instrument does not detect water drops no matter how large they are. The concentrations of ice particles in the air detected by the optical ice particle counter are displayed in the aircraft in real-time.

Fig. 3.6 shows the average distribution across the Cascade Mountains of the concentrations of ice particles detected by the optical ice particle counter. The results are based on measurements obtained on eight flights along the V-2 airway during the 1971-72 winter season. Five of the flights were close to 10,000 ft. and three at about 8,000 ft. It can be seen that the concentrations reach maximum values at approximately 7 nautical miles west and 25 nautical miles east of the Cascade crest and a minimum value about 7 nautical miles east of the crest. These results are generally consistent with the data obtained from the CPS (Figs. 3.4 and 3.5), although the latter (perhaps due to lack of spatial resolution) did not resolve the maximum and minimum counts to the east of the crest. The concentrations of ice particles measured with the optical ice particle counter were about a factor of 1000 less than those collected by the CPS; this is no doubt due to the fact that all ice particles down to about 80 μm in size can be detected with the CPS, whereas, the minimum size ice particle detectable with the present optical counter is about 100 μm and only a fraction of the particles of this size are counted.

Fig. 3.7(a) indicates the research flight route over the Cascade Mountains on December 9, 1971, and the air temperatures, dew points and winds obtained from a rawinsonde launched from Greenwater at 1110 PST are shown in Fig. 3.7(b). Figs. 3.7(c) and (d) show the concentrations of the particles measured with the optical ice particle counter and the continuous particle sampler at the two flight levels. It can be seen that the variations in count from the two instruments were in reasonable agreement. Particles collected by the CPS during this flight are listed in Table 3.1.

A preliminary investigation was carried out to see if the concentrations of ice particles in the air over the Cascades are correlated with air turbulence (as measured by the MRI Air Turbulence Meter). However, the degree of air turbulence appeared to be fairly randomly distributed across the mountains, except for possibly slightly higher values over the Cascade crest.

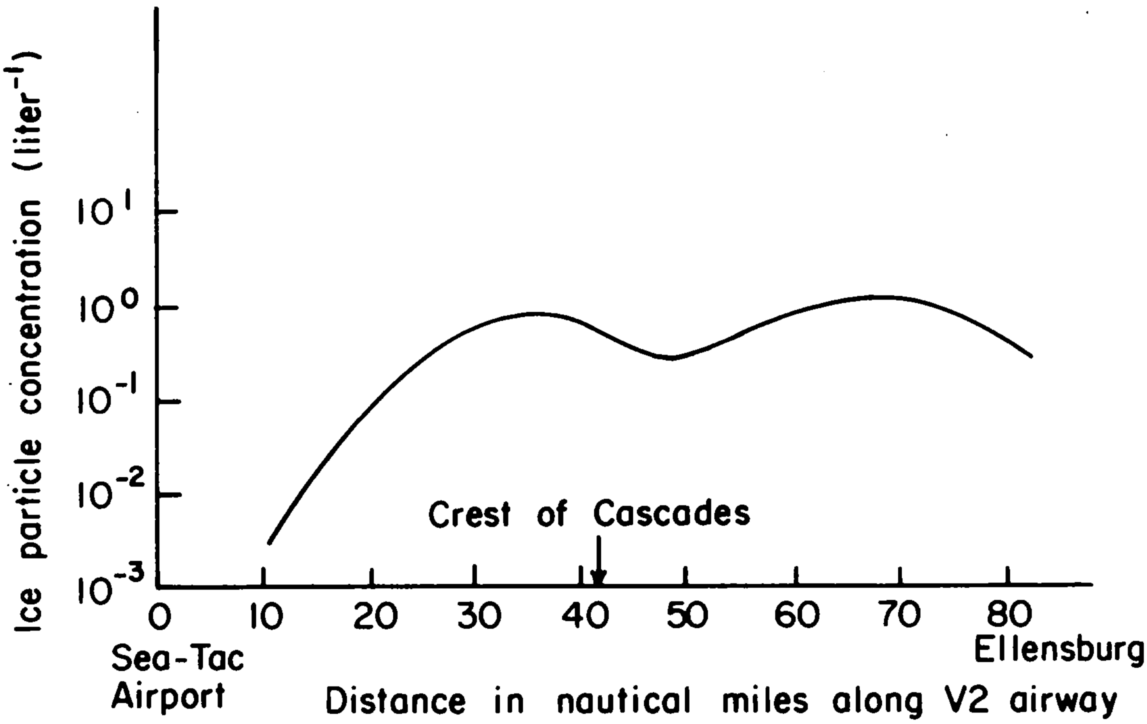

Fig. 3.6 Average ice particle concentrations across the Cascade Mountains measured with the University of Washington optical ice particle counter.

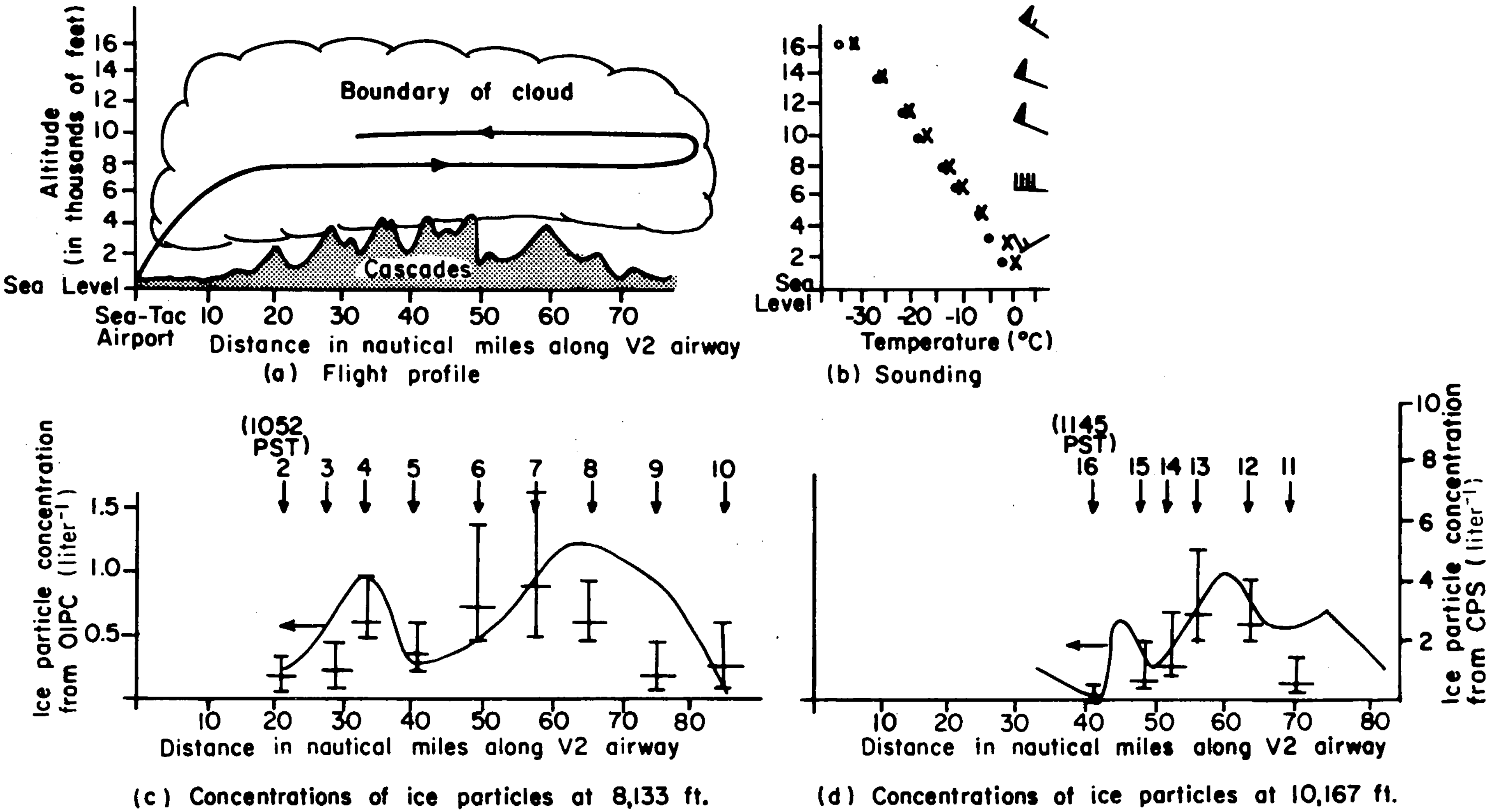

Fig. 3.7 Concentrations of ice particles measured with the University of Washington optical ice particle counter (OIPC) and continuous particle sampler (CPS) across the Cascade Mountains on December 9, 1971. The maximum, minimum and logarithmic mean concentrations from the CPS are shown by the bars (Ɨ). The flight route is indicated in (a) by ⟶. The air temperature (X), dew point (∘) and winds (arrows) are indicated in (b). The measured concentrations of ice particles at the two flight levels are shown in (c) and (d) where arrows at numbers indicate the positions and run numbers where cloud particles were sampled with the continuous particle replicator (see Table 3.1).

TABLE 3.1

SUMMARY OF CLOUD PARTICLES COLLECTED WITH CONTINUOUS PARTICLE SAMPLER ON DECEMBER 9, 1971

(See Fig. 3.7 for position of each run.)

Run No.	Water Drops		Ice Particles		Number Ratio of Water to Ice
	Diameter (μm)	Concentration (cm^{-3})	Type & Maximum Dimension (μm)	Concentration (cm^{-3})	
2	10-70 Mean 50.	5-30	30-200. Frozen drops, some in groups. Isolated rimed irregular ice. 1 400 μm irregular plate-like.	0.4-1.5	25:1
3	30-60 Mean 50.	2.5-16	50-300. Some stellar parts. Some rimed frozen drops. Mainly at beginning.	0.4-2	10:1
4	20-40	0.1-1 Isolated.	100-800. Plate-like ice. Branch and stellar parts, some riming and frozen drops. A few dendritic parts.	2-4	Virtually all ice.
5	20-60	1-8	50-700. Frozen drops. Rimed irregular ice to 350. Isolated stellars to 700. Small plate-like ice 50 to 150.	1-2.5	2:1
6	20-40	0.2-4	60-300. Rimed irregular ice, some plate-like. Some rimed aggregates. Isolated stellar parts.	2-6	1:5
7	20-30	0.1-1	50-600. Small plate-like ice. Rimed irregular ice. Small branch arms. Small rimed aggregates.	2-7	1:20

TABLE 3.1 (cont.)

Run No.	Water Drops		Ice Particles		Number Ratio of Water to Ice
	Diameter (μm)	Concentration (cm^{-3})	Type & Maximum Dimension (μm)	Concentration (cm^{-3})	
8	20-40	<0.2 Isolated.	50-300. Irregular ice & hexagonal plates. Branch parts. Some frozen drops. Some columnar. Some bullets. Isolated aggregates.	2-4	1:30
9	———	———	50-300. Plate-like & hexagonal plates. Irregular Some bullets. Some columns.	0.4-2	All ice.
10			50-400. Irregular, columnar & plate-like ice. Bullets mainly <200.	0.4-2.5	All ice.
11	30-50	Isolated.	50-250. Irregular, columnar & plate-like ice. Short columns. Some bullets. Hexagonal plates.	0.2-1.5	Virtually all ice.
12	———	———	70-600. Irregular ice. Bullets to 400. Some smaller plate-like. Isolated aggregates. Some columns.	2-4	All ice.
13	30-50	Isolated.	50-300. Irregular ice. Hexagonal plates & plate-like ice. Bullets. Columns. Small rimed aggregates.	2-5	Virtually all ice.
14	30-50	Isolated.	50-300. Irregular ice. Rimed bullets. Isolated small aggregates.	0.4-3	Virtually all ice.

TABLE 3.1 (cont.)

Run No.	Water Drops		Ice Particles		Number Ratio of Water to Ice
	Diameter (μm)	Concentration (cm^{-3})	Type & Maximum Dimension (μm)	Concentration (cm^{-3})	
15	30-50	2-7 Beginning & end. <1 middle.	50-200. Irregular rimed ice. Isolated bullets.	0.2-2	5:1
16	15-50	4-25 Highest last part.	40-150. Isolated irregular ice.	<0.1	100:1

3.2 Maximum Concentrations of Ice Particles

Data collected in winter clouds over the Cascade Mountains have shown that peak concentrations of ice particles in the clouds are regularly many orders of magnitude greater than would be predicted from conventional ice nucleus measurements. Results of this kind, which were obtained in clouds which were not artificially seeded, are described below. Concentrations of ice particles in artificially seeded clouds are presented in §6.1.

3.2.1 Procedures

The concentrations of ice particles in clouds were deduced from the numbers of particles collected on the continuous particle sampler on the B-23 research aircraft. The collection area of the CPS is about 0.1 cm^2 and the volume of air sampled during a 15 second (≈ 1 km) run of the CPS is typically about 10 liters. The minimum concentration of ice particles in the air which can be detected is about 0.1 to 0.2 $liter^{-1}$. Due to the long but narrow path of air which is sampled, the number of particles collected can vary widely in a short time period. The log-average of the ice particles collected during a given run (1 km) is referred to as the <u>sustained ice particle concentration</u>. For example, if the concentrations in a run of the CPS varied from 1 to 100 per liter, the sustained ice particle concentration would be 10 $liter^{-1}$. (This is equivalent to assuming a log-normal distribution of concentrations for each CPS run.)

The fragmentation of ice particles during collection by the CPS can be a serious problem, particularly when one wishes to deduce the concentrations of particles in the free air. Fragmentation of crystals can be reduced by the use of the decelerators described in Res. Rpt. VI. However, when these decelerators are used on the CPS the collection efficiency for smaller crystals is reduced by, as yet, an undetermined amount. Without a decelerator, the collection efficiency of the CPS should be about 90 per cent for particles greater than 100 μm in size. In the results reported below decelerators were not used. Instead, all ice particles which were obviously associated with fragmentation <u>on collection</u> were ignored in determining concentrations. The deduced maximum sustained concentrations of ice particles prescribed below are therefore believed to be conservative estimates but are probably valid to within plus or minus a factor of 3.

3.2.2 Results

The <u>maximum</u> sustained ice particle concentration for each flight was determined and the cloud top temperature obtained from inspection of the aircraft observations and radiosonde data. The results for every flight made in 1971-72 for which such measurements were available are shown in Fig. 3.8. Also indicated in this figure are the typical concentrations of ice nuclei which are normally assumed to be present in the air (i.e., 1 per liter at -20°C and increasing by a factor of 10 for each 4°C of cooling), and the predominant types of clouds present when the measurements were made. It can be seen that with the possible exception of three flights in stratocumulus, in which the ice particle concentrations were below the detection threshold of the CPS, the maximum sustained concentration of ice particles on every flight was much greater than would have been predicted from the assumed ice nucleus spectrum. The ratio of the maximum sustained ice particle concentration to the assumed ice nucleus concentration is plotted against cloud top temperature in Fig. 3.9, where it is seen that the ratio is generally between 10^3 and 10^5 and on one occasion was in excess of 10^6! The ratio decreases with decreasing temperature, as first noted by Hobbs (1969). A least-squares best fit to the results shown in Fig. 3.9 (excluding the five points below or just above the detection threshold) yields

$$R(\Delta T) = 5.89 \times 10^6 \exp(-0.4\Delta T)$$

where, $R(\Delta T)$ is the ratio of the maximum sustained ice particle concentration to the assumed ice nucleus concentration at ΔT°C below 0°C.

The lowest cloud top temperature for which ice was not detected during a flight was -8.5°C. The highest cloud top temperature for which ice was detected was -6°C in altostratus cloud; this same flight yielded the highest value of R observed during the 1971-72 season.

3.2.3 Discussion

The high ratios of ice particles to ice nuclei discussed above is commonly referred to as "ice multiplication."† This phenomenon has been observed previously in cumulus clouds by Koenig (1963), Mossop *et al.* (1968) and Mossop *et al.* (1970), in stratocumulus and nimbostratus clouds by Koenig (1968), in cap clouds by Auer *et al.* (1969), and in orographic clouds by Hobbs (1969) and Burrows and Robertson (1969). Although many mechanisms have been proposed to explain the unexpectedly high concentration of ice particles (for a review see Mossop, 1970), none has as yet been proven.

The results presented in §3.2.2 are the first substantial set of measurements which show that ice particle concentrations many orders of

†This term is not very desirable since it implies a general explanation for a phenomenon which is not understood.

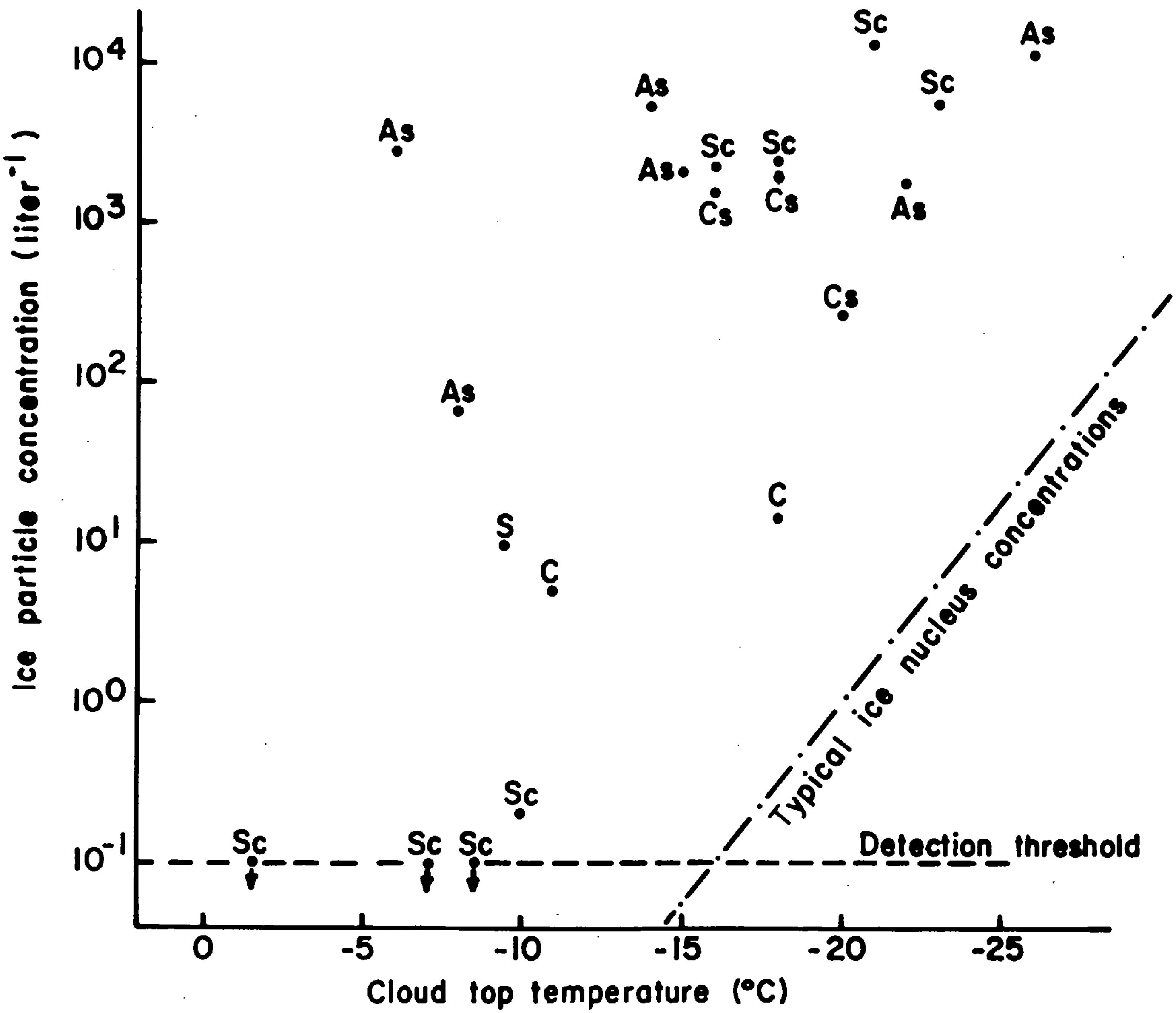

Fig. 3.8 Maximum sustained ice particle concentrations in clouds over the Cascade Mountains against cloud top temperature. Each point represents one flight. Cloud types are indicated by As - altostratus, S - stratus, Sc - Stratocumulus, C - cumulus, Cs - cumulus with stratified tops.

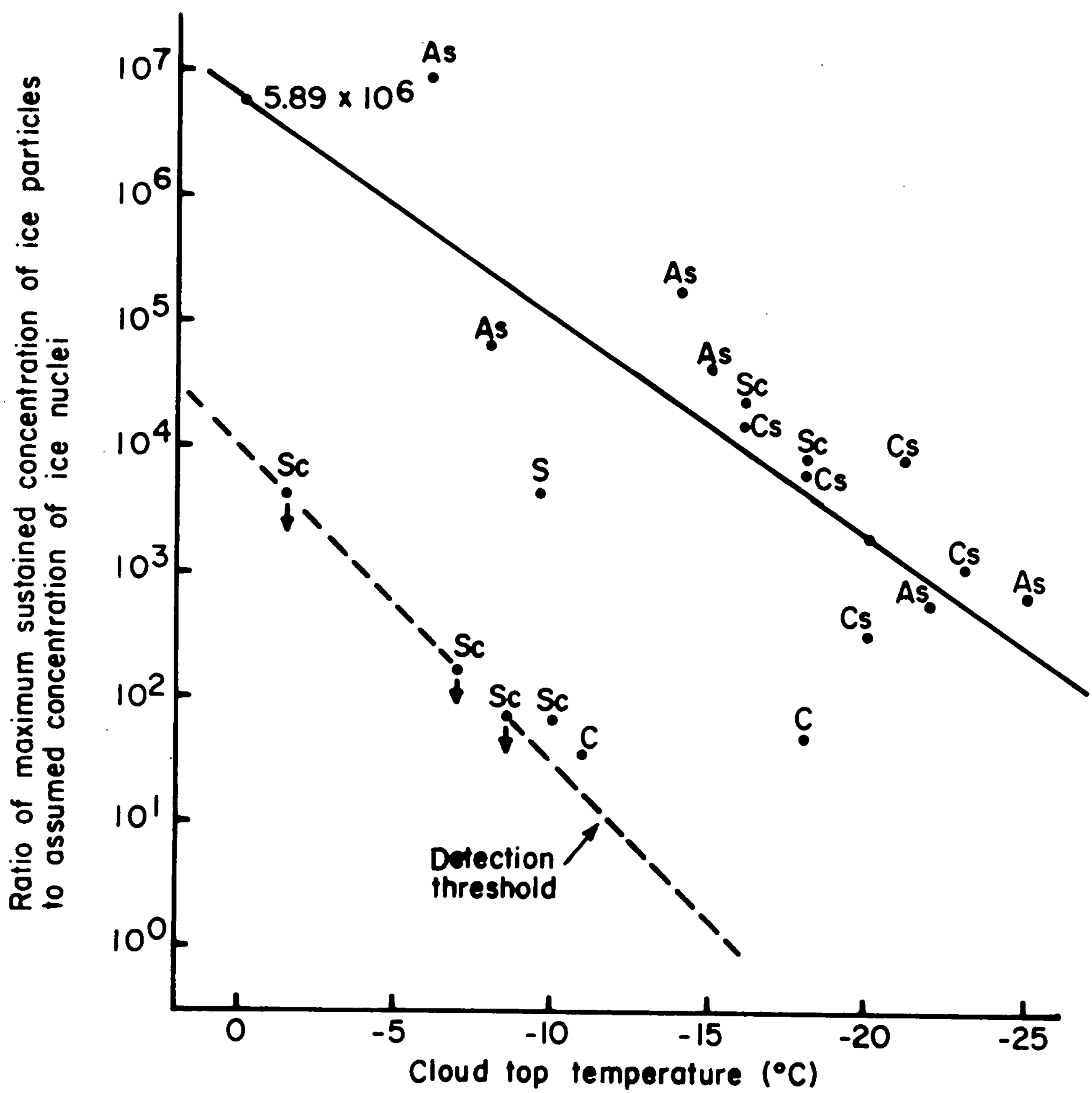

Fig. 3.9 Ratio of maximum sustained ice particle concentration to assumed concentration of ice nuclei against cloud top temperature. Each point represents one flight. Cloud types are indicated by As - Altostratus, S - Stratus, Sc - Stratocumulus, C - Cumulus, Cs - Cumulus with stratified tops.

magnitude greater than typical ice nucleus measurements exist in layer clouds such as altostratus, stratocumulus, and stratus. Our measurements have shown that for winter clouds over the Cascade Mountains, these high ice particle concentrations are the normal situation rather than a rarity. Moreover, altostratus, stratocumulus and cirrostratus exhibited this phenomenon to an even greater degree than the few cumulus clouds which we studied in the same area (Figs. 3.8 and 3.9).

In seeking an explanation for these observations the possibility of "seeding" by blowing snow from the tops of the mountains should be considered. Plume dispersion studies (e.g. Turner, 1969) for particles of negligible fall speed indicate that under stable and neutral conditions the angle of elevation of the plume with respect to the wind is less than 1°. In this case, any blowing snow would not reach the altitude of the aircraft (generally about 5,000 ft. above terrain) over the Cascade Mountains. Under unstable conditions the angle of elevation of the plume can be as much as 10° and updrafts in excess of the fall speeds of precipitation particles are possible. Therefore, under these conditions, blowing snow might be carried upwards and "seed" clouds over the Cascades. It seems unlikely, however, that blowing snow can explain the commonly observed high ice crystal concentrations described in the previous section for the following reasons. The overcast conditions in which our measurements were typically taken are conducive to neutral stability conditions. In the most favorable conditions for blowing snow to "seed" the clouds, namely convective, the ice crystal counts were among the lowest observed (Figs. 3.8 and 3.9). Furthermore, surface winds sufficient to raise blowing snow are rare over the Cascade Mountains on "storm days" and snow blown off mountain ridges is launched into downdrafts. Finally, the case against the high ice particle concentrations in the clouds being due to blowing snow receives further strong support from the results shown in Fig. 3.10 where the locations of the maximum sustained ice particle concentrations are plotted on a map of the Puget Sound and Cascade areas. It can be seen that the high ice particle concentrations were not confined to clouds over the mountains but occurred also over the Puget Sound Basin which was not snow covered.

Detailed reduction and analysis of simultaneous in-flight data characterizing other properties of the clouds in which these measurements were obtained are still in progress. However, it is our impression at this

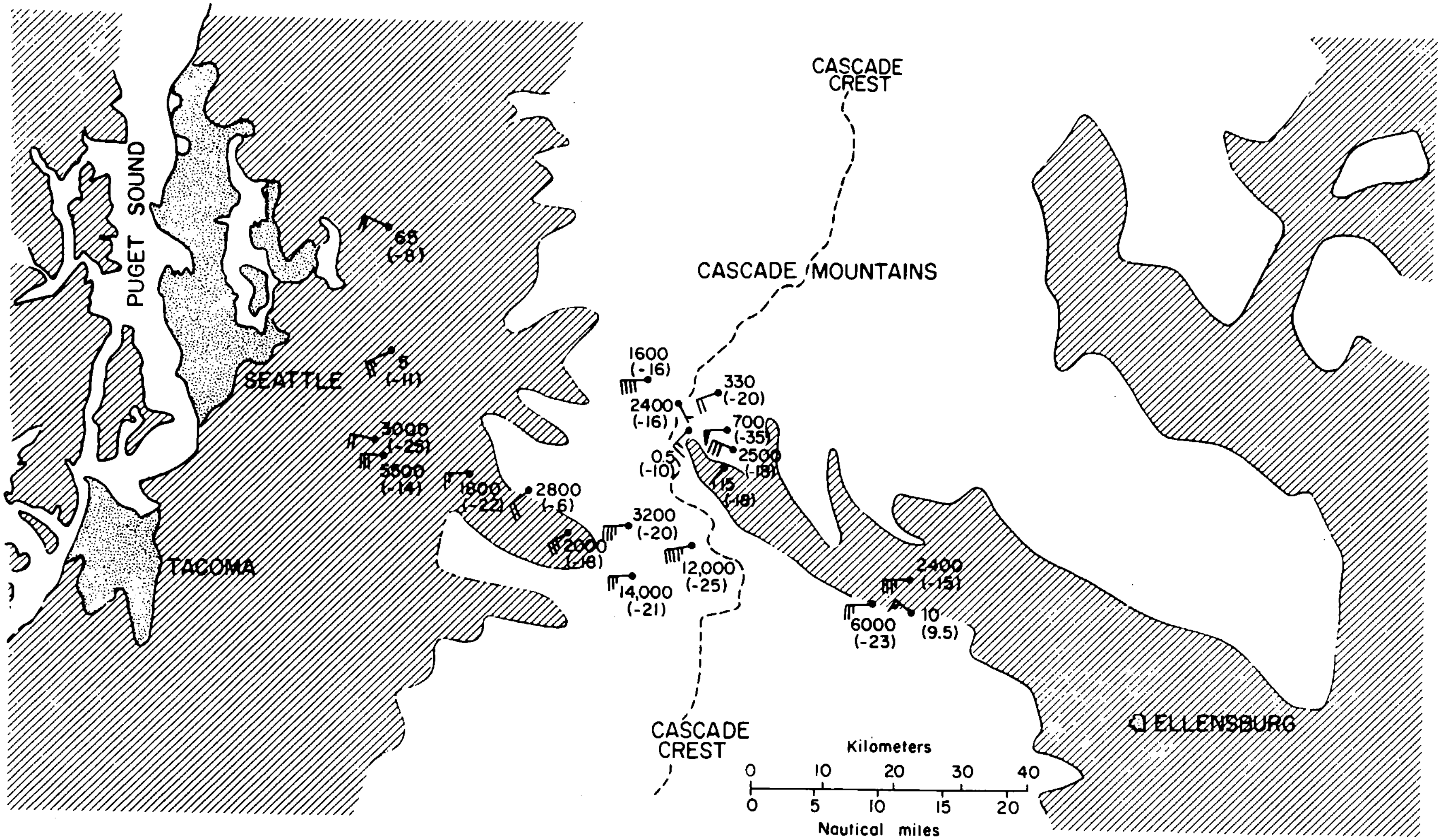

Fig. 3.10 Location of maximum sustained ice particle concentrations (before seeding) for each flight shown in Figs. 3.8 and 3.9. Also shown are winds at 8000 feet, ice concentration per liter and temperature (°C) at flight level in parentheses. Diagonally shaded areas indicate ground elevations below 3000 feet.

time that "old" clouds are far more likely to exhibit high ice crystal concentrations than are "young" clouds at the same temperature. We suggest that a possible explanation for the high ratio of ice particles to measured ice nuclei in "old" clouds is that contact nuclei have sufficient time to come into contact with and nucleate appreciable numbers of supercooled droplets in "old" clouds. In devices for measuring ice nuclei, on the other hand, contact nuclei are either excluded from measurement (e.g. in the millipore filter technique or drop freezing method) or are given very little time to act (e.g. in expansion or mixing chambers). Some independent experimental evidence indicating the possible importance of contact nucleation is presented in §4.9. However, direct measurements of the concentrations of contact nuclei in the air are needed to check these ideas.

3.3 Aggregation of Ice Particles in Clouds

In this section we present some preliminary data on the aggregation of ice particles in clouds. The results are based mainly on an examination of particles replicated with the continuous particle sampler on the aircraft but some of the replicas obtained at the ground stations were always analyzed. A more detailed examination of aggregation based on the ground data is contained in §4.7.

3.3.1 Correlations Between Occurrence of Aggregates and Air Temperature

Ice particles replicated with the continuous particle sampler (and also some of the replicas obtained at the ground stations) were analyzed to see if any correlations existed between the occurrence of aggregates and air temperature (at cloud top and at the point they were collected). The probability for the occurrence of aggregates at each temperature was estimated by determining the number of occasions on which aggregates were observed at that temperature compared to the number of occasions they were not observed.

Results are shown in Fig. 3.11 where it can be seen that the probability of aggregates forming generally decreases with decreasing temperature. However, there is a local peak in the probability of occurrence at temperatures between about -10 and -15°C. This is probably due to the fact that dendritic crystals form within this temperature range and their structures are conducive to the formation of aggregates.

3.3.2 Correlations Between Occurrence of Aggregates, Temperature and Concentration of Ice Particles

Smoothed isopleths showing the probability of ice aggregates occurring as a function of the air temperature and the total concentration of ice particles in the air are shown in Fig. 3.12. The figure is based on CPS data collected in the aircraft flying over the Cascade Mountains.

It can be seen that aggregation is profoundly affected by both temperature and the concentration of ice particles in the air. At temperatures below -15°C, and for ice particle concentrations less than 0.1 cm^{-3}, aggregates are unlikely to form. For temperatures above -5°C and particle concentrations in excess of 1 cm^{-3}, there is more than a 50 per cent probability of finding aggregates.

3.3.3 Dimensions of Aggregates

The maximum dimensions of aggregates estimated from replicas of crystals collected from the aircraft and on the ground are shown plotted against the air temperature at the level they were collected in Fig. 3.13. Below 0°C the sizes of the aggregates generally decrease with decreasing temperature. However, around the dendritic growth region (-12 to -17°C), there is a secondary maximum in the maximum dimensions of the aggregates.

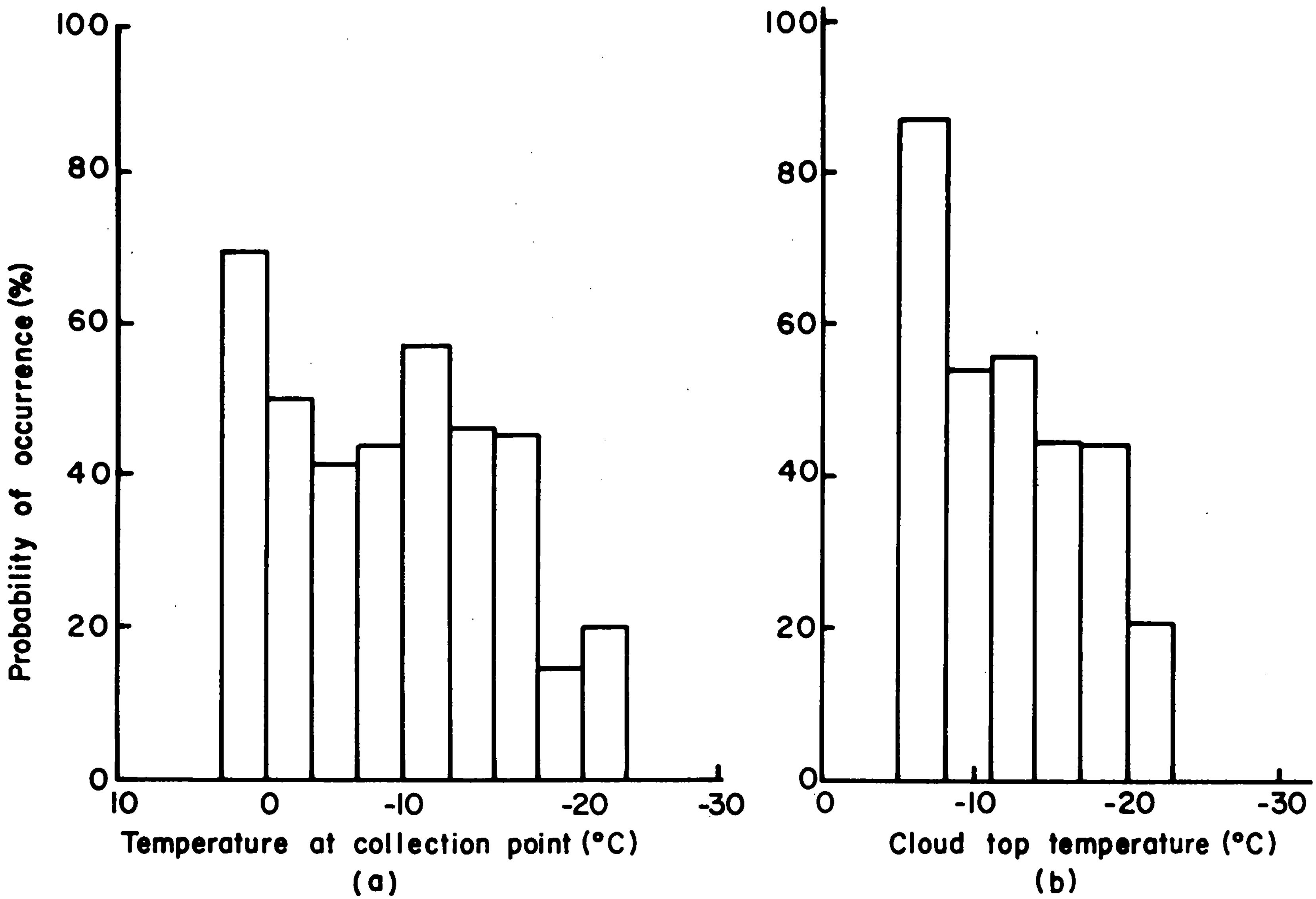

Fig. 3·11 Probability of occurrence of aggregates (a) as a function of temperature at which crystals were collected and (b) as a function of cloud top temperature. Results are averaged over temperature intervals of 3°C.

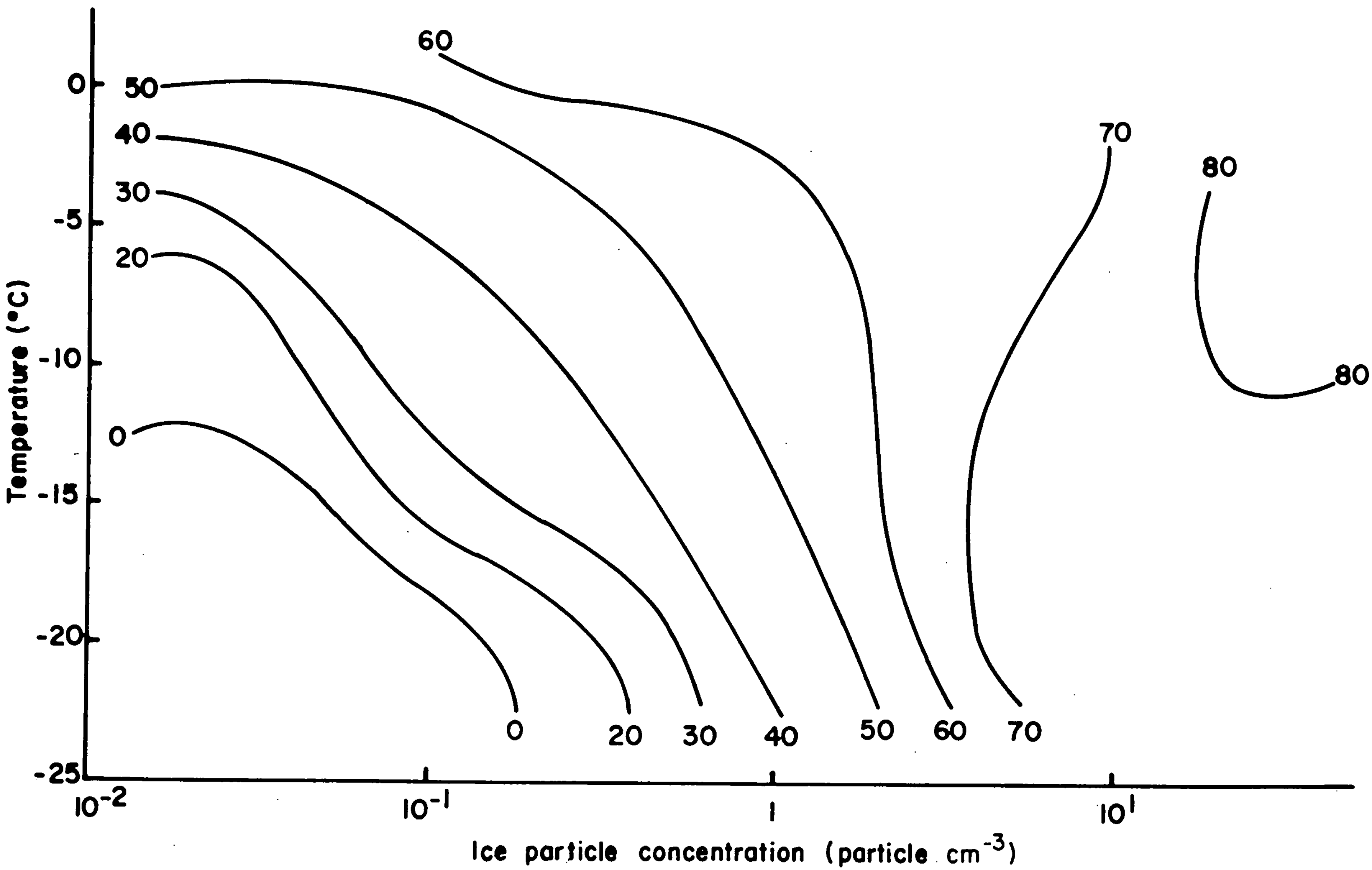

Fig. 3.12 Isopleths for the probability (in per cent) of finding aggregates in a cloud as a function of air temperature and the total concentration of ice particles in the air.

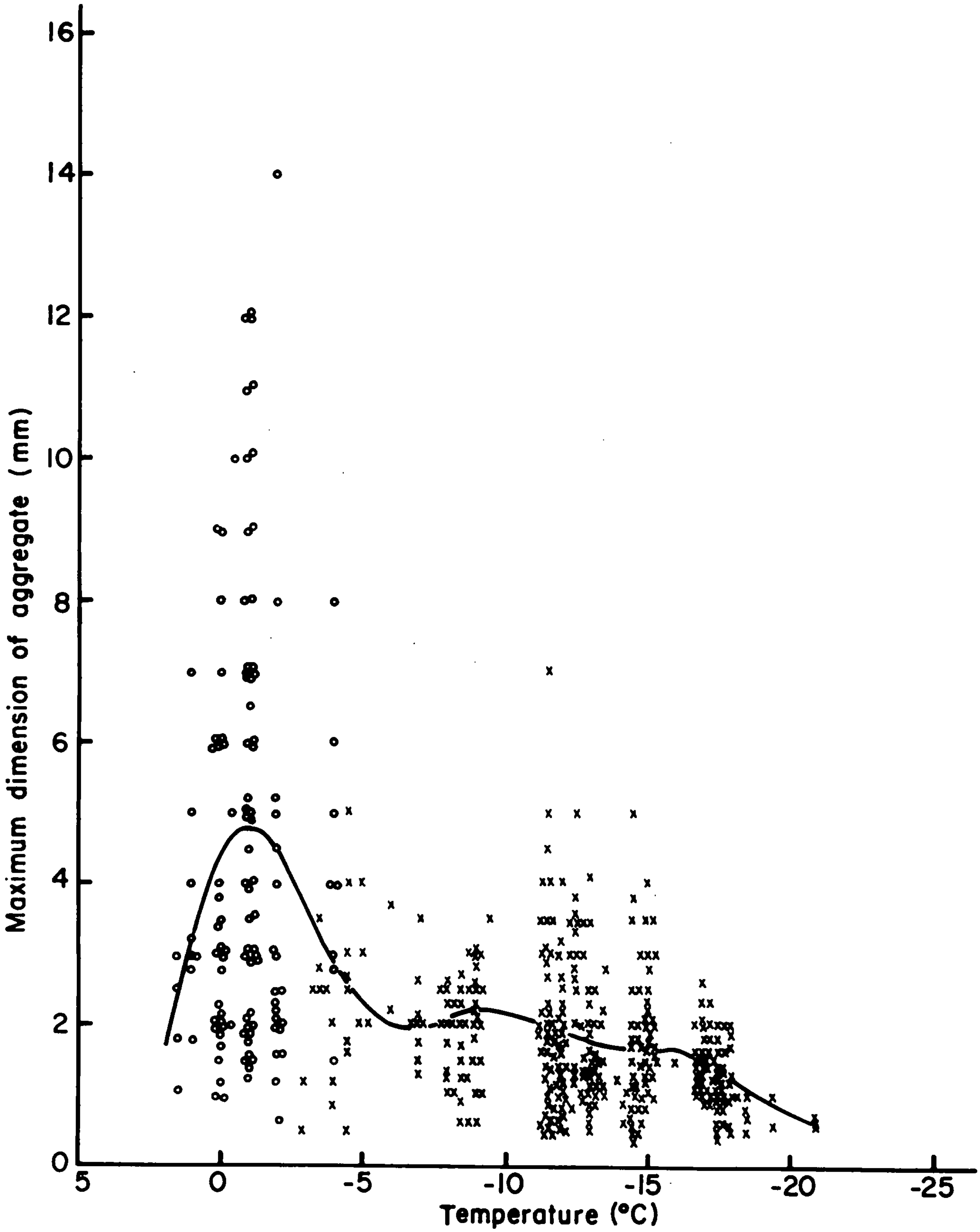

Fig. 3.13 Maximum dimensions of aggregates as a function of the temperature at which they were collected. o - ground data, x - aircraft data. The solid line gives the most probable maximum dimension of the aggregates.

SECTION 4

GROUND OBSERVATIONS

This section is concerned with the results obtained during the winter of 1971-72 from the network of ground stations in the Cascade Mountains shown in Fig. 1.4. However, results obtained when artificial seeding experiments were carried out are described in §5.

4.1 General Synoptic Conditions in 1971-72 Compared to 1970-71

The winters of 1970-71 and 1971-72 were successive record snow years in the Cascade Mountains of Washington State. The average snowfall at Stampede Pass during the period November through March, based on the period 1931-65, was 376.6 inches. During this same period the snowfall at Stampede Pass was 502.4 inches and 605.3 inches in 1970-71 and 1971-72, respectively. In 1970-71 the snowfall in each month except February was far above average, and in 1971-72 three of the five months had above normal snowfall with January setting a record and December seven inches short of the record. Paradise, on Mt. Rainier, set world records for the most snowfall throughout the season at any officially recognized weather station. In 1970-71, Paradise exceeded the previous record (of 1,000.3 inches set at Paradise in 1955-56) with a world record snowfall of 1,027 inches. This record was surpassed in the 1971-72 season when 1,122 inches of snow fell at Paradise.

The conditions under which our ground observations were made in 1971-72 were more variable than in 1970-71. For example, in 1970-71, observations were made at Alpental Base during snowfall for a total of 85.5 hours, of which 37 hours (43.3%) were in pre-frontal conditions. At this same site in 1971-72, measurements were taken during 110.75 hours of snowfall, of which only 21.75 hours (19.6%) were pre-frontal. The large quantity of additional data collected in 1971-72 allows us to improve and extend the analysis given in Res. Rpt. VI which was based on the 1970-71 data. However, in some cases (e.g., correlations between riming, winds, moisture and precipitation), due to the wider variety of conditions under which measurements were obtained in 1971-72, the new data have failed to sharpen the earlier conclusions.

4.2 Types of Precipitation Particles at the Ground Stations

Solid precipitation particles reaching the ground were replicated and analyzed as described in Res. Rpt. VI and classified as shown in Table 4.1.

TABLE 4.1

CLASSIFICATION AND SYMBOLS FOR SNOW PARTICLES

Symbol	Explanation	Conditions under which particles grow
⟷	Includes both needles & sheaths (separate, bundles & combinations	-4 to -6°C. Above water saturation.
>—<	Sheaths (separate, bundles & combinations)	-6 to -8°C. Above water saturation.
	Dendrites	-13 to -17°C. Above water saturation.
	Radiating assemblages of dendrites	-15 to -22°C. Above water saturation.
+	Crystals with broad branches	-13 to -17°C. Below water saturation.
✳	Stellars	-13 to -17°C. Above water saturation.
	Side planes	-20 to -25°C. Above water saturation.
	Assemblages of plates	-18 to -22°C. Above water saturation.
⬡	Plates	Several temperature ranges.
	Assemblages of sectors	-18 to -22°C. Above water saturation.
	Bullets	-25 to -30°C. Above water saturation.
▯	Columns	Several temperature ranges.
	Plates with extensions	Several temperature ranges.
Ⓢ	Crystal with sector-like branches	Several temperature ranges and saturations
	Capped columns	Varied temperature ranges
	Frozen water drops	
Ⓖ	Graupel (hexagonal, cone-like & graupel)	
(GS)	Graupel-like snow	
	Irregular	
	Undetermined	
N	Nothing on slide	
M	Melted crystals	
○	Unrimed - no frozen drops on particle	
◔	Light riming - few frozen drops on particle	
◑	Moderate riming - about one-half of particle covered with frozen drops.	
●	Densely rimed - particle completely covered with frozen drops	
A	Aggregates of ice crystals (due to difficulties in replications the absence of an "A" does not necessarily mean there were no aggregates at that time)	
HD	Majority of the plane crystals on a slide are double crystals (two parallel crystals separated by a frozen water drop at their center)	
MD	Approximately half of the plane crystals on a slide are double crystals	
FD	Few of the plane crystals on a slide are double crystals	

The frequency of occurrence of "dominant slide particles" are shown in Fig. 4.1. As explained in Res. Rpt. VI, these plots can be used for comparing the relative frequency of occurrence of "dominant" particles of different types at the various stations. The general patterns are similar to those obtained in 1970-71 (see Figs. 5.5 and 5.6 in Res. Rpt. VI). However, graupel particles were more common in 1971-72 than in 1970-71; this is no doubt due to the fact that more of the measurements were made in post-frontal conditions in 1971-72 than in 1970-71. In 1971-72 additional observations were made at the top of a ski lift at Alpental which is 5440 ft. above sea level (compared to Alpental Base which is 2940 ft.). It can be seen from Fig. 4.1 that graupel particles were far less common at the top of Alpental than at the bottom. Thus, appreciable riming occurred in the 2500 ft. separating the top from the bottom of Alpental (see §4.4 for further discussion of this point).

Fig. 4.2 shows the frequency of occurrence of "dominant day particles" at three ground stations. These plots indicate the relative frequency of occurrence of "dominant" particles of different types at each station but they should not be used for comparing one station with another. The main difference between these results and those obtained in 1970-71 is that in 1971-72 graupel particles were among the most common on both the western and eastern slopes of the Cascade Mountains. Again, this is probably due to the more convective (post-frontal) conditions investigated in 1971-72.

4.3 Riming

More detailed information on the degrees of riming of the precipitation particles on the ground across the Cascades during the winter of 1971-72 is contained in Figs. 4.3 and 4.4. The results shown in Fig. 4.3 are for comparing one station with another, while those in Fig. 4.4 show the relative frequency of occurrence of different degrees of riming at each station. The main points to be noted in Fig. 4.3 are that the degree of riming is greatest immediately to the west of the Cascade Divide (Alpental Base), is slightly less just east of the divide (Hyak), and is lower still well east of the divide (Keechelus Dam). However, riming at Alpental Top was much less than at Alpental Base. Fig. 4.4 shows that moderately to heavily rimed particles occurred with about the same frequency as unrimed to lightly rimed particles at Alpental Base, Hyak and Keechelus Dam, but at Alpental Top unrimed to lightly rimed particles were more common than moderately to heavily rimed particles.

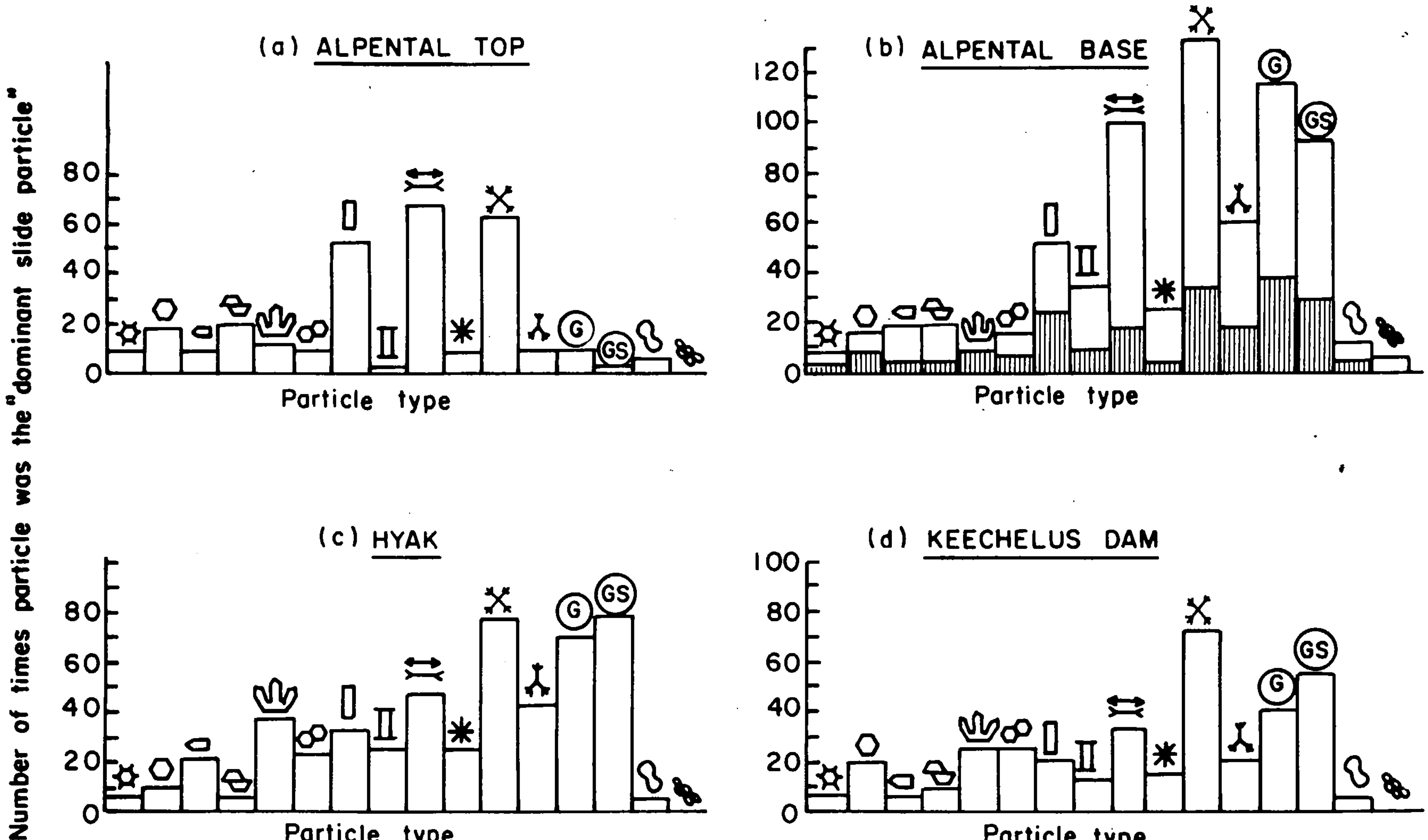

Fig. 4.1 Occurrence of "dominant slide particle" (for comparing the relative differences in the frequencies of occurrence of "dominant particles between stations). Shaded regions in (b) indicate data collected on the same days as for (a). See Table 4.1 for key to symbols.

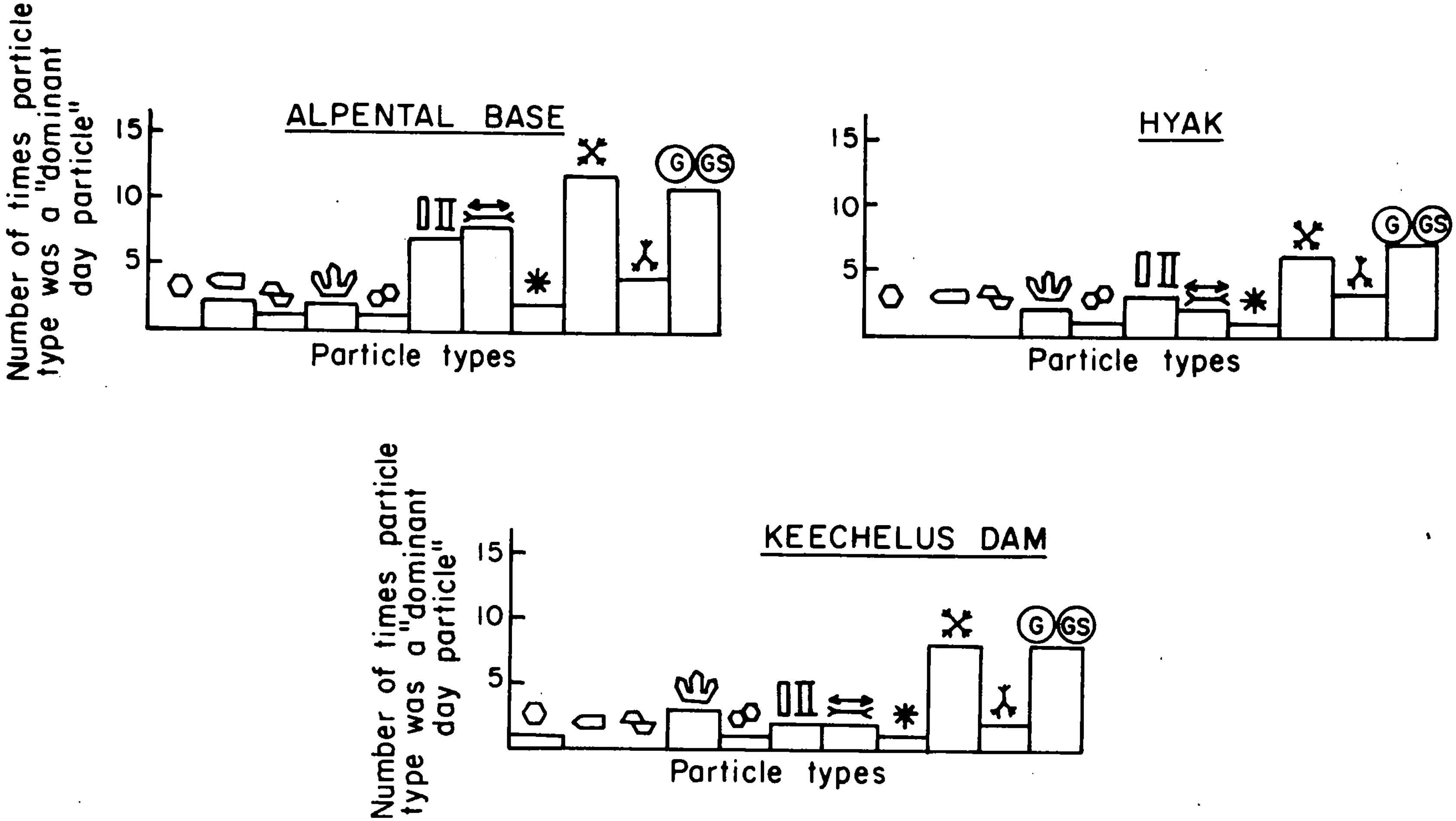

Fig. 4.2 Occurrence of "dominant day particles" (for comparing relative frequency of occurrence of "dominant" particles at a particular station). See Table 4.1 for key to symbols.

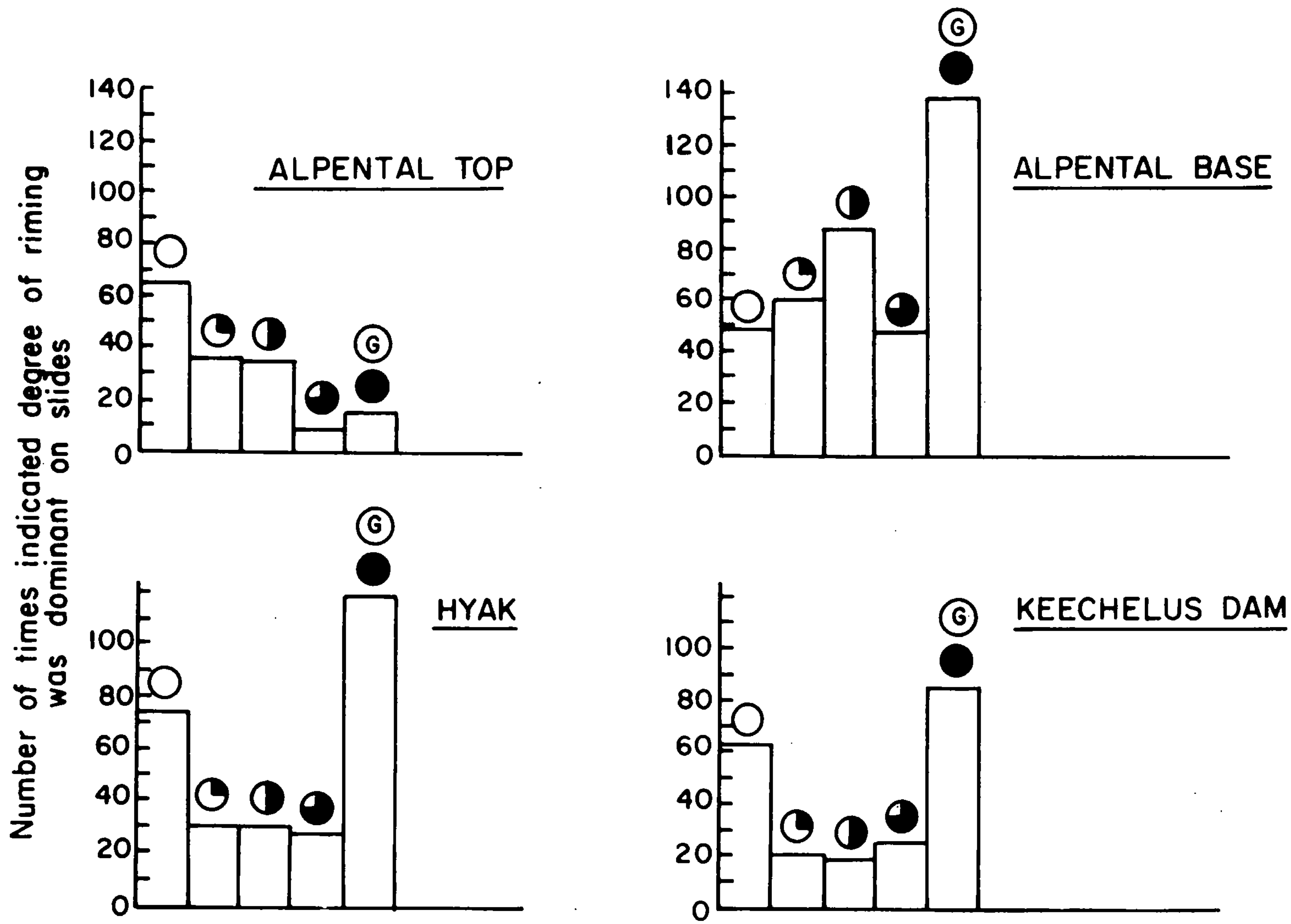

Fig. 4.3 Occurrence of dominant degree of riming from individual slides (for comparing the relative differences in the frequencies of occurrence of various degrees of riming between stations). See Table 4.1 for key to symbols.

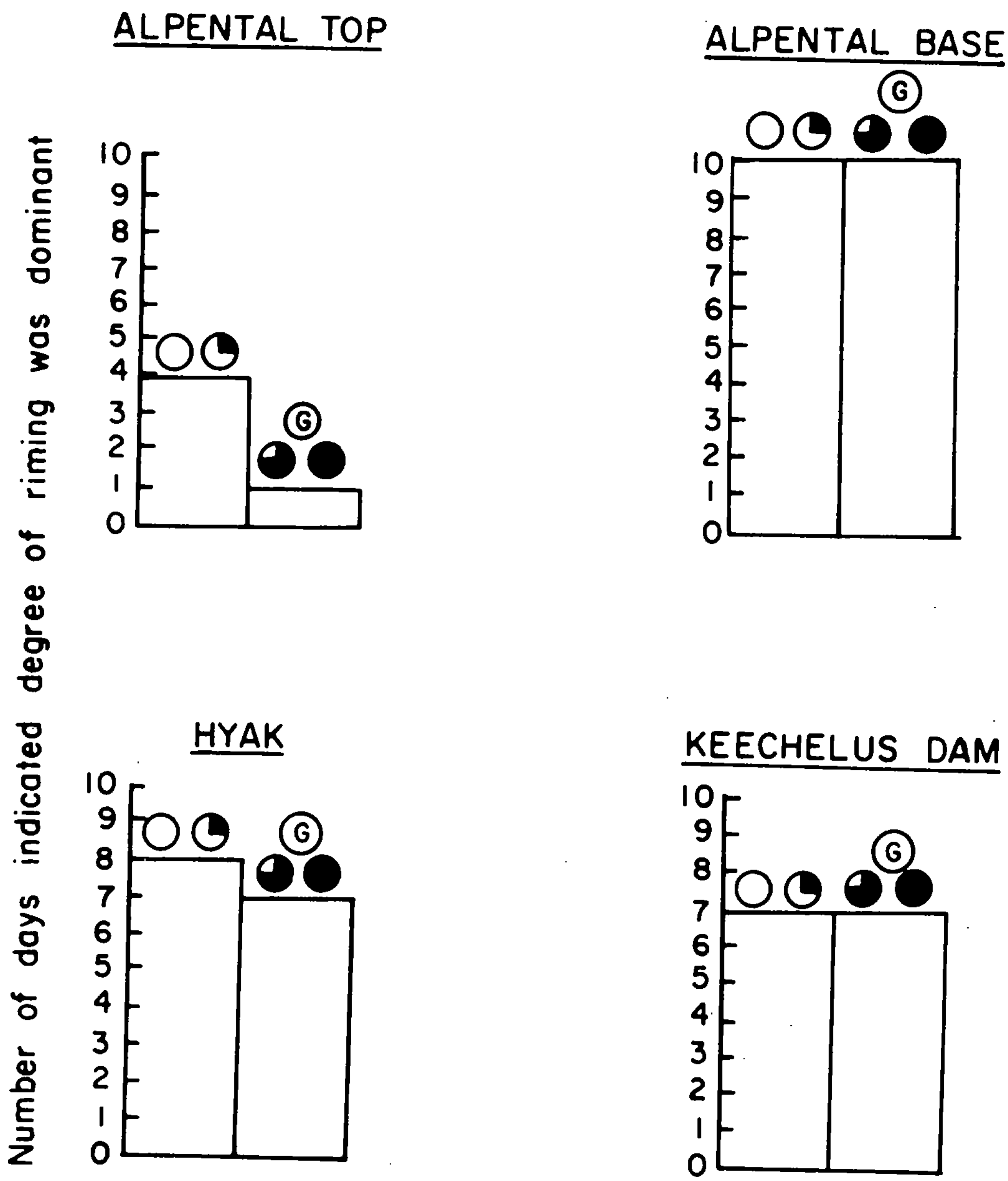

Fig. 4.4 Number of days various degrees of riming were dominant at each station (for comparing relative frequency of occurrence of different degrees of riming at a particular station). See Table 4.1 for key to symbols.

Variations in the degree of riming with the type of particle are shown in Fig. 4.5 where each dot shows the degree of riming of a "dominant slide particle." The results generally confirm the data obtained in the previous winter (see Fig. 5.11 in Res. Rpt. VI) in that needles, sheaths and dendrites were often heavily rimed while plates, sectors, sideplanes and bullets were generally unrimed or lightly rimed. In addition, data were obtained on some crystals (radiating assemblages of dendrites, capped columns, and broad-branched crystals) not identified previously.

4.4 Comparison of Crystal Types at Two Different Altitudes at Alpental

We have already mentioned the differences in the dominant crystal types and their degree of riming at the top of Alpental (5,440 ft.) and the base of Alpental (2,940 ft.). In this section we analyze the data collected at these two stations in more detail.

Slide replicas taken during the same time periods at the top and bottom of Alpental were examined for the types of crystals present without regard to the number of crystals of each type on each slide. The results are shown in Fig. 4.6 where each event represents an occasion on which at least one crystal of the specified type appeared on a slide. Since the number of slides exposed on different days may have been quite different, the results shown in Fig. 4.6 should not be used for comparing the relative frequency of occurrence of different crystal types at one station. However, since approximately the same number of slides were exposed at the top of Alpental as at the bottom and for the same periods of time, the results can be used for comparing the relative likelihoods of a particular type of crystal appearing at Alpental Top and Alpental Base.

It can be seen from Fig. 4.6 that more identifiable crystals of every type were observed at Alpental Top than at Alpental Base, with the one exception of radiating assemblages of dendrites. However, more graupel-like snow and graupel fell at the base than at the top. Similar plots for comparing the relative frequencies of occurrence of various degrees of riming at Alpental Base and Top are shown in Fig. 4.7. It can be seen that unrimed crystals are much more likely to be observed at the top of Alpental than at the bottom. These observations show that at 5,440 ft. above mean sea level most of the crystals in the air are unrimed or lightly rimed. As they fall through 2,500 ft. to the base of Alpental they become increasingly more rimed and many arrive at the base as graupel particles.

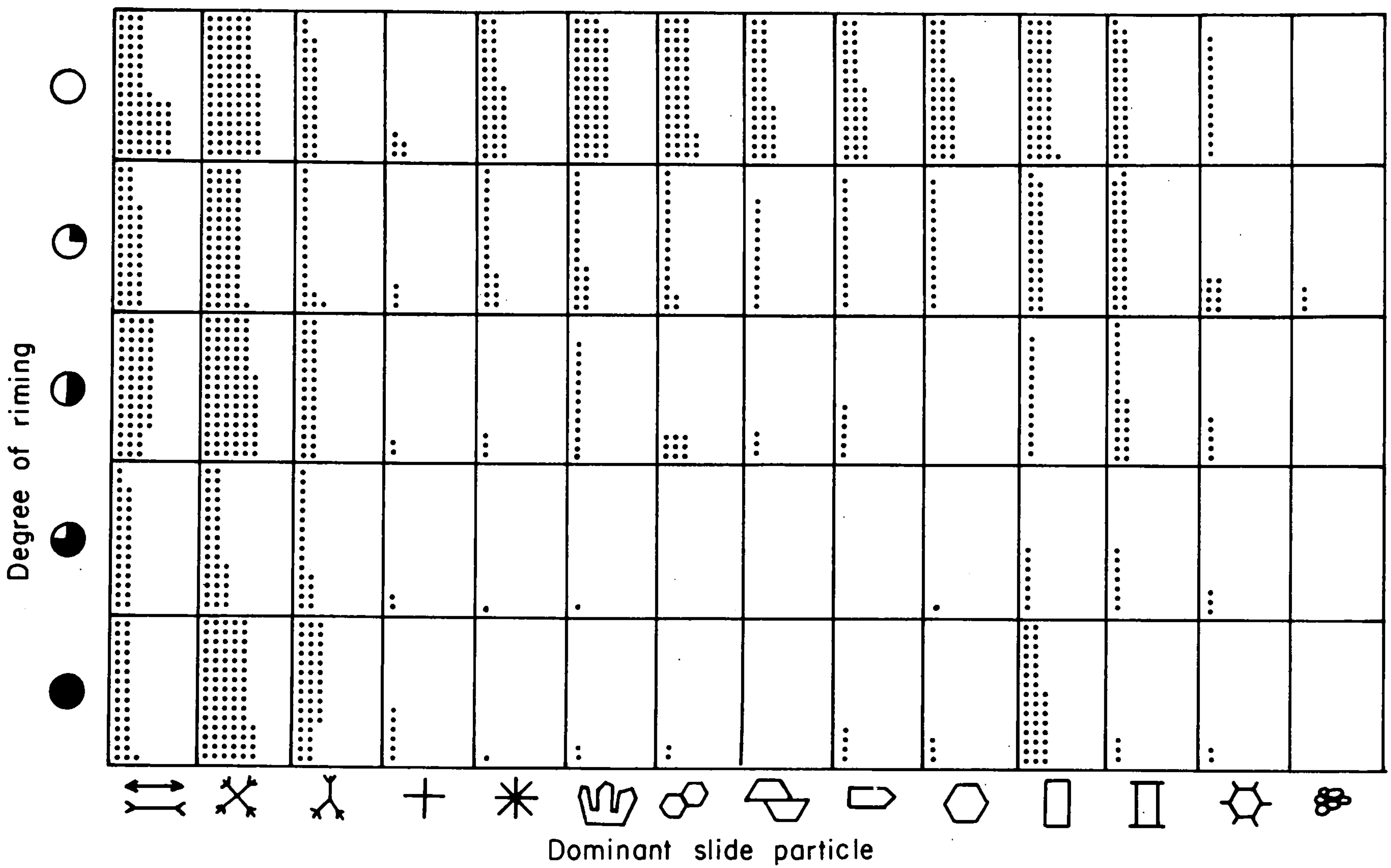

Fig. 4.5 Degree of riming of dominant slide particles. (See Table 4.1 for key to symbols.)

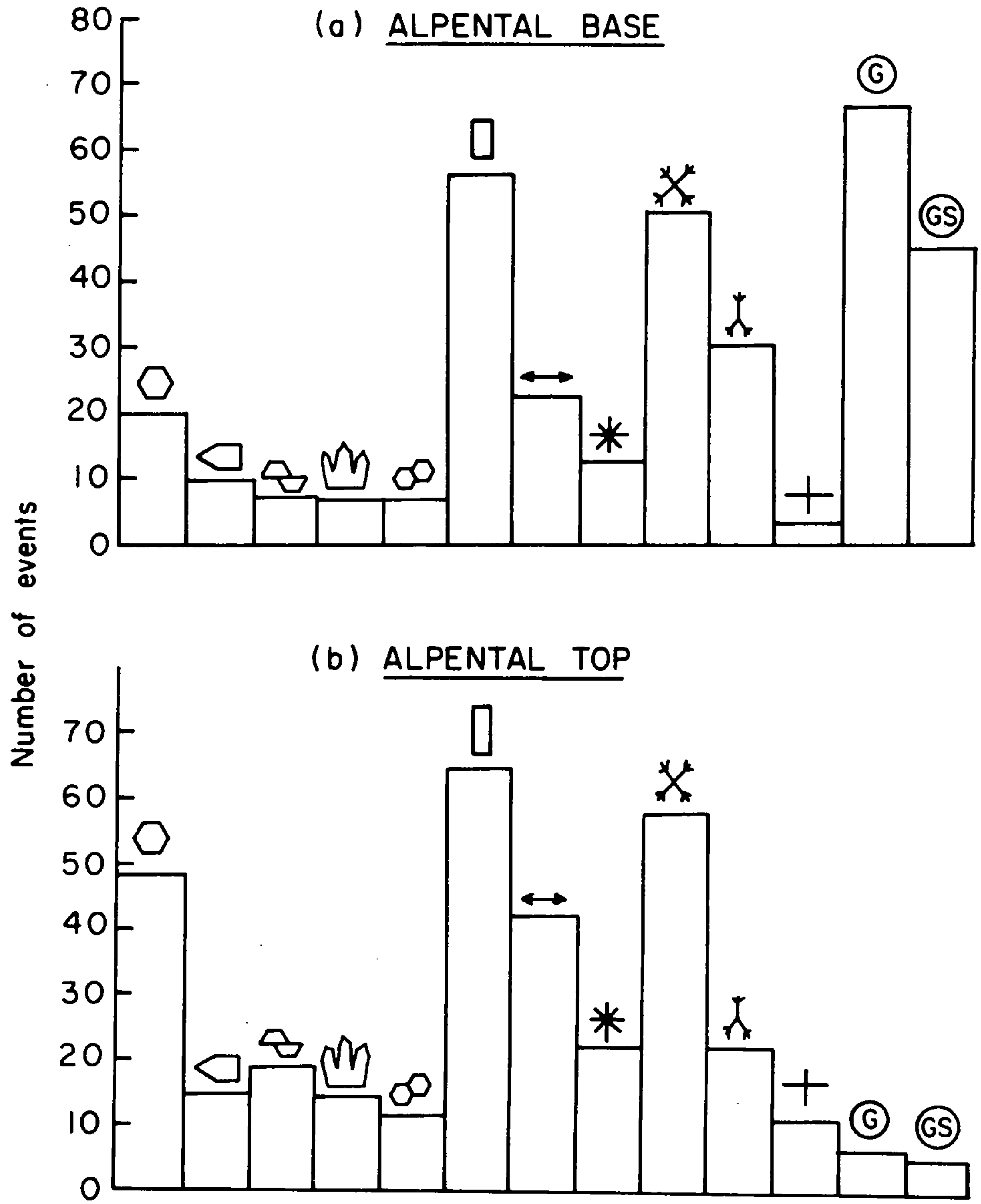

Fig. 4.6 Histograms for comparing the relative frequencies of occurrence of a particular crystal type at the base and top of Alpental. For key to symbols see Table 4.1.

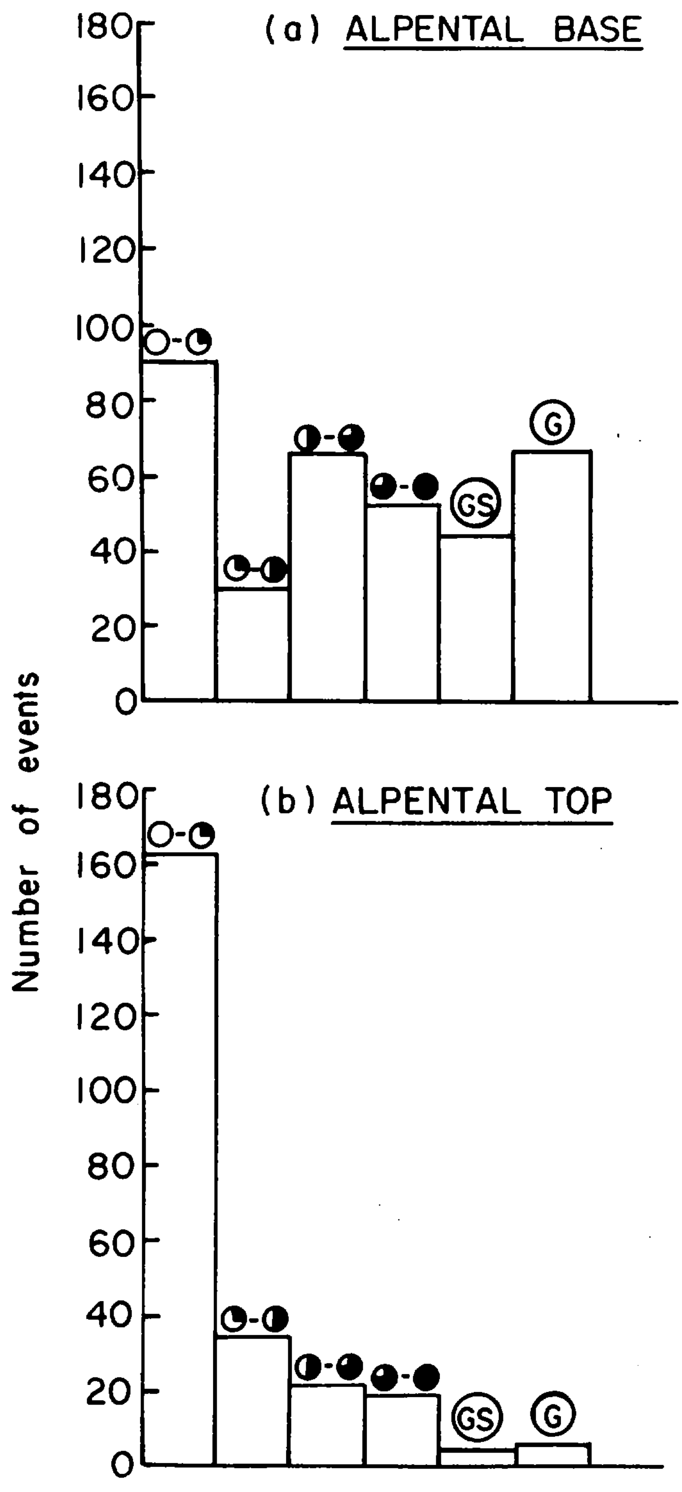

Fig. 4.7 Histograms for comparing the relative frequencies of occurrence of various degrees of riming at the base and top of Alpental. For key to symbols see Table 4.1.

Figs. 4.8 and 4.9 show comparisons between the maximum dimensions of ice crystals collected at Alpental Base and Top. With the exception of columns, the size distributions for a particular type of crystal are the same at both stations. This suggests that little diffusional growth occurs in the 2,500 feet of fall from the top to the base of Alpental. The columns collected at Alpental Top were definitely smaller and they occurred more frequently than at the Alpental Base. This is due to the fact that small columns, with lengths comparable to their diameters and with no visible internal structure, often appeared in high concentrations in clouds at the top of Alpental. These crystals grew, and sometimes changed their habit, as they fell the 2,500 feet to the bottom of Alpental.

If the maximum dimensions of the ice particles shown in Figs. 4.8 and 4.9 are compared, it will be seen that only dendrites are significantly larger than graupel particles. It would be expected therefore that comparatively few dendrites are transformed into graupel by riming. This conclusion is confirmed by the results shown in Fig. 4.6 which shows that only 12 per cent fewer dendritic events occurred at the base of Alpental than at the top. The spectra of maximum dimensions for needles, broad-branched crystals and stellars (Figs. 4.8 and 4.9) suggests that no more than about half of these crystals should become graupel. The average percentage decrease in events for these three crystal types is 45 per cent (Fig. 4.6). In view of the small sizes of bullets, plates and columns compared to graupel particles they should all be eligible for growth to graupel. However, the decrease in the number of events for these crystals between the top and base of Alpental was only about 25 per cent (Figs. 4.6). Since supercooled droplets were present between the two stations when these crystals were falling, they should have had the opportunity to rime. The fact that they were not converted to graupel as efficiently as we might have expected, might be due to their smaller sizes and low fall speeds reducing their collection efficiencies for supercooled droplets.

4.5 Maximum Sizes of Ice Crystals

Ice crystals collected at the ground stations were divided according to their maximum dimensions into the following eight groups: less than 0.25 mm, 0.25 - 0.5 mm, 0.5 - 1.0 mm, 1.0 - 1.5 mm, 1.5 - 2.0 mm, 2.0 - 3.0 mm, 3.0 - 5.0 mm and greater than 5.0 mm. Only those ice crystals with regular shapes were classified in this way (sideplanes, assemblages of plates, and

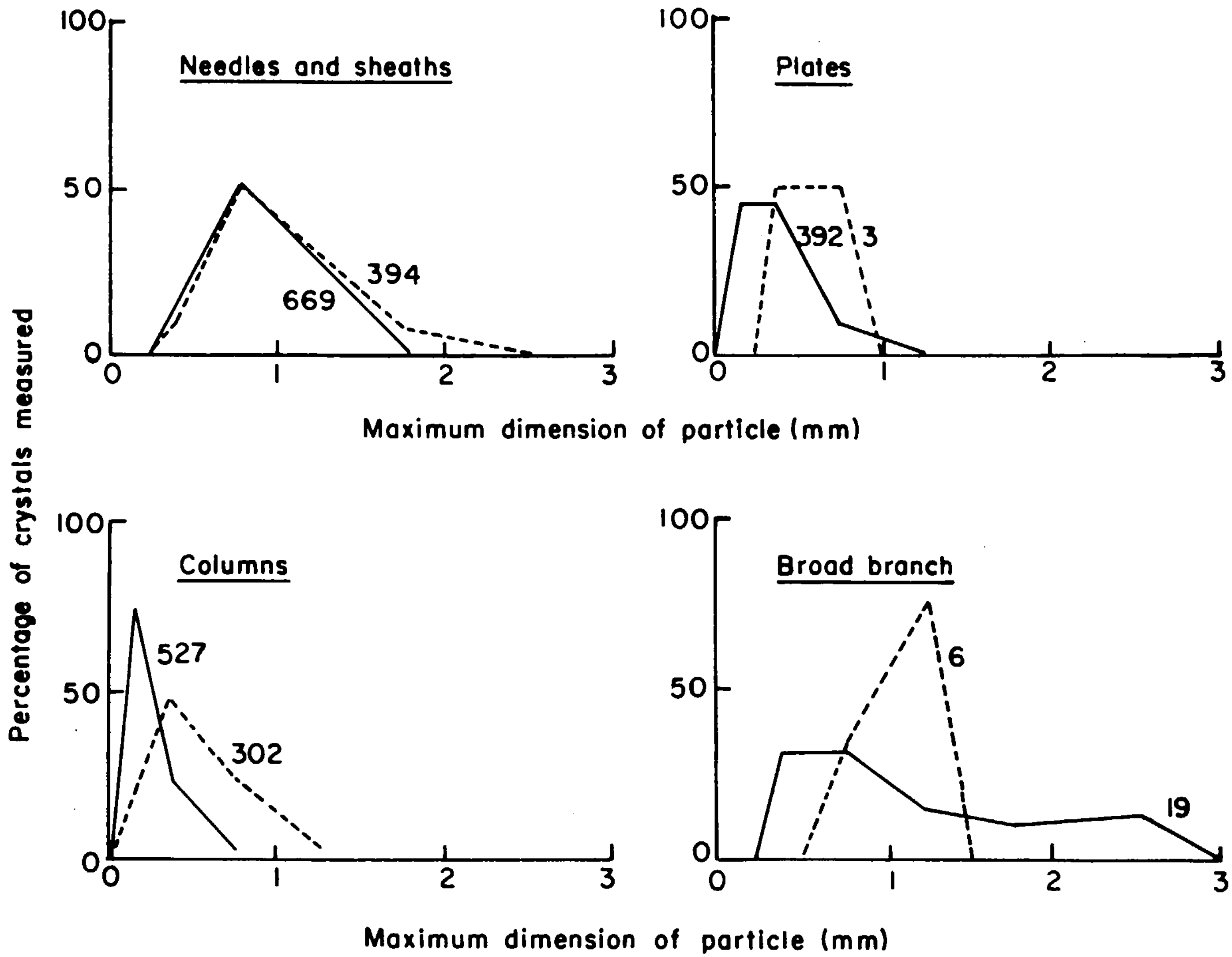

Fig. 4.8 Size distributions of ice crystals at the top (———) and bottom (- - - -) of Alpental. The number by each curve is the total number of crystals sampled. The two stations are separated by a height of 2500 feet.

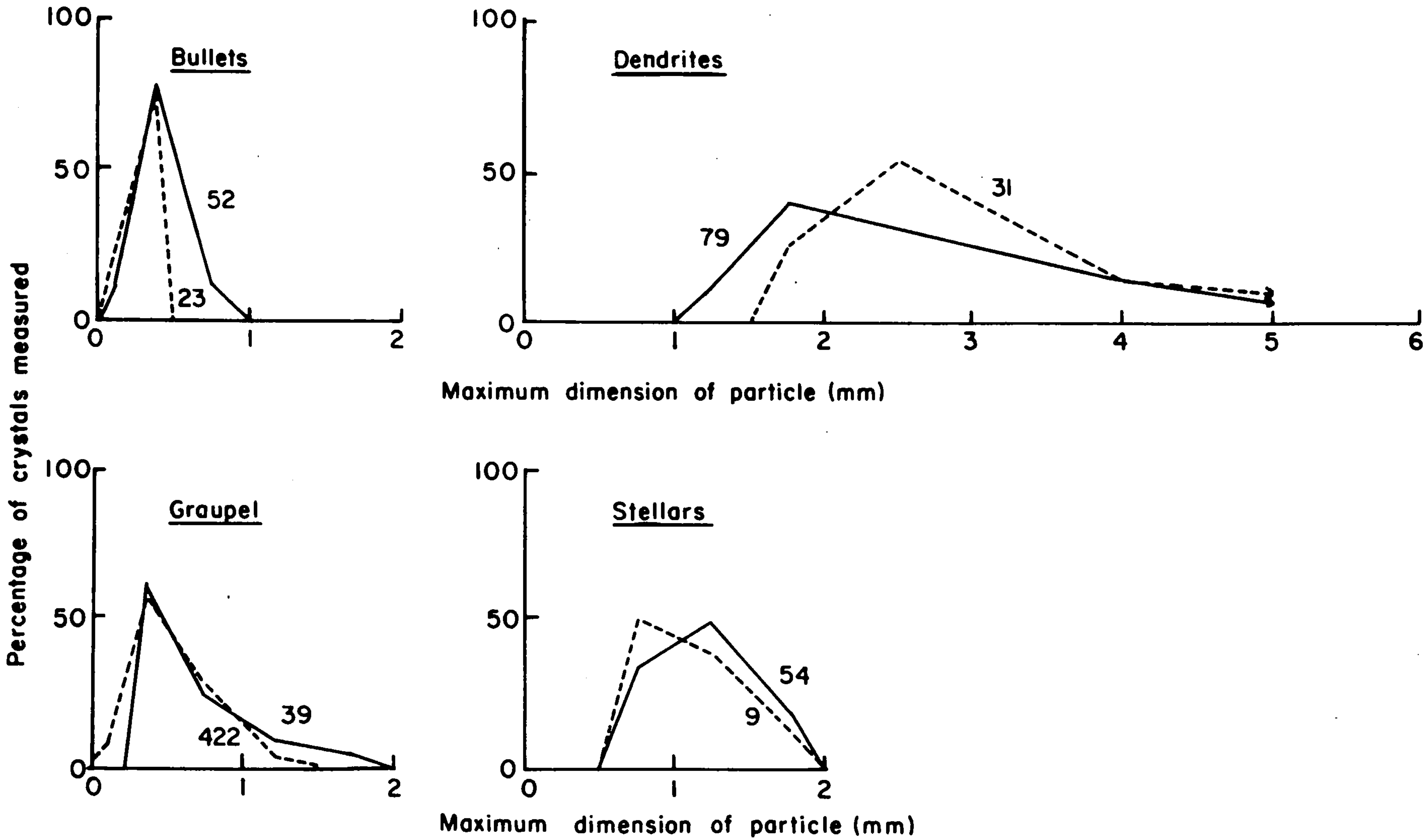

Fig. 4.9 Size distributions of ice crystals at the top (———) and bottom (----) of Alpental. The number by each curve is the total number of crystals sampled. The two stations are separated by a height of 2500 feet.

assemblages of sectors were excluded). However, if a crystal had irregular branches it was classified according to the average diameter of its branches.

The size distributions of the particles collected at Alpental Base, Keechelus Dam and Kachess Dam showed no significant differences, therefore, the results from these three stations were combined (Fig. 4.10). A noticeable feature of the results is the large sizes of the dendrites compared to the other crystals. The results are consistent with the data collected in 1970-71 (see Fig. 5.7 in Res. Rpt. VI).

4.6 Dimensions of Ice Crystals†

The data described in this section are based on crystals collected and replicated using the continuous particle sampler on the B-23 research aircraft and from slide replicas made at the ground stations in the Cascade Mountains during the winters of 1970-71 and 1971-72. Empirical relationships between the dimensions of the crystals were derived by fitting polynomial functions to the diameter and thickness data for plate-like crystals, and to the length and width data for columnar-like crystals, using a least-squares best-fit technique.

4.6.1 Needles

Observed length-width relationships for needles are shown in Fig. 4.11. The empirical best-fit relationship between the width W (in μm) and the length L (in μm) over the range of measurements is:

$$\ln W = -10.76 + 4.159 \ln L - 0.2882(\ln L)^2$$

and this is shown as a solid line in Fig. 4.11.

These results (referred to as Cascade Data) are compared to those of other workers in Fig. 4.12. Our results indicate that when needles reach a width of about 70 μm the dominant growth is along the c-axis. Ono's (1969) data shows a limiting width for needles of 40 μm, while Magono (1954) and Auer and Veal (1970) found no limit to the width of needles.

4.6.2 Sheaths and Long Solid Columns

The observed lengths and widths of sheaths and long solid columns are shown in Fig. 4.13. When the results for these two types of crystals are combined, the empirical relationship between the width (in μm) and length L (in μm) is

†For convenience both ground and aircraft data are considered in this section.

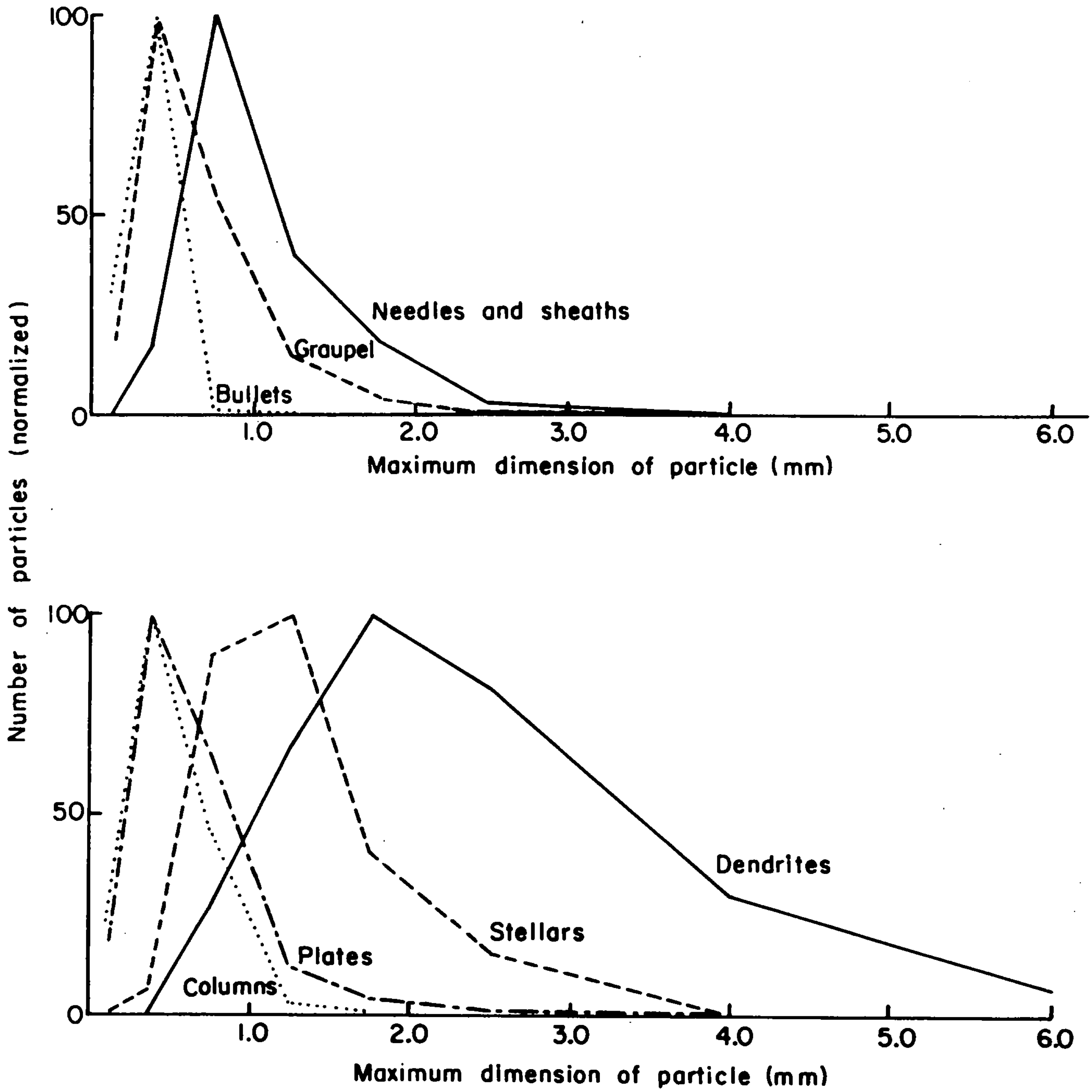

Fig.4.10 Size distributions of ice crystals collected at Alpental Base, Hyak and Keechelus Dam.

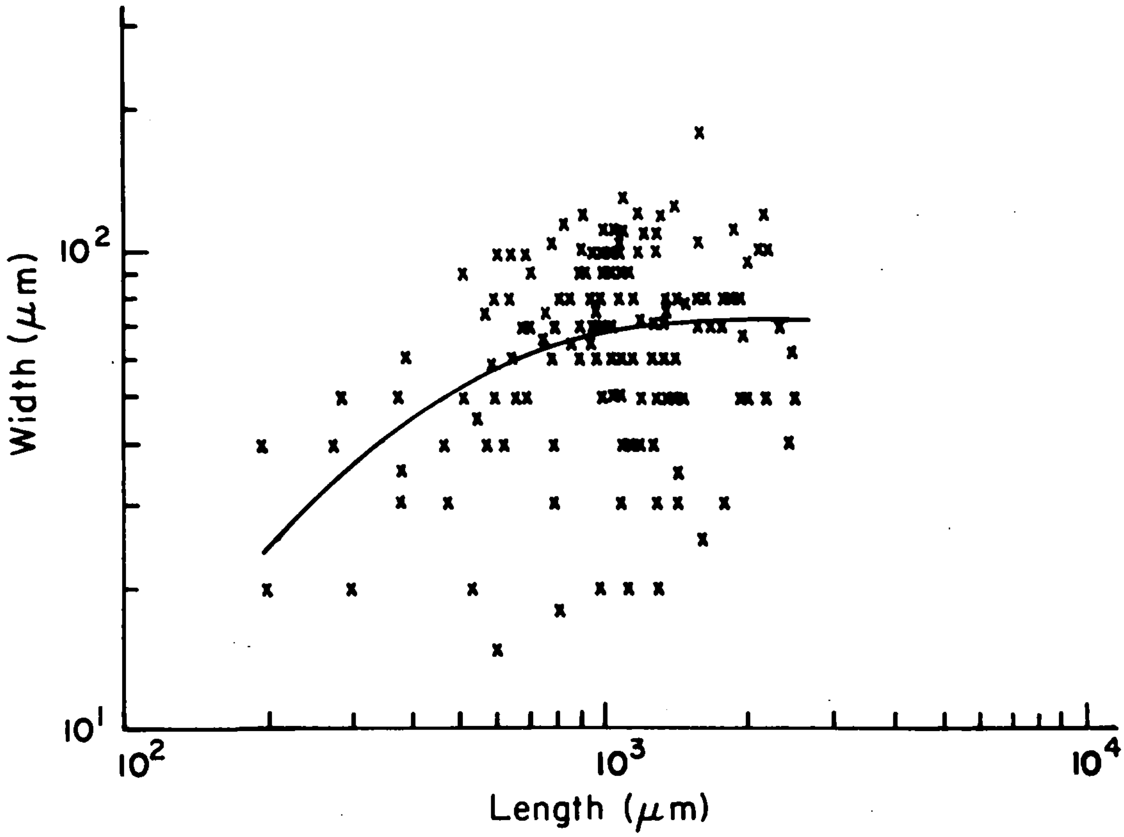

Fig. 4.11 Observed length-width relationship for needles.

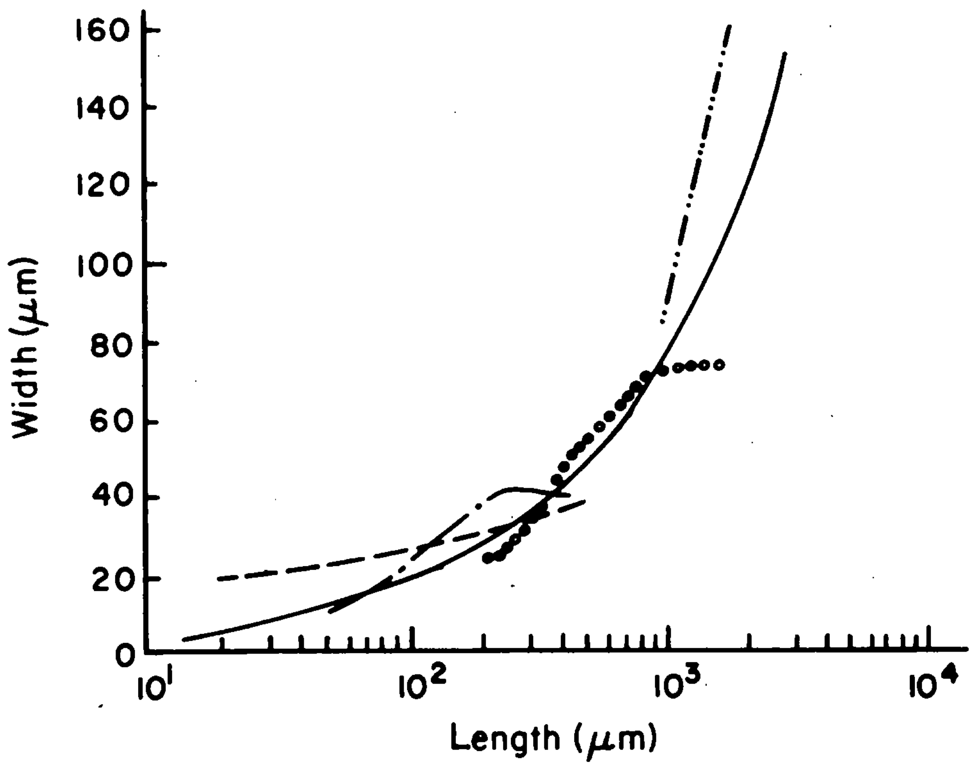

Fig. 4.12 Comparison of measurements on dimensions of needles. —··— Magono (1954). ——— Isono (1959). —·— Ono (1969). ——— Auer and Veal (1970). ooooo Cascade data.

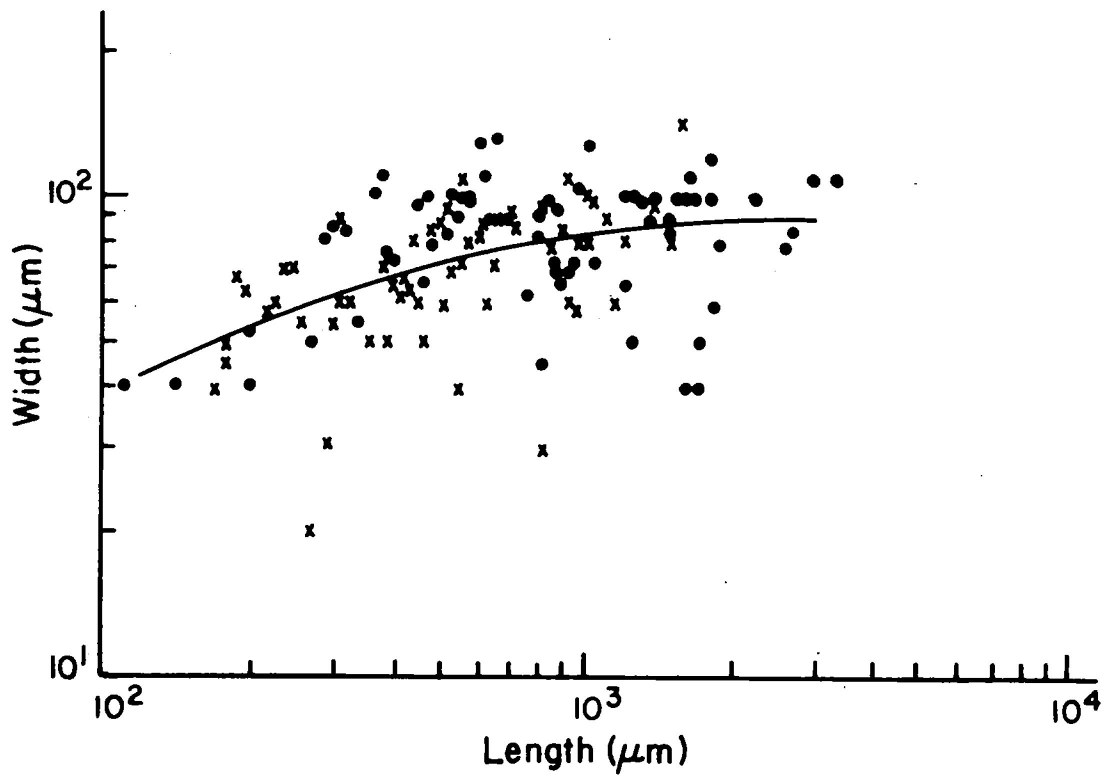

Fig. 4.13 Observed length-width relationship for sheaths (•) and long solid columns (x).

$$\ln W = -0.6524 + 1.32 \ln L - 0.0846 (\ln L)^2$$

Our observations indicate that after sheaths and long solid columns attain a width of about 90 μm, the dominant growth is along the c-axis.

4.6.3 Solid and Hollow Columns

Warm-region columns occur between -5 and -10°C and cold-region columns below -20°C. Warm-region columns were collected more frequently than cold-region columns. The observed length-width relationship for columns collected at ground level only are shown in Fig. 4.14 and the solid line through the data points is represented by

$$\ln W = -0.7349 + 1.558 \ln L - 0.1025(\ln L)^2$$

where W and L are the width and length in μm.

The results for columns collected both on the ground and from the aircraft are shown in Fig. 4.15 and are fitted by

$$\ln W = 1.384 + 0.2396 \ln L + 0.0507(\ln L)^2$$

It can be seen from Fig. 4.16 that our measurements on the warm-region columns collected on the ground and in the air are in reasonable agreement with those of other workers. If we consider our data for warm-region columns collected on the ground only, it is in almost exact agreement with Auer and Veal's results (1970) over the range common to both sets of measurements.

4.6.4 Hexagonal Plates

The thicknesses of plates were determined only for crystals collected on the ground. The results are shown in Fig. 4.17 and the empirical relationship between the thickness T (in μm) and the diameter D (in μm) of the hexagonal plates is

$$T = 99.17 - 37.49 \ln D + 3.844 (\ln D)^2$$

These results are compared with those of other workers in Fig. 4.18 where it can be seen that our thicknesses are somewhat less than those reported previously. However, the general trend of the various results are similar. It appears that the thickness of a plate remains constant as its diameter increases up to a 100 μm or so, but thereafter it increases as the diameter increases.

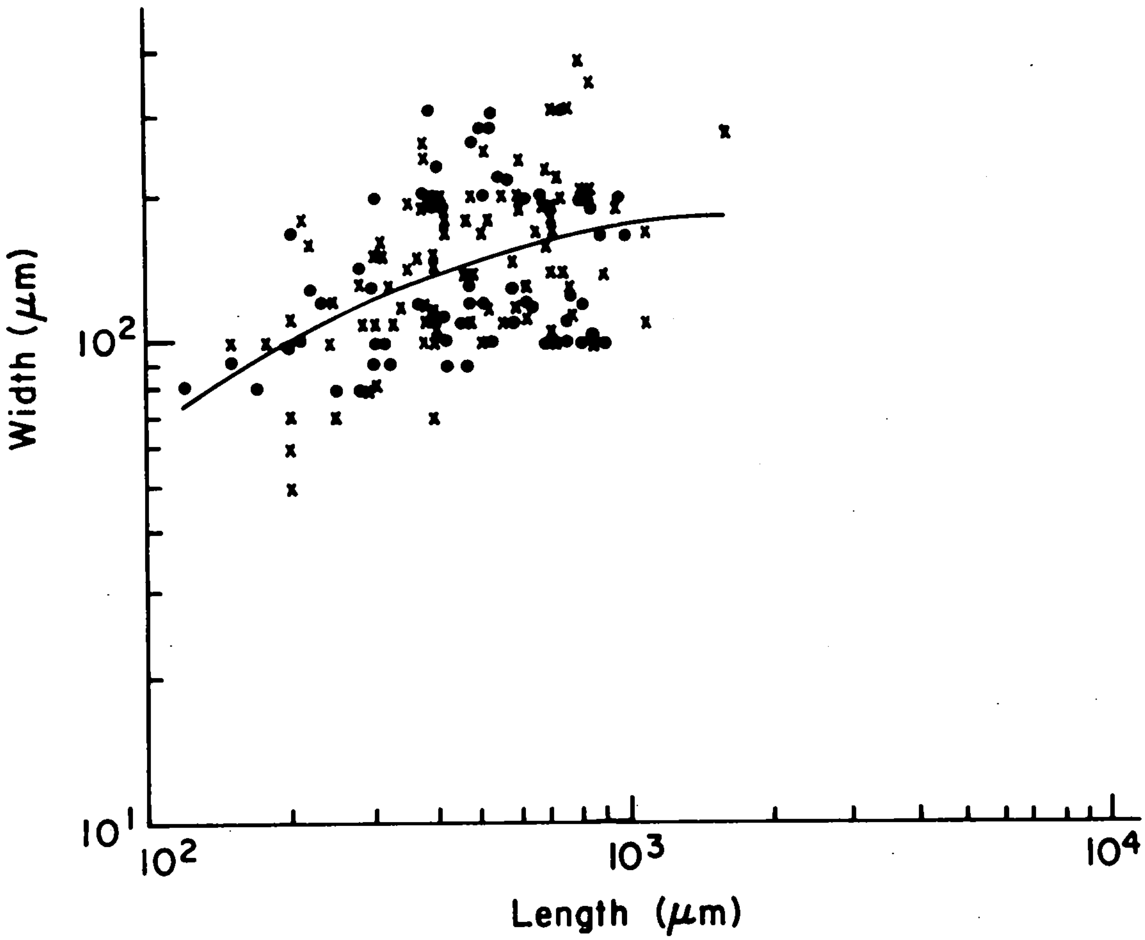

Fig. 4.14 Observed length-width relationship for solid (•) and hollow (x) columns collected at ground level in the Cascade Mountains.

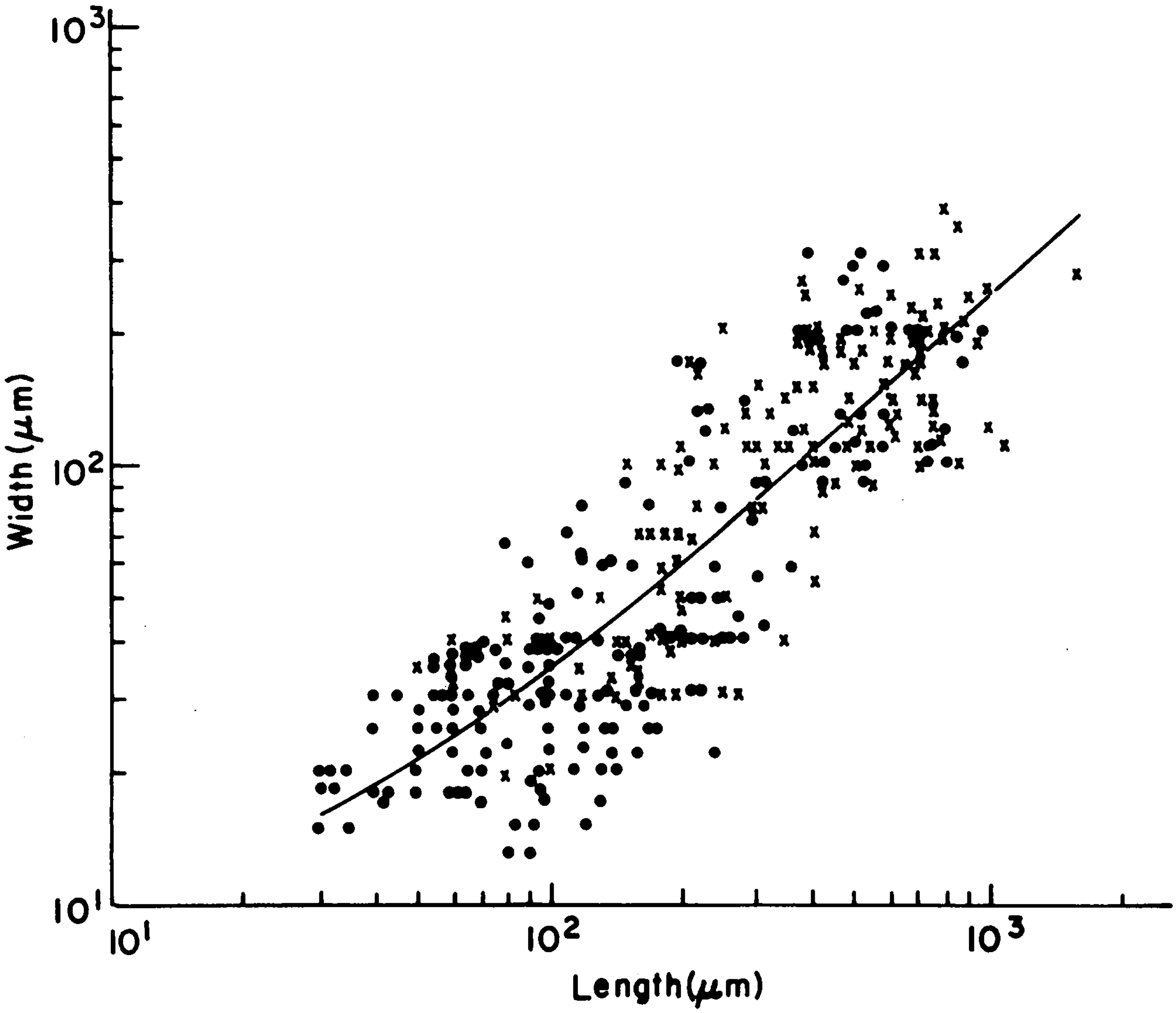

Fig. 4.15 Observed length-width relationship for solid (•) and hollow (x) columns collected at the ground and in the air.

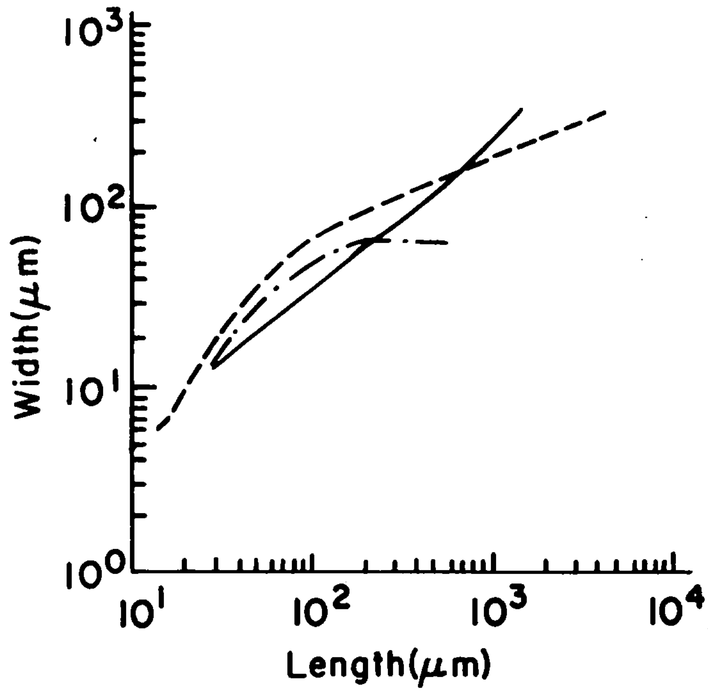

Fig. 4.16 Comparison of measurements on dimensions of warm-region columns. The Cascade data was based on crystals collected on the ground and in the air. —·— Ono (1969). ---- Auer and Veal (1970). —— Cascade data.

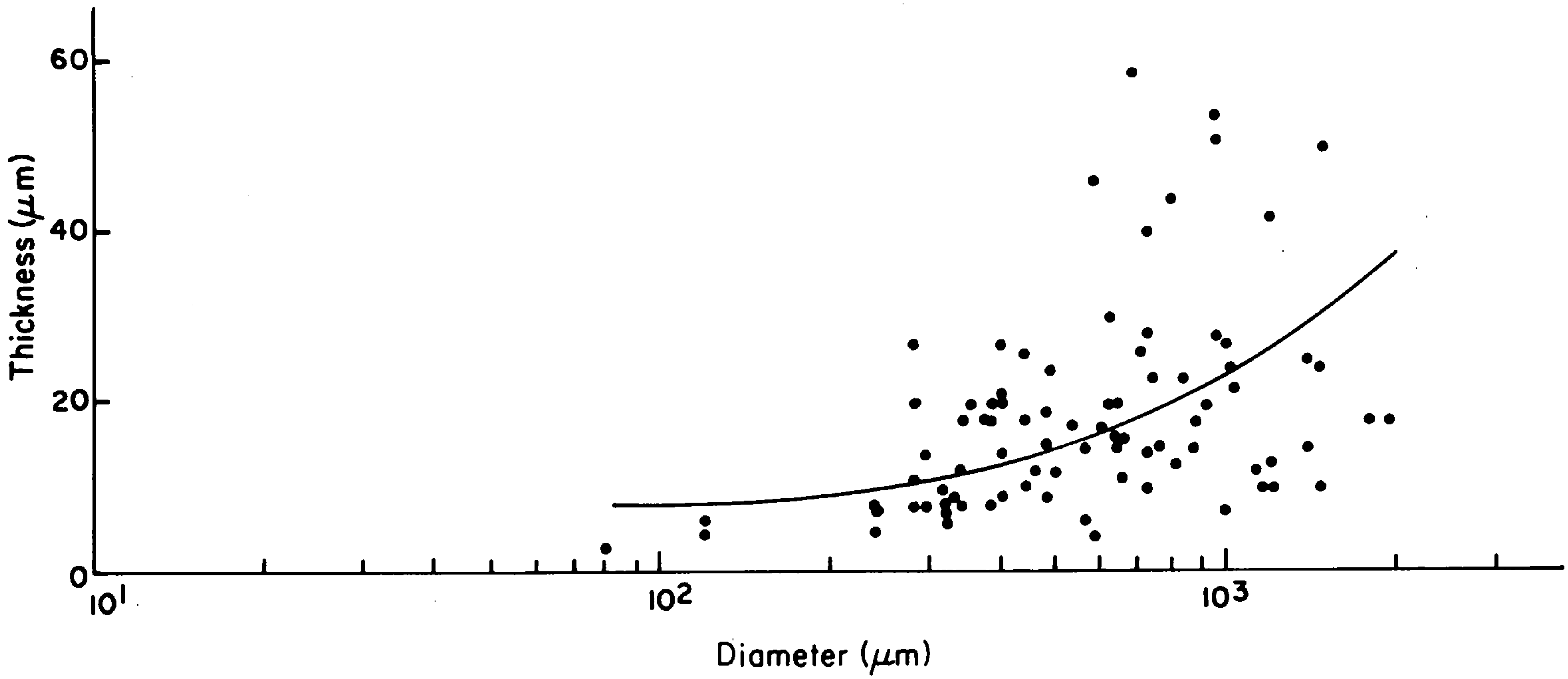

Fig. 4.17 Diameter-thickness relationship for hexagonal plates collected at ground level.

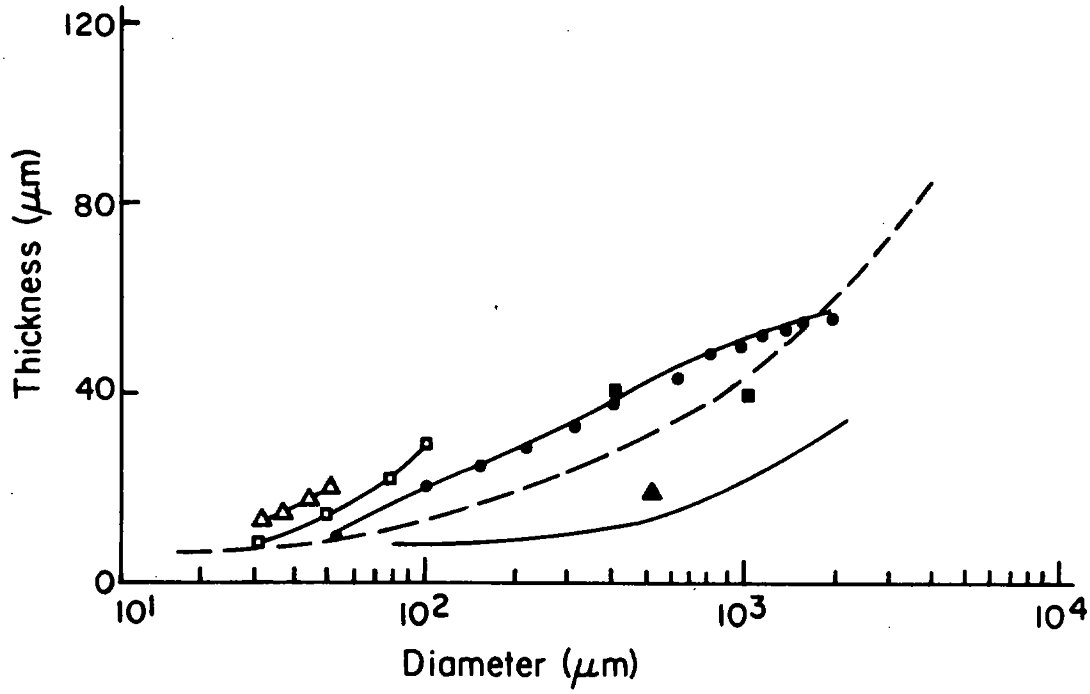

Fig. 4.18 Comparison of measurements on dimensions of hexagonal plates. ■ - Schaefer (1947). ▲ - Weickmann (1947). □——□ - Reynolds (1952). △——△ - Mason (1953). ●——● - Ono (1969). ----- Auer and Veal (1970). ——— Cascade data

4.7 Aggregates

In §3.3 we discussed the effects of temperature and concentration of ice particles on the aggregation of crystals in the air. This analysis was based primarily on aircraft data, although some ground data was also used. In this section we describe the results of further analysis of the solid precipitation particles collected at the ground stations which has yielded additional information on the sizes of aggregates under various conditions. Variables most likely to affect aggregation are crystal type, temperature and snowfall rate, but other less obvious variables may also play a role (e.g. riming). The results described below were based on observations made on a large number of days and under a wide variety of conditions. However, where possible an attempt is made to separate the more important variables.

4.7.1 Sizes of Aggregates Versus Crystal Types

The size of an aggregate was measured by defining an effective diameter. This was defined as the estimated diameter of a circle on the slide into which the aggregate could be fitted without changing its density.

The aggregate size distributions obtained from each slide replica were separated according to crystal type regardless of the degree of riming, precipitation rate or ground temperature. By combining the data from various slides, size-distributions of aggregates were then obtained for the main crystal types. Since both Keechelus Dam and Hyak are at the same elevation, data from these two stations were combined. Alpental Base station, being somewhat higher (by about 500 ft.), was treated separately. The aggregates analyzed consisted of a combination of two or more of the following crystal types which typically fall in pre-frontal conditions: bullets, sideplanes, columns, assemblages of plates, and assemblages of sectors. In addition, aggregates of needles, dendrites and radiating assemblages of dendrites were studied. Finally, aggregates of certain similar crystals (radiating assemblages of dendrites and dendrites were analyzed. It should be noted that the crystals referred to as comprising an aggregate are the dominant crystals in the aggregate.

Fig. 4.19 shows the distribution of aggregate sizes for aggregates composed of several different crystal types which were collected at Hyak and Keechelus Dam and at Alpental Base. It can be seen from these results that the size distribution varies for different types of aggregates. Aggregates of dendrites, radiating assemblages of dendrites, and these two types of crystalscombined, had very similar size distributions at Hyak and Keechelus

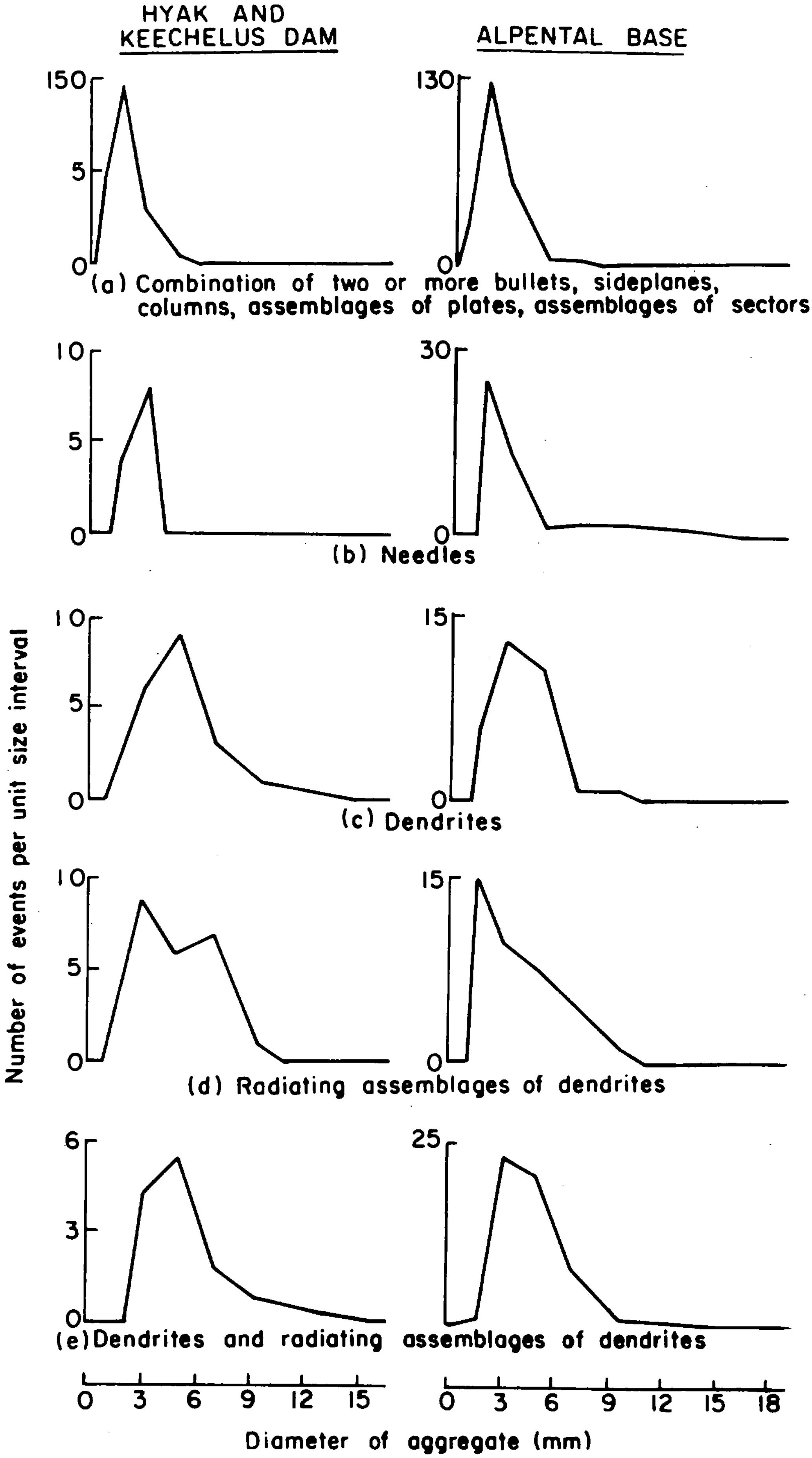

Fig. 4.19 Size distributions of aggregates of different types of crystals collected at Hyak and Keechelus Dam (left-hand column) and Alpental Base (right-hand column).

Dam and at Alpental Base. For these aggregates the diameters between 2 and 6 mm were most likely. However, diameters greater than 15 mm were observed on occasions; diameters less than 1 mm were not observed for these aggregates. Aggregates composed of two or more bullets, sideplanes, columns, assemblages of plates and assemblages of sectors had, most commonly, diameters between 1 and 4 mm. Also, these aggregates never exceeded 8 mm diameter and up to one-quarter of them were less than 1 mm. The size distribution for aggregates of needles had characteristics similar to certain features of both groups referred to above. The maximum diameters extended up to 15 mm but the most likely value was 1 - 4 mm. Aggregates of needles less than 1 mm in diameter were never collected.

The ground temperatures and precipitation rates during which the aggregates referred to above were collected were generally very similar from one type of aggregate to the next. Moreover, the higher ground temperatues at Hyak and Keechelus Dam compared to Alpental Base did not affect the size distributions of the aggregates. It appears, therefore, that the differences in the sizes of the various types of aggregates is due to differences in the crystals comprising them rather than to differences in ground temperature or precipitation rates. In Res. Rpt. VI and §4.4 above, we have shown that as far as individual crystals reaching the ground in the Cascades are concerned, dendrites (including radiating assemblages of dendrites) are rarely below 1 mm in diameter and the most likely value is 4 mm, bullets and columns are rarely larger than 2 mm with the most likely size less than 1 mm, and needles grow over 4 mm long but the most likely length is closer to 1 mm. Also, we estimate an upper limit of 2 mm for the maximum dimensions of unaggregated assemblages of sectors, sideplanes and assemblages of plates. Hence, the larger the size of the individual crystals the larger are the aggregates which they form. This may be due to smaller crystals packing into denser aggregates than do larger crystals. Preliminary measurements which we have made of the mass of various types of aggregates as a function of their size supports this hypothesis.

4.7.2 Effects of Temperature and Precipitation Rate on Sizes of Aggregates

We have concluded above that the differences in the size distributions of various kinds of aggregates are due mainly to differences in the types of crystal comprising the aggregates. We turn our attention now to the possible effects of temperature and precipitation rate on the size of a particular type of aggregate.

Fig. 4.20 shows size distributions for two types of aggregates for different precipitation rates from which it can be seen that the distributions appear to be essentially independent of the precipitation rate. Aggregate size distributions as a function of ground temperature are shown in Fig. 4.21; again, there are no marked variations in the distributions over the range of temperatures shown. These results are surprising and need to be examined further. Since only one variable (precipitation rate or ground temperature) is held constant in Figs. 4.20 and 4.21, it could be argued that if the precipitation rate increases as the ground temperature falls (or vice versa) these two effects could combine to produce no net effect on the size distribution of aggregates. To check this possibility we show in Figs. 4.22 and 4.23 the simultaneous values of the precipitation rates and ground temperatures under which aggregates were collected. Both of these figures indicate a tendency for high precipitation rates to be associated with high ground temperatures. Therefore, if, as it might seem reasonable to expect, high ground temperatures and high precipitation rates favor more aggregation, these two effects should reinforce each other in the data shown in Figs. 4.20 and 4.21 rather than cancel each other.

A further attempt was made to separate the possible effects of temperature and precipitation rate on the aggregate size distribution. It can be seen from Figs. 4.20 and 4.21 that there were not sufficient data to investigate the effect of precipitation rate on aggregation at a constant temperature. However, there were sufficient data at precipitation rates in the range 0.05 - 0.1 inches per hour to compare aggregate size distributions at -3 to -2°C with those at 0 to +1°C. In this case, the aggregates were composed of either dendrites or radiating assemblages of dendrites or combinations of both. The results (Figs. 4.24) show no significant change in the aggregate size distribution between 0 to +1°C and -3 to -2°C at a precipitation rate of 0.05 to 0.1 inches of water per hour.

We conclude from this discussion that ground temperatures in the range +1°C to -7°C, and precipitation rates at the ground from 0.005 to 0.1 inches of water per hour, do not have a significant effect on the size distribution of the aggregates investigated or if such effects exist they are masked by other variables. It should be noted, however, that aggregates of the same crystal type and size distribution collected on different days may not have the same distribution of mass.

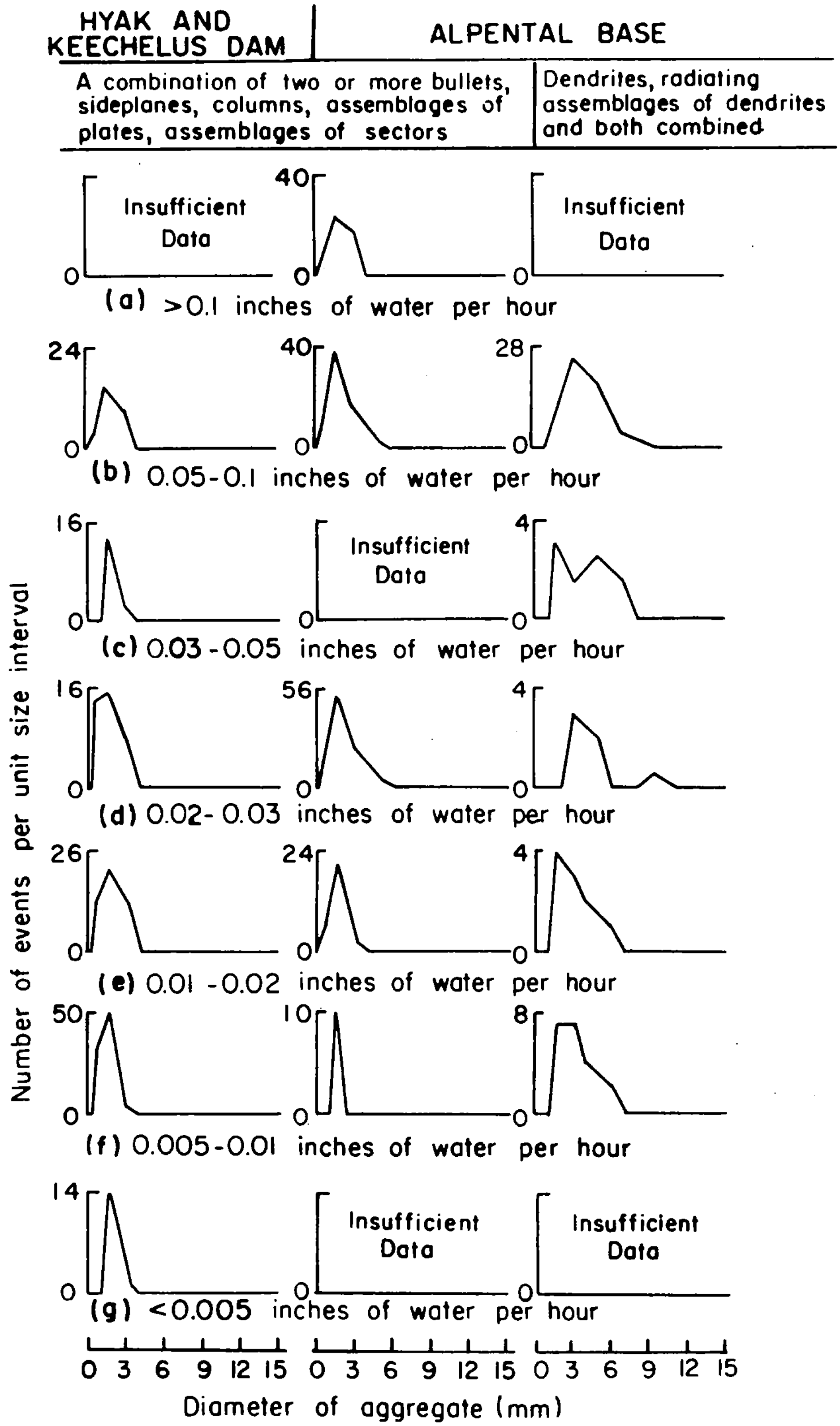

Fig. 4.20 Aggregate size distributions at different precipitation rates.

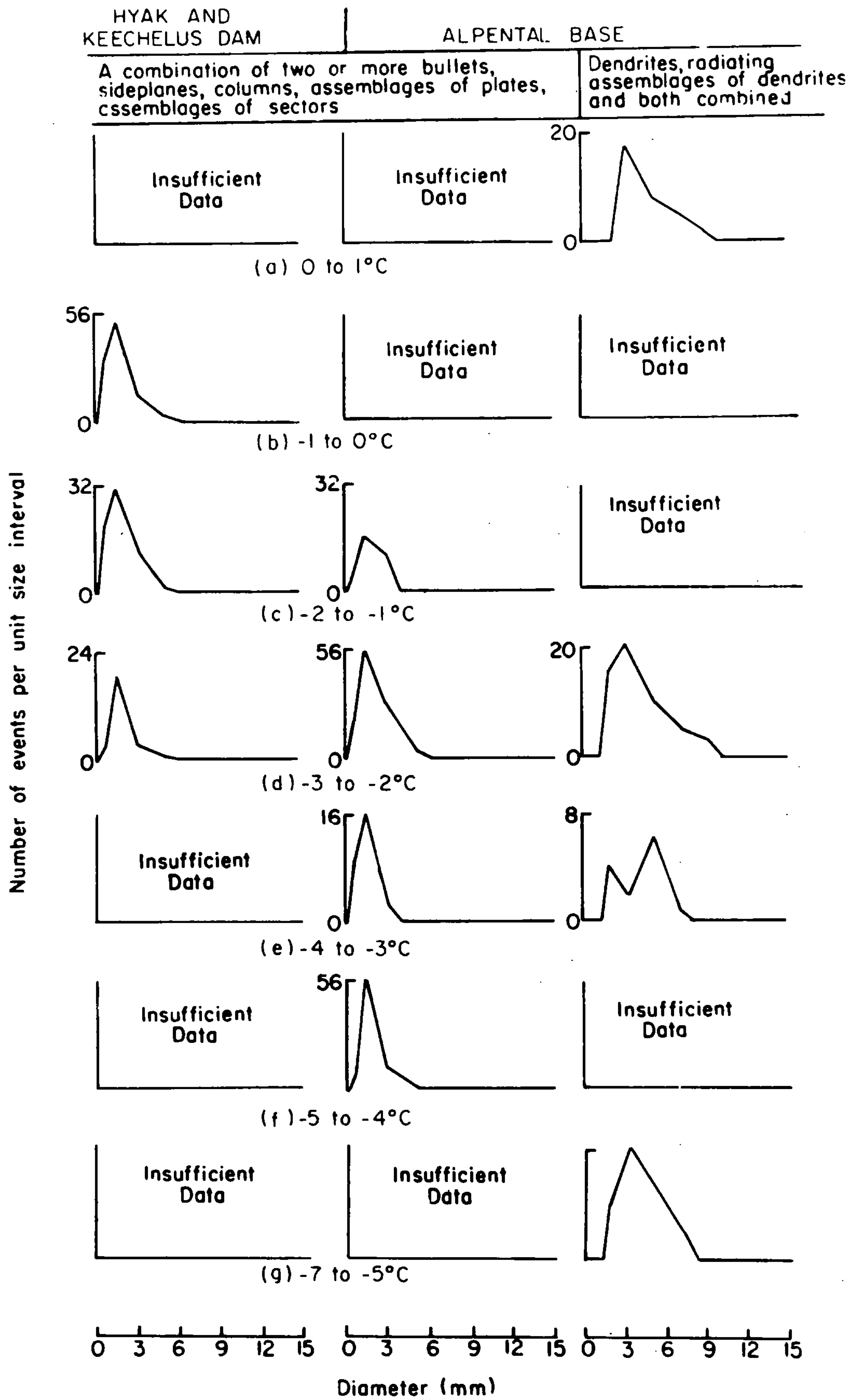

Fig. 4.21 Aggregate size distributions at different ground temperatures.

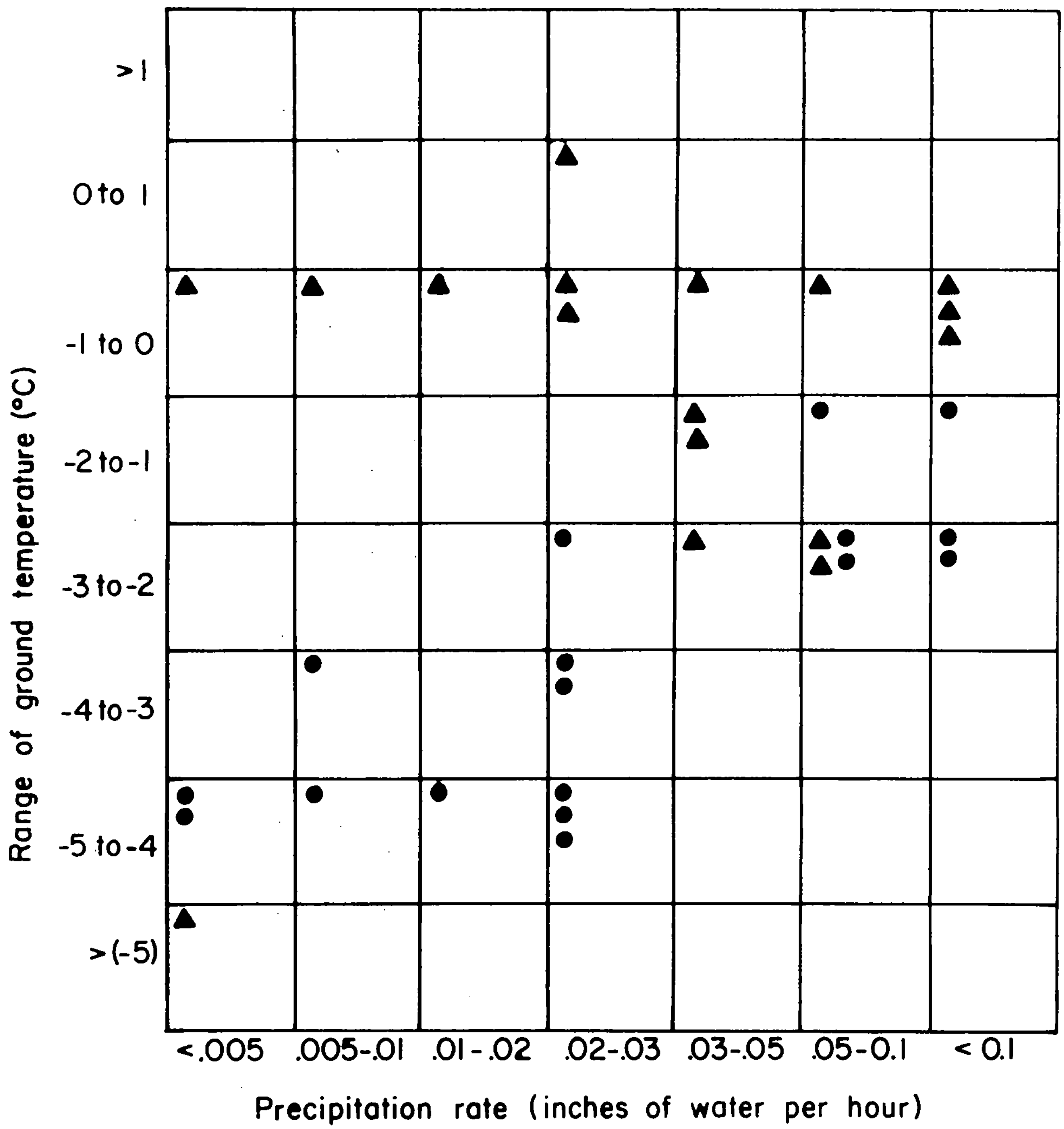

Fig. 4.22 Precipitation rates and ground temperatures at which aggregates composed of two or more bullets, sideplanes, columns, assemblages of plates, and assemblages of sectors were collected at Hyak and Keechelus Dam (▲) and at Alpental Base (●).

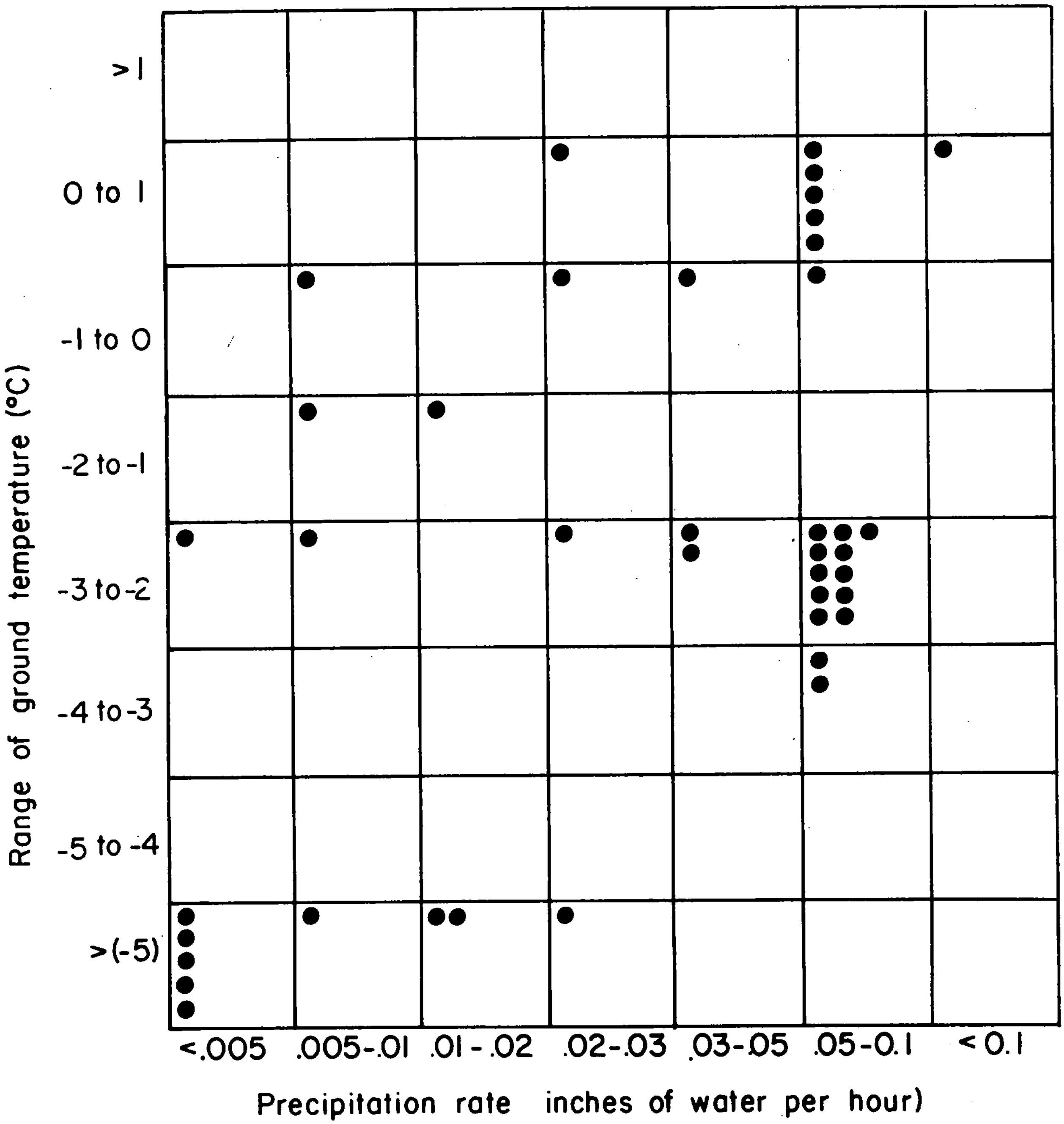

Fig. 4.23 Precipitation rates and ground temperatures at which aggregates composed of dendrites, assemblages of dendrites or both crystals combined were collected at Alpental Base.

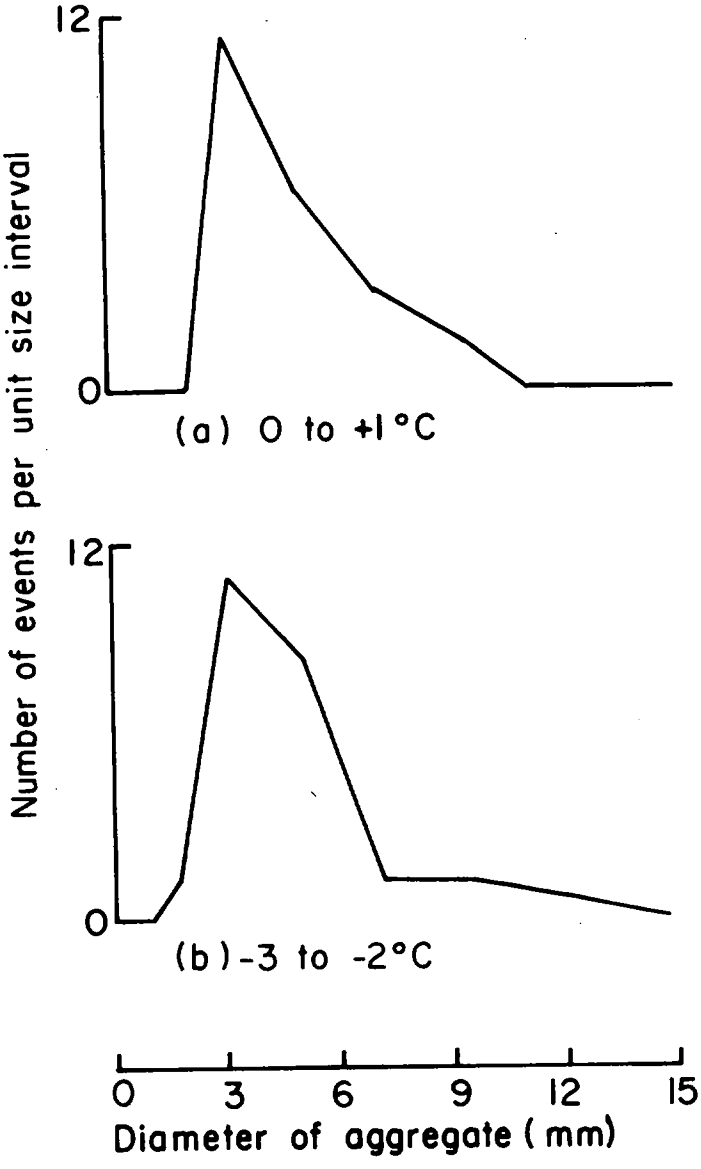

Fig. 4.24 Size distributions for aggregates of dendrites, radiating assemblages of dendrites and both combined at two ground temperature ranges with a precipitation rate from 0.05 - 0.1 inches of water per hour.

4.8 Pre-frontal, Stable and Unstable Precipitation

The conditions under which measurements were obtained at the ground stations in 1971-72 were divided into pre-frontal, stable post-frontal (i.e., stratiform clouds and/or cumulus clouds with tops below 10,000 ft.) and unstable post-frontal (cumulus clouds with tops above 10,000 ft., stratiform clouds at any level could also be present).

The degree of riming, types of particles and heights of the "diffusional growth layer" for precipitation collected at Alpental Base under these different synoptic conditions are shown in Fig. 4.25. In 1970-71 the precipitation particles at Alpental Base in pre-frontal conditions were more often unrimed than rimed (see Fig. 5.13 in Res. Rpt. VI). However, it can be seen from Fig. 4.25, that in 1971-72 equal numbers of rimed and unrimed particles were collected at Alpental Base in pre-frontal conditions. This difference illustrates the variety of conditions which can occur even in pre-frontal conditions. Thus, there is evidence (see §4.9) that prior to a frontal passage, both unrimed cold-type ice crystals (sideplanes, assemblages of plates, bullets) and rimed warm-type crystals (dendrites, needles) can reach the ground in the Cascade Mountains. The warm-type crystals form if there is a clear separation of warm and cold fronts, or if there is a warm front ahead of an occluded front. On some occasions pre-frontal precipitation combines with orographic precipitation that follows a previous frontal passage. In 1971-72 the majority of our data was collected in post-frontal or orographic precipitation. The pre-frontal data were fairly limited and, depending on the synoptic conditions, either unrimed cold-type crystals or rimed warm-type crystals were collected.

A comparison of the degrees of riming in stable and unstable post-frontal conditions (Fig. 4.25) shows that in the latter case the crystals are all moderately or heavily rimed, whereas, in stable conditions unrimed to lightly rimed crystals predominate. It can also be seen from Fig. 4.25 that graupel particles dominated in unstable conditions. These results reflect, of course, the relatively large liquid water contents of the large cumulus clouds which occur in unstable conditions.

The most striking results come from comparing the median heights of the "diffusional growth layer" for pre-frontal, stable and unstable precipitation. Pre-frontal precipitation had the highest "diffusional growth layers" followed by unstable and stable precipitation. The high "diffusional growth layers" in pre-frontal conditions reflects the lifting of moisture ahead of the front to high altitudes, sometimes above 20,000 ft. In contrast, stable precipitation,

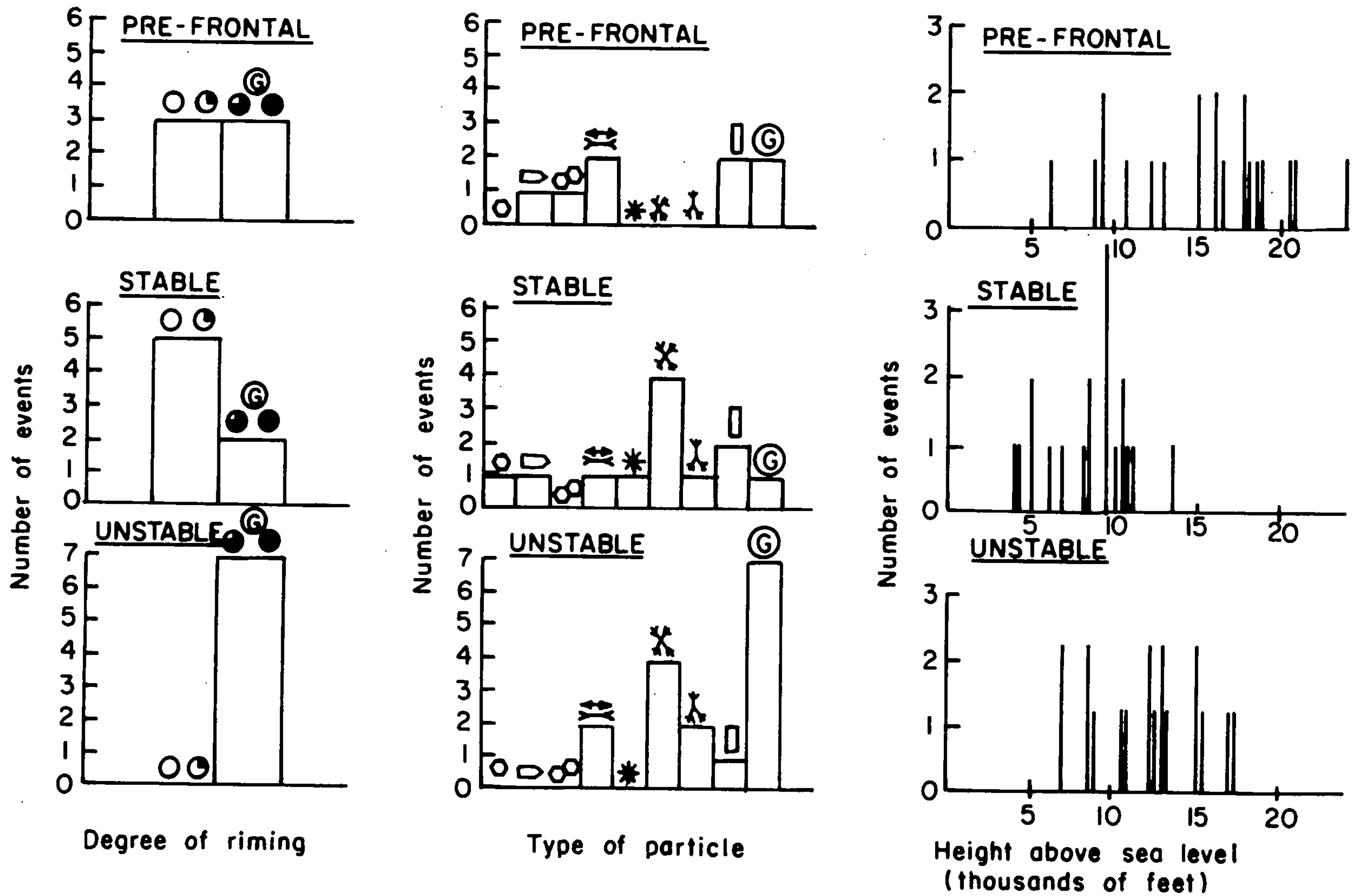

Fig. 4.25 Degree of riming, types of particles and median height of "diffusional growth layer" for precipitation at Alpental Base in pre-frontal, stable and unstable conditions. See Table 4.1 for key to symbols.

which occurs in the absence of frontal lifting or large cumulus, had "diffusional growth layers" below 15,000 ft., and the majority were between 5,000 and 10,000 ft. Interestingly, the "diffusional growth layers" for unstable precipitation were all below 20,000 ft. This is because cumulus clouds over the Cascades are generally not very large.

Fig. 4.26 shows the relationship between the degree of riming of dominant slide particles and the median height of their "diffusional growth layer." The results are essentially the same as those obtained from the 1970-71 data (see Fig. 5.12 in Res. Rpt. VI). It can be seen that the higher an ice crystal originates in the atmosphere the less likely it is to be rimed when it reaches the ground. Crystals which originate below about 10,000 ft., and in some cases below 5,000 ft., are more heavily rimed than crystals originating at higher levels. The reason why crystals which form at low temperatures are generally unrimed is that they form mainly in pre-frontal conditions in which liquid water contents are low at higher levels and dry cold easterly winds at lower levels inhibit riming.

4.9 Effects of a Frontal Passage: A Case Study

In Res. Rpt. VI (§5.8) we described changes in the types of solid precipitation particles reaching the ground in the Cascade Mountains during the passage of an occluded front. In this case, after the front had passed the heights of the "diffusional growth layers" fell and riming increased. Accordingly, the snow crystals changed from unrimed, cold-type crystals (assemblages of sectors and plates, sideplanes and bullets) to rimed, warm-type crystals (needles, sheaths). We describe below another set of measurements, obtained on March 1, 1972, during the passage of a front over the Cascade Mountains.

At 1000 PST on March 1, 1972, a very deep surface low was located off the coast of British Columbia with a frontal system still well out in the Pacific Ocean. The 850 and 500 mb synoptic maps for 0400 PST and the time cross-section based on soundings from Quillayute (Fig. 4.27) showed warm advection at all levels with a low centered in the Gulf of Alaska. The surface synoptic map for 1300 PST (Fig. 4.28) showed a warm front just off the Washington Coast and generally light precipitation with a solid overcast over most of Washington State. This pre-frontal situation was characterized by the typical strong off-shore flow at the surface, while aloft the winds were southwest to west. By 1600 PST, an occluded front was shown 300 miles off

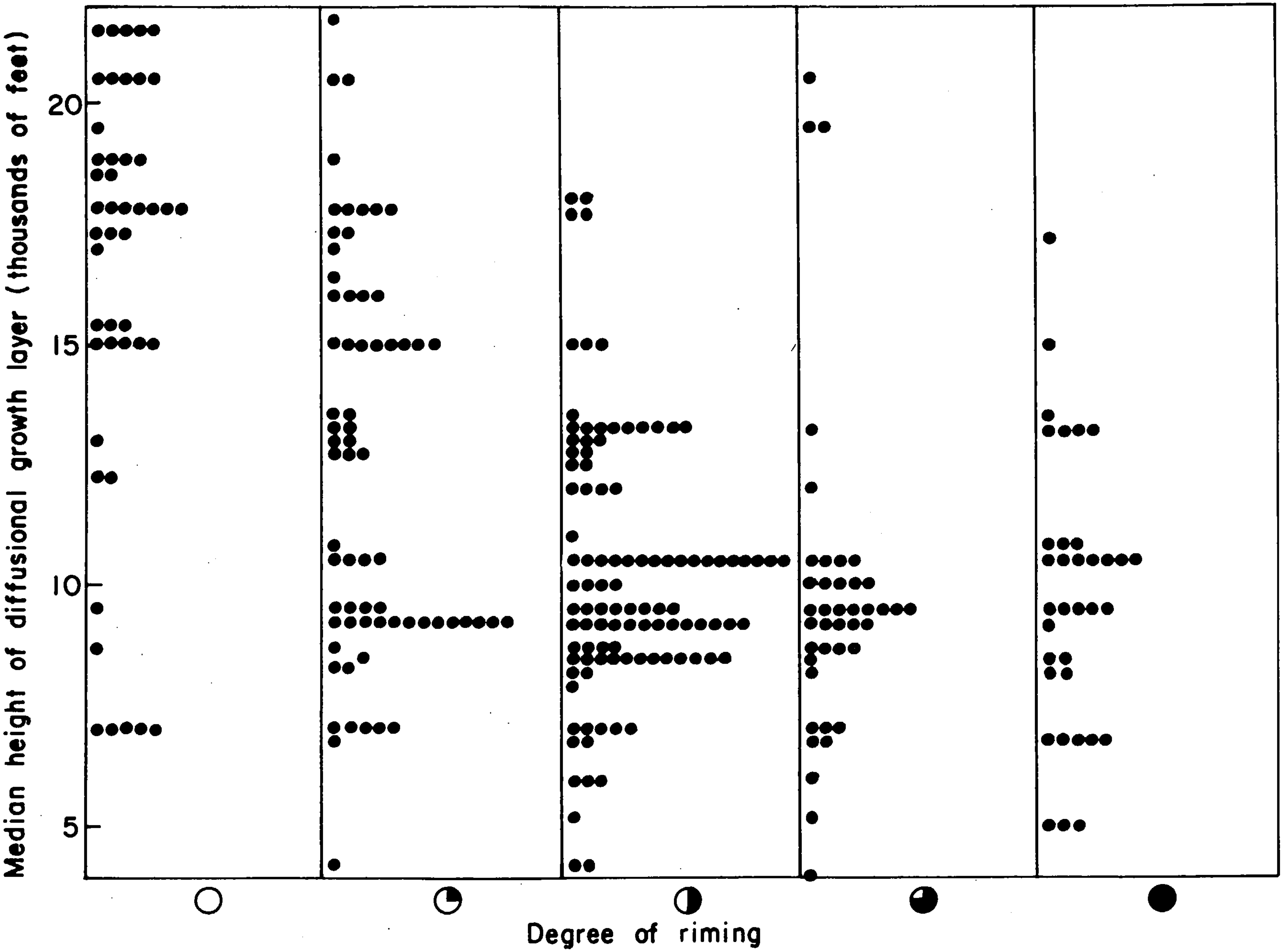

Fig. 4.26 Degree of riming of dominant slide particles against the median height of the "diffusional growth layer" of the particle.

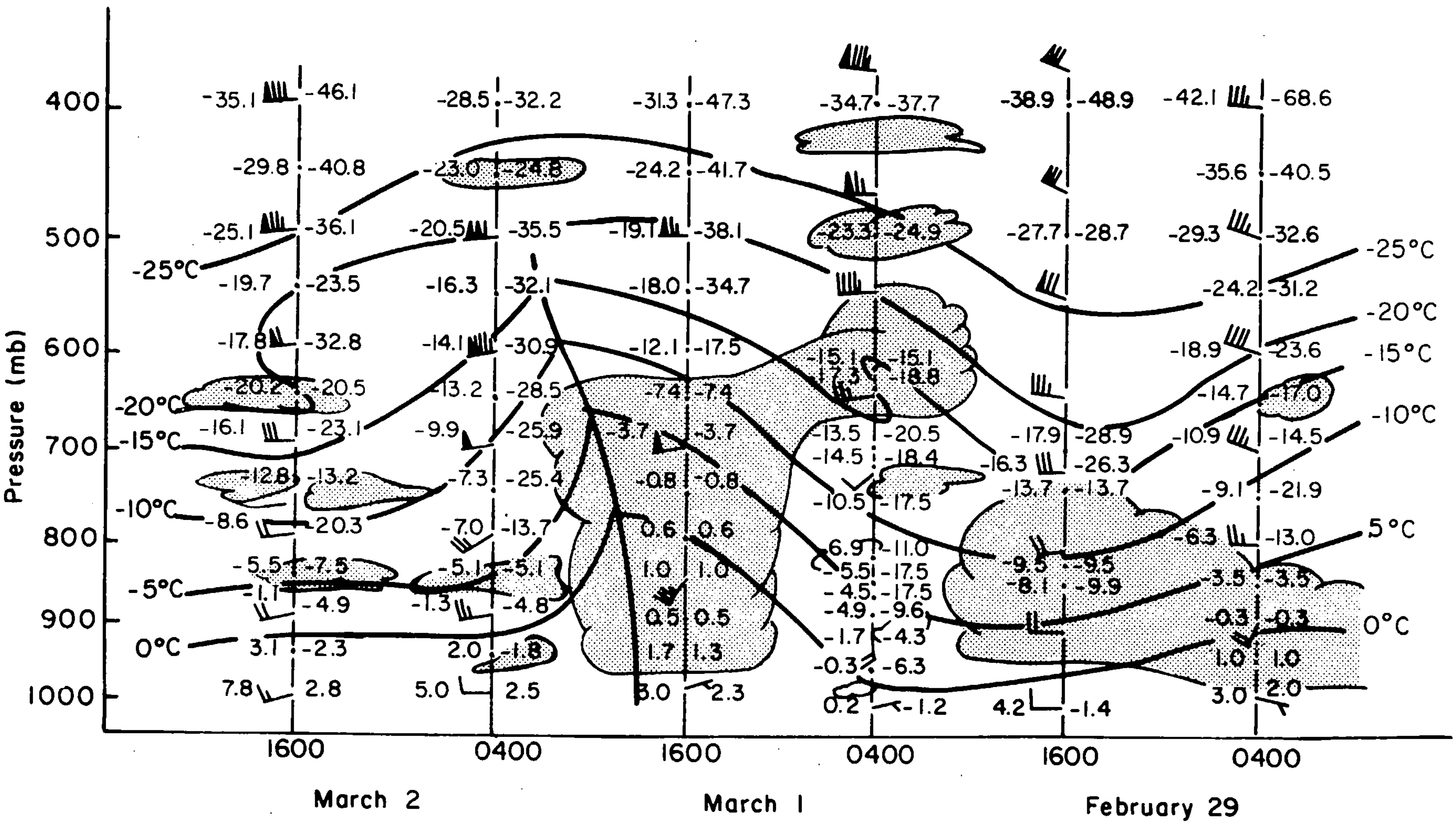

Fig. 4.27 Time cross-section for soundings at Quillayute between February 29 and March 2, 1972. Hours refer to Pacific Standard Time. Temperatures in °C.)

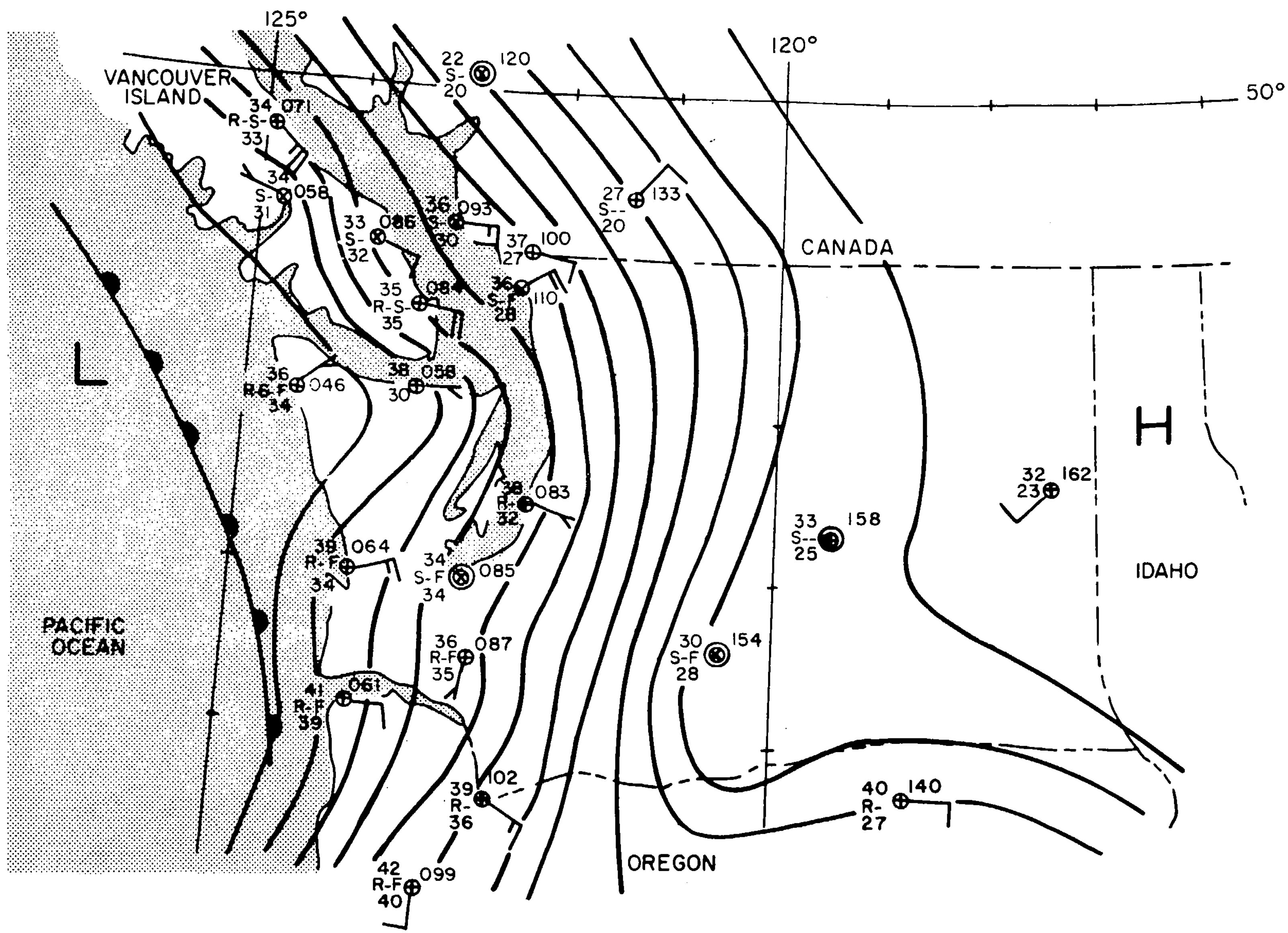

Fig. 4.28 Surface synoptic conditions at 1300 PST on March 1., 1972.

the Washington Coast. The pressure pattern and winds remained basically unchanged from 1000 PST and there was strong warm advection ahead of the front. Fig. 4.29 shows the surface map for 0000 PST on March 2. According to the National Weather Service, the occluded front at the surface passed over Snoqualmie Pass at about 2300 PST on March 1. Our observations in the Cascade Mountains (Fig. 4.30) indicate that the effects of a warm front aloft were experienced in the Cascades at about 1300 PST and this was followed by the effects of the cold or occluded front at about 2400 on March 1. (Note: warm fronts in Washington are generally weak and difficult to locate. On this occasion the front may have been occluded on the surface but with the upper level warm front passing over the Cascade crest). After the passage of the cold or occluded front shown by the Weather Service, the wind at Keechelus Dam shifted from southeast to northwest and the temperature increased. This is an interesting feature of the local situation in which, after a frontal passage, the upper atmosphere may cool but the surface temperatures increase. This is because prior to the frontal passage cold air is moving up the valleys from Eastern Washington, but after the front moves through relatively warm air is swept up the valleys from Western Washington.

The results shown in Fig. 4.31 indicate that when the warm and cold fronts are separated, the characteristic changes which we have previously associated with the passage of occluded fronts (i.e., lowering of the diffusional growth layer, and changes from unrimed cold-type crystals to rimed warm-type crystals) occur when the warm front moves through. The structure of a warm front is, in fact, more conducive to lifting moisture over large areas to high altitudes than is a cold front and therefore to producing the observed changes. The sharp changes in crystal types and degree of riming at Hyak and Keechelus Dam between 1245 and 1300 show that the warm front was very well defined.

The measurements shown in Fig. 4.30 cover both the pre-frontal and post-frontal portions of the storm including the subsequent showery weather in the westerly flow. It should be noted that there was a definite increase in precipitation rate up to the passage of the cold or occluded front at which time the rate decreased sharply. Twelve hours after the frontal passage the precipitation rates increased again. Our detailed crystal data only occupy a small portion of the total storm. (An attempt will be made next year to obtain continuous observations during the life cycle of a storm.) However,

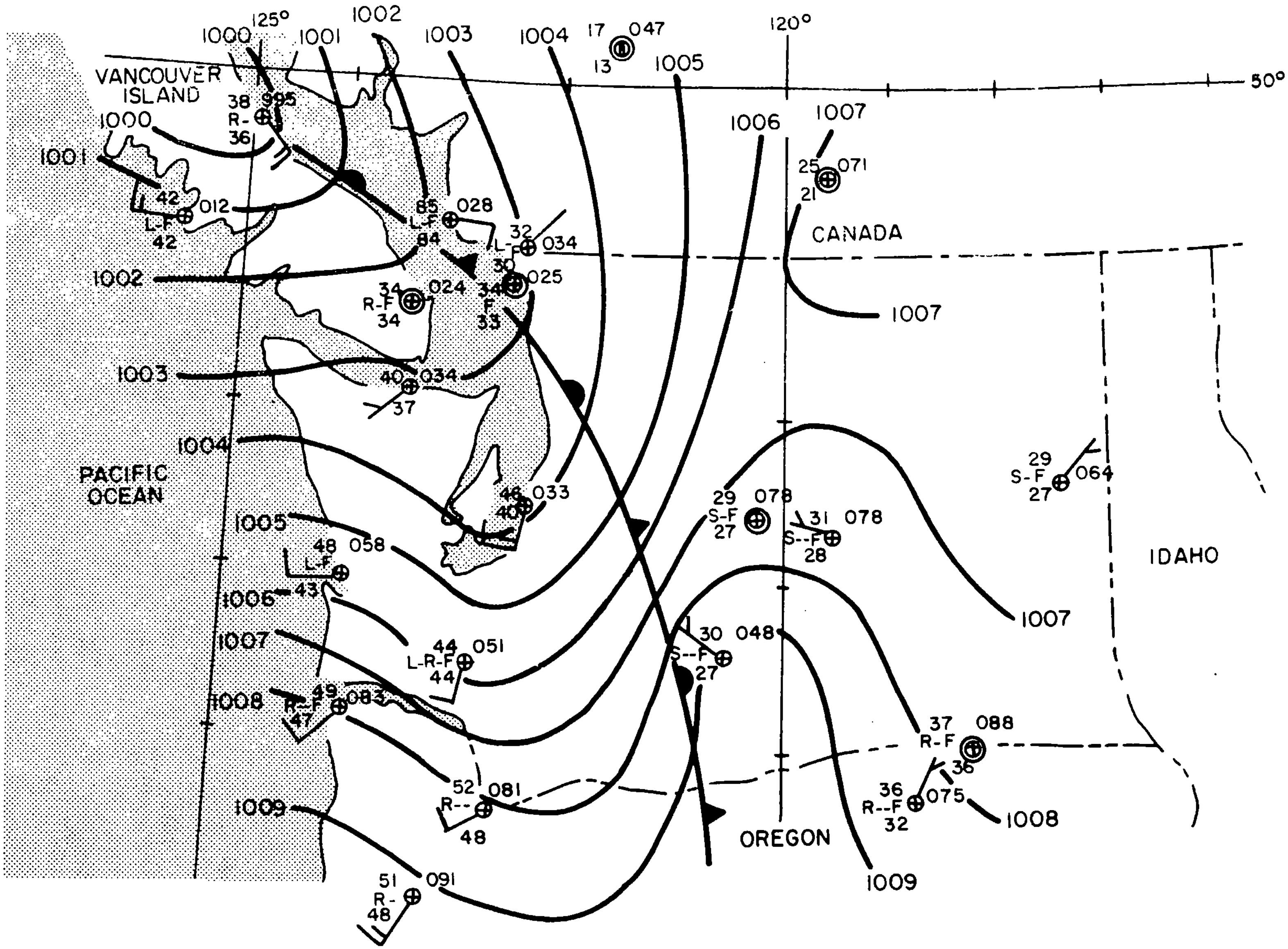

Fig. 4.29 Surface synoptic conditions at 0000 PST on March 2, 1972.

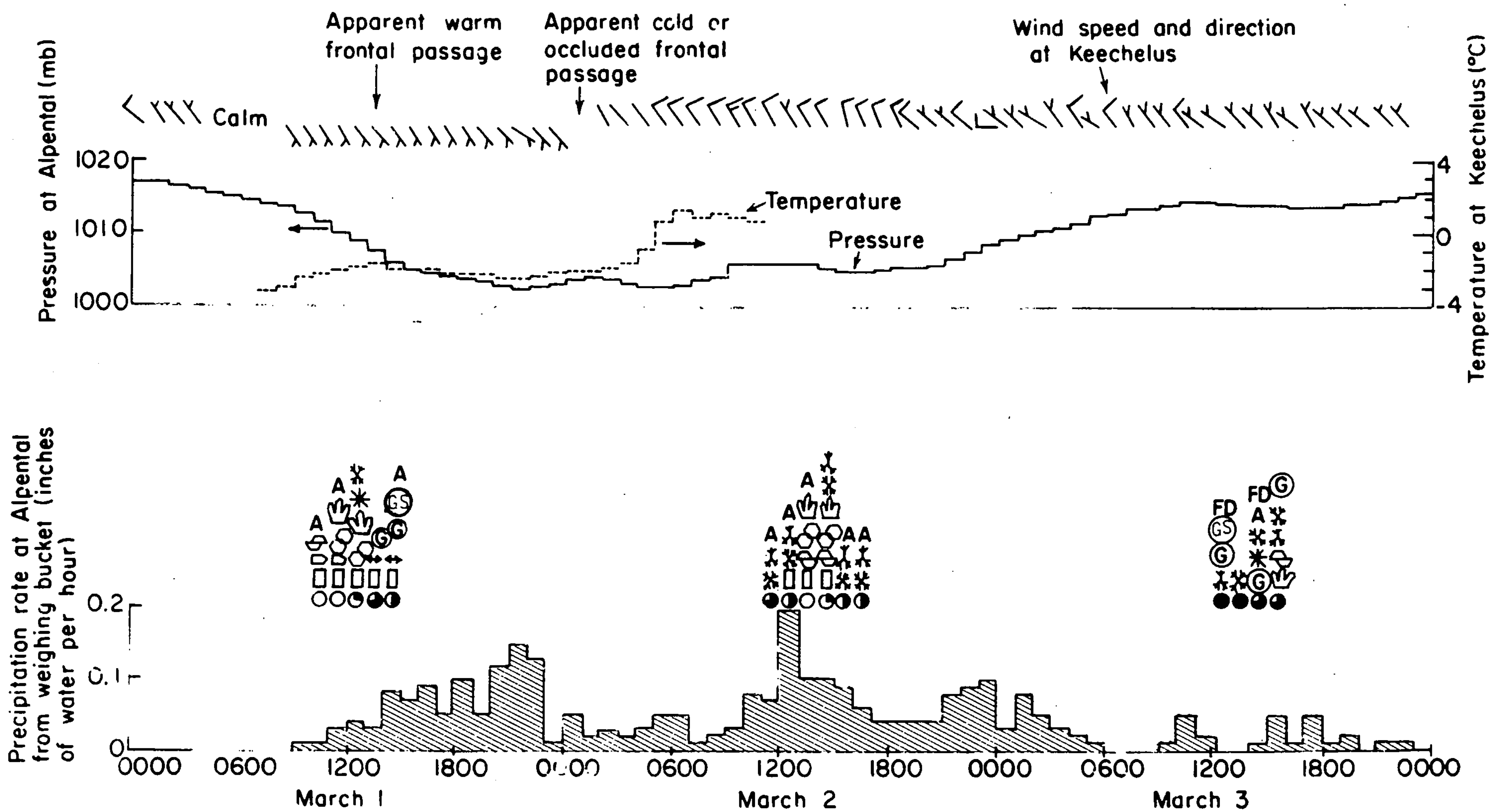

Fig. 4.30 Observations at Alpental and Keechelus Dam on March 1-3, 1972. (Hours refer to Pacific Standard Time. Key to crystal types is given in Table 4.1.)

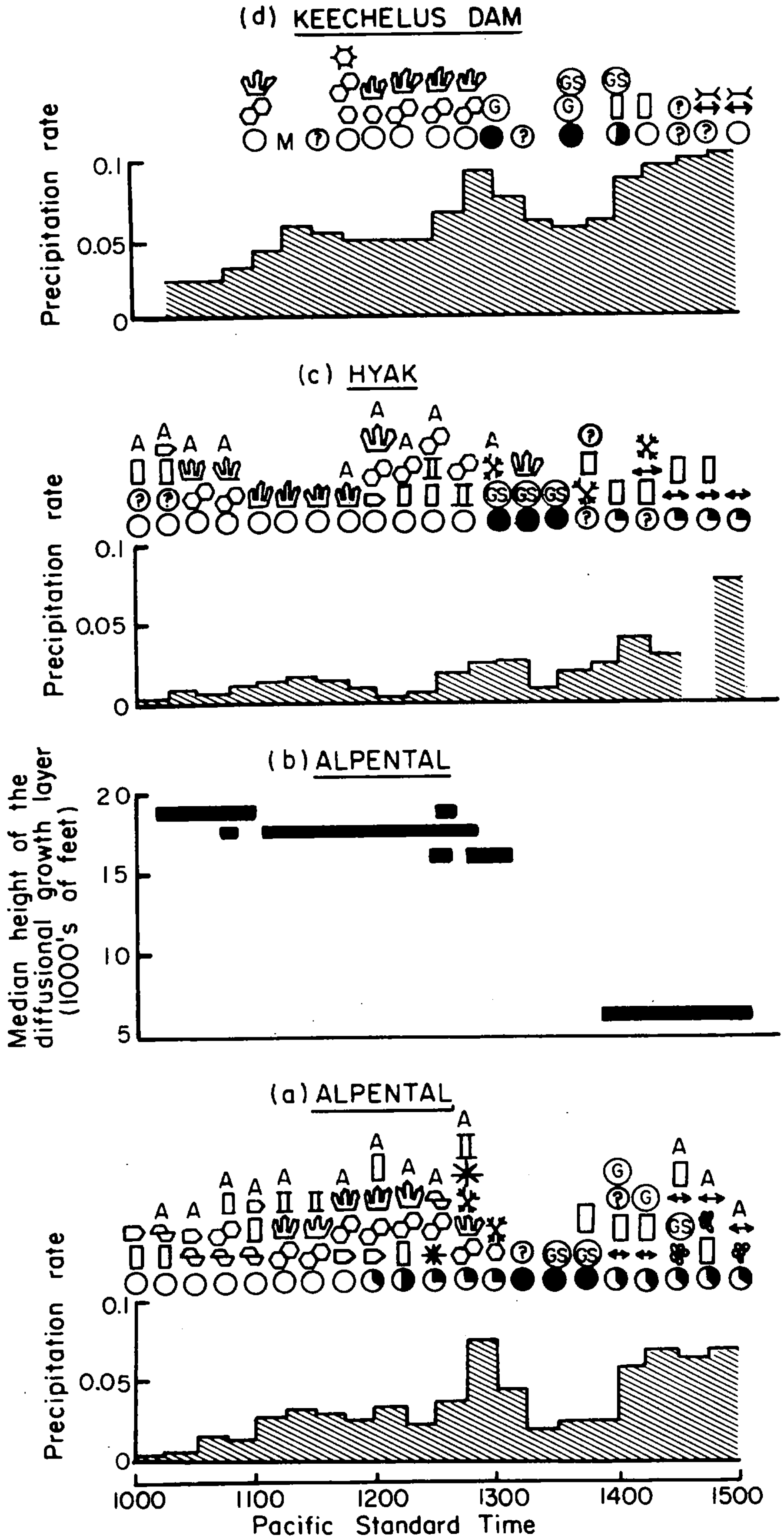

Fig. 4.31 Precipitation rates and crystal types at ground stations in Cascade Mountains on March 1, 1972. There was a warm frontal passage at 1300 hours. (Precipitation rates are from snow sample bags and are in inches of water per hour. Key to crystal symbols is given in Table 4.1.)

it appears that changes in crystal type and riming similar to those which occur during a frontal passage can also occur during the post-frontal period (e.g. 1100 - 1800 PST on March 2).

Some of the aircraft data obtained on March 1, 1972, are shown in Fig. 4.32. The observations taken at 1213, 1220 and 1229 PST at 8,000 ft. in the pre-frontal warm advection show a cooling trend as the aircraft flew eastward and also a decrease in the ratio of water to ice. The clouds over the western and eastern slopes of the Cascade Mountains were essentially glaciated at this time. The contrast between the measurements made between 1220 and 1229 PST and those between 1252 and 1303 is striking. From 1220 to 1229 the clouds contained predominantly ice particles, while from 1252 to 1303 they were changing from mainly ice to predominantly water clouds. At 1252 the water to ice ratio was 1:10 while at 1303, 8 miles to the northeast and 2000 ft. higher, it was 5:1. This transition fits in very nicely with the changes in crystal type and riming observed on the ground between 1200 and 1300 (Fig. 4.31). Cold-type unrimed crystals occurred on the ground when glaciated clouds were aloft, while warm-type rimed crystals reached the ground when the clouds were transforming into predominantly water droplet clouds.

4.10 Double Snow Crystals with a Common Drop Center

Snow crystals are sometimes collected which consist of two planar crystals, with their large (basal) faces parallel, connected by a frozen drop at their center (Fig. 4.33). It has been suggested that crystals of this type, which we will call double crystals, form in water saturated conditions in which cloud drops freeze and then act as embryo on which double crystals subsequently grow (Bentley, 1924; Weickmann, 1947; Auer, 1971, 1972).

Snow crystals collected at Alpental Base and Hyak during the 1971-72 Cascade Project were analyzed for double crystals. The results obtained from these two sites were similar, therefore, only the data from Alpental Base are presented. Also, since the majority of the double crystals consisted of stellar-like or dendritic crystals, only data for this type of crystal are considered.

Slide replicas for which the dominant crystal types were either stellar-like or dendritic were examined for double crystals. These slides were then classified as having no double crystals, few, moderate or high numbers of double crystals. Fig. 4.34 shows the frequencies with which these categories

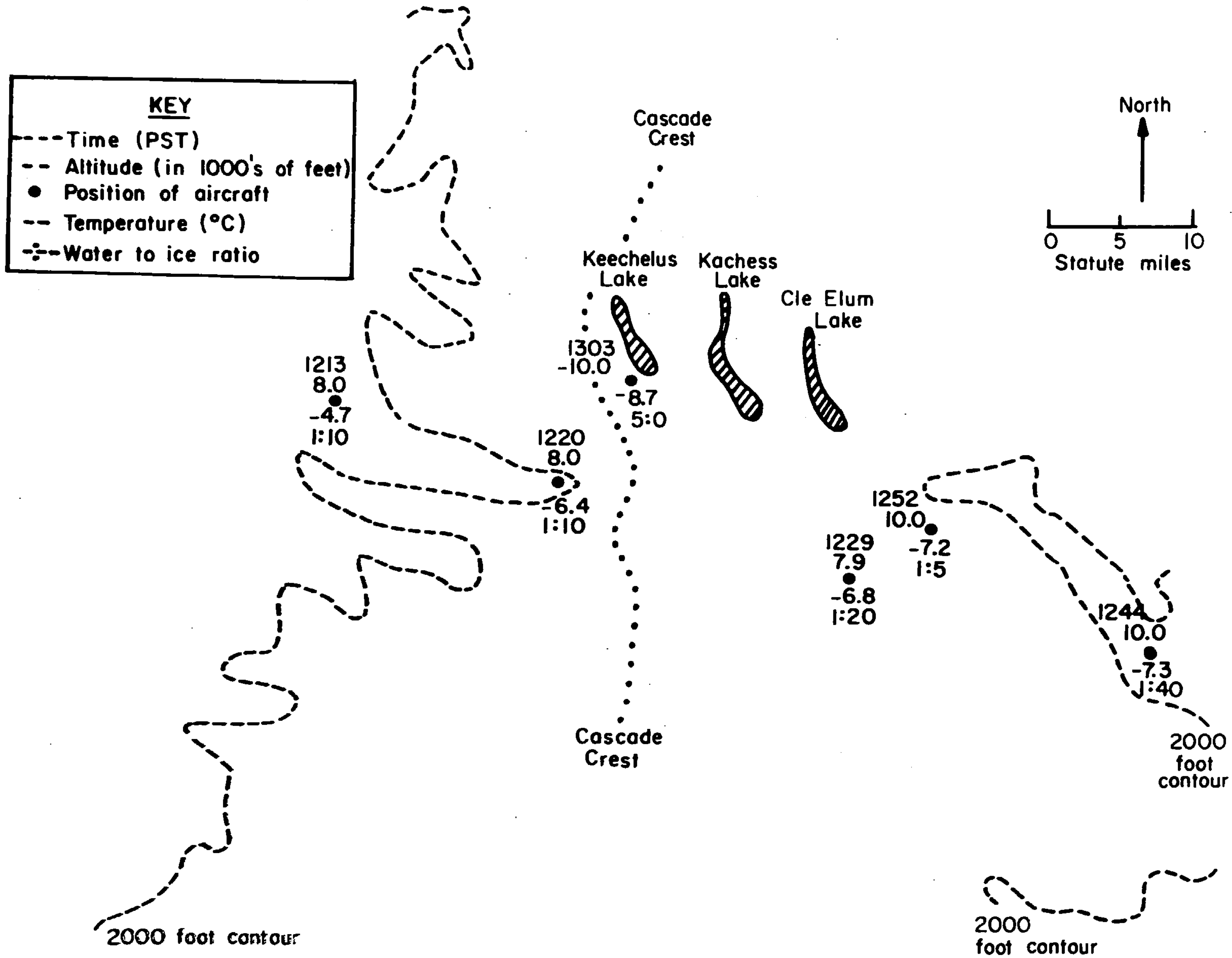

Fig. 4.32 Airborne measurements on March 1, 1972 over Cascade Mountains.

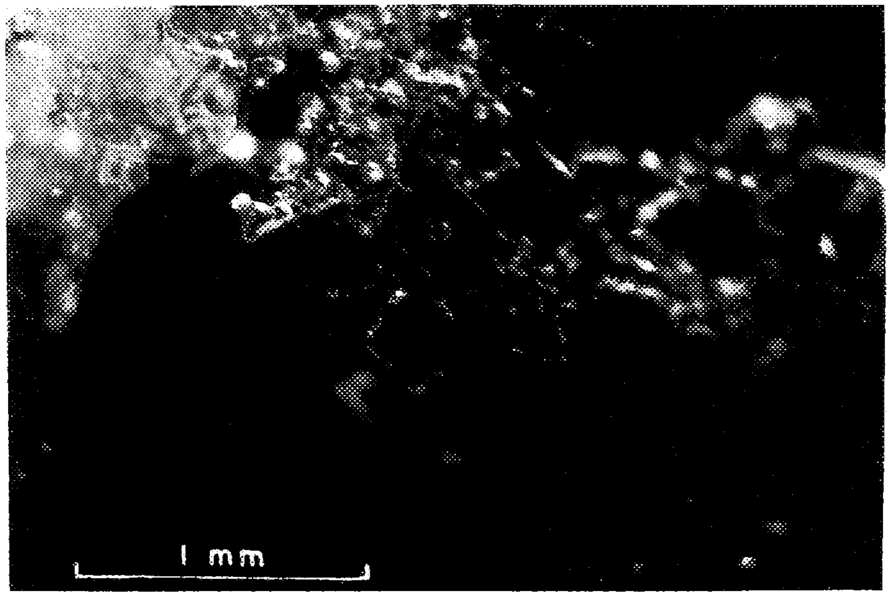

(a)

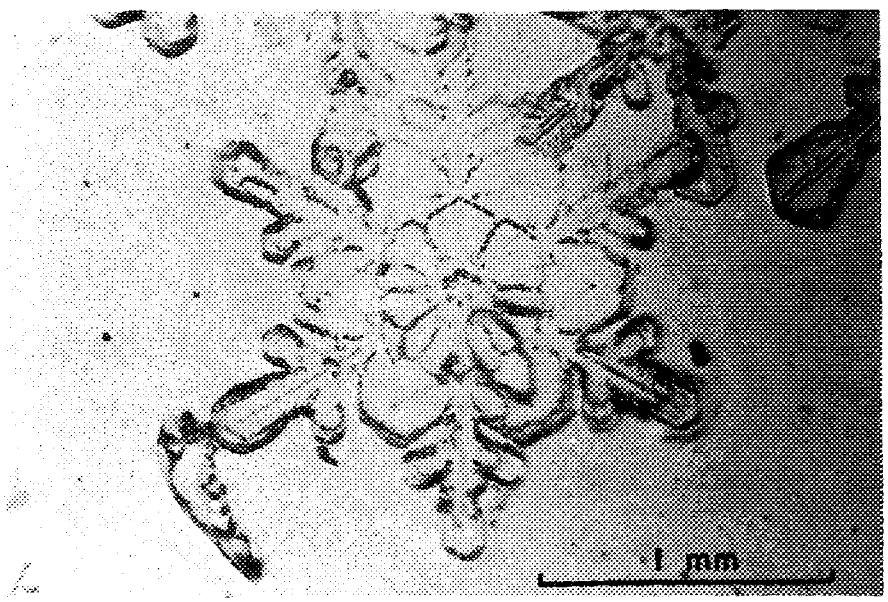

(b)

Fig. 4.33 (a) Double crystal with drop at center. (b) Double crystal, drop at center cannot be discerned at this magnification.

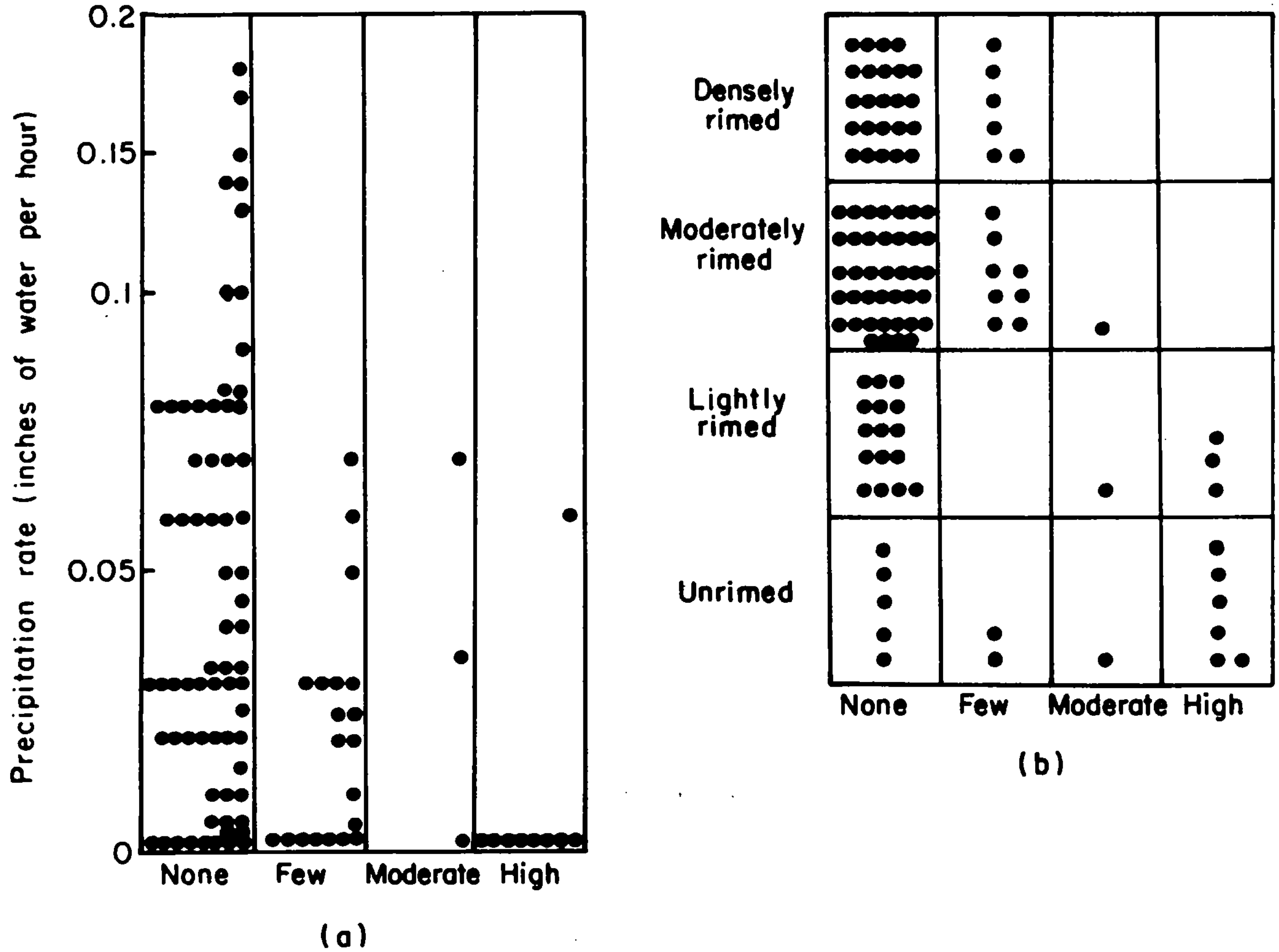

Fig. 4.34 Each dot represents a slide replica which had stellar-like or dendritic crystals on it. The relative number (none, few, moderate or high) of double crystals on the replica is shown plotted against (a) the precipitation rate and (b) degree of riming.

appeared as a function of the precipitation rate and the degree of riming of all of the crystals on the slide. It can be seen from these figures that double crystals are more likely to occur at light precipitation rates and under conditions of little or no riming. It can be seen from Fig. 4.35 that double crystals are also more likely the lower the height of the "diffusional growth layer" of stellar-like or dendritic crystals. The latter is the more fundamental relationship for when the air over the Cascade Mountains is cold enough to lower the -13°C isotherm to below about 7,000 ft., there is generally insufficient moisture to cause heavy riming or high precipitation rates. On some occasions the precipitation rate and degree of riming were low but the height of the "diffusional growth layer" was above 7,000 ft.; in these cases, double crystals were rare.

The above observations indicate that frozen drops, which lead to double crystals, are more likely to occur when the "diffusional growth layer" for stellar-like or dendritic crystals is low over the Cascade Mountains. It should be noted that when this "diffusional growth layer" is low it is generally due to the fact that there is an intrusion of cold Arctic air into the region which is presumably relatively clean air, at least at higher levels. The more frequent appearance of double crystals under these conditions may be due to higher concentrations of contact or freezing nuclei being present at lower altitudes. Since we have concluded previously from drop-freezing measurements (see §5.10 of Res. Rpt. VI) that freezing nuclei do not appear to play an important role in the nucleation of ice over the Cascade Mountains, we suggest that contact nuclei are largely responsible for the nucleation of drops in the lower levels of the atmosphere (say below about 7,000 ft.) over the Cascades. When, in addition, the -13°C isotherm is below about 7,000, the frozen drops then lead to the growth of double crystals. As we have suggested in §3.2.3, the nucleation of droplets by contact nuclei may also be responsible for the high concentrations of ice particles frequently observed over the Cascade Mountains. Also, we have observed on many occasions that ice particles might be quite numerous at lower levels in clouds over the Cascades while not present in higher clouds. This condition is consistent with the present arguments.

4.11 Ice Nucleus Measurements

As mentioned in §1.3.3, ice nucleus measurements were made at the ground stations with millipore filters, a modified NCAR counter and by the drop freezing technique.

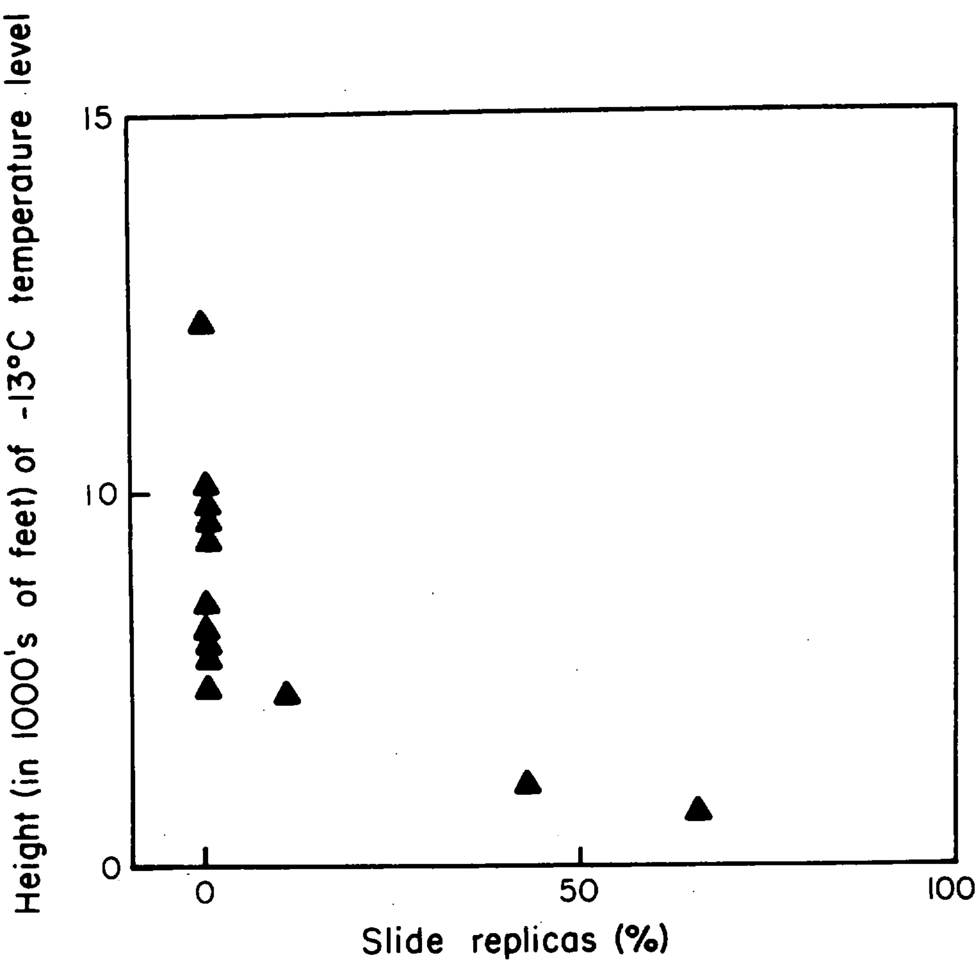

Fig. 4.35 Percentage of slide replicas on a given day which had a relatively large number of double crystals compared to the number of single stellar-like or dendritic crystals.

The concentrations of ice nuclei in the free air were measured at Keechelus Dam using both an NCAR mixing chamber and millipore filters. It should be noted that the station at Keechelus Dam is a relatively isolated and clean mountainous site; the ground is snow covered in winter and, apart from a highway located 1/2 mile from Keechelus Dam (see Fig. 1.4), there are no anthropogenic sources of ice nuclei in its general vicinity.

The NCAR counter was operated at a temperature of -21°C during several "storm days" (usually from 1100 to 1600 hours local time). Air was drawn through it at a rate of 10 liters per minute. One millipore filter was exposed for one hour (usually 1200 to 1300 hours local time) at Alpental on each "storm day", during which time 300 liters of air was drawn through the filter. The filters were subsequently "developed" in the laboratory at -15°C and under water saturated conditions using a similar technique to that described by Stevenson (1968). It was originally intended to "develop" the millipore filters at -20°C, however, the background count due to erroneous nucleation at this temperature was found to be too high. It should be noted that for "development" at -15°C it would have been preferable if the volume of air sampled had been at least 2,500 liters.

Some of the results obtained from the millipore filters are shown in Table 4.2. Although these data are not numerous they were analyzed to see whether the concentrations of ice nuclei at Keechelus Dam showed any tendencies to vary with seeding activity from the aircraft (generally carried out west of the Cascade crest) or meteorological conditions. This analysis is shown in Table 4.3 where it can be seen that the measured average concentrations of ice nuclei were significantly greater when seeding was carried out from the aircraft at some time during the period when air was drawn through the filter. Also, the ice nucleus counts were higher when the wind was westerly than when it was easterly and lower when precipitation was falling than when it was not. These last two observations confirm previous measurements obtained in the Cascade Mountains by Hobbs and Locatelli (1970) using an NCAR ice nucleus counter. The higher counts in westerly winds may be due to anthropogenic ice nuclei produced in the Seattle area, and the lower concentrations of ice nuclei in the free air during precipitation could be a result of scavenging of the nuclei by the precipitation. The reason for the higher ice nucleus counts at temperatures below 0°C is not clear.

Some of the ice nucleus measurements obtained with the NCAR counter and by the drop-freezing technique are described in §5 in connection with artificial seeding effects.

TABLE 4.2

CONCENTRATIONS OF ICE NUCLEI AT -15°C AT KEECHELUS DAM FROM MILLIPORE FILTERS

Date (1972)	Local time	Average concentrations of ice nuclei per liter at -15°C during hour†	Average precipitation rate during sampling hour (inches/hr)	Average wind speed and direction during sampling hour (degree/knot)	Average ground temperature during sampling hour	Remarks
Jan. 13	1200-1300	0.087	0	300/08	-3.8	Seeding with 20 gm of AgI from aircraft from 1245 to 1313.
Jan. 14	1200-1300	0.003	0	330/10	+0.6	
Jan. 17	1300-1400	0 (blank)	0.05	320/17	-0.9	Seeding with 960 gm of AgI from aircraft from 1333 to 1441. Note: Unknown to the person who "developed" the filter, this filter was <u>not exposed</u> to any airflow.
Jan. 31	1200-1300	0.030	0	290-120/06	-4.5	
Feb. 14	1200-1300	0.063	0.07	130/04	-1.5	
Feb. 15	1230-1330	0.003	0.14	?	+2.0	—
Feb. 22	1235-1335	0.033	0	280/03	+3.7	—
Feb. 23	1300-1400	0.027	0	220/02	+4.0	Seeding with 192 gm of AgI from aircraft from 1238-1402.
Mar. 1	1230-1330	0.023	0.04	140/08	-1.8	—
Mar. 2	1245-1345	0.047	0.03	320/10	+0.2	Seeding with 1210 gm of AgI from aircraft from 1320-1455.
Mar. 3	1300-1400	0.133	0	300/07	0.0	Seeding with 340 gm of AgI from 1251-1440.

†Background "count" on filters at -15°C was about 0.005.

TABLE 4.3

COMPARISON OF ICE NUCLEUS CONCENTRATIONS AT -15°C AT KEECHELUS DAM

MEASURED WITH MILLIPORE FILTERS UNDER DIFFERENT CONDITIONS

Conditions	Average Concentration of Ice Nuclei per liter at -15°C	Number of Filters Averaged
No seeding with AgI	0.026	6
Seeding with <100 gm of AgI from aircraft	0.057	2
Seeding with >100 gm of AgI from aircraft	0.090	2
Wind direction easterly	0.043	2
Wind direction westerly	0.055	6
Ground temperature <0°C	0.067	5
Ground temperature >0°C	0.023	5
No precipitation	0.052	6
Precipitation falling	0.034	4

SECTION 5

SOME CASE STUDIES OF ARTIFICIAL SEEDING

To test the degrees to which clouds and precipitation over the Cascade Mountains can be artificially modified, artificial seeding from the aircraft with silver iodide pyrotechnics or "dry ice" was carried out for short periods of time (generally an hour or so) on 23 occasions during the winter of 1971-72. The principle objective of these studies was to determine whether snowfall could be modified and redistributed across the Cascade Mountains in a deterministic manner within our small target area on the ground in the manner predicted by our theoretical model (see §2.5). Whenever possible, effects of seeding were evaluated through a comprehensive series of physical measurements made before, during and after seeding using the airborne, radar and ground facilities.

Subsequent analysis of all the data collected showed that on five occasions a sufficiently unified sequence of modifications to clouds and precipitation were observed in the target area to conclude that there was a "good" chance that the changes were produced by the artificial seeding. Another eight occasions were classified as "fair" in this respect and eight as "poor" (the remaining experiments have not been analyzed). We describe below the five experiments on which a "good" sequence of effects attributable to seeding was observed. The first two cases are described at some length (§5.1 and §5.2) in order to illustrate the detail with which the efficacy of artificial seeding can be tested through physical measurements. The remaining three cases are described more briefly.

5.1 January 31, 1972

On January 31, 1972, clouds over the western slopes of the Cascade Mountains were seeded to reduce the riming and fall velocities of the solid precipitation particles in order to divert snowfall from the western to the eastern slopes of the Cascade Mountains. Observations and measurements, which are described below, showed that the clouds were glaciated by the artificial seeding, the crystal habits were modified and the riming of the precipitation particles reduced, and snowfall rates decreased at the crest and simultaneously increased 20 km east of the crest during the predicted period of effect of the seeding at ground level.

5.1.1 Synoptic Situation

The synoptic situation on January 31, 1972, over Washington State was influenced primarily by a sharp upper level trough. This northeast-southwest oriented trough lay off the coast of Washington on the 500 mb analysis for 0400 PST*. Influenced by a strong blocking ridge west of California and the persistent movement of the maritime Pacific anticyclone out of the Gulf of Alaska, the trough advanced through the Pacific Northwest at a rate of approximately 22 knots. The trough orientation at 1600 is depicted in Fig. 5.1. Temperatures at the 500 mb level decreased 6°C and the 500 mb geopotential heights fell 70 meters in the Cascade Mountains area between 0400 and 1600. The 850 mb chart depicts a closed cyclonic feature in northeastern Washington. This feature drifted to the southwest during the 12 hour period due to the encroachment of the maritime Pacific anticyclone and the blocking ridge to the south (Figs. 5.2 and 5.3). Temperatures and geopotential heights at 850 mb decreased over the Cascade Mountains but not as strongly as at the 500 mb level.

A surface synoptic analysis for 1300 is shown in Fig. 5.4. This chart is most likely not representative of the actual surface conditions due to the high sea level pressures attributed to the effect of cold air trapped over the mountain stations. The 850 mb analyses are considered more representative of the low level synoptic situation that prevailed over the area. A time cross-section based on rawinsondes launched from Quillayute, Washington, is shown in Fig. 5.5. This chart vividly depicts the cold advection accompanying the passage of the trough aloft. Note that below the 880 mb level very little change in the temperature and dew point depression is discernible, whereas, above this level the thermal trough is readily apparent. The low level temperature uniformity is attributable to the maritime influence of the Pacific Ocean. The east-to-west tilt of trough is apparent in the chronological earlier passage of the thermal trough at the 400 mb to 550 mb levels versus the 600 mb to 750 mb levels. The net effect of this trough was the production of extensive layered stratus, stratocumulus, and altocumulus clouds with some embedded cumulus. Precipitation in the form of light snow and snow showers was observed at most surface reporting stations in the area.

Fig. 5.6 depicts a portion of a vertical cross section from Seattle, Washington, to Ellensburg, Washington, valid for the period 1130 to 1300 hours.

---

*All times are local (Pacific Standard Time - PST).

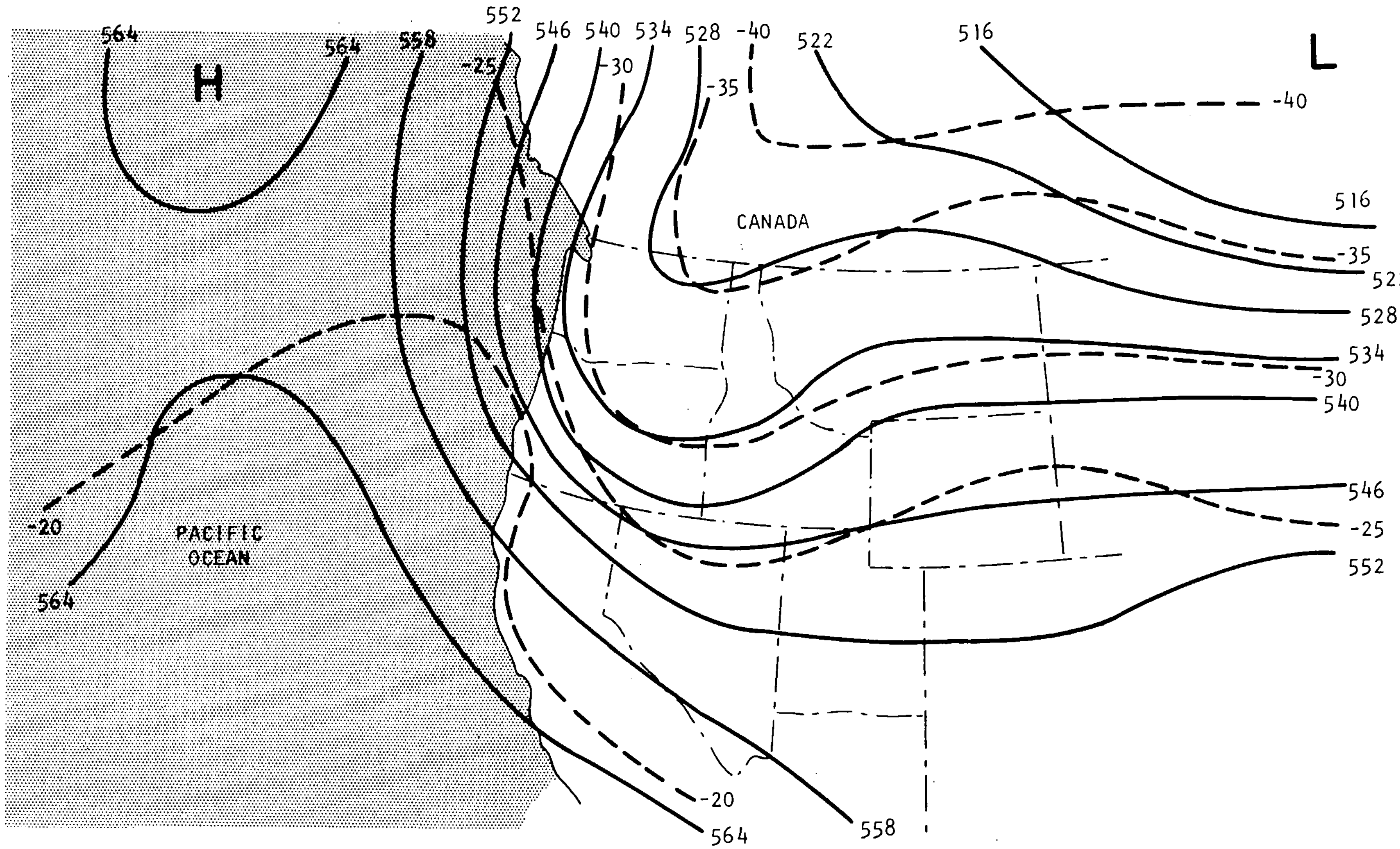

Fig. 5.1 500 mb synoptic map for 1600 PST on January 31, 1972. ——— Height in 10's of geopotential meters of 500 mb surface. — — — Temperature (°C).

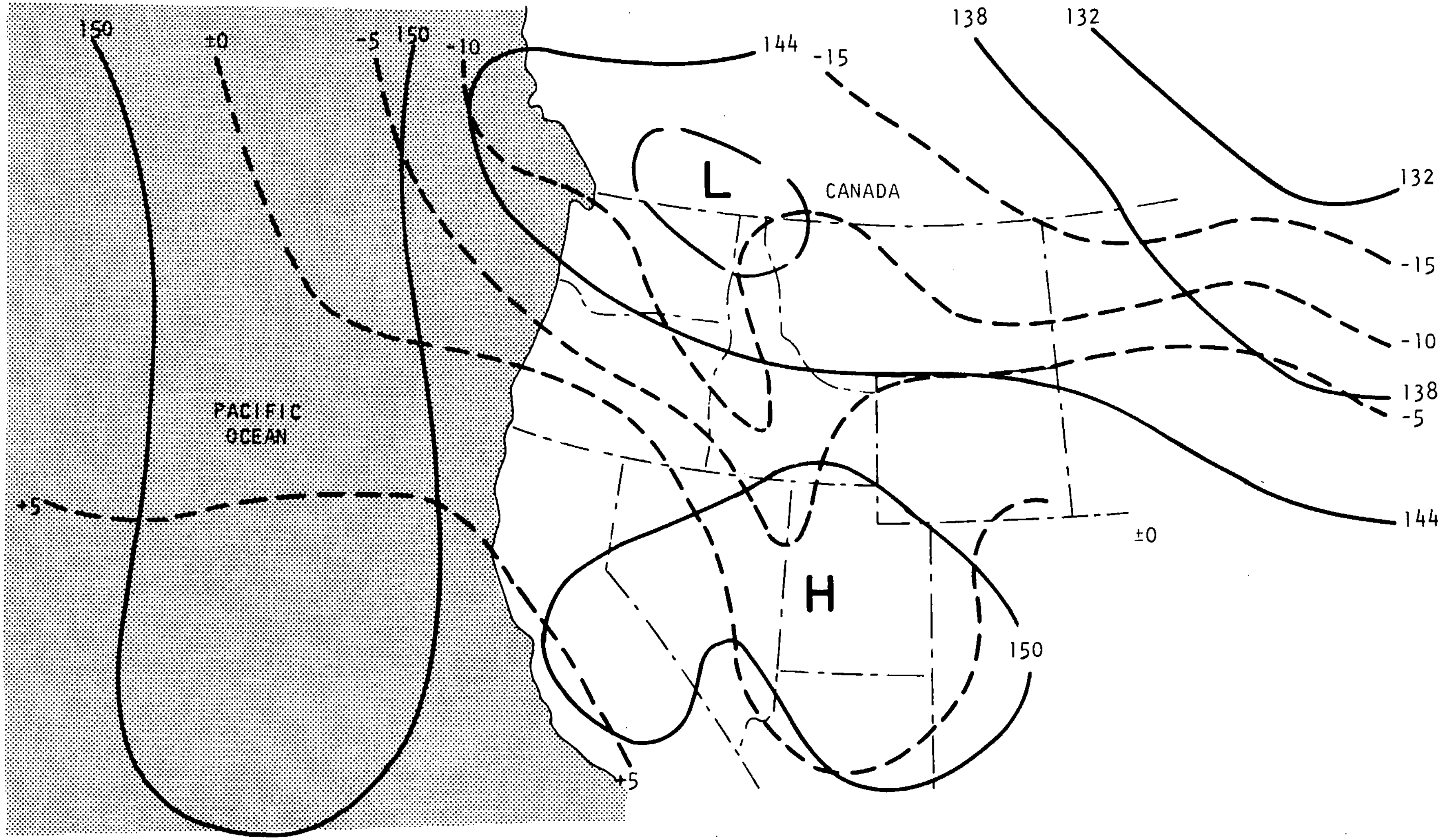

Fig. 5.2 850 mb synoptic map for 0400 PST on January 31, 1972. ——— Height in 10's of geopotential meters of 850 mb surface. – – – Temperature (°C).

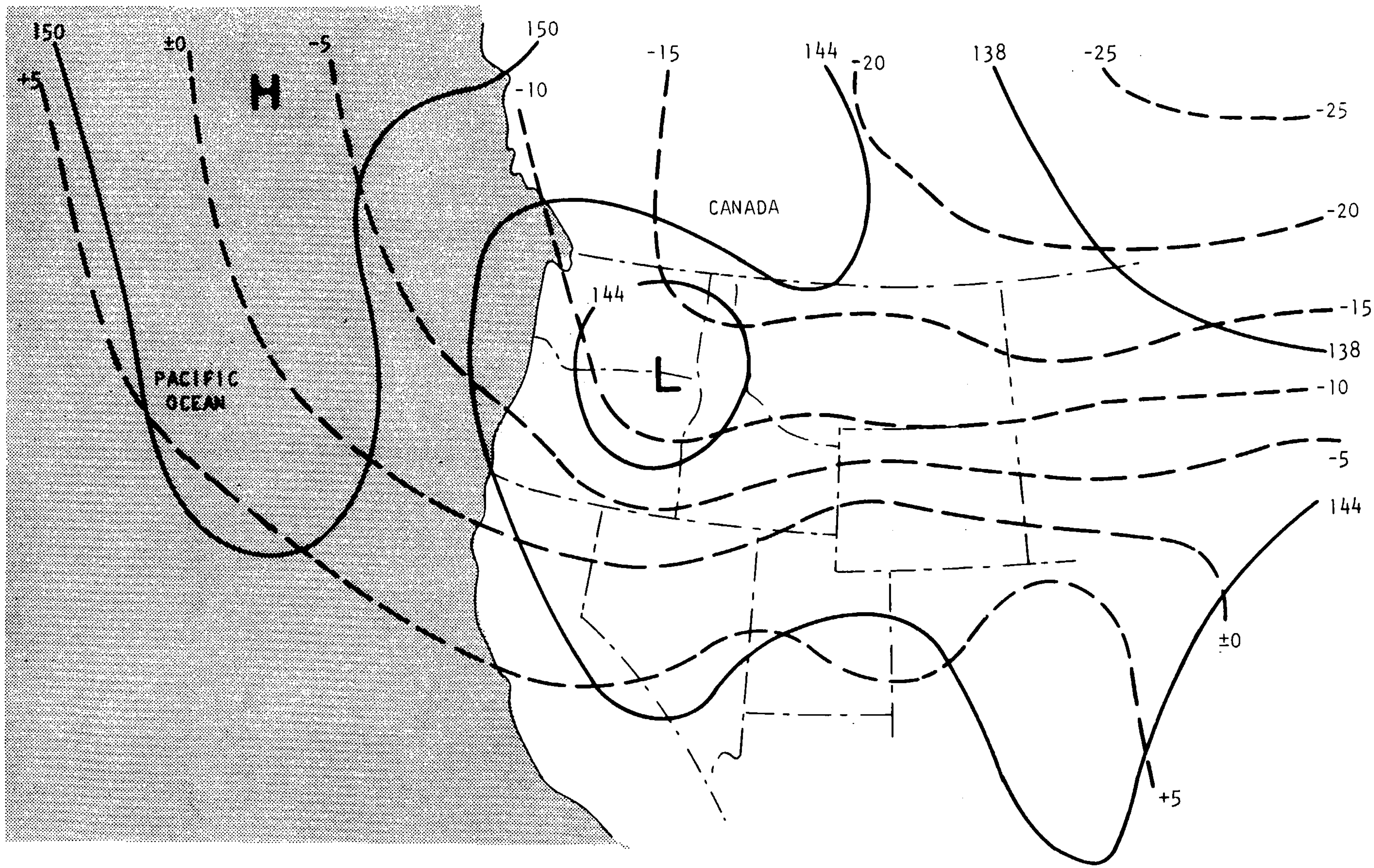

Fig. 5.3 850 mb synoptic map for 1600 PST on January 31, 1972. —— Height in 10's of geopotential meters of 850 mb surface. ---- Temperature (°C).

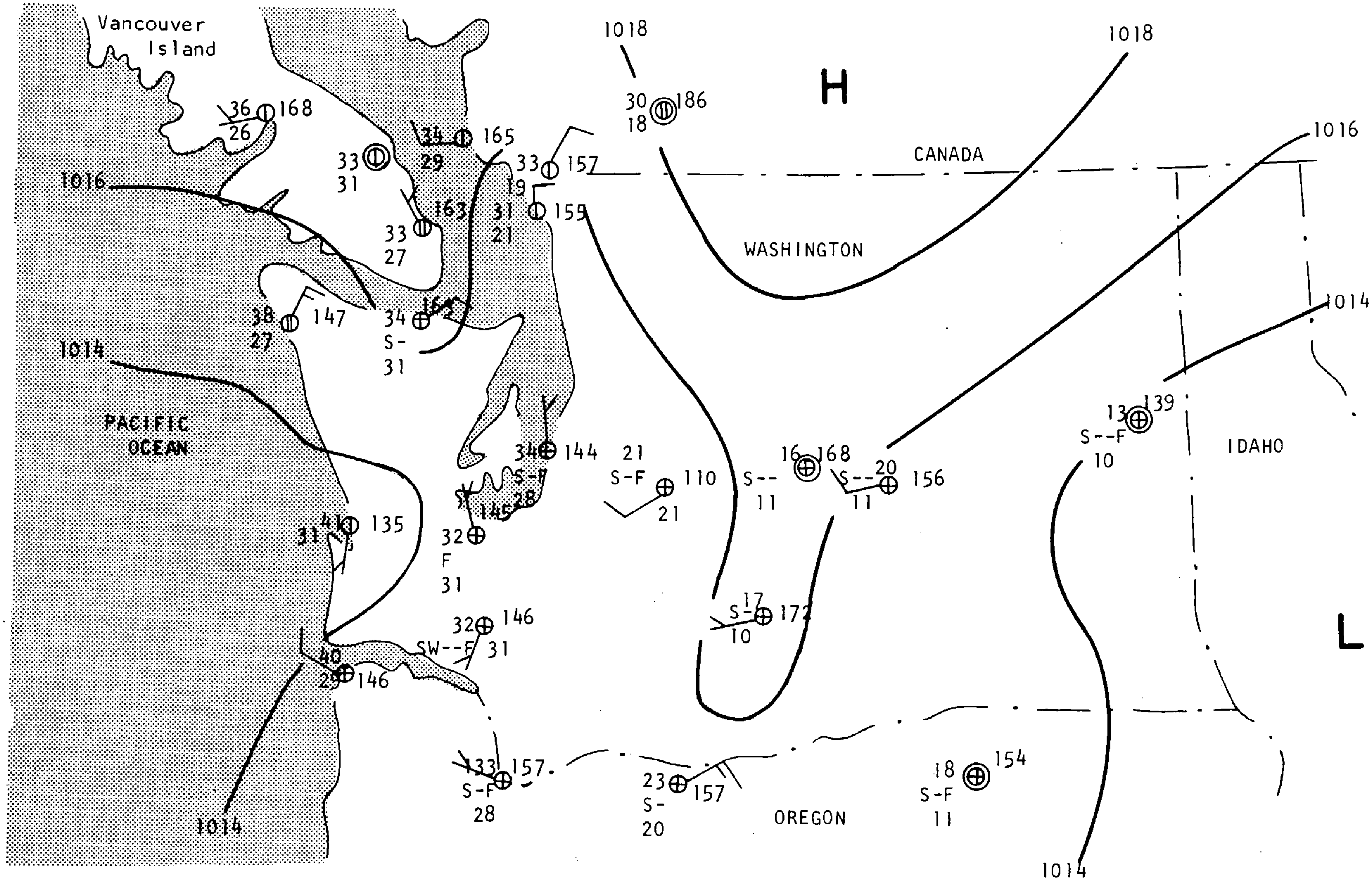

Fig. 5.4 Surface synoptic situation at 1300 PST on January 31, 1972.

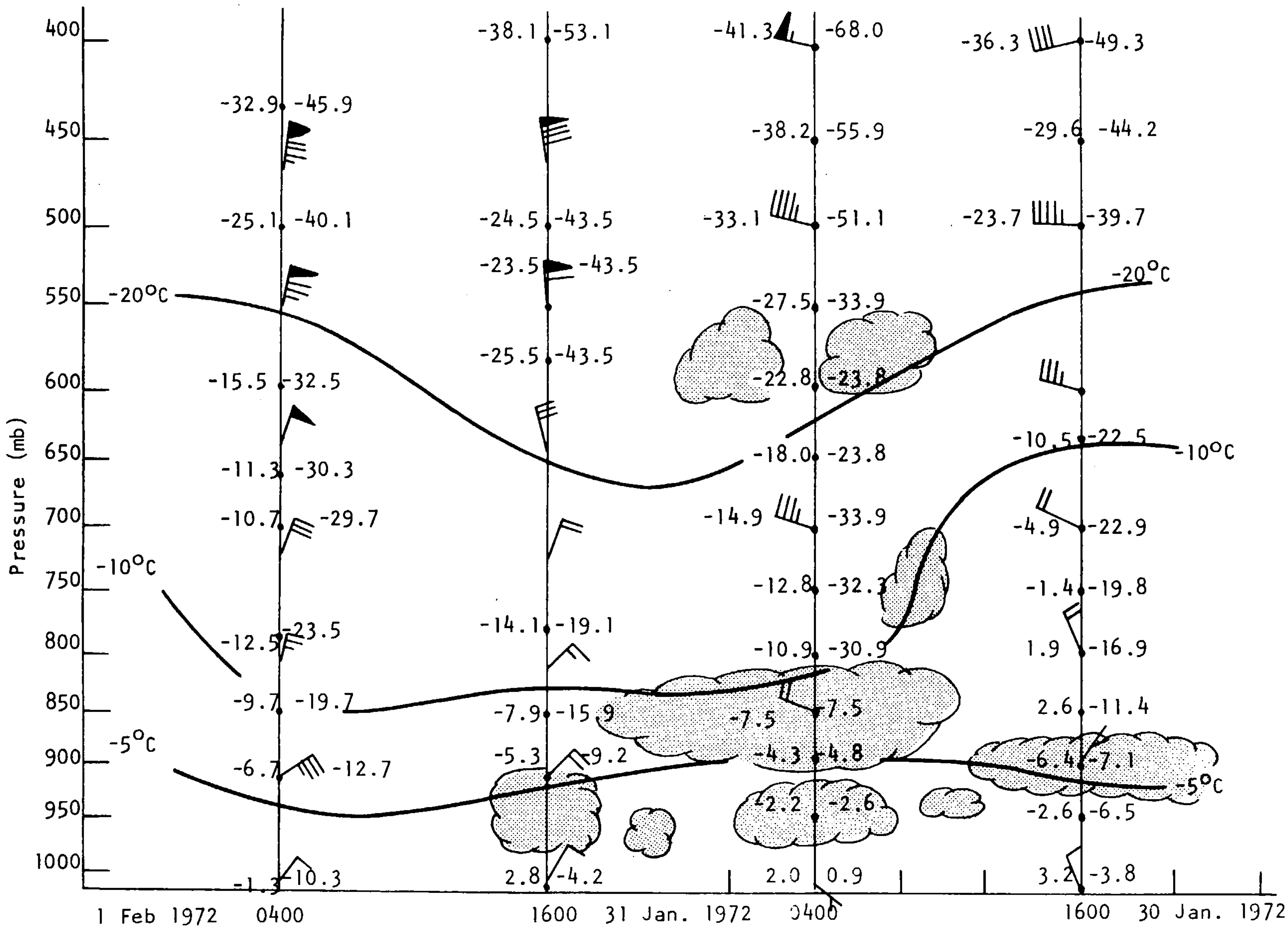

Fig. 5.5 Time cross-section for soundings at Quillayute between January 30 and February 1, 1972.

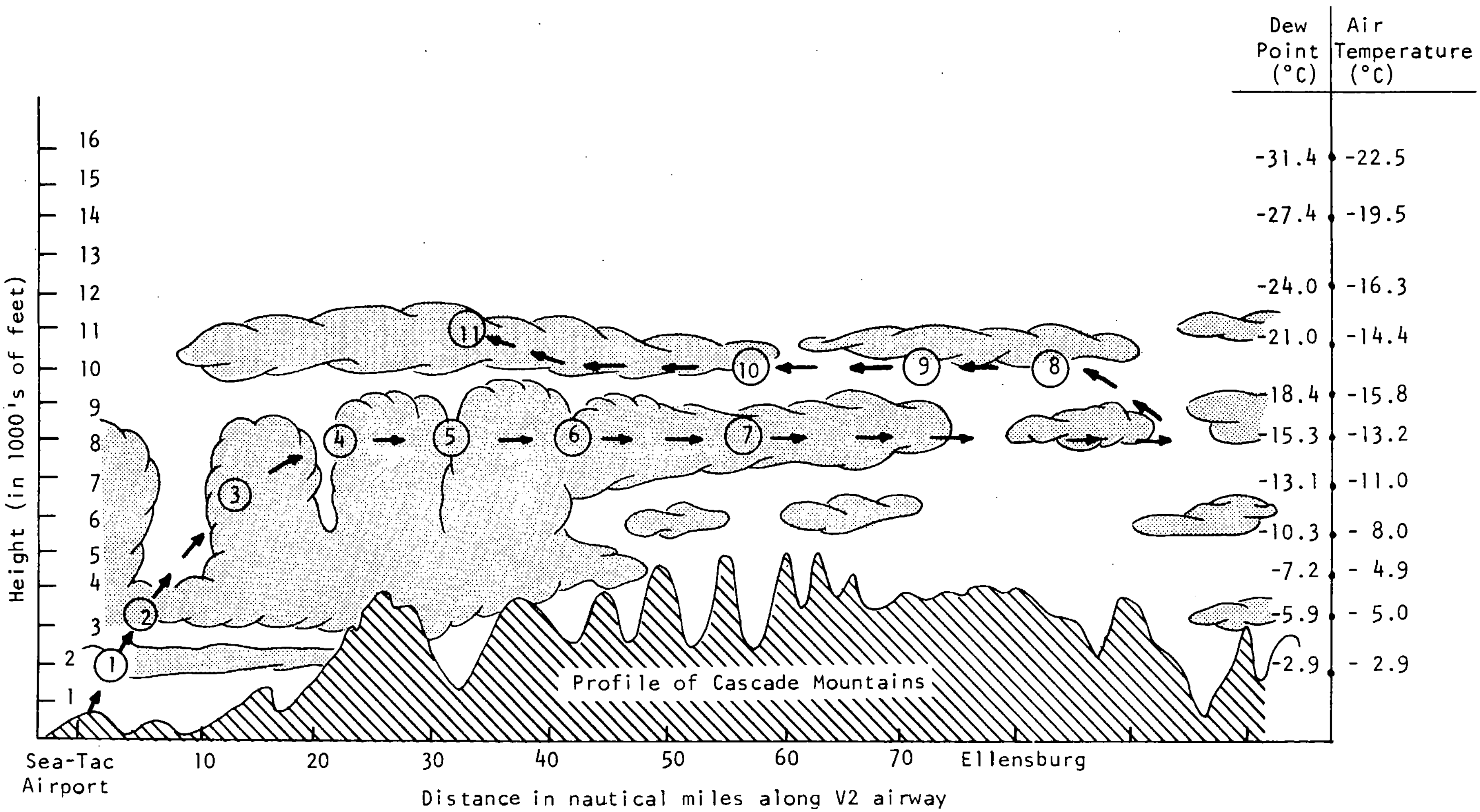

Fig. 5.6 Vertical cross-section from Seattle, Washington, to Ellensburg, Washington, valid from 1130 to 1300 PST on January 31, 1972. The air temperatures and dew points (in °C) and winds shown are based on the 1103 PST rawinsonde launched from Greenwater which is located approximately 31 miles southeast of Sea-Tac Airport. (1) Continuous particle sampler run position. ← Flight path of research aircraft.

Fig. 5.7 depicts the same information for the period 1300 to 1600 hours. These charts are a composite of upper air data, surface data and observations taken from the research aircraft. The upper level trough was passing through the Cascade Mountain region during this period. The Greenwater sounding for 1300 suggests that the trough axis above 10,000 ft.[†] had already passed the station since the wind directions above that level were all northwesterly. The westerly winds below that level but above the mountainous terrain indicate that the lower portion of the trough axis is just passing Greenwater at 1300 hours. Unfortunately, the wind data for the 1100 sounding were not obtained to verify wind shifts at discrete levels. Comparison of the temperature data between the 1100 and 1300 soundings shows that the temperatures at all levels above 900 mb decreased during this period. The maximum decrease of 1.2°C occurred at 740 mb and an average of 0.5°C occurred throughout the sounding.

During the period 1130 to 1300 the cloud formation over the Cascade Mountains consisted of extensive layered stratus and stratocumulus with bases near 3,000 ft. on the western slopes to 6,500 ft. over the mountains. Cloud tops of this layer were reported at 8,500 to 9,500 ft. A second distinct layer of altocumulus was based at 10,000 ft. and was approximately 2,000 ft. thick. A thin cirrus layer near 20,000 ft. was also observed. The lower layers were composed of mixed water and ice clouds.

During the period 1300 to 1600 the two layers with cirrus overhead persisted, however, some changes in the cloud structure were evident. The lower deck became more cumuliform as evidenced by the ground and airborne observations and complete glaciation of the upper layer at times was observed from the aircraft.

5.1.2 Aircraft Operations

5.1.2.1 Flight Profile

The research flight for January 31, 1972, commenced at 1145 from Boeing Field. The aircraft climbed to 8,000 ft. and proceeded along the Vector-2 airway to Ellensburg, Washington (Figs. 5.6, 5.7 and 5.8). During this period the on-board instruments were calibrated and routine observations and measurements were made. After reaching Ellensburg, the aircraft reversed course, climbed to 10,000 ft. altitude and continued observations in preparation

---

[†] All heights are above Mean Sea Level unless specified otherwise.

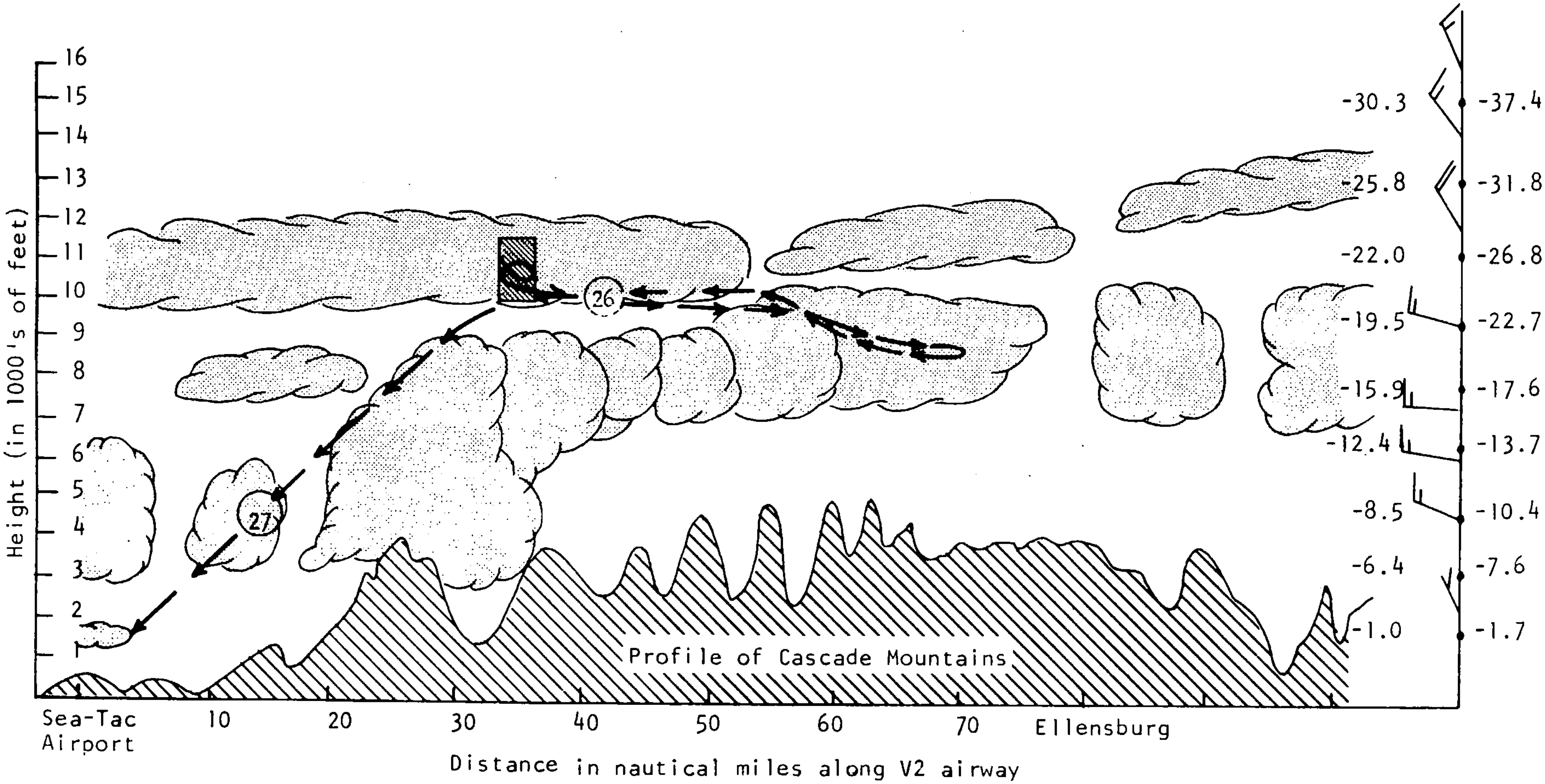

Fig. 5.7 Vertical cross-section from Seattle, Washington, to Ellensburg, Washington, valid from 1300 to 1600 PST on January 31, 1972. The air temperatures and dew points (in °C) and winds shown are based on the 1300 PST rawinsonde launched from Greenwater which is located approximately 31 miles southeast of Sea-Tac Airport. Continuous particle sample runs 15 through 25 were taken within the seeding orbit. (1) Continuous particle sampler run position. ← Flight path of research aircraft. ▨ Seeding orbit.

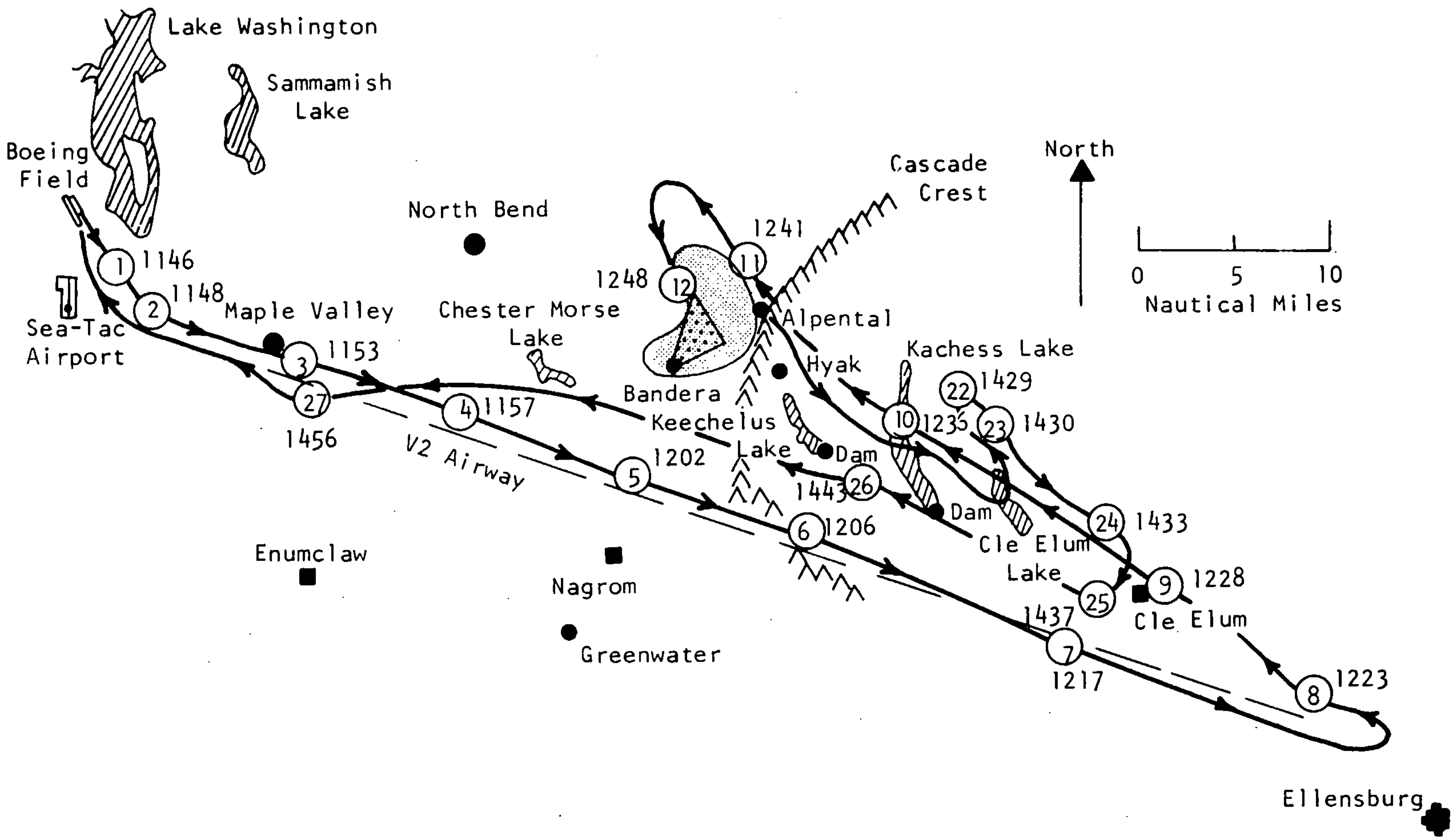

Fig. 5.8 Sketch of flight route (⟶) on January 31, 1972. The symbol (1) refers to continuous cloud particle sampler runs. Four figure numbers give local time. Prescribed seeding area. Actual seeded area.

for the seeding operation. All instruments with the exception of the weather radar and the radar altimeter were operational.

The seeding orbit was determined from predicted ice crystal trajectories based on the observed crystal types at the ground stations and the Quillayute 0400 rawinsonde. The prescribed seeding area is shown in Fig. 5.8. The seeding plan called for in situ end-burning AgI flares to be continuously expended until the on-board supply was exhausted, and for one ejection flare to be fired every three minutes while the aircraft flew the prescribed orbit. The actual seeding operation followed the plan closely, however, the seeding orbit was larger than specified (Fig. 5.8).

After seeding ceased the aircraft flew downwind from the seeded area at various altitudes sampling for seeding effects. It returned to Boeing Field at 1510 hours.

5.1.2.2 Seeding Operation

Nine Colspan in situ flares each containing 64 grams of AgI were expended in series from 1254 until seeding ceased at 1406. Twenty-four ejection flares each containing 40 grams of AgI were expended at approximately three-minute intervals during the same period. The initial seeding operation encompassed an area of approximately 23 square miles horizontally (Fig. 5.9). The vertical extent of the seeding varied due to altitude changes of the aircraft and the use of delay-fused ejection flares. These flares fell for 2,000 ft. before ignition and then burned during the next 3,000 ft. of fall. A schematic representation of the initial vertical seeded profile is also shown in Fig. 5.9. Dispersion of the AgI plume via diffusion has not been considered in this profile. Ice nuclei production rates for formulation CSP-009A (Model No. 600-001 Aircraft End-Burning Flare) were measured in the Colorado State University isothermal cloud chamber.

Three methods were used to estimate the downstream concentration of ice nuclei produced by the seeding and the extent of the seeded region. The first was based on the diffusion model of Pasquill as modified by Gifford (Turner, 1969; Beals, 1970). This model assumes Gaussian distributions in the horizontal and vertical planes of the concentration of pollutant and defines horizontal and vertical dispersion coefficients as the standard deviations of these distributions. Nomograms for estimates of dispersion coefficients as functions of downwind distance for various stability categories are given by Turner (1969). The neutral stability category was selected as representative of the atmosphere in the seeded area based on the cloud cover and wind velocity criteria

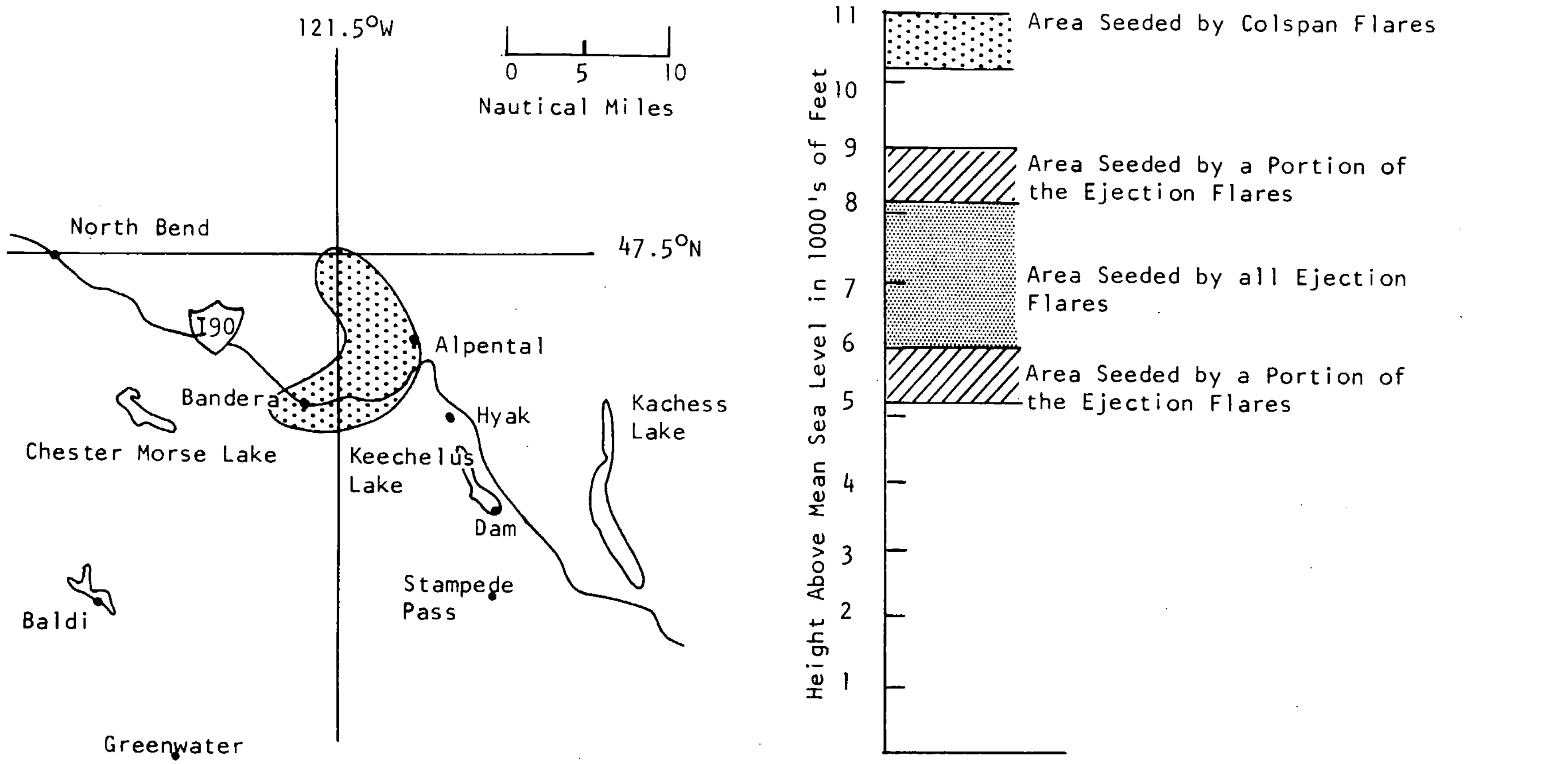

PLAN VIEW OF SEEDED AREA

VERTICAL VIEW OF SEEDED AREA

Fig. 5.9 Plan and vertical views of seeded area without the effects of turbulent diffusion on January 31, 1972. Stippling in plan view indicates the seeded area.

established by Beals (1970). An average wind speed of 15 knots, invariant in speed and direction from 6,000 to 11,000 ft., was assumed. A continuous horizontal line source model was assumed for the *in situ* burning flares and an instantaneous vertical line source was assumed for the ejection flares. Calculations of ice nucleus concentrations for the *in situ* flares were made using the nomograms from Beals (1970) and an ice nuclei production rate of 3.5×10^{15} nuclei per gram of AgI active at -21.5°C. Fig. 5.10 depicts the computed seeded volume for the *in situ* flares as represented by a 10 km long continuous line source. For a downwind distance of 6 km, concentrations of nuclei equal to or greater than 1,000 per liter would occur for approximately 750 ft. above and below the seeding level and concentrations of nuclei equal to or greater than 1 per liter would occur for approximately 1,500 ft. above and below the seeding level. Fig. 5.11 depicts the calculated seeded volume for one ejection flare with only three levels shown for clarity. An ice nucleus production rate of 4×10^{16} nuclei per gram of AgI active at -17.5°C, 1.2×10^{16} nuclei per gram active at -15.3°C, and 3.2×10^{15} nuclei per gram active at -13.3°C were assumed for the three levels 9,000 ft., 7,500 ft., and 6,000 ft., respectively. In this case, for a downwind distance of 6 km, concentrations of nuclei equal to or greater than 1,000 per liter would occur for approximately 1,000 ft. from the center line at the 9,000 ft. level and approximately 700 ft. for the 6,000 ft. level. Very heavy concentrations exist along the center line for a considerable distance downstream and the effect of lateral and vertical diffusion in expanding the seeded volume is readily apparent.

The second estimation of the downstream concentrations of ice nuclei was based on Batchelor's (1950) work in which it is suggested that the spreading of a cloud puff in the inertial subrange should follow the law:

$$d^2 = C\varepsilon t^3$$

where d is the diameter of the plume, C is a constant of order unity, ε is the turbulent dissipation rate, and t is time. An average value for ε during the seeding period of 0.112 $cm^2\ sec^{-3}$ was calculated from the turbulence data measured aboard the aircraft (see Fig. 5.19). Using the turbulence magnitude scale suggested by MacCready (1964), this value of ε would be indicative of only negligible turbulence.

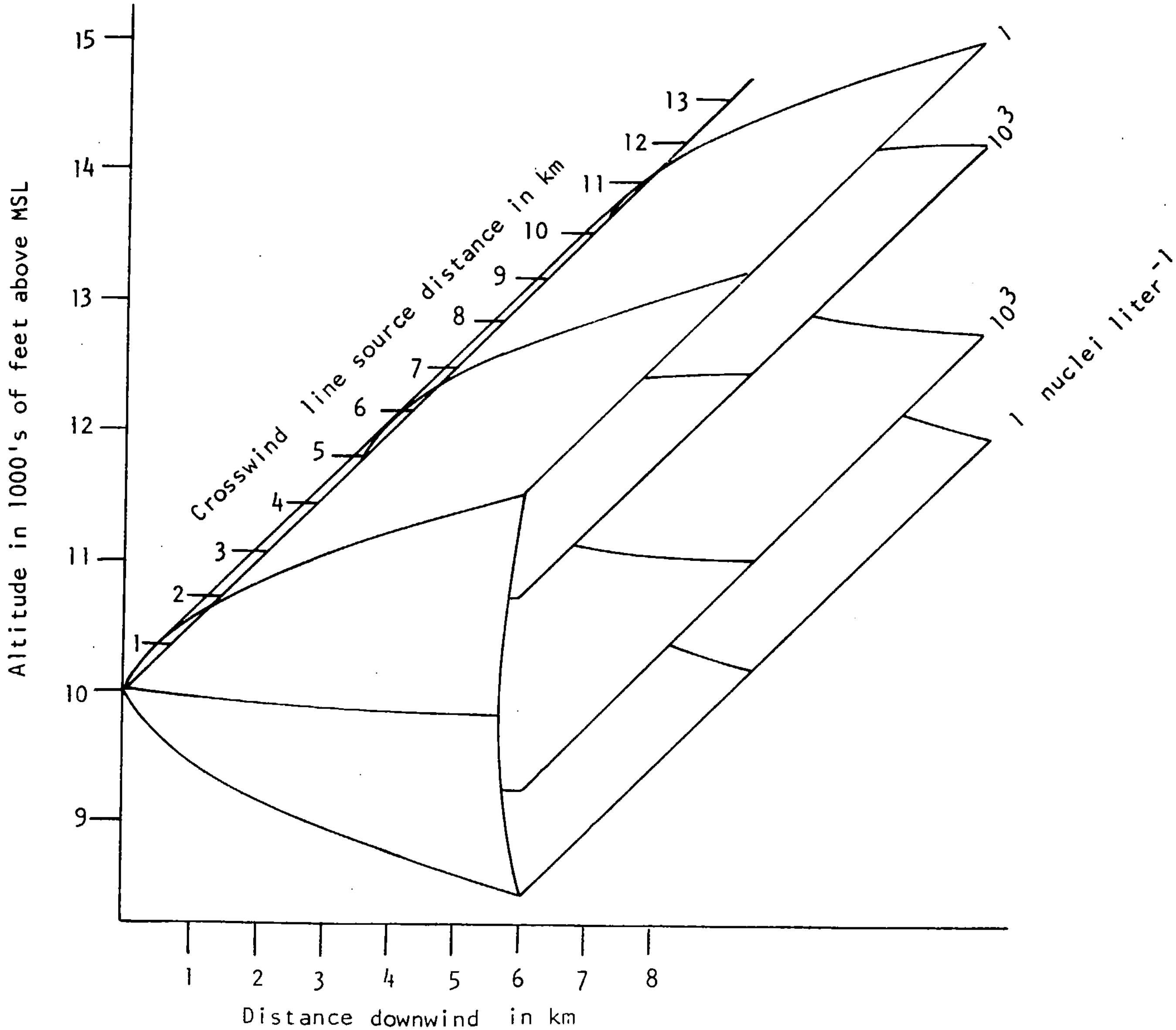

Fig. 5.10 Schematic view of AgI ice nucleus diffusion from Pasquill-Gifford model for an in situ burning flare as a 10 km line source at 10,000 feet MSL on January 31, 1972.

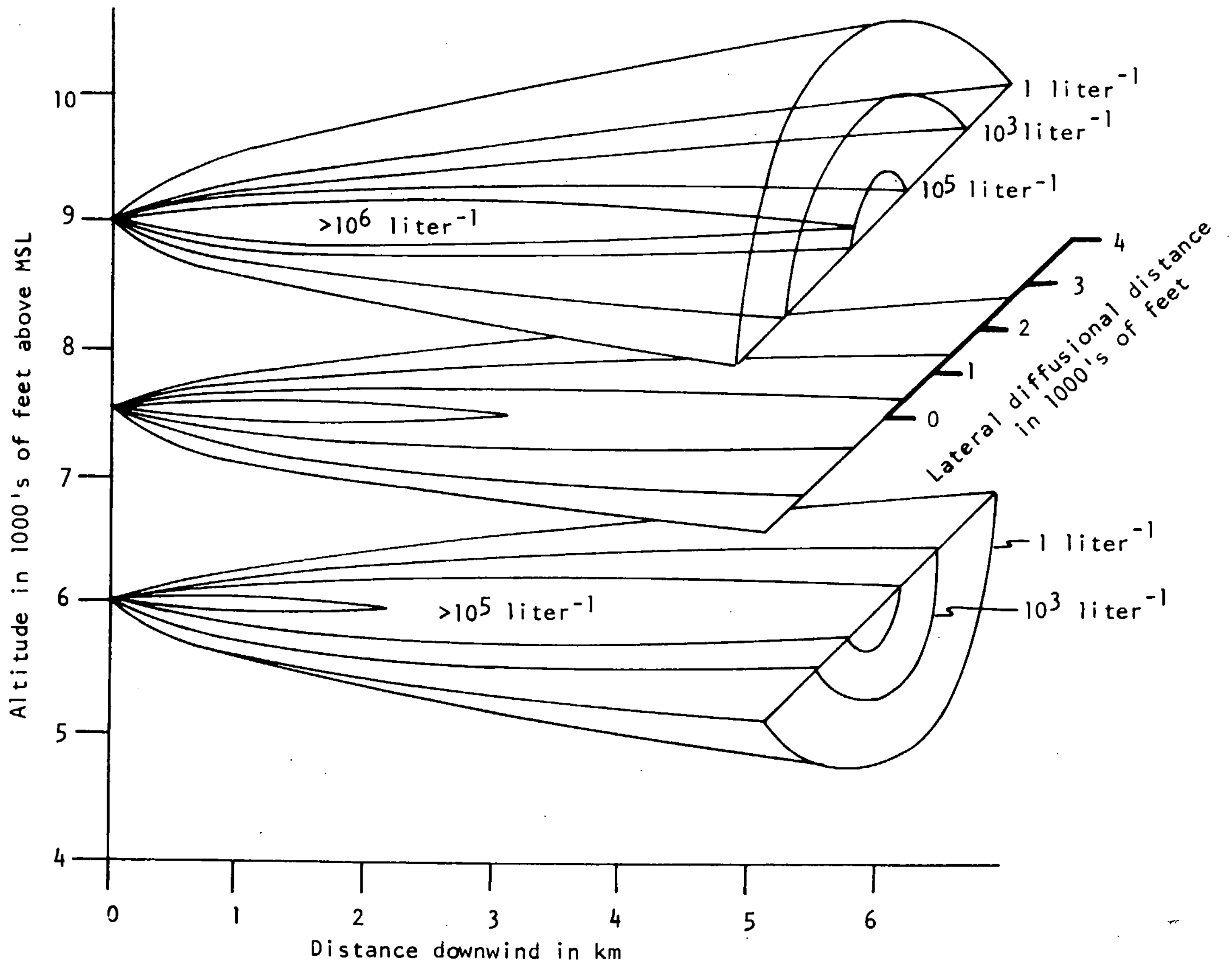

Fig. 5.11 Schematic view of AgI ice nucleus diffusion from the Pasquill-Gifford model for one 40 gram ejection flare on January 31, 1972. For clarity only three levels are shown.

Finally, Krasnovskaya et al. (1971) investigated horizontal turbulent diffusion characteristics of artificially seeded clouds. Four sets of empirical functions are given for the width of the zone of glaciation versus time, classified according to wind speed and turbulence. Calculations of the lateral dimension versus distance downwind were made based on the applicable curve from Krasnovskaya for ε less than 5 $cm^2\ sec^{-3}$.

Table 5.1 gives the comparison of the computed lateral dimension of the seeded plume from one ejection flare between the Pasquill-Gifford model and the Kransnovskaya model and between the Pasquill-Gifford model and the Batchelor model. The seeded plume models after Kransnovskaya and Batchelor assume a uniform ice nucleus concentration within the seeded volume, whereas, the Pasquill-Gifford method presents a gradient of concentrations. The lateral dimensions predicted by Krasnovskaya et al. are larger than those calculated with the Pasquill-Gifford model, but the lateral dimensions from Batchelor are smaller than those calculated with the Pasquill-Gifford model. It was assumed in all of these calculations that no decrease in AgI nucleus concentrations occurred due to precipitation, coagulation, reaction to sunlight, etc. From the above it is concluded that the seeded volume depicted in Figs. 5.10 and 5.11 are indeed somewhat representative of the actual ice nucleus concentrations downstream and that these concentrations are sufficient to promote glaciation.

An estimation of the increase in volume due to diffusion of the region seeded with in situ flares is shown in Figs. 5.12 and 5.13. The seeded region depicted in Fig. 5.9 was considered a continuous source region of ice nuclei with average nucleus concentrations equal to or greater than 10^3 $liter^{-1}$. This volume was then advected with the mean wind at 10,500 ft. and enlarged at the diffusion expansion rate of the 10^3 nuclei per liter isopleth from Fig. 5.11. Ice crystals collected within this region, or the trajectories of which passed through this region and intercepted the ground, were considered to be influenced by seeding. Continuous particle sampler runs 13 through 24 were within this area. The seeded volume produced by the ejection flares is much less continuous than that produced by the in situ flares. At an average true air speed of 150 knots and a three-minute delay between firings, the flare separation would be of the order of 7 nautical miles. Using the diffusive expansion rate from Fig. 5.10, it is obvious that the AgI plume produced by two flares separated by 7 miles would not intersect. Furthermore,

TABLE 5.1

A COMPARISON OF COMPUTED LATERAL DIMENSIONS OF THE SEEDED PLUME AT 8,500 FEET M.S.L. FOR ONE 40-GRAM EJECTION FLARE

Distance From Source (km)	Concentration (nuclei $liter^{-1}$)	Lateral Dimension after Pasquill-Gifford[†] (m)	Lateral Dimension after Krasnovskaya[‡] (m)	Lateral Dimension after Batchelor[§] (m)
1	9×10^7	80	140	
2	2×10^7	140	300	
3	5×10^6	190	580	
4	4×10^6	235	680	
5	2×10^6	275	870	
6	1×10^6	305	1100	
1	1×10^{10}	25		11
2	8×10^9	35		15
3	2×10^9	75		26
4	1×10^9	80		41
5	8×10^8	65		59
6	4×10^8	75		76

[†] Lateral dimensions taken from Fig. 5.11 using the Pasquill-Gifford diffusion model for respective concentrations.

[‡] Lateral dimension taken from Krasnovskaya _et al_. (1971) curve for $\varepsilon < 5\ cm^2\ sec^{-1}$ for respective concentrations.

[§] Lateral dimension computed from the relation $d^2 = C\varepsilon t^3$ after Batchelor (1950).

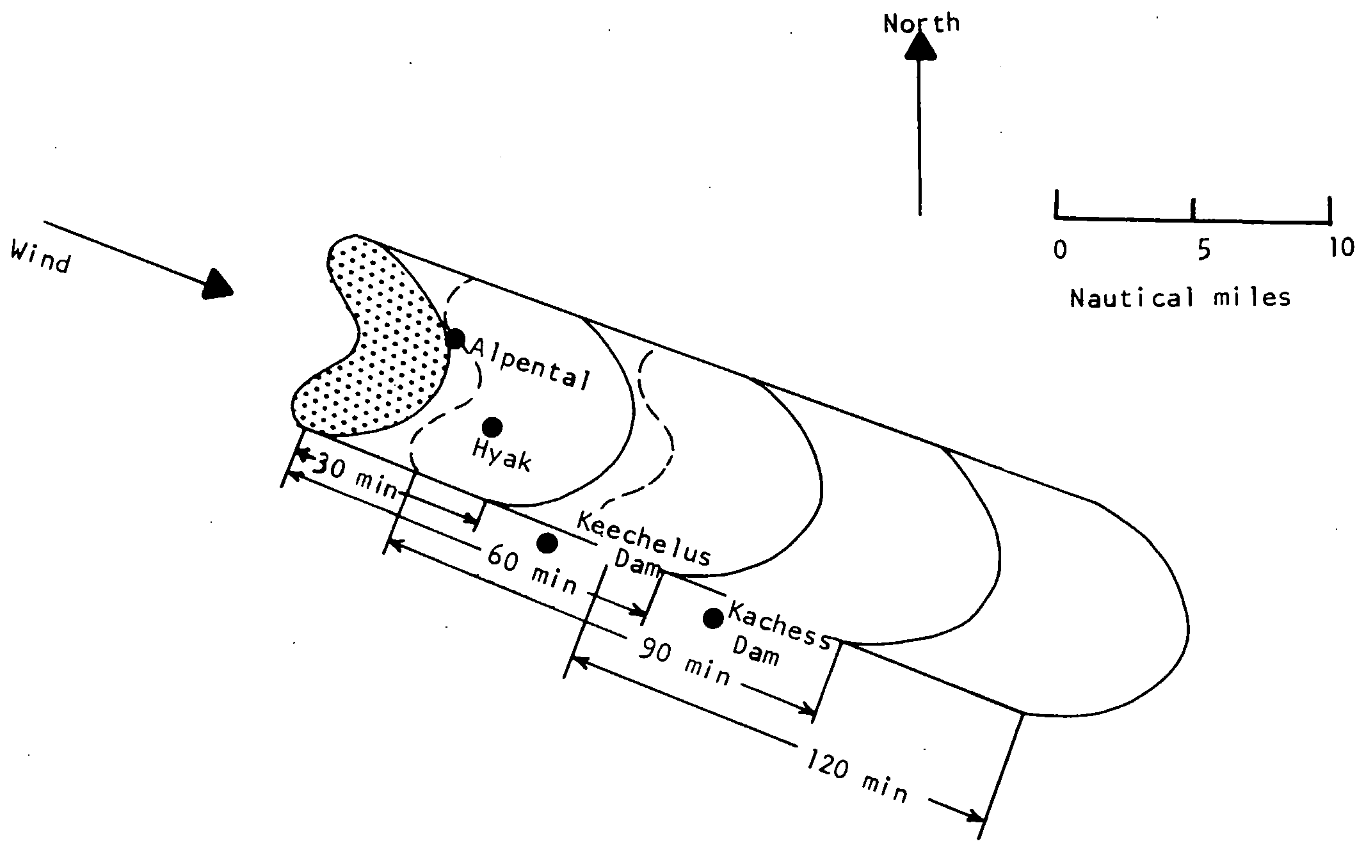

Fig. 5.12 Horizontal profile of increase in seeded region with time due to turbulent diffusion on January 31, 1972. Seeded region defined by elapsed time in minutes after seeding began. [dotted symbol] Initial seeded area.

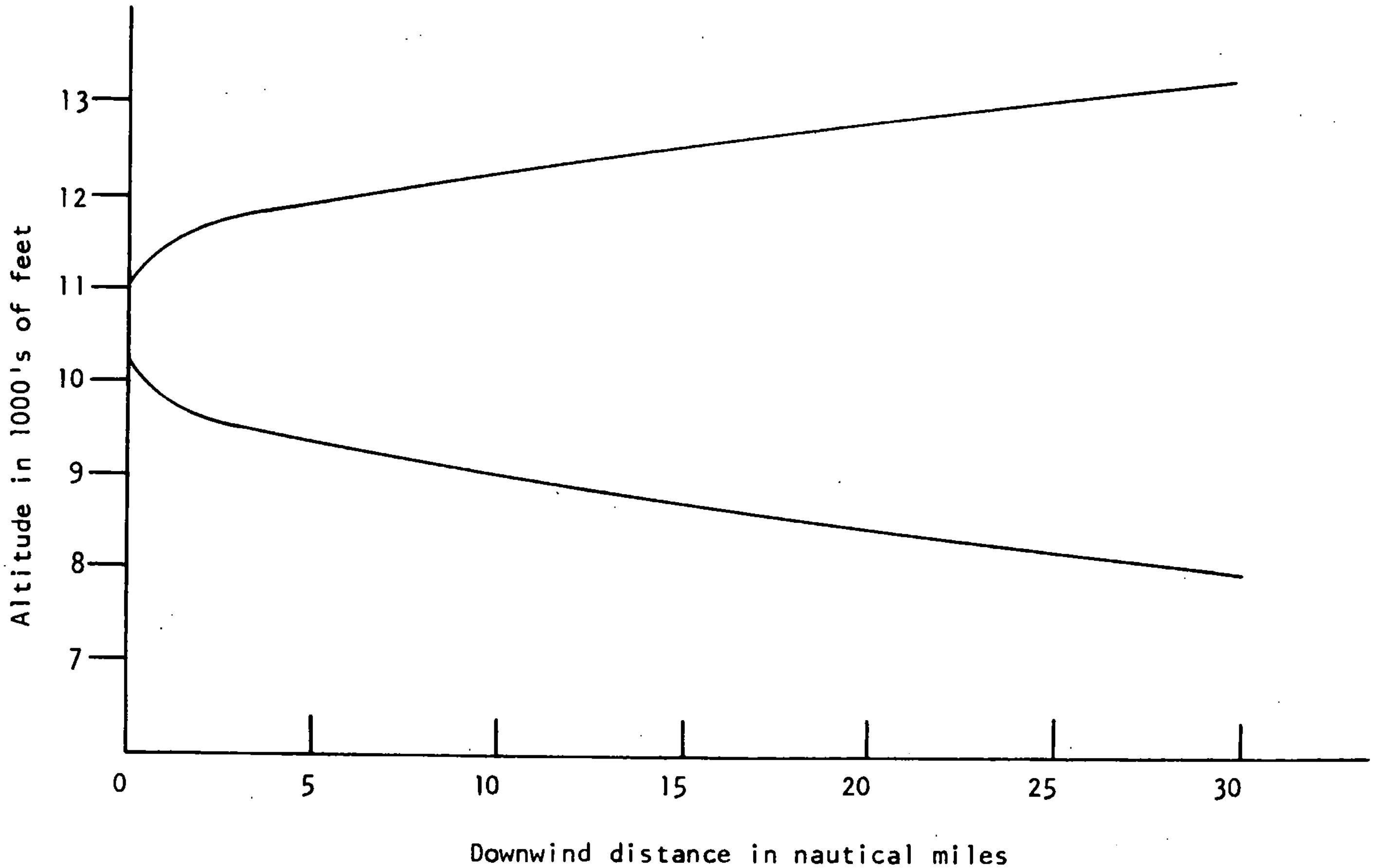

Fig. 5.13 Vertical profile of increase in seeded region due to diffusion on January 31, 1972.

any flares fired at the same location would be separated in time by at least three minutes, or 0.7 miles at a wind speed of 14 knots. From the above, it is apparent that the seeded volume developed by the ejection flares would not produce glaciated conditions throughout the volume. Rather, a series of vertical columns glaciated by the AgI of the order of 0.2 miles in diameter, separated by 7 miles laterally or 0.7 miles along the wind direction, would be produced. Ice crystals collected at the ground whose trajectories happened to have passed through these glaciated regions were considered as affected by seeding.

5.1.3 Ice Crystal Trajectories

Predictions of ice crystal trajectories for the various types of crystals observed at the three ground stations were made using the trajectory model described on page 171 of Hobbs *et al*. (1971). A spatial comparison of the crystal trajectories with the seeded volume was made to determine which crystal types could have been affected by seeding.

Figs. 5.14 and 5.15 are examples of the horizontal and vertical comparisons, respectively, of the trajectories of unrimed stellar crystals and the seeded volume. Over one-half of the trajectory of the smallest and all of the trajectory of the largest stellar crystals coincided with the horizontal extent of the seeded region. Seeding from the *in situ* flares occurred above the diffusional growth region and the riming region of the crystals collected at Hyak. Seeding from the ejection flares occurred in a large portion of the diffusional growth region of the larger stellar crystals. In addition, these flares also seeded from 800 to 1600 feet into the riming region. Juxtaposition of the seeded volume over a substantial portion of the diffusional growth layer and riming region gives justification for assuming that the artificial nuclei would have affected the nucleation and riming of stellar crystals in the region. Based on the time and position of seeding relative to the crystal trajectories, effects of seeding could be expected at Hyak from 1306 until 1420 hours.

Similar analyses were done for the dominant crystal types observed at all three ground stations. Tables 5.2 - 5.4 give the results of these analyses.

5.1.4 Airborne Observations

Analyses of the data obtained from the research aircraft are presented in Figs. 5.16 through 5.19 and in Tables 5.5 and 5.6.

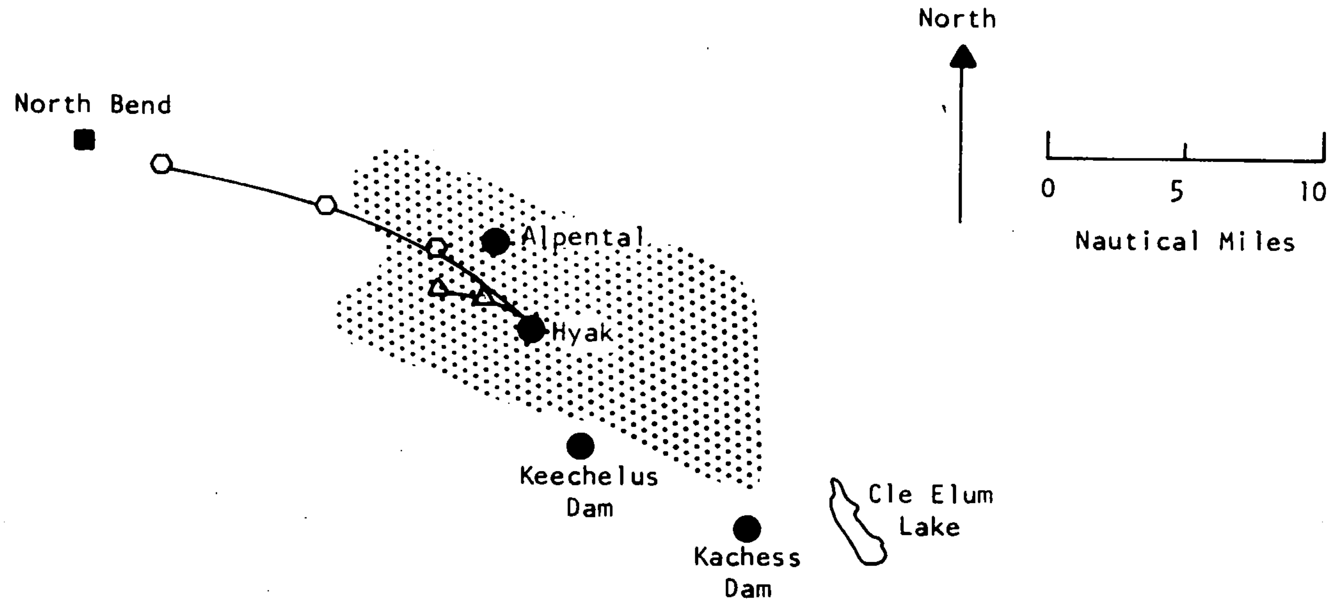

Fig. 5.14 Plan view of trajectories of unrimed stellar crystals and seeded region on January 31, 1972. Seeded region. Trajectory of smallest crystals. Trajectory of largest crystals.

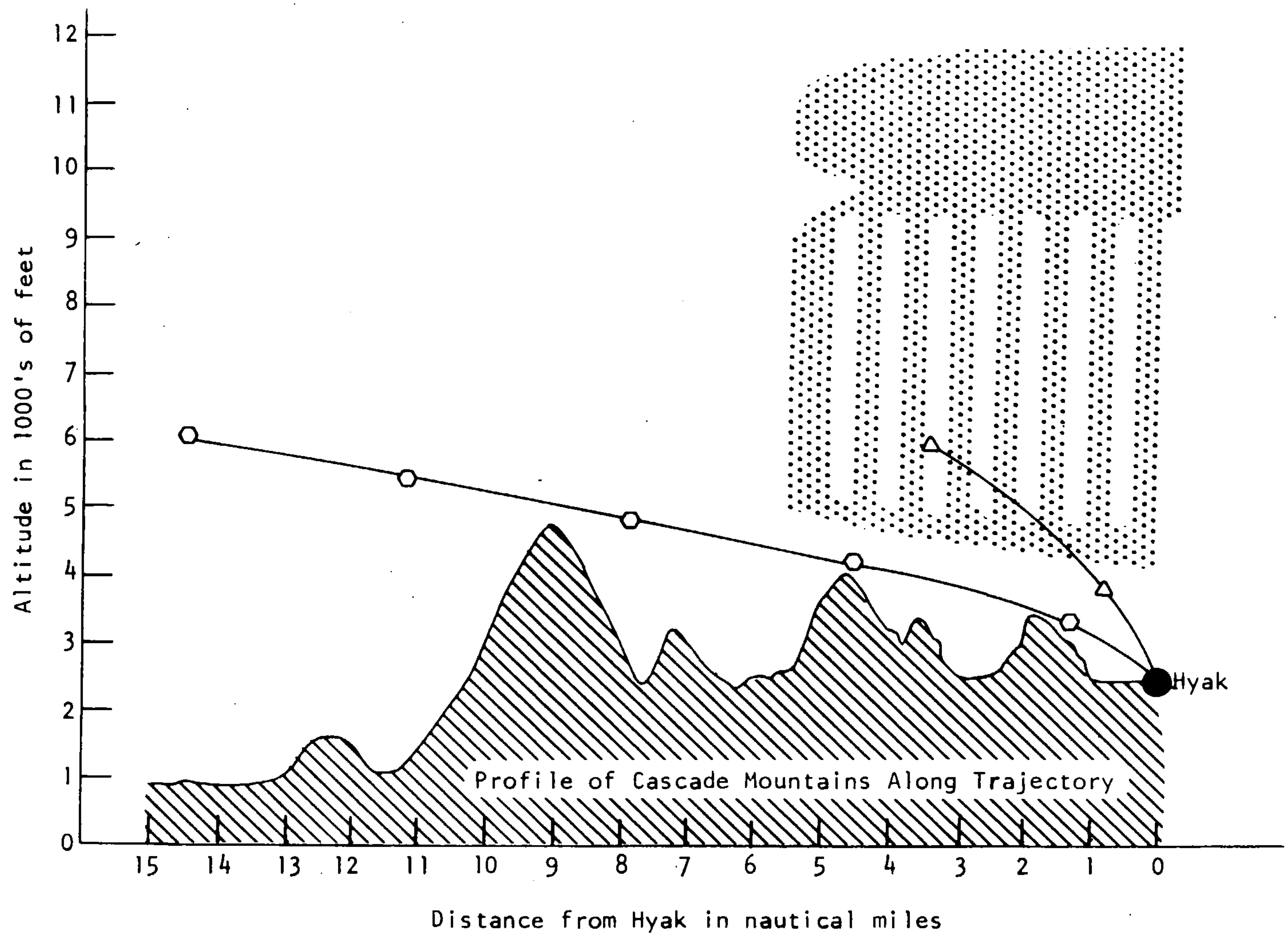

Fig. 5.15 Vertical profile of trajectories of unrimed stellar crystals and seeded region on January 31, 1972. Seeded region.
O Trajectory of smallest crystals. Δ Trajectory of largest crystals.

TABLE 5.2

COMPARISON OF CRYSTAL TRAJECTORIES REACHING ALPENTAL WITH SEEDED VOLUME

Crystal Type	Comparison of Trajectory with Seeded Volume		Qualitative Assessment of Seeding Effect	Time (PST) Seeding Effect Expected on Ground
	Horizontal	Vertical		
Rimed Dendrites	Last 30% of trajectory coincided with seeded area.	Seeding occurred above trajectory.	None	———
Rimed Stellars	Last 30% of trajectory coincided with seeded area.	Last 800 ft. of lower ejection flares seeded in riming region.	Slight chance	1301 - 1430
Rimed Aggregates	Last 40% of trajectory coincided with seeded area.	Ejection flares seeded lower 1600 ft. of diffusional growth region and 2,200 ft. into riming region.	Fair chance	1257 - 1436

TABLE 5.3

COMPARISON OF CRYSTAL TRAJECTORIES REACHING HYAK WITH SEEDED VOLUME

Crystal Type	Comparison of Trajectory with Seeded Volume		Qualitative Assessment of Seeding Effect	Time (PST) Seeding Effect Expected on Ground
	Horizontal	Vertical		
Rimed Dendrites	Last 60% of trajectory of small crystals and 100% of large crystals coincided with seeded area.	Ejection flares seeded from 800 to 1,600 ft. into the riming region.	Good chance	1312 - 1430
Unrimed Dendrites	Last 30% of trajectory of small crystals and last 55% of large crystals coincided with seeded area.	Seeding occurred just above trajectory.	Slight chance	1318 - 1436
Rimed Stellars	Last 50% of trajectory of small crystals and 100% of large crystals coincided with seeded area.	Ejection flares seeded diffusional growth region of medium to large crystals and 800 to 1,600 ft. into riming region.	Excellent chance	1312 - 1442
Unrimed Stellars	Last 30% of trajectory of small crystals and 100% of large crystals coincided with seeded area.	Ejection flares seeded diffusional growth region of medium to large crystals and 800 to 1,600 ft. into riming region.	Excellent chance	1318 - 1450

TABLE 5.3 (Cont.)

Crystal Type	Comparison of Trajectory with Seeded Volume		Qualitative Assessment of Seeding Effect	Time (PST) Seeding Effect Expected on Ground
	Horizontal	Vertical		
Rimed Aggregates	Last 90% of trajectory of small crystals and 100% of large crystals coincided with seeded area.	Ejection flares seeded diffusional growth region of medium to large crystals and from 2,200 to 3,000 ft. into riming region.	Excellent chance	1310 - 1436
Unrimed Aggregates	Last 50% of trajectory of small crystals and 100% of large crystals coincided with seeded area.	Ejection flares seeded diffusional growth region of medium to large crystals and 2,200 to 3,000 ft. into riming region.	Excellent chance	1316 - 1442
Graupel (0.05 cm dia.)	Last 65% of trajectory coincided with seeded area.	Ejection flares seeded 400 to 800 ft. into riming region.	Slight chance	1316 - 1442
Unrimed Assemblages of Sectors	Last 25% of trajectory of small crystals and 50% of large crystals coincided with seeded area.	Ejection flares seeded just above trajectory.	Slight chance	1316 - 1442
Unrimed Plates	Last 30% of trajectory of small crystals and 100% of large crystals coincided with seeded area.	Ejection flares seeded diffusional growth region of medium to large crystals and 800 to 1,600 ft. into the riming region.	Excellent chance	1318 - 1450

TABLE 5.4

COMPARISON OF CRYSTAL TRAJECTORIES REACHING KEECHELUS DAM WITH SEEDED VOLUME

Crystal Type	Comparison of Trajectory with Seeded Volume		Qualitative Assessment of Seeding Effect	Time (PST) Seeding Effect Expected on Ground
	Horizontal	Vertical		
Unrimed Dendrites	Last 25% of trajectory of small crystals and 50% of large crystals coincided with seeded area.	Ejection flares seeded diffusional growth region of all crystals and 800 to 3,000 ft. into the riming region.	Excellent chance	1326 - 1509
Unrimed Stellars	Last 25% of trajectory of small crystals and 50% of large crystals coincided with seeded area.	Ejection flares seeded diffusional growth region of all crystals and 800 to 3,000 ft. into the riming region.	Excellent chance	1326 - 1509
Unrimed Assemblages of Sectors	Last 25% of trajectory of small crystals and 50% of large crystals coincided with seeded area.	Colspan flares seeded diffusional growth region of large crystals Ejection flares seeded diffusional growth region of medium sized crystals and from 3,450 to 5,600 ft. into riming region.	Excellent chance	1326 - 1453

TABLE 5.4 (Cont.)

Crystal Type	Comparison of Trajectory with Seeded Volume		Qualitative Assessment of Seeding Effect	Time (PST) Seeding Effect Expected on Ground
	Horizontal	Vertical		
Unrimed Sideplanes	Last 25% of trajectory of small crystals and 50% of large crystals coincided with seeded area.	Colspan flares seeded diffusional growth region of large crystals. Ejection flares seeded diffusional growth region of medium sized crystals and from 2,400 to 4,500 ft. into riming region.	Excellent chance	1326 - 1453
Unrimed Sectors	Last 25% of trajectory of small crystals and 50% of large crystals coincided with seeded area.	Ejection flares seeded in the diffusional growth region of the medium to large crystals and 1,000 ft. into riming region.	Excellent chance	1326 - 1453
Unrimed Bullets	Last 50% of trajectory of small crystals and last 50% of large crystals coincided with seeded area.	Colspan flares seeded diffusional growth region of large crystals. Ejection flares seeded 5,000 ft. into riming region.	Excellent chance	1313 - 1453

TABLE 5.4 (Cont.)

Crystal Type	Comparison of Trajectory with Seeded Volume		Qualitative Assessment of Seeding Effect	Time (PST) Seeding Effect Expected on Ground
	Horizontal	Vertical		
Unrimed Aggregates	Last 50% of trajectory of small crystals and last 40% of large crystals coincided with seeded area.	Ejection flares seeded diffusional growth region and 2,200 ft. into riming region.	Excellent chance	1313 - 1453
Unrimed Plates	Last 25% of trajectory of small crystals and last 40% of large crystals coincided with seeded area.	Ejection flares seeded diffusional growth region of all crystals and 800 to 3,000 ft. into the riming region.	Excellent chance	1326 - 1509

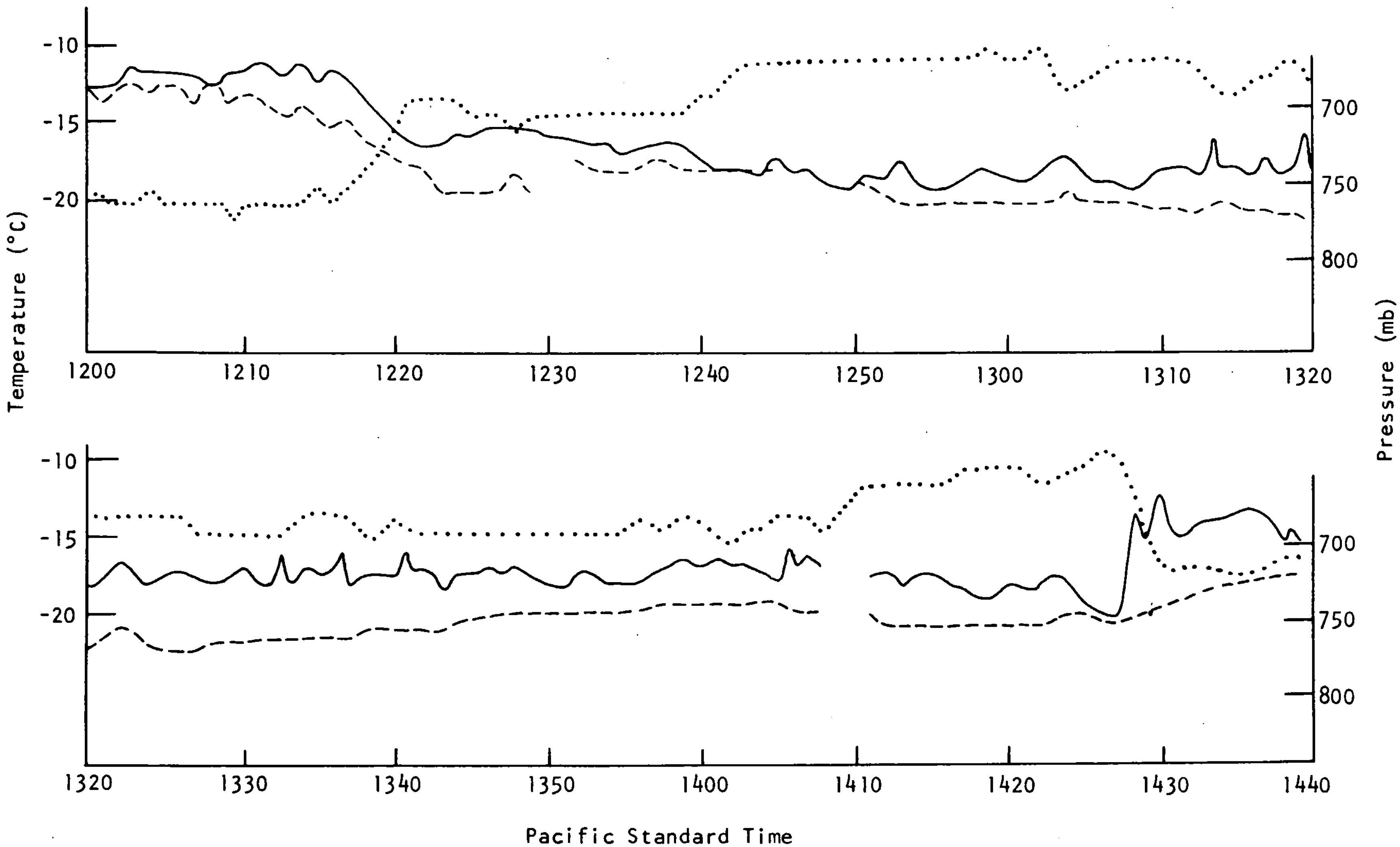

Fig. 5.16 One minute averages of temperature (in °C), dew point temperature (in °C), and pressure (in mb) from airborne sensors on January 31, 1972.
——— Temperature. ---- Dew point temperature. ····· Pressure.

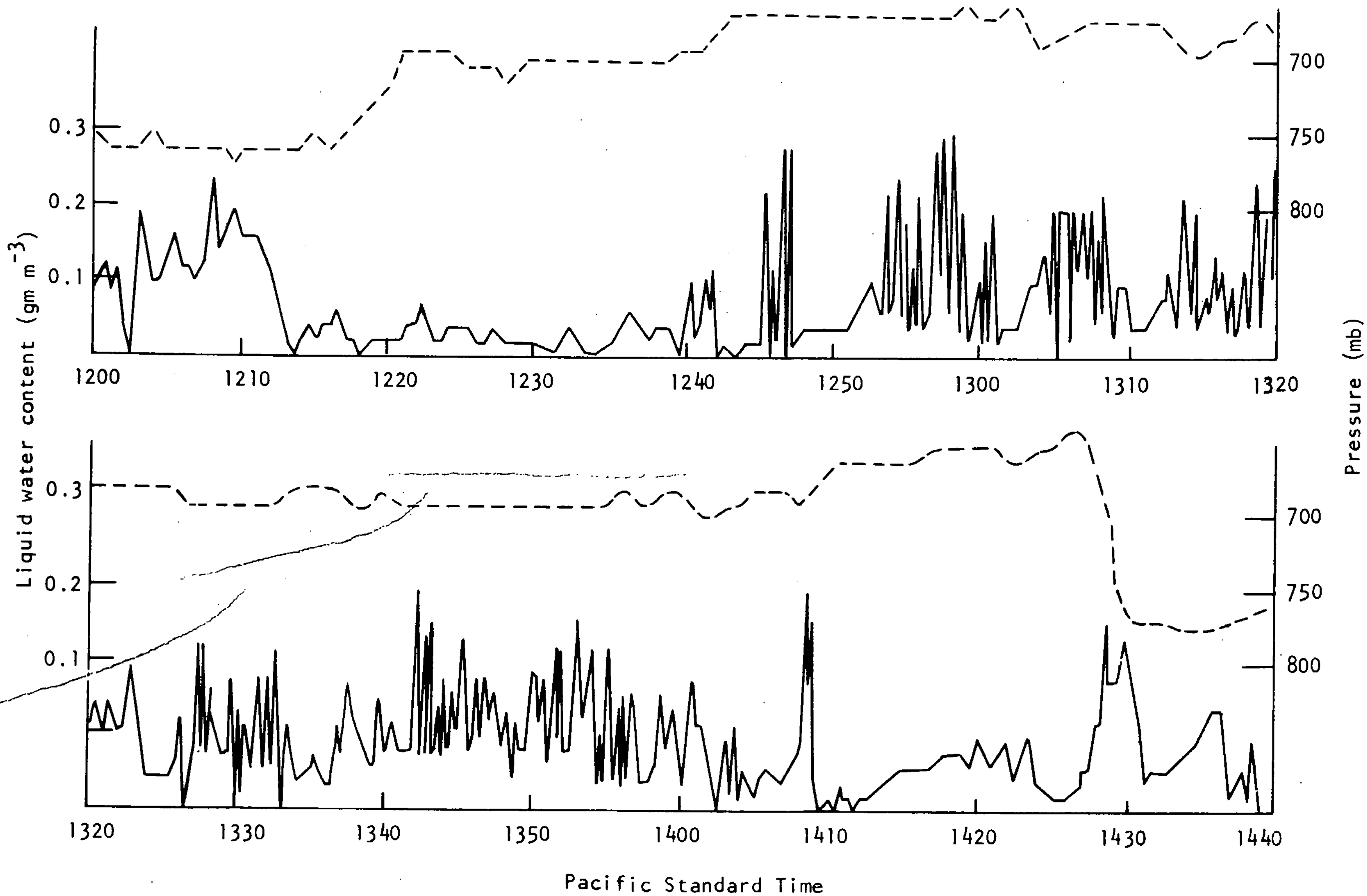

Fig. 5.17 Fifteen second averages of liquid water content (——) and one minute averages of pressure (----) from airborne sensors on January 31, 1972.

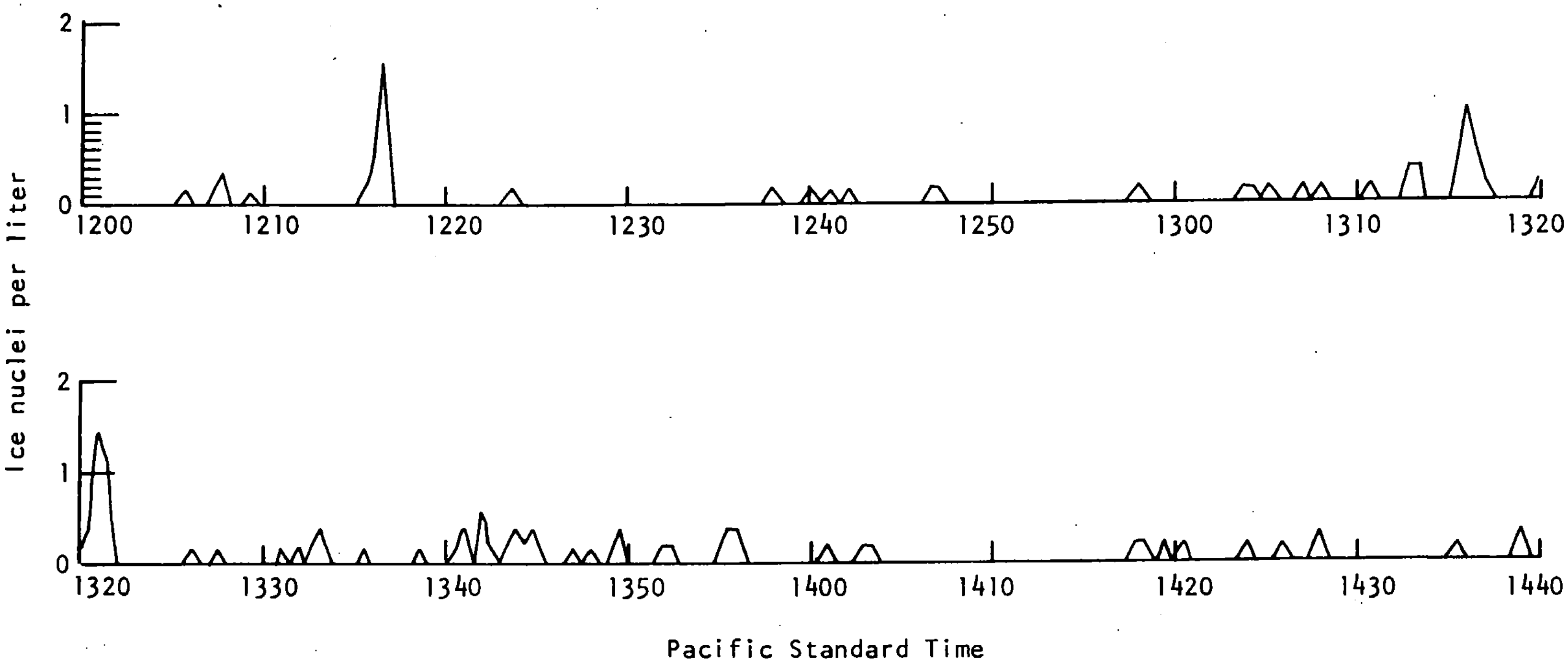

Fig. 5.18 Thirty second averages of ice nuclei concentrations measured by the Mee Industries Counter on January 31, 1972.

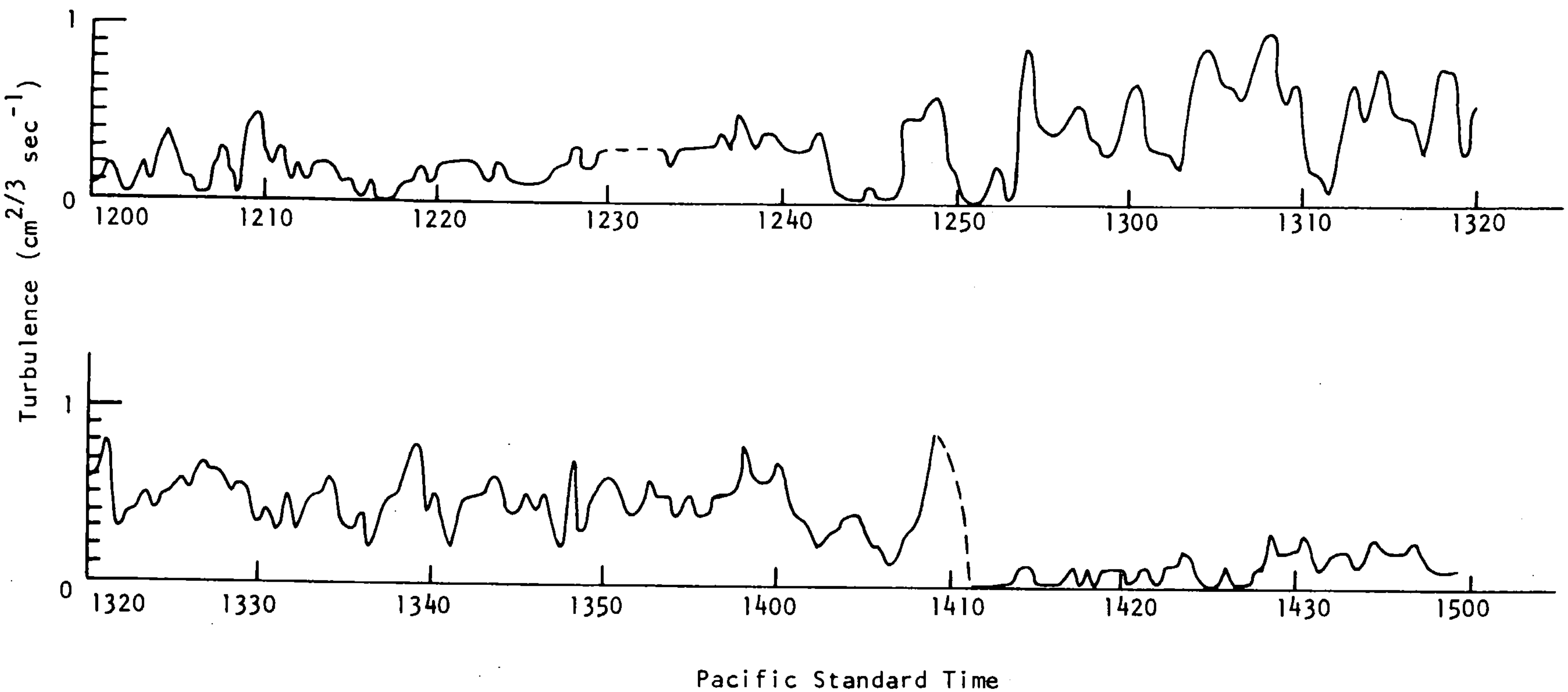

Fig. 5.19 Thirty second average measurements of air turbulence on January 31, 1972.

TABLE 5.5

SUMMARY OF CLOUD PARTICLES COLLECTED WITH CONTINUOUS

PARTICLE SAMPLER ON JANUARY 31, 1972

(See Figs. 5.6, 5.7 and 5.8 for Run Position)

Run No.	Water Drops		Ice Particles		Number Ratio of Water to Ice
	Diameter (μm)	Concentration (cm^{-3})	Type & Maximum Dimension (μm)	Concentration (cm^{-3})	
1	10-35	< 1	Isolated, irregular plates. 30-100 μm.	< 1 Tops of lower cloud layer.	Unknown
2	15-30 Occasionally 100.	111-193	Irregular plates. Isolated riming. 50-100 μm.	< 0.1 Ran clear during run.	10^4
3	10-20	18-74 (In drop areas)	Aggregates, plate-like crystals with some hexagonal plates with ribs. Riming toward end. 80-400 μm.	Average 0.1	50:1 in drop areas. All ice elsewhere.
4	10-15	54-133 Last part of run only.	Mainly plate-like. Some dendrite parts. Large sectored crystals. Some hexagonal plates and aggregates. Occasional riming. To 1,000 μm.	0.9 - 4.5	All ice first 90% of run. 30:1 in last part.
5	10-20	15-26 First part of run only.	Large sectored crystals. Portions of stellars. Plates and aggregates of plates. Occasional riming. To 1,300 μm.	0.8 - 2.4	30:1 to 1:5
6	——	——	Small aggregates. Plate-like to irregular crystals. Some frozen drops. Moderate riming. Mainly 50-150 μm. To 400 μm.	0.2 - 3.1	All ice.
7	——	——	Few larger shattered crystals. Frozen drops. Irregular and plate-like crystals. 20-150 μm to 400 μm.	0.2 - 3.2	All ice.

TABLE 5.5 (Cont.)

Run No.	Water Drops		Ice Particles		Number Ratio of Water to Ice
	Diameter (μm)	Concentration (cm^{-3})	Type & Maximum Dimension (μm)	Concentration (cm^{-3})	
8	———	———	Irregular crystals, some plate-like. Small aggregates. Some riming. 50-400 μm.	0.1 - 2.2 (Data last part only)	All ice.
9	———	———	Irregular crystals, few hexagonal plates. Moderate riming. 50-400 μm.	< 0.1	All ice.
10	10-20	22-52 Lower concentration last 50% of run.	Small, irregular crystals. Few small aggregates. Some riming. 50-200 μm.	0.1 - 1.5	30:1
11	10-30	13-43	Occasional, irregular rimed crystals. 50-150 μm.	<0.1 - 0.4	100:1
12	15-40	8.3-16.5	———	———	Unknown
13	10-35	19-38 Clear last 60% part of run.	———	———	All drops.
14	15-40	23-47	Isolated, small irregular crystals. 100 μm.	< 0.1	>500:1
15	10-40	22-52	Irregular crystals. 60-150 μm.	< 0.1	>500:1
16	10-30	7.7-69	Low density ice. Bullets and columnar at first becoming irregular very small aggregates. 50-400 μm.	<0.1 - 0.1	50:1
17	15-35	0.1-4.1	Isolated irregular crystals. 50-150 μm	< 0.1	5:1
18	10-35	13-56 Average 43	Isolated irregular crystals. 50-400 μm Mainly 150 μm.	<0.1 - 0.4	>500:1
19	10-25	22-67 Last part of run only.	Short columns. Thick hexagonal plates. Irregular crystals. 60-150 μm	<0.1 - 2.2	First 2/3 all ice. Then 100:1.
20	10-25	45 Patchy with many clear areas	Short columns (60-100 μm). Thick hexagonal plates. Irregular crystals. 40-150 μm.	Unknown	Variable (See Fig. 5.22)

TABLE 5.5 (Cont.)

Run No.	Water Drops		Ice Particles		Number Ratio of Water to Ice
	Diameter (μm)	Concentration (cm^{-3})	Type & Maximum Dimension (μm)	Concentration (cm^{-3})	
21	———	———	Columnar and thick plates. Numerous irregular crystals 50-200 μm.	0.8 - 3.0	All ice.
22	40-60	0.1 Isolated (possibly spurious)	Low density, irregular crystals. Some thick plates to 250 μm. Some columnar. Shattered large ice. 50-400 μm	<0.1 - 1.2	1:20
23	50-70	0.1 In first 50% (Possibly spurious)	Low density irregular crystals. Few thick hexagonal plates. Some shattered ice. 50-300 μm.	<0.1 - 0.9	1:30
24	———	———	Plate-like crystals and hexagonal crystals to 250 μm. Larger crystals toward end of run with bullets and irregular crystals. 50-500 μm.	0.2 - 1.2	All ice.
25	———	———	Shattered large crystals. Hexagonal plates and irregular plate-like crystals. 50-400 μm.	0.4 - 1.5	All ice.
26	5-25	13-54 Patchy. Mainly clear.	Isolated plate-like crystals. Shattered large crystals. 50-400 μm.	< 0.1	500:1
27†	———	Isolated drops.	Isolated small, irregular crystals.	———	———

†Instrument may have iced up during descent.

TABLE 5.6

VISUAL OBSERVATIONS FROM THE AIRCRAFT OF OPTICAL PHENOMENA

ON JANUARY 31, 1972

Time (PST)	Optical Phenomena Observed	Predominant Cloud Composition Required To Produce Optical Phenomenon
1215	Corona (faint)	Water
1223	Sub-sun (pale)	Ice
1228	Sub-sun (Alternating vivid to pale)	Ice
1237	Corona (weak)	Water
	Glory	Water
1257	Glory	Water
	Cloud bow	Water
1312	Sub-sun	Ice
	Parhelia	Ice
	Antisolar point arc	Ice
1314	Glory (No ice optics visible)	Water
1316	22° halo	Ice
	Parhelia	Ice
1317	Parhelia (removed from halo)	Ice
1319	Sub-sun	Ice
	22° halo	Ice
1320	Sub-sun (intensity increasing)	Ice
1323	Glory	Water
1325	22° halo	Ice
	Glory (weak)	Water
1326	Sub-sun	Ice
1327	Glory	Water
	Corona	Water
	22° halo	Ice
	Sub-sun	Ice
	Sub-sun parhelia	Ice
1328	22° halo	Ice
	Parhelia	Ice
	Sub-sun	Ice
	Sub-sun parhelia	Ice
	Corona (in cloud tops)	Water

TABLE 5.6 (Cont.)

Time (PST)	Optical Phenomena Observed	Predominant Cloud Composition Required To Produce Optical Phenomenon
1331	Sub-sun	Ice
	46° halo	Ice
1332	Glory	Water
	Cloud bow	Water
1333	Sub-sun	Ice
	Sub-sun parhelia	Ice
1335	22° halo	Ice
	Sun pillar	Ice
	Sub-sun	Ice
	Sub-sun parhelia	Ice
1337	Sub-sun parhelia (diffuse)	Ice
1341	Corona	Water
	Glory	Water
1353	Glory	Water
1356	Lower tangent arc	Ice
	Sub-sun	Ice
	Glory	Water
1406	22° halo	Ice
	Water drop optics (not defined)	Water
1410	22° halo	Ice
	46° halo	Ice
	Lower tangent arc	Ice
	Sub-sun	Ice
	Sub-sun parhelia	Ice
1414	Antisolar point arc	Ice
	Water drop optics (not defined)	Water
1415	Sub-sun (brilliant)	Ice
	Sub-sun parhelia	Ice
	Antisolar point arc	Ice
1418	Parhelia circle	Ice
	120° parhelia	Ice
	22° halo	Ice
	Sub-sun	Ice
	Sub-sun parhelia	Ice
	Antisolar point arc	Ice
	Circle of parhelia	Ice

TABLE 5.6 (Cont.)

Time (PST)	Optical Phenomena Observed	Predominant Cloud Composition Required To Produce Optical Phenomenon
1421	Sub-sun	Ice
	Sub-sun parhelia	Ice
1423	Sub-sun (bright)	Ice
	Sub-sun parhelia	Ice
	Lower tangent arc	Ice
	22° halo (lower portion)	Ice
1438	22° halo	Ice
1446	Sub-sun (weak)	Ice
	Corona	Water
1449	Parhelia	Ice
	Circumzenithal arc	Ice

5.1.4.1 Temperature and Dew Point

The temperature and dew point profiles are shown in Fig. 5.16. Sharp fluctuations occurred while the aircraft was in the seeded zone. Departures of the order of 2°C in 30 seconds were measured at 1313 and 1319 hours and several departures of 2°C in one minute occurred at other times. Departures of this order are indicative of mesoscale warm and cold areas, such as those associated with cumulus activity.

5.1.4.2 Liquid Water

Measurements of liquid water content are shown in Fig. 5.17. Consistent values of greater than 0.1 gm m^{-3} were measured in the lower cloud deck from first penetration of the cloud deck near Maple Valley, Washington, at 1152 until near Cle Elum, Washington, at 1212 (see Figs. 5.6 and 5.8). Much lower liquid water values were observed until the upper cloud deck was entered at 1245. Measurements taken during the course of the seeding operation, 1254 through 1405, exhibited considerable fluctuations ranging from 0 to 0.30 gm^{-3}. After the seeding operation ceased, the aircraft climbed to the top of the upper cloud deck where the liquid water content remained low but did not exhibit the rapid fluctuations noted during the seeding operation. The rapid fluctuations in liquid water content noted during the seeding operation are indicative of glaciated versus non-glaciated regions within the cloud deck. The time period for two successive low readings is of the order of 30 seconds. For a true air speed of 130 knots, these glaciated regions would be of the order of 1 nautical mile wide.

5.1.4.3 Ice Nucleus Concentrations

Ice nucleus concentrations measured from the aircraft with the Mee Industries Ice Nucleus Counter are shown in Fig. 5.18. The absolute values of concentrations appear several orders of magnitude less than anticipated based on the estimations made in §5.1.2.2. This discrepancy could be a result of two factors. First, the ice nucleus concentration estimates were based on several rather restrictive simplifying assumptions all of which would tend to produce higher values than expected. Secondly, the Mee Counter might not detect all the silver iodide particles in the air. However, a definite increase in frequency of measured concentrations of ice nuclei are apparent from 1303 until 1405 hours. The fact that an increase in concentration was not observed until 1303, while seeding started at 1245, can be explained by the time required for the aircraft to repenetrate the area seeded during the initial seeding run.

5.1.4.4 Turbulence

Measurements of air turbulence (as represented by $\varepsilon^{1/3}$) are shown in Fig. 5.19. The maximum observed value for the turbulent dissipation rate observed was 1 $cm^2\ sec^{-3}$, a value normally associated with light to negligible turbulent conditions. However, the frequency and intensity of turbulence observed during the seeding operation (1254 through 1405 hours) are greater than during the non-seeded period. Turbulent conditions of this nature may be attributed to convective activity in the lower cloud layer. Although the static stability of the atmosphere decreased naturally during the day (see §5.1.1) it will be shown later that artificial seeding probably enhanced the instability.

5.1.4.5 Cloud Particles and Visual Observations

Analysis of the data collected with the continuous particle sampler is presented in Table 5.5. The aircraft position during individual runs is shown in Figs. 5.6, 5.7 and 5.8. Runs 1 and 2, which were in the lower clouds west of the mountains, produced the largest cloud drops (100 μm) and the heaviest concentrations of cloud drops. Some riming of the ice crystals was noted. Runs 3 through 7 were in the extensive cloud deck over the mountains. Cloud drop concentrations decreased markedly from the western (Fig. 5.20a) to the eastern side of the divide. Conversely, ice crystal concentrations increased over the mountains. Similar results were reported by Hobbs et al. (1971). The ice crystal types replicated were basically plate-like as opposed to columnar. The largest crystals observed during flight were replicated on runs 4 and 5. They were sectored and plate-like crystals reaching a length of 1300 μm. In addition, some larger but shattered crystals were observed. Hobbs et al. (1971) reported the length of similar crystals ranged from 400 to 3000 μm. Some frozen drops were also observed on runs 6 and 7.

Visual observations from the aircraft of optical phenomena produced by water droplets or ice crystals are listed in Table 5.6 and examples are shown in Fig. 5.21. These observations give a qualitative assessment of the composition of the cloud in which various phenomena are observed. However, since the cloud in which a particular optical phenomenon was observed was at some unknown distance from the aircraft, exact correlation of these data with sensor data obtained by the aircraft is difficult. It can be seen from Table 5.6 that a corona was observed at 1215 hours, indicating that a cloud containing water droplets with diameters from 14 to 20 μm was situated to the right and above the aircraft.

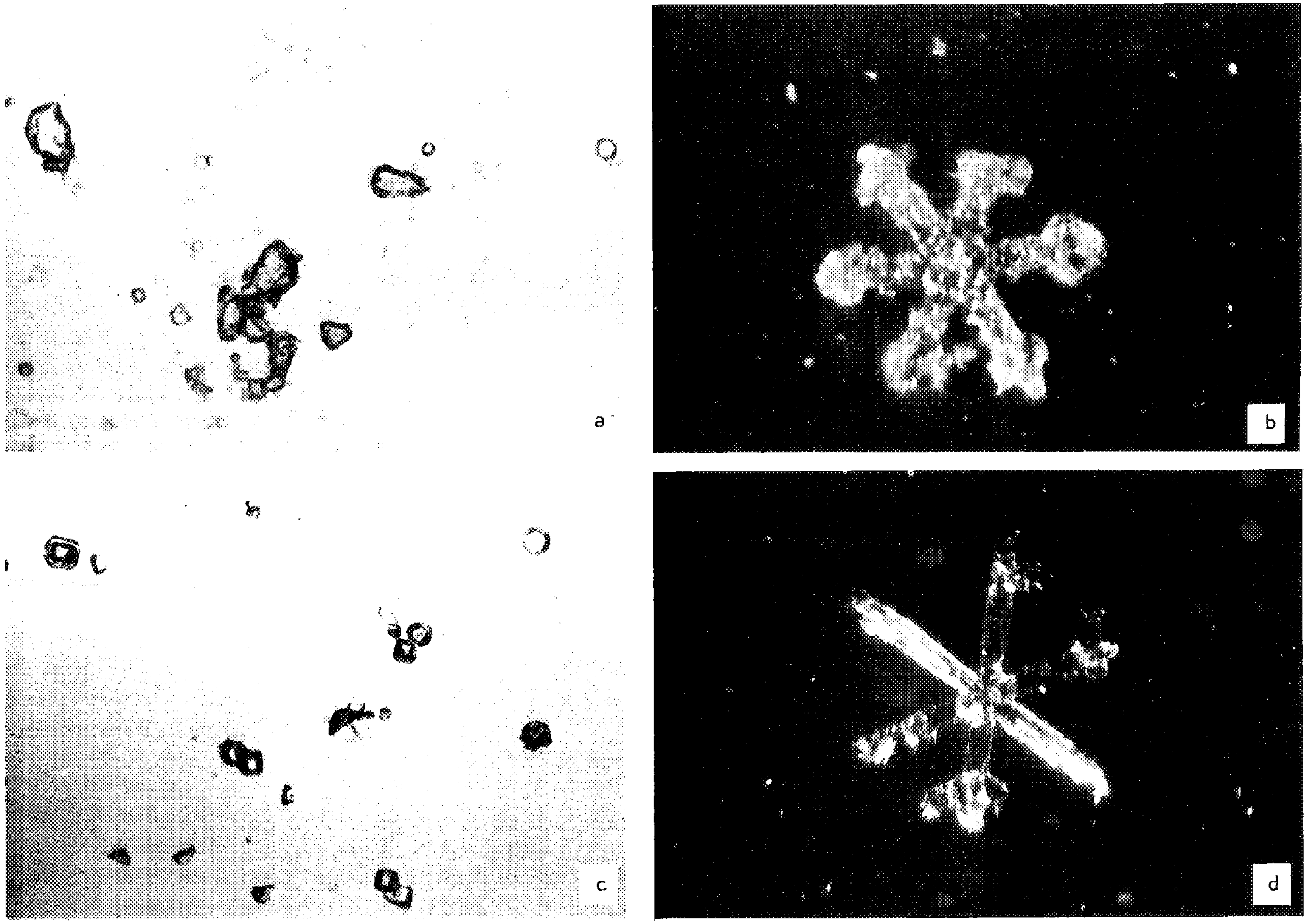

Fig. 5.20 Crystals collected from the aircraft and at ground level on January 31, 1972. Magnification x50. (a) Small supercooled cloud droplets collected from aircraft flying over western slopes of Cascades prior to seeding (CPS Run 4). (b) Rimed stellar crystals collected on ground at Hyak prior to seeding. (c) Unrimed ice crystals collected from aircraft over western slopes of Cascades after seeding (CPS Run 20). (d) Unrimed stellar crystals collected on ground at Hyak following seeding.

Fig. 5.21 (facing page) Optical effects photographed from aircraft on January 31, 1972. (a) Cloud bow, supernumerary bows and glory over western slopes of Cascades prior to seeding. Following seeding optical effects due to ice were observed: Sub-sun, pillar and sub-parhelia (b); 22° halo, sun dogs and circumhorizontal arcs (c); and the paranthelic circle (d).

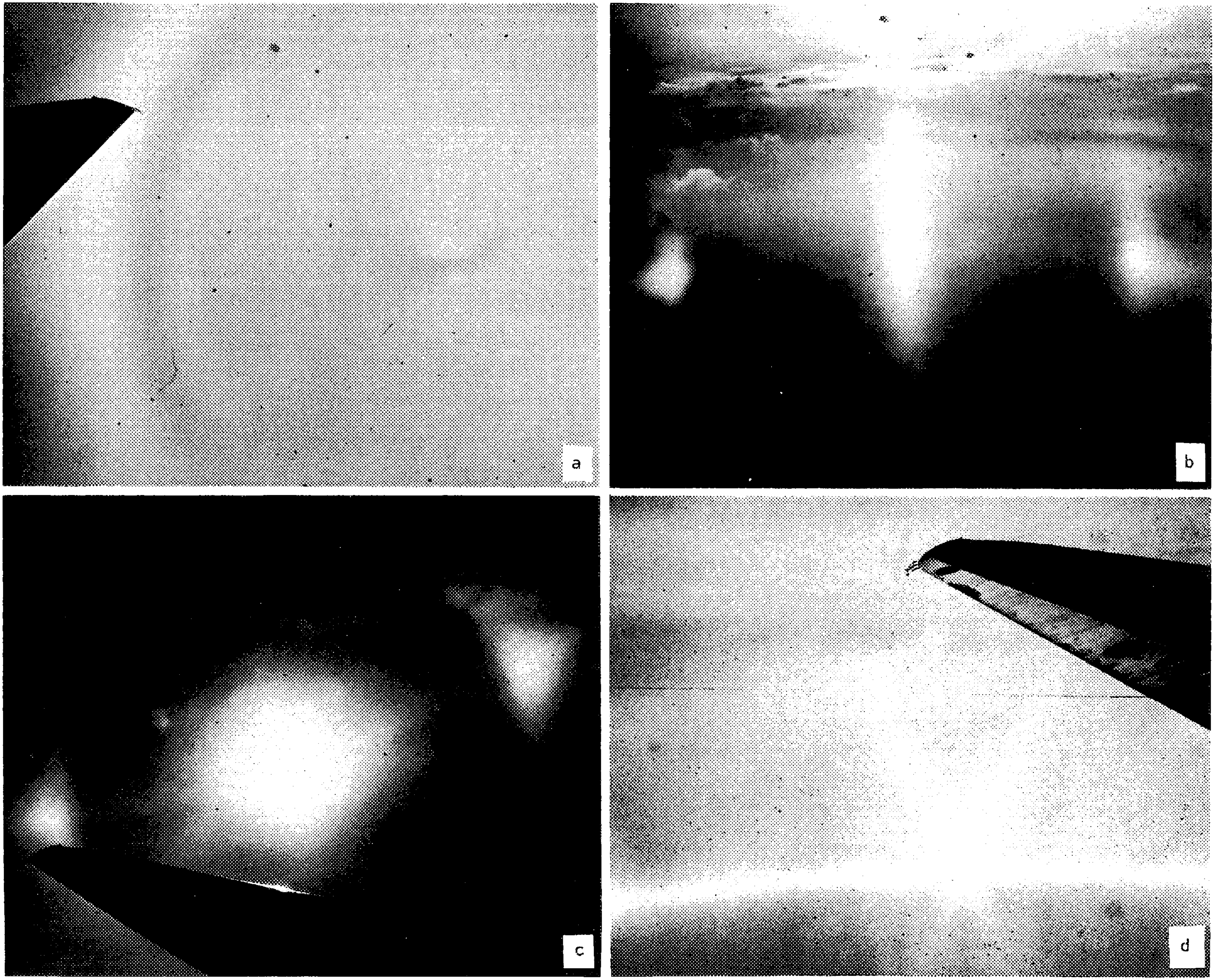
a
b
c
d

Runs 8 through 12 on the continuous particle sampler were taken at a higher altitude in or near the upper cloud deck. The cloud was composed of both ice crystals and water droplets, with the ice predominant east of the divide and water to the west. Both ice crystal and water droplet concentrations were less than those observed in the lower cloud deck. Dendritic and stellar-like crystals were not observed at temperatures below -15°C. Riming was observed on all runs in this region. Optical phenomena also indicated predominantly ice clouds to the east and water clouds to the west of the divide. Cloud bows, supernumeraries and glories (Fig. 5.21a) were observed about 10 minutes prior to the start of seeding and in the area where seeding was subsequently carried out. These optical phenomena indicate the presence of cloud droplets less than 100 μm in size (Tricker, 1970).

Runs 13 through 21 of the continuous particle sampler were taken during the seeding operation. In general, cloud in the seeding area was composed primarily of water droplets when seeding began as indicated on runs 12 and 13. A glory and a cloud bow were observed. No ice optics were observed until 1312, some 18 minutes after seeding commenced, which allows sufficient time for the effect of AgI nucleation to be dispersed along a line approximately 4.5 nautical miles downstream. Brilliant optical effects due to ice crystals then began to appear. These included sub-suns, pillars and sub-parhelia (Fig. 5.21b), 22° haloes, sun dogs and circumhorizontal arcs,(Fig. 5.21c). Low concentrations of small irregular ice crystals were observed in runs 14 and 15. Rather high concentrations of water droplets were measured on runs 15 and 16 and a glory was observed on run 16. These crystals have a crystal habit threshold temperature near -18°C (Hobbs et al., 1971). From Fig. 5.16 it can be seen that the observed temperature in the seeding area was -18°C at 1313 hours. Since these crystals were not observed in this region prior to seeding, it is presumed that their appearance is a direct effect of seeding. Towards the end of seeding the cloud particles collected were mainly small, unrimed ice crystals (Fig. 5.20c). Fig. 5.22 shows the rapid transitions between glaciated (seeded) and droplet (unseeded) clouds observed with the continuous particle sampler on run 20.

Continuous particle sampler runs 22 through 25 were made in the vicinity of Cle Elum Lake as the aircraft descended through the glaciated cloud. Concentrations of water droplets were near zero, whereas, ice crystal concentrations were consistently high with a maximum of 1.5 cm^{-3}. Thick plates, columns, and bullets were noted as well as common irregular crystals. No riming or aggregation of the crystals were observed. Some

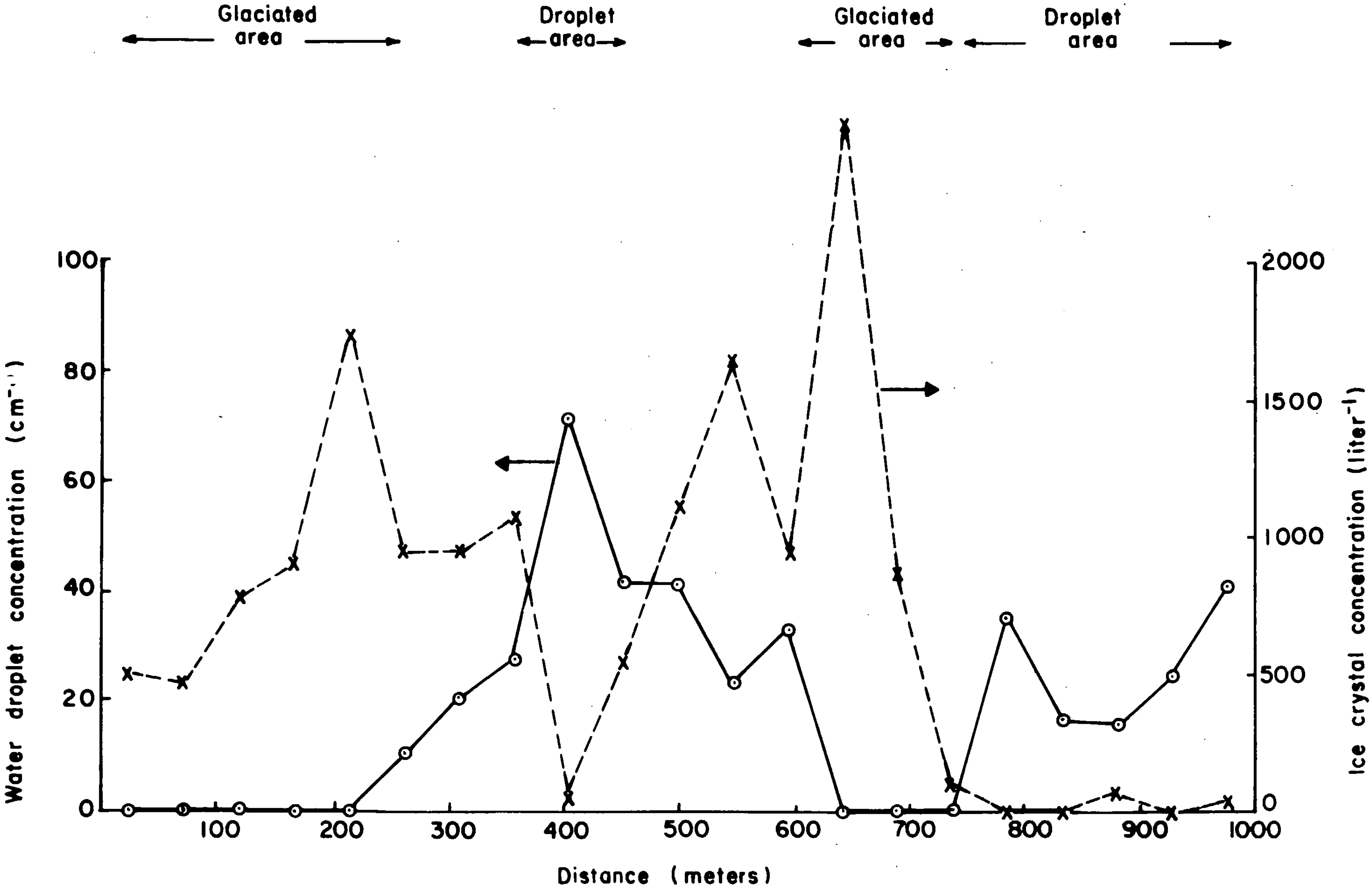

Fig. 5.22 Concentrations of water drops (——) and ice crystals (----) measured from the aircraft as it flew in (glaciated area) and out (droplet area) of a region of cloud seeded five minutes previously with silver iodide on January 31, 1972. CPS run number 20. Air temperature -21.3°C. Flight altitude 10,600 feet.

shattered large ice crystals were noted. In this area the unusual paranthelic circle was observed (Fig. 5.21d).

Continuous particle sampler run 26 was made just south of the seeded area. Water drop concentrations increased and low concentrations of large shattered crystals were noted.

5.1.5 Ground Observations

Ground observations were made as discussed in §1.3. Sky conditions were generally overcast at Hyak, Alpental and Keechelus Dam with cloud bases estimated from 3,000 to 5,000 ft. above ground level. Very light to light snow fell at all three stations during the day. Some breaks in the overcast occurred at Hyak from 1330 until 1600 and at Keechelus Dam from 1400 until 1600. Breaks in the overcast at Alpental did not occur until 1530 hours.

5.1.5.1 Snow Crystal Analysis and Precipitation Rates

A summary of the types of snow crystals collected at the three ground stations are shown in Figs. 5.23 and 5.24. In addition, data on snowfall rates from the bulk analysis of the snow bags and from the optical snow rate sensor are included. As discussed in §5.1.3, the effects of artificial seeding would have been most likely observed at the Keechelus Dam and Hyak stations. Seeding effects at Alpental should have been slight if present at all. From Tables 5.2, 5.3 and 5.4 the periods of times that seeding effects might have been expected to have appeared at the ground stations are: Alpental (1300-1435), Hyak (1310-1450), and Keechelus Dam (1315-1510).

Snow crystal types observed at Alpental prior to 1300 consisted primarily of unrimed to moderately rimed dendrites, plates, stellars, and aggregates of these crystals. From 1300 until 1530 similar crystals, but light to densely rimed, were observed. After 1530 only unrimed dendritic crystals were observed. A precipitation rate from the snow bags of approximately 0.01 inches of water per hour was measured until near 1500 when a sharp increase to 0.035 inches per hour was recorded. At 1515 the precipitation rate decreased considerably. Data from the optical snow rate sensor were not available until 1500 hours. This instrument recorded continuous precipitation from 1500 until 1800 hours with exception of the period from 1600 until 1630 hours.

Ice crystal types observed at Hyak prior to the period of expected seeding effects were moderate to lightly rimed dendrites, radiating assemblages of dendrites, stellars (Fig. 5.20b), graupel-like snow, and aggregates of these crystals. Riming of these crystals ceased completely after 1300 (Fig. 5.20d). Several other species of crystals were also observed including

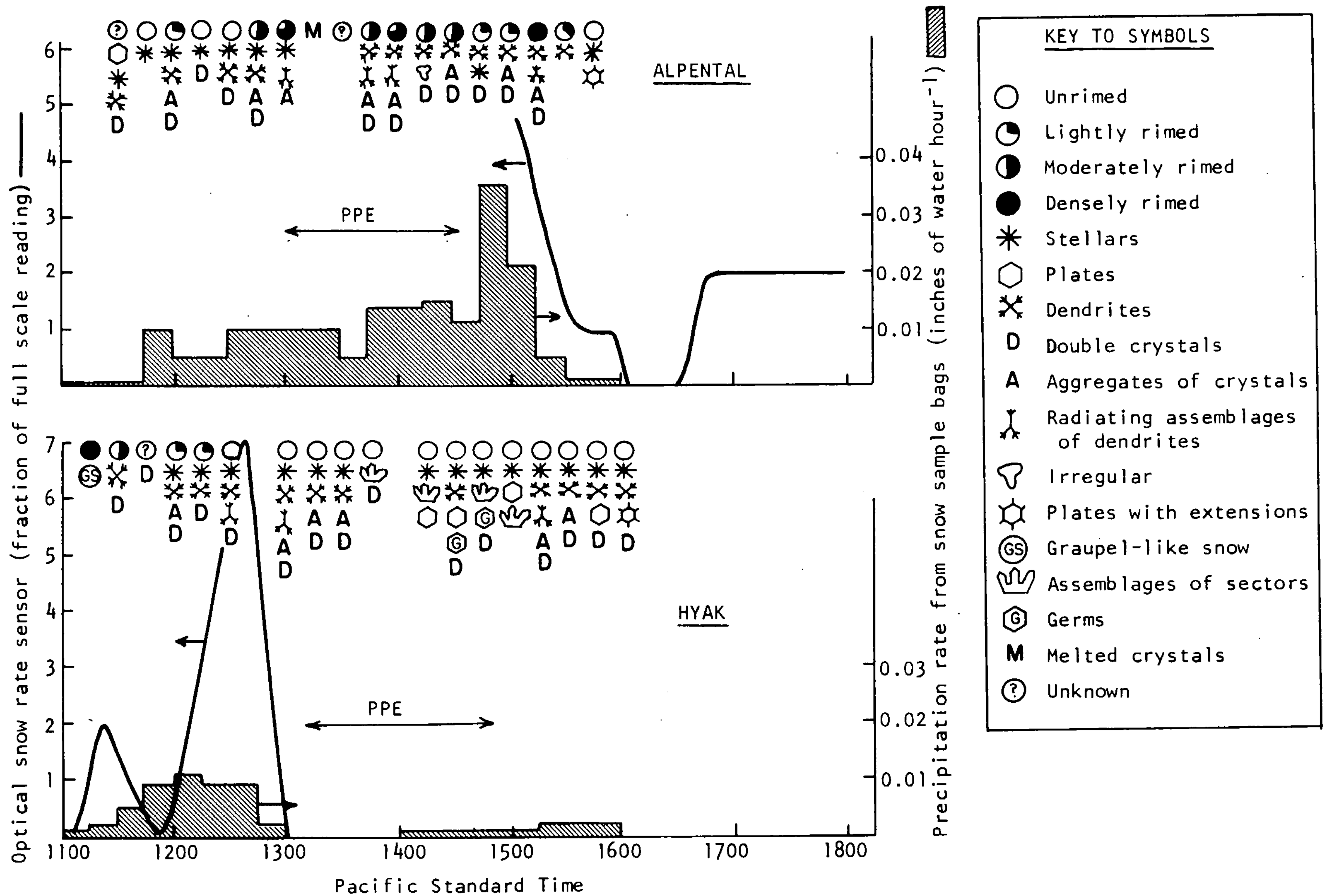

Fig. 5.23 Types of snow particles and precipitation rates at Alpental and Hyak on January 31, 1972. The predicted period of effect (PPE) of the artificial seeding at each ground station is noted.

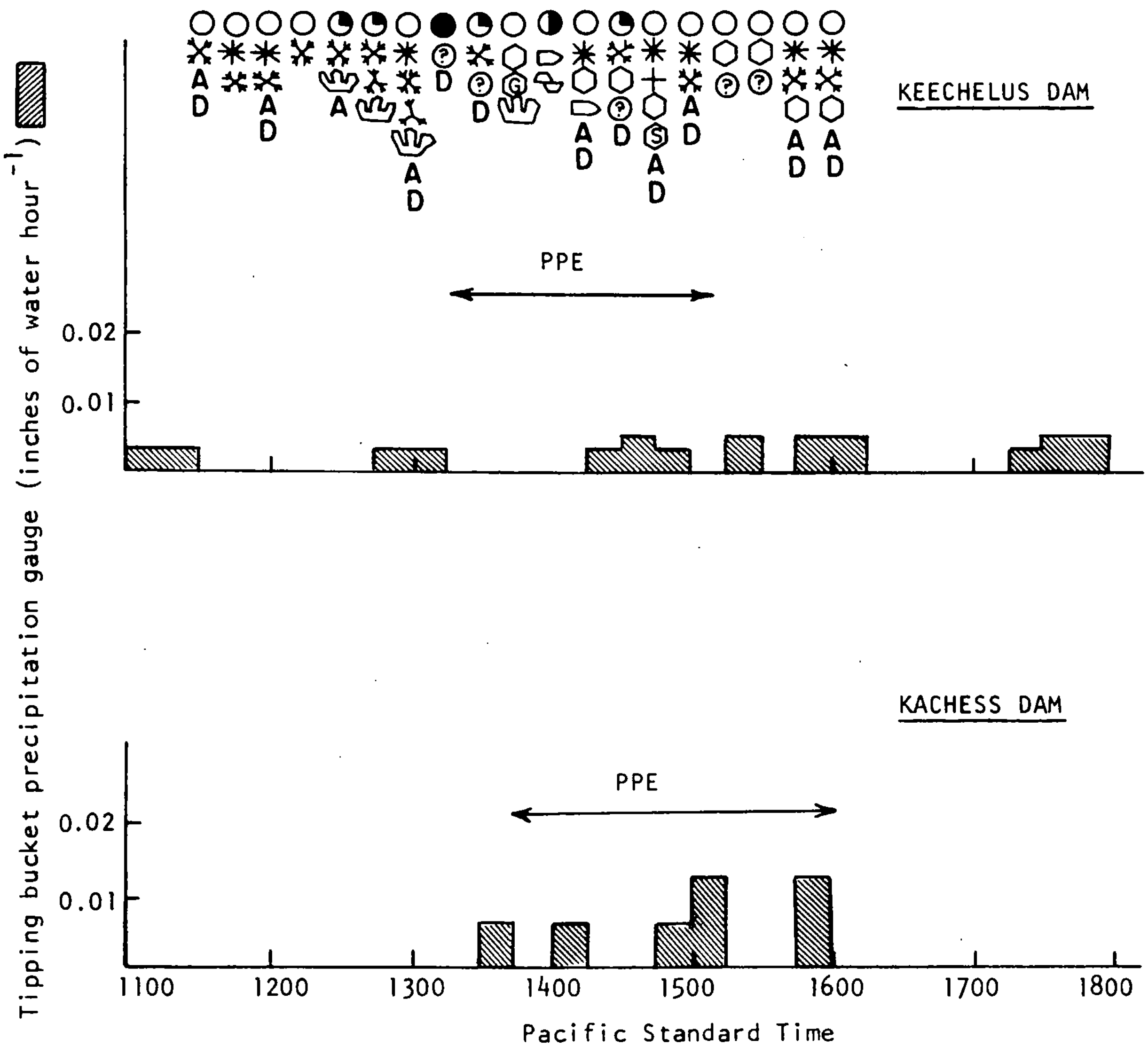

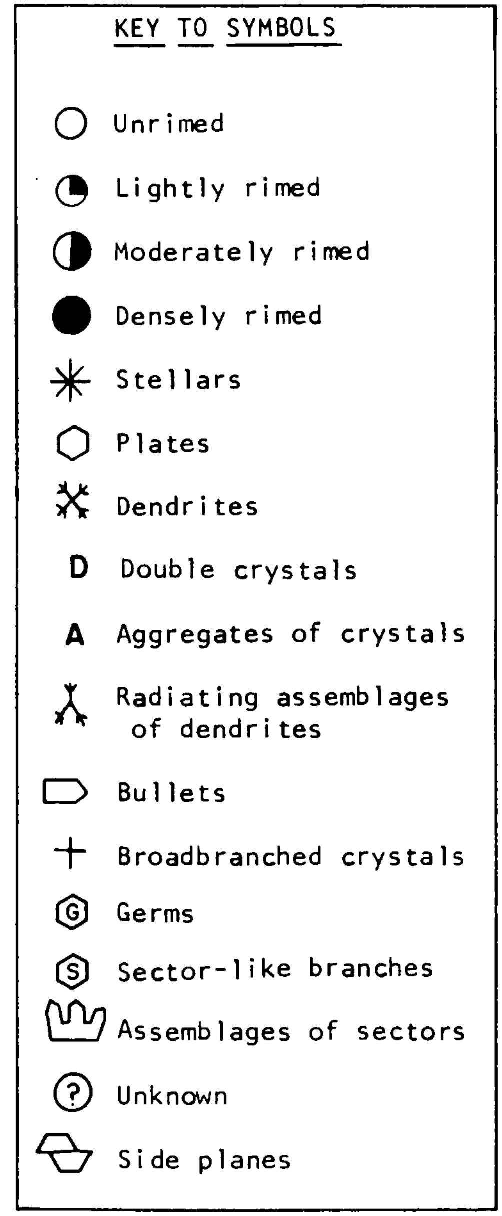

Fig. 5.24 Types of snow particles and precipitation rates at Keechelus Dam and Kachess Dam on January 31, 1972. The predicted period of effect (PPE) of the artificial seeding at each ground station is noted.

assemblages of sectors, radiating assemblages of dendrites, plates and very minute plates listed as "germs." The precipitation rate from the snow bags ran near 0.01 inches per hour until 1300 hours at which time the rate fell to near zero. A very low precipitation rate was noted from 1400 until the end of record at 1600 hours. The optical sensor also recorded a measurable precipitation rate until 1300 hours at which time the reading fell to zero for the remainder of the record.

Ice crystal types observed at Keechelus Dam prior to the period of expected seeding effects were unrimed to heavily rimed dendrites, radiating assemblages of dendrites, stellars, assemblages of sectors, and aggregates of these crystals. During the period of expected seeding effects, unrimed to occasionally moderately rimed dendrites, stellars, sector-like branches, broad-branched crystals, plates, sideplanes, bullets and some aggregates of these crystals were observed. Similar unrimed crystals were observed for the remainder of the observational period. Precipitation at Keechelus Dam was very light throughout the period.

A recording tipping bucket precipitation gauge was located at Kachess Dam approximately 7 nautical miles downwind from Keechelus Dam. Precipitation rate data from this instrument are shown in Fig. 5.24 with the Keechelus Dam data. Recordable precipitation fell from 1330 until 1600 hours.

Table 5.7 contains a summary of the changes in precipitation rates for the four stations categorized according to periods before, during, and after the seeding effects should have occurred. This summary clearly shows that the precipitation rate at Hyak and Keechelus Dam decreased to zero during the seeding effect period. The rate increased during the post-seeding effect period at Hyak and remained at zero at Keechelus Dam. The precipitation rate at Alpental and Kachess Dam increased during the seeding effect period and remained at a relatively high value in the post-seeding effect period.

Table 5.8 is a presentation of the definable transitions of crystals at Hyak and Keechelus Dam prior to seeding to different species of crystals during seeding. The transitions are from crystals that grow in an environment of relatively high saturation to those which grow at lower saturations. A similar transition was not noted for Alpental.

5.1.5.2 Freezing Nucleus Concentrations

Concentrations of freezing nuclei in the precipitation were obtained from snow samples taken at Hyak and Keechelus Dam. Analyses of these data are shown in Figs. 5.25 and 5.26.

TABLE 5.7

SUMMARY OF PRECIPITATION RATES CATEGORIZED BY PRE-SEEDING, DURING SEEDING, AND POST-SEEDING EFFECT TIMES

Station	Period Prior to Seeding		Period During Seeding Effect		Period After Seeding Effect	
	Snow Bag (inches $hour^{-1}$)	Optical Sensor (% of scale)	Snow Bag (inches $hour^{-1}$)	Optical Sensor (% of scale)	Snow Bag (inches $hour^{-1}$)	Optical Sensor (% of scale)
Hyak	0.01	2-7	0-Trace	0	Trace 0.005	0
Keechelus Dam	0.005	†	0	†	0	†
Kachess Dam	0‡	---	0.006 - 0.012‡	---	0 - 0.012‡	---
Alpental	0.01	§	0.01 - 0.035	§	Trace - 0.021	0-4

† Optical snow rate sensor inoperative

‡ Precipitation rate from tipping bucket precipitation gauge

§ Optical sensor malfunction until 1500 hours

TABLE 5.8

TRANSITION OF ICE CRYSTAL HABIT BASED ON THOSE WHICH GROW AT A RELATIVELY HIGH SATURATION AND AT A RELATIVELY LOW SATURATION

Station	Period Prior To Seeding (High Saturation Crystals)	Period During Seeding Effect (Low Saturation Crystals)	Period After Seeding Effect (High Saturation Crystals)
Hyak	Radiating Assemblages of Dendrites Dendrites and Stellars	Radiating Assemblages of Sectors Plates and Germs	Radiating Assemblages of Dendrites Plates with Extensions Aggregates
Keechelus Dam	Dendrites and Stellars Radiating Assemblages of Dendrites Radiating Assemblages of Sectors	Plates and Sectors Broad-branched Crystals Plates and Sideplanes Bullets	(Low Saturation Crystals)

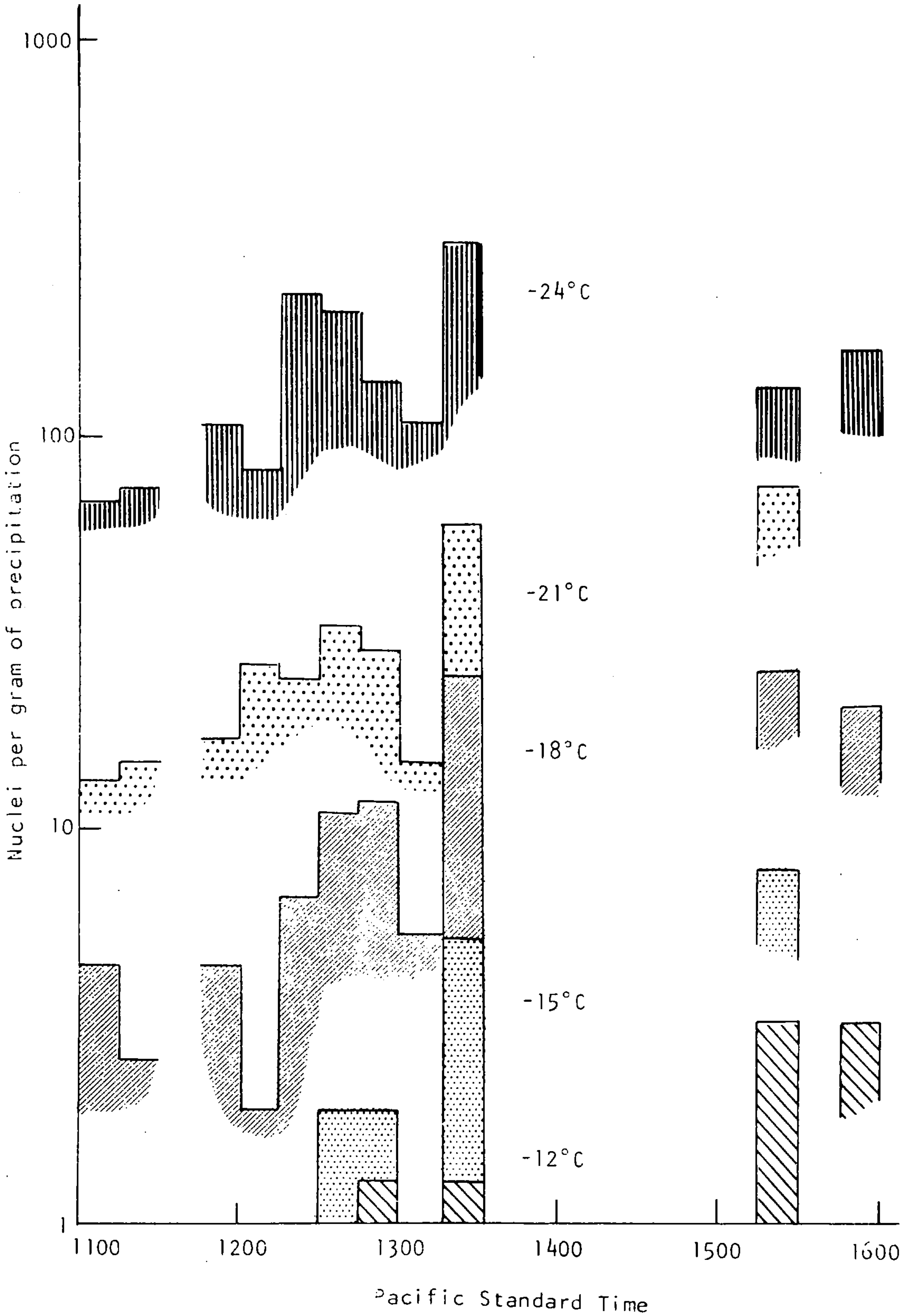

Fig. 5.25 Concentrations of freezing nuclei active at five temperatures in snow samples collected at Hyak on January 31, 1972.

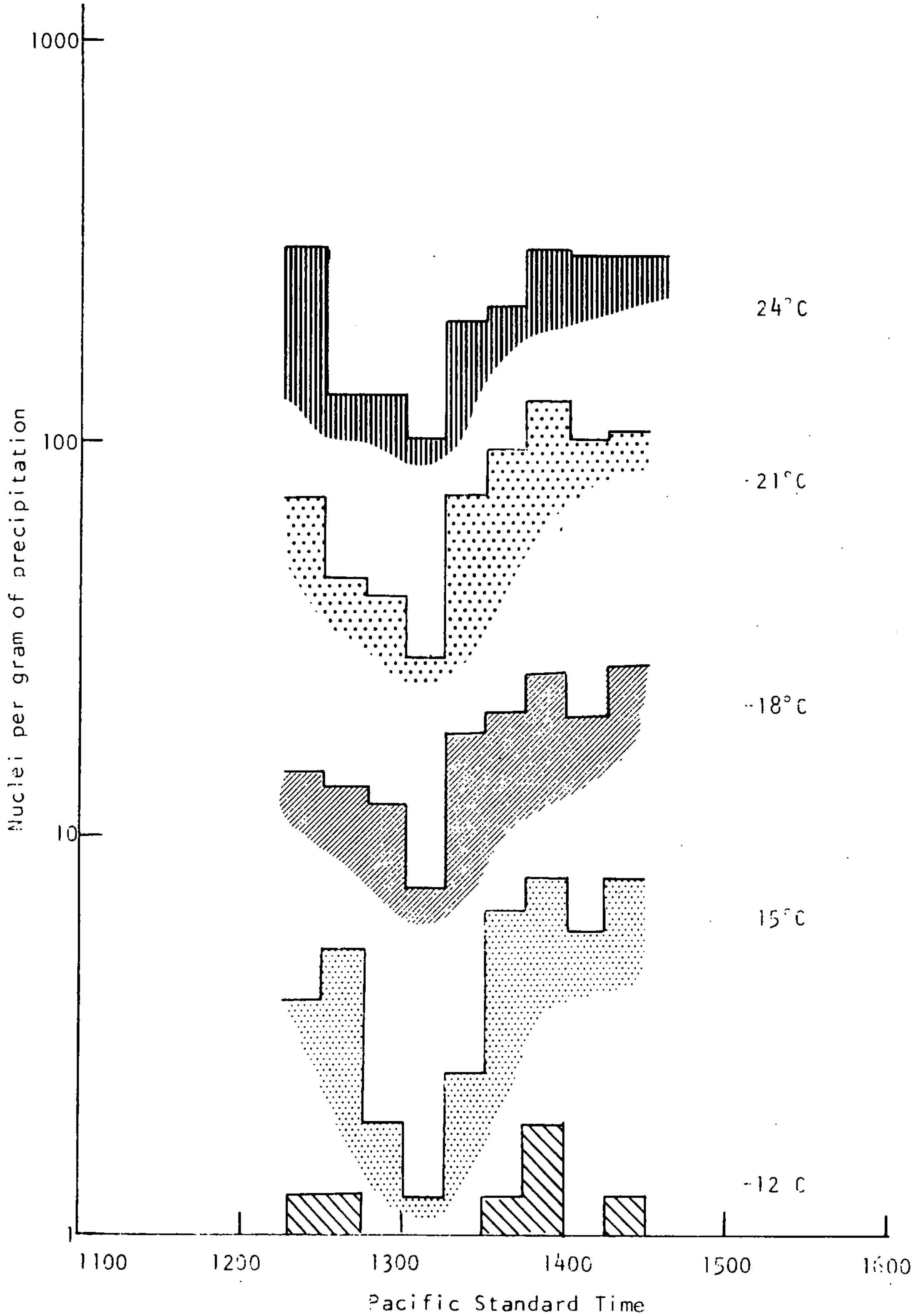

Fig. 5.26 Concentrations of freezing nuclei active at five temperatures in snow samples collected at Keechelus Dam on January 31, 1972.

At Hyak an increase, relative to prior observations, in freezing nucleus concentrations active at -15°C, -18°C, -21°C and -24°C occurred at 1315 hours. Between 1330 and 1515 there was insufficient precipitation for analysis to be performed. This decrease in precipitation, which did not occur at Alpental, could have been the result of overseeding in the region where the snow crystals that fell at Hyak originated. Overseeding would cause the ice crystals to compete for available moisture and thus produce a high concentration of very small crystals that would drift farther downwind (see §2.5). Freezing nucleus concentrations measured from 1515 until 1530 were higher than prior readings for nuclei active at -12°C, -15°C, and -18°C. Subsequent measurements at 1545 showed a significant decrease in concentrations active at all temperatures.

At Keechelus Dam an increase in freezing nucleus concentrations active at all temperatures occurred after 1315. Again, insufficient precipitation fell after 1430 for freezing nucleus analysis.

Snow samples from Alpental were not available for freezing nucleus concentration analysis. However, it can be seen in Fig. 5.23 that the precipitation rate was higher and more precipitation was measured with the tipping bucket precipitation gauge at Alpental than at the other two stations. Since Alpental was not affected by seeding, it can be concluded that natural precipitation in the area did not decrease significantly and the decrease in precipitation at Hyak and Keechelus Dam was indeed caused by seeding.

Insufficient precipitation was collected at all three stations for silver analysis to be performed.

5.1.6 Summary of Effects Attributable to Seeding

5.1.6.1 Enhancement of Convective Clouds

There were numerous indications that convective clouds developed in the seeded area. As discussed in §5.1.4, the temperature, liquid water content, and turbulence traces indicated that cumulus activity developed during the seeding operation. In addition, the Flight Scientist observed cumulus clouds with well-defined towers developing below flight level (10,000 ft.) after seeding began. Furthermore, ground personnel at Keechelus Dam and Hyak reported that the predominantly overcast sky conditions had large breaks after 1330 and cumulus clouds were visible.

Rough calculations can be made of the increase in temperature of a seeded column of air due to one silver iodide ejection flare using mean values of drop size and concentration from Table 5.5. Assuming complete glaciation by AgI nuclei within the seeded volume, approximately 378 joules of latent heat of freezing would be released in a 1 centimeter radius column 3,000 ft. deep. This amount of latent heat would warm the column 1.27°C. Thus a seeded column should become more buoyant than the surrounding unseeded clouds and produce narrow cumulus towers.

Clearly it is feasible to conclude that artificial seeding produced a notable effect on the cloud structure which was observed and measured both in the air and from the ground.

5.1.6.2 Ice Nucleus Concentrations

Ice nucleus concentrations in the seeded volume would be expected to increase several orders of magnitude as a result of seeding. As discussed in §5.1.4.3, increases of this magnitude were not measured. However, an increase in frequency of measured concentrations from 0.22 events per minute prior to seeding to 0.61 events per minute during the seeding period was noted. The frequency dropped to 0.23 events per minute during the period after seeding. This increase in frequency of measured ice nucleus concentrations is deemed a direct effect of the seeding.

5.1.6.3 Cloud Particles and Visual Observations

The continuous particle sampler on the aircraft was operated for short periods of time, approximately 20 seconds, at various locations during the flight. The crystals collected show some general trends which can be attributed to seeding (see Table 5.5). Firstly, cloud droplet concentrations decreased in the seeded area after 1345. Secondly, ice crystal concentrations increased in the seeded area after 1330. Thirdly, the number ratio of water to ice decreased after 1316 (with the exception of continuous particle sampler run 18 at 1331). Fourthly, different types of crystals were replicated within the seeded area as seeding progressed. Finally, the ice crystals replicated within the seeded region were unrimed, whereas rimed crystals were observed prior to seeding. These trends all indicate that seeding influenced ice crystal growth in the seeded region.

Comparing data from the continuous particle sampler runs in the same area, one prior to seeding and one after seeding, should reveal any specific seeding effects. Continuous particle sampler runs 10 and 22 meet this criteria. Considering first water drop concentrations, run 10 had a maximum concentration of drops of 52 cm^{-3}, whereas, concentrations of near zero were found during run 22. Ice crystal concentrations were similar for both runs, however, the number ratio of water to ice decreased considerably. Riming and aggregation of the ice crystals were apparent on run 10 but only single unrimed crystals were noted on run 22. From these observations it is concluded that seeding affected the area near Kachess Lake and Cle Elum Lake. Continuous particle sampler run 26 was made south of the area affected by the seeding plume. Significant water drop concentrations and low ice crystal concentrations were observed. This run is considered representative of a control area for run no. 22 which was taken in the seeded area, and supports the occurrence of a seeding effect.

Visual observations made during the flight as shown in Table 5.6, also give qualitative proof of the effect of seeding. The optical phenomena prior to seeding were basically those caused by water drops, with some weak ice optical phenomena observed indicating low ice crystal concentrations. As seeding progressed, a mixture of water and ice optics were observed. Later as the aircraft flew downwind strong optical effects due to ice crystals predominated. Most of these effects were observed toward the sun or in the seeded region, as defined in Fig. 5.12.

5.1.6.4 Ground Observations

Significant changes in snow crystal type and riming did not occur at Alpental, although the precipitation rate increased during the seeding period (see §5.1.5.1). We conclude that Alpental was not affected by the seeding operation and this agrees with the predictions based on ice crystal trajectories (§5.1.3)

Riming of the snow crystals falling at Hyak ceased completely after 1300 (Fig. 5.20), although moderate to heavy riming continued at Alpental, four miles upwind (§5.1.5.1). Since seeding occurred in the riming growth region of the crystals which fell at Hyak, it is inferred that the decrease in riming observed at Hyak was a direct consequence of seeding. The lack of riming continued after the predicted period of seeding effect. Although this may have been due to natural causes it is unlikely since riming continued at Alpental. It is therefore conjectured that the seeding agent was trapped in the lower portions of the riming region by the mountains and remained active near Hyak. The decrease in the precipitation rate at Hyak during the seeding period correlates well with the cessation of riming. Also, plates and germ crystals appeared at Hyak during the predicted period of effect of seeding. These crystals were not observed prior to seeding and, as shown in Table 5.3, seeding was carried out within their diffusional growth region.

Seeding effects at Keechelus Dam were noted primarily in the appearance of new crystal types, particularly plates and bullets. Bullets were observed by the aircraft on continuous particle sampler run 16 at 1316 hours at an altitude of 10,700 ft. (see Fig. 5.8 and Table 5.5). These crystals are considered a direct result of seeding. Trajectory calculations for large unrimed bullets indicate that these crystals would fall out of the diffusional growth region within the seeded volume and should have reached the ground at Keechelus Dam in approximately 42 minutes or at 1358 hours. Fig. 5.24 shows that bullets were in fact observed from 1400 until 1430 hours at Keechelus Dam. Therefore, it is concluded that these crystals were produced by seeding. Interestingly, continuous particle sampler run 20 was taken at 1401 within one nautical mile of the position of run 16. Bullets were not observed on this run which correlates well with the 1440 observed at Keechelus Dam which contained no bullets. In addition, the precipitation rate measured with the tipping bucket precipitation gauge at Keechelus Dam increased slightly from 1430 until 1445 (see Fig. 5.24).

Seeding effects at Kachess Dam, located seven miles in the downwind direction from Keechelus Dam, would be expected from 1343 until 1538 hours. The only precipitation of the day fell at Kachess Dam between 1330 and 1600 hours (Fig. 5.24). During this period the precipitation rates were sporadic but measurable. This correlation between the anticipated seeding effect time and the occurrence of precipitation at Kachess Dam verifies our theoretical predictions that precipitation can be shifted from across the Cascade crest by overseeding with artificial ice nuclei (see §2.5).

It can be seen from Table 5.8 that the crystal types at Hyak and Keechelus Dam showed a transition during the predicted period of seeding effect from crystals that grow in a relatively higher ice or water saturation environment to those which grow at lower supersaturation. This implies that the water vapor content in the region in which these crystals grew was reduced. The crystal habit at Hyak during the post-seeding period returned to high saturation environment crystals. The water vapor content could have been reduced by nucleation of ice crystals and it follows that such nucleation could have been due to the AgI seeding. Since the trajectory analysis showed that these crystals came from the seeded volume, it is concluded that the observed transition in crystal habits was a consequence of seeding. Since no such transition occurred at Alpental, it is concluded that seeding did not affect the crystals falling there; this agrees with the prediction made in §5.1.5.1.

Measurements of freezing nucleus concentrations were discussed in §5.1.5.2. The increases in concentrations which correlated well with the decreases in precipitation rate during the period of expected seeding effects are considered a direct effect of the artificial seeding.

5.2 December 10, 1971

5.2.1 Synoptic Situation

The synoptic situation at the 500 mb level on December 10, 1971, over Washington State was influenced primarily by a broad, long wave trough (Fig. 5.27). This trough was also evident at the 850 mb level (Fig. 5.28). From the isotherm field it is apparent that a thermal trough at the 850 mb level was situated over the western portion of the state at 0400 hours. The closed upper level cyclonic feature located over Central Canada was moving eastward and a Pacific maritime occluded frontal system was associated with this feature.

The surface synoptic situation at 1300 hours is shown in Fig. 5.29. This chart depicts a pressure trough oriented east-west across Washington State. Low level westerly winds persisted throughout the day over the state bringing moist unstable maritime air into the Cascade Mountains.

Fig. 5.30 is a time cross-section based on rawinsondes at Quillayute, Washington. The strong occlusion passed through the station on December 8th with considerable cooling at all levels. After December 8 the upper level flow pattern remained rather uniform.

The net effect of the long wave trough and the onshore wind flow was the production of multi-layered clouds over the entire state. Stations in the Puget Sound area reported precipitation varying from light drizzle and light snow to rain and snow showers. Mountain stations reported light to moderate snow and fog.

Fig. 5.31 depicts a vertical cross-section from Seattle, Washington, to Ellensburg, Washington, valid for the period 1000 to 1315 hours. Fig. 5.32 depicts the same information for the period 1315 to 1600. The cloud structure prior to artificial seeding over the Cascade Mountains was primarily stratus and altostratus layers with some imbedded cumulus. Bases of the main cloud deck were near 6,000 ft. Tops of the layered clouds were near 12,000 ft. while some of the cumulus clouds had tops rising to 14,000 ft. Broken cirrus were noted above with cloud bases near 22,000 ft. and tops reported at 23,500 ft.

During the afternoon the cloud structure became more cumuliform (see Fig. 5.32) with cloud bases near 3,000 ft. and tops near 10,500 ft. A layer of altostratus persisted from 10,000 ft. to 12,500 ft. and higher clouds were also observed. During this portion of the flight the Flight Scientist reported several holes in the clouds through which the ground was visible. Broken sky conditions were reported by Keechelus Dam at 1400 hours.

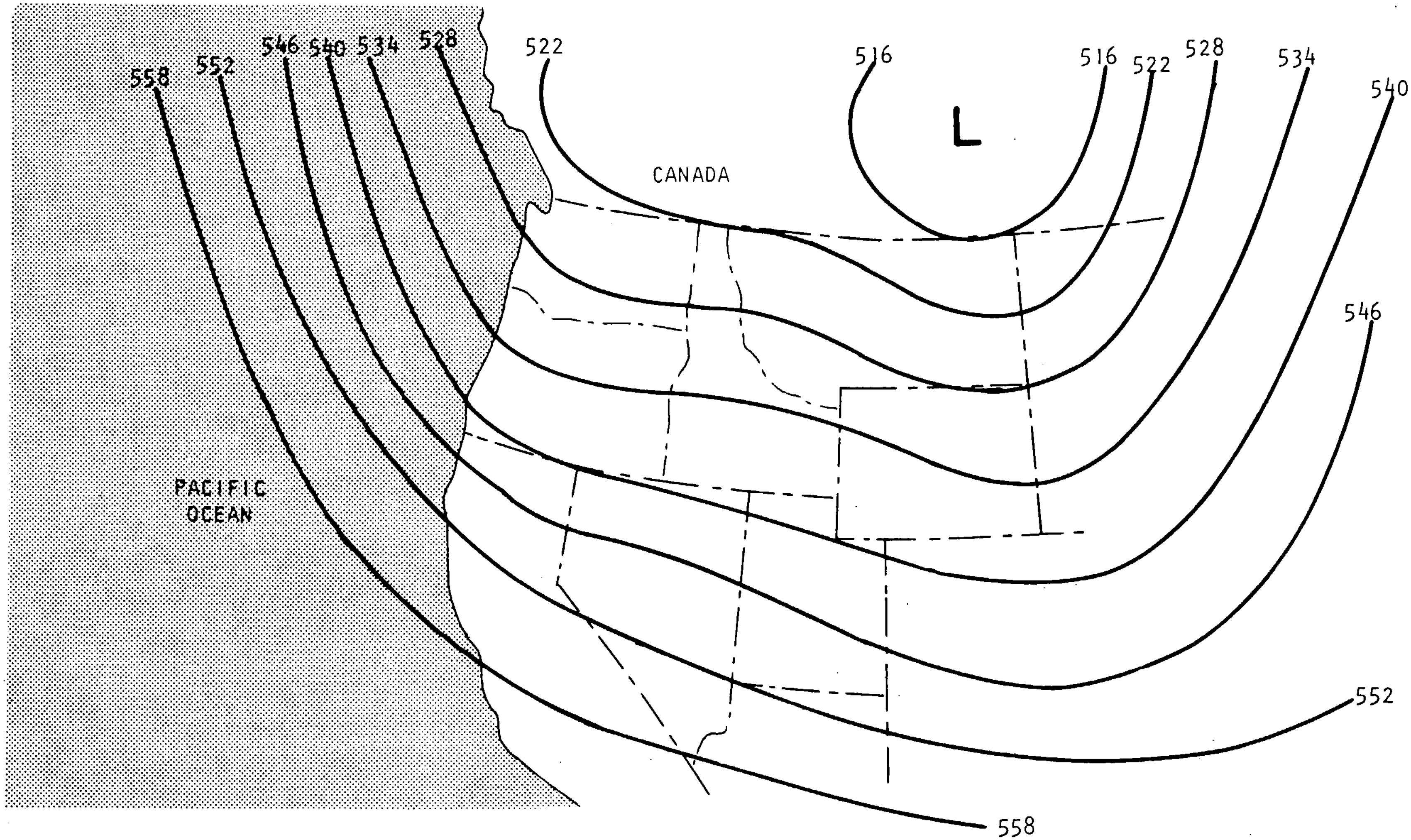

Fig. 5.27 500 mb synoptic map for 0400 PST on December 10, 1971.
—— Height in 10's of geopotential meters of 500 mb surface.

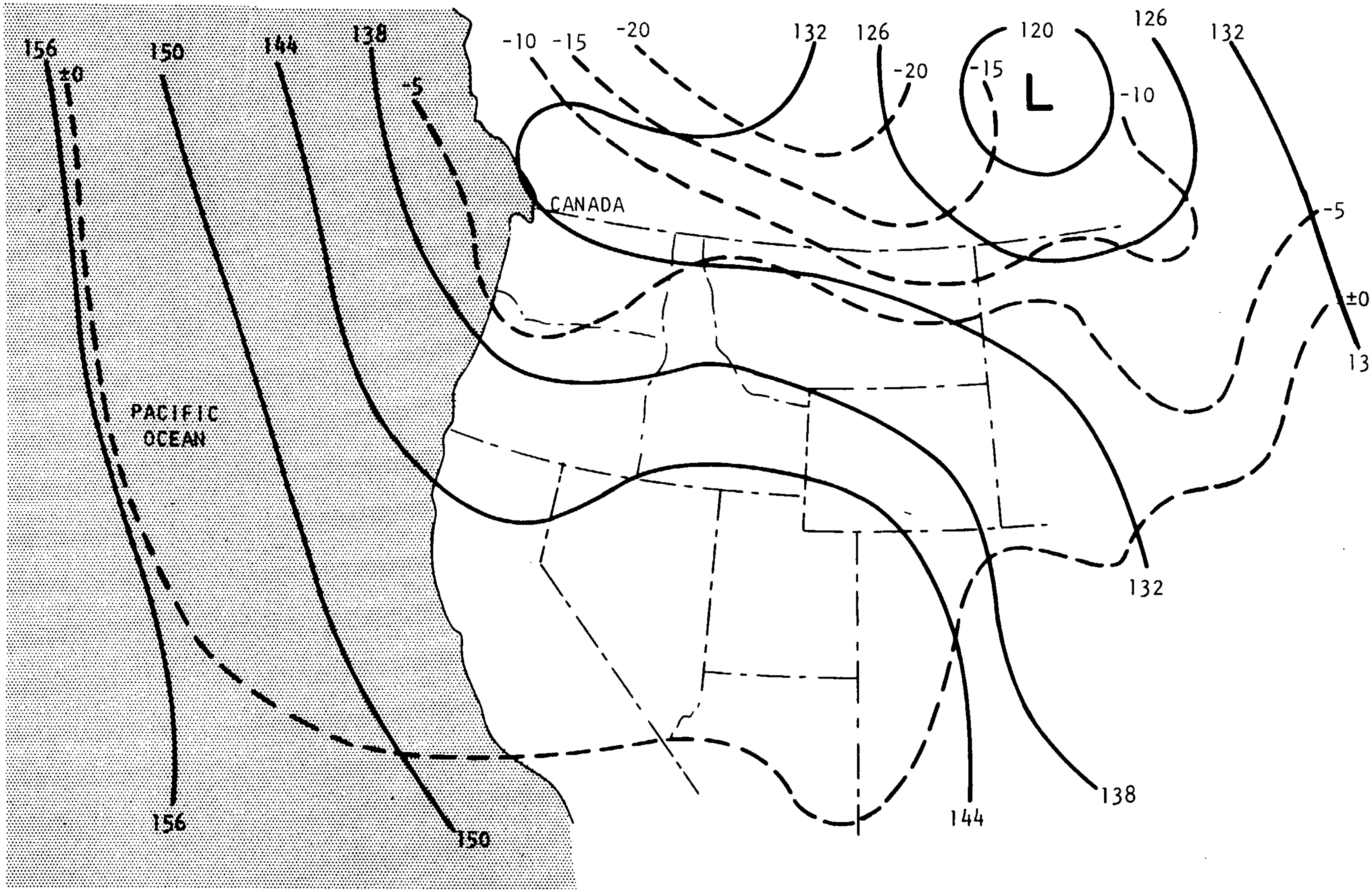

Fig. 5.28 850 mb synoptic map for 1400 PST on December 10, 1972. ——— Height in 10's of geopotential meters of 850 mb surface. — — Temperature (°C).

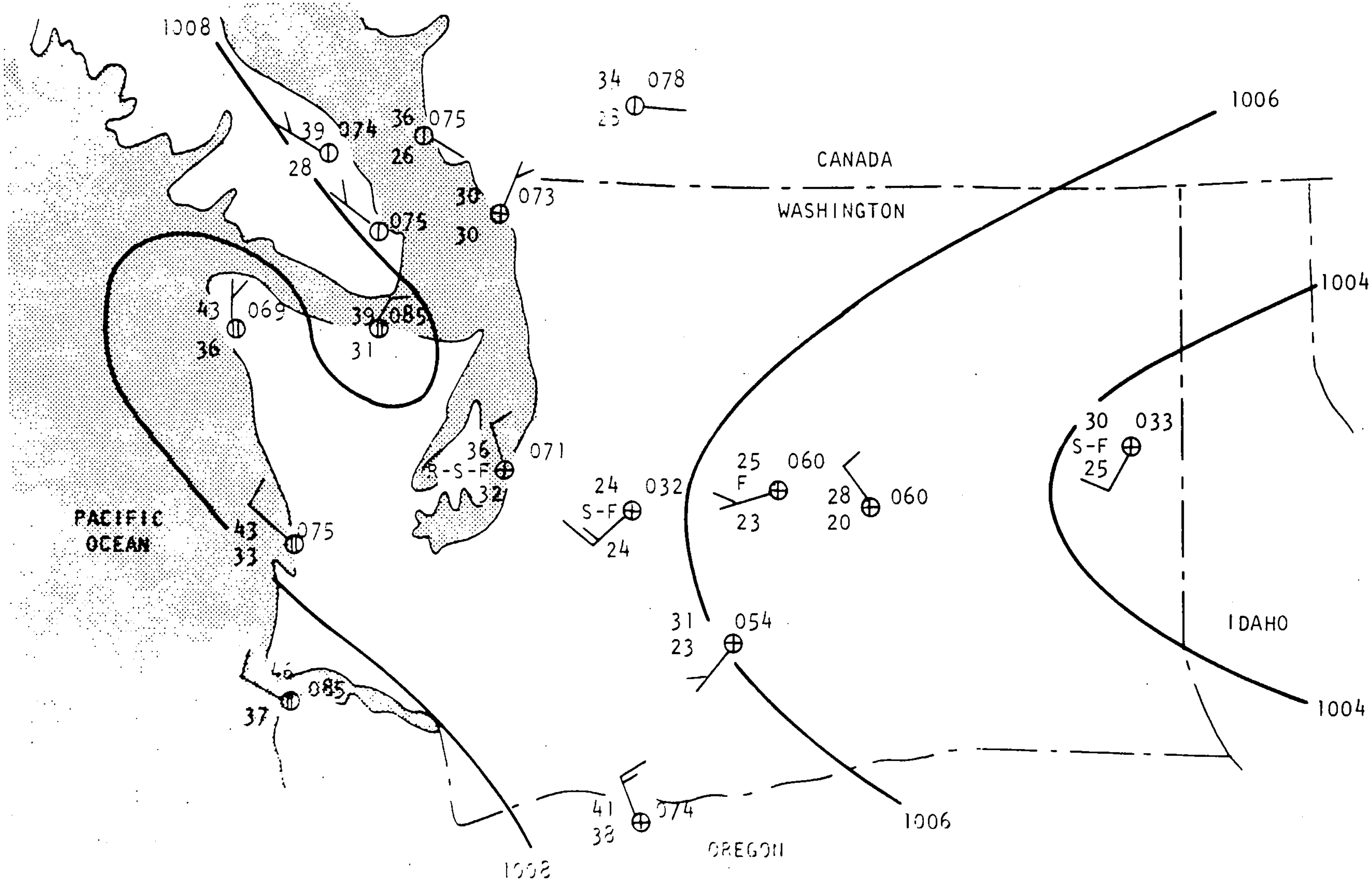

Fig. 5.29 Surface synoptic situation at 1300 PST on December 10, 1971.

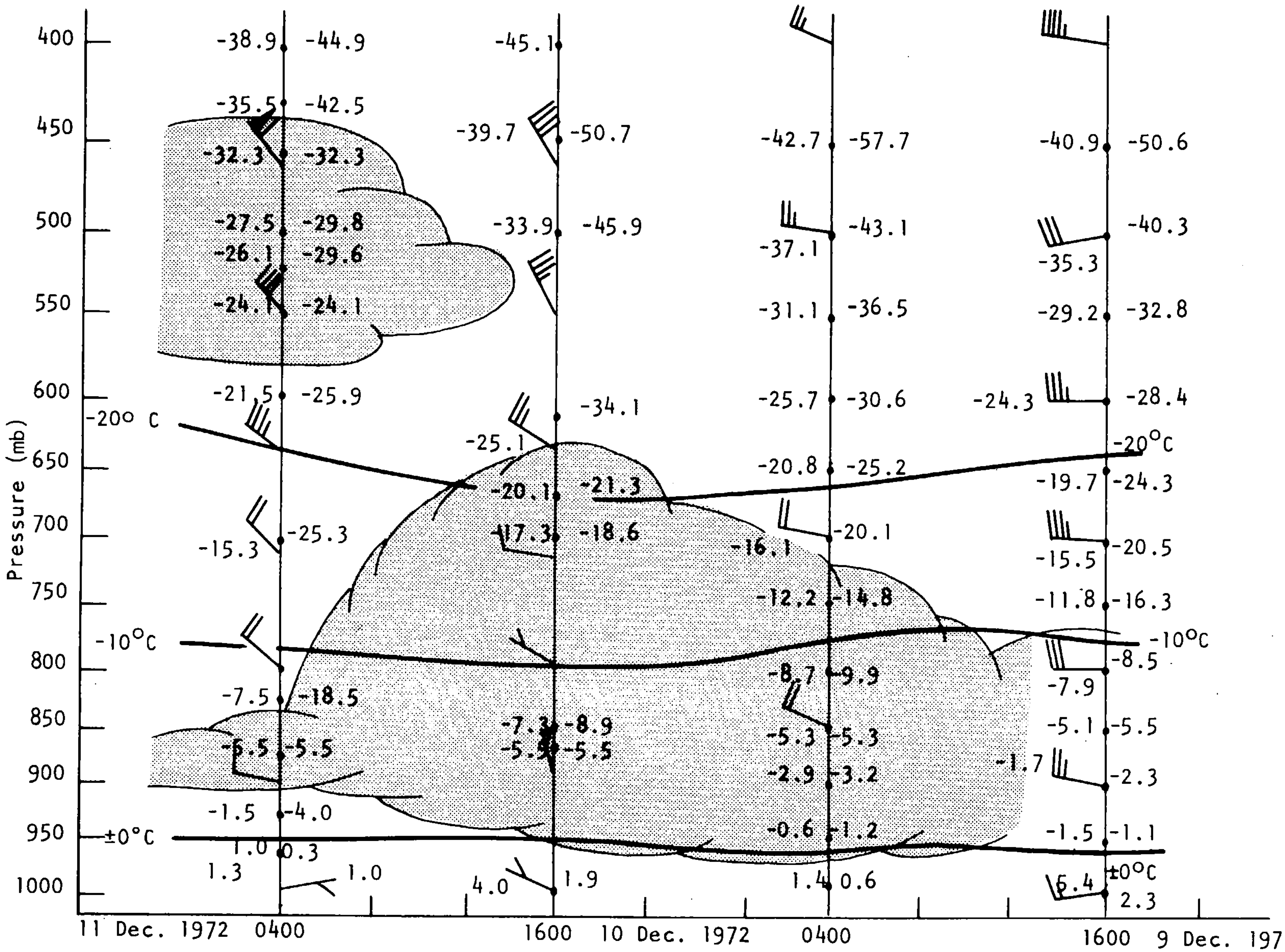

Fig. 5.30 Time cross-section for soundings at Quillayute between December 9 and December 11, 1971.

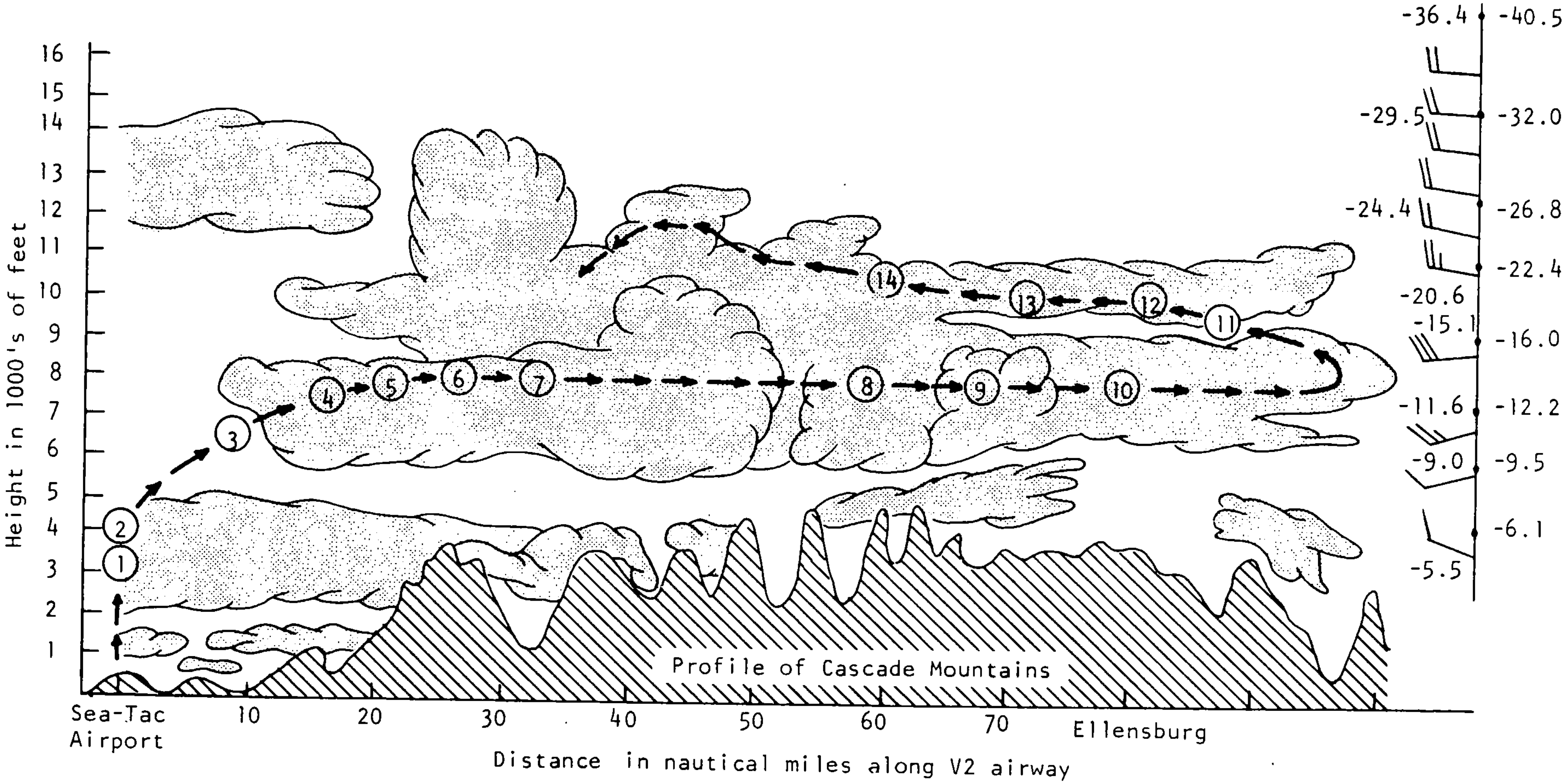

Fig. 5.31 Vertical cross-section from Seattle, Washington to Ellensburg, Washington, valid from 1120-1315 PST on December 10, 1971. The temperatures (in °C) and winds shown are based on the 1100 PST rawinsonde launched from Greenwater which is located approximately 31 miles southeast of Sea-Tac Airport. (1) Continuous particle sampler run position. ← Flight path of research aircraft.

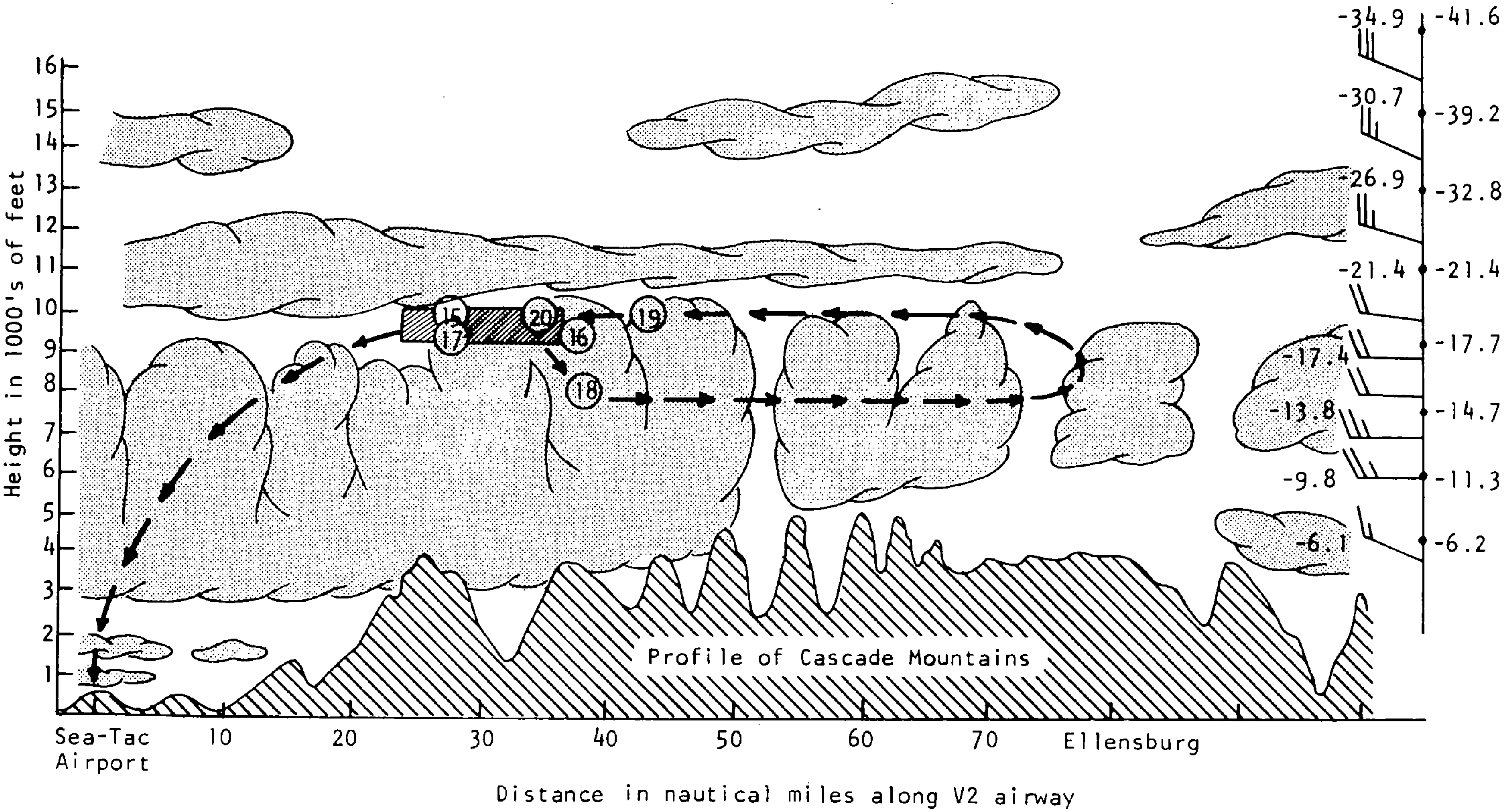

Fig. 5.32 Vertical cross-section from Seattle, Washington, to Ellensburg, Washington, valid from 1315 to 1600 PST on December 10, 1971. The temperatures (in °C) and winds shown are based on the 1353 PST rawinsonde launched from Greenwater which is located approximately 31 miles southeast of Sea-Tac Airport. 1 Continuous particle sampler run position. ← Flight path of research aircraft. Seeding orbit.

Comparing data from the two Greenwater rawinsondes it was found that the atmosphere cooled an average of 1°C below 16,000 ft. and warmed above that level. Maximum cooling of 2.0°C in the three hour period occurred near 7,700 ft. Wind speeds increased approximately five knots from the surface to 6,000 ft., and above 12,000 ft. the velocities increased as much as 15 knots. From 6,000 to 12,000 ft. the wind speeds decreased approximately five knots. The stronger low level winds could induce stronger orographically induced vertical wind components over the mountains which, coupled with the light mid-level winds and cooling, could account for the development of the cumuliform cloud structure.

5.2.2 Aircraft Operations

5.2.2.1 Flight Profile

The research flight for December 10, 1971, commenced at 1120 from Boeing Field. Routine instrument calibrations and meteorological observations were made as the aircraft climbed to 8,000 ft. and proceeded along Victor 2 airway to Ellensburg, Washington (Figs. 5.31, 5.32, 5.33 and 5.34). The aircraft then proceeded northwest from Ellensburg at 10,100 ft. to an orbit over the Hyak area. From Hyak the aircraft flew a circuitous route to the prescribed seeding area. All instruments on-board were operational with the exception of the radar altimeter, true airspeed indicator, the Johnson-Williams liquid water instrument, and the Mee Industries ice nucleus counter.

The seeding orbit was determined from predicted ice crystal trajectories based on the observed crystal types at the ground stations and the Greenwater 1100 PST rawinsonde. The prescribed seeding area is shown in Fig. 5.34. The seeding plan called for 10-gram AgI ejection flares to be expended at a rate of one per minute until the on-board supply was exhausted, and dry ice to be expended at a rate of 5 pounds per mile while the aircraft flew the prescibed orbit. The actual seeding operation followed the plan closely, however, the seeding orbit was larger than prescribed (Fig. 5.34).

After seeding was completed, the aircraft flew toward Ellensburg along the Victor 2 airway at 8,000 ft., then turned north and flew over the Kachess Dam area at 10,000 ft. The aircraft landed at Boeing Field at 1547 hours.

5.2.2.2 Seeding Operation

Dry ice was dispensed at the prescribed rate of 5 pounds per mile for 24 minutes commencing at 1312 and ending at 1336 hours. This seeding rate yields a spectrum of dry ice particles in which 86 per cent are from 0.47 to 0.9 cm diameter. Theoretical fall distances from 5,000 to 14,000 ft. were

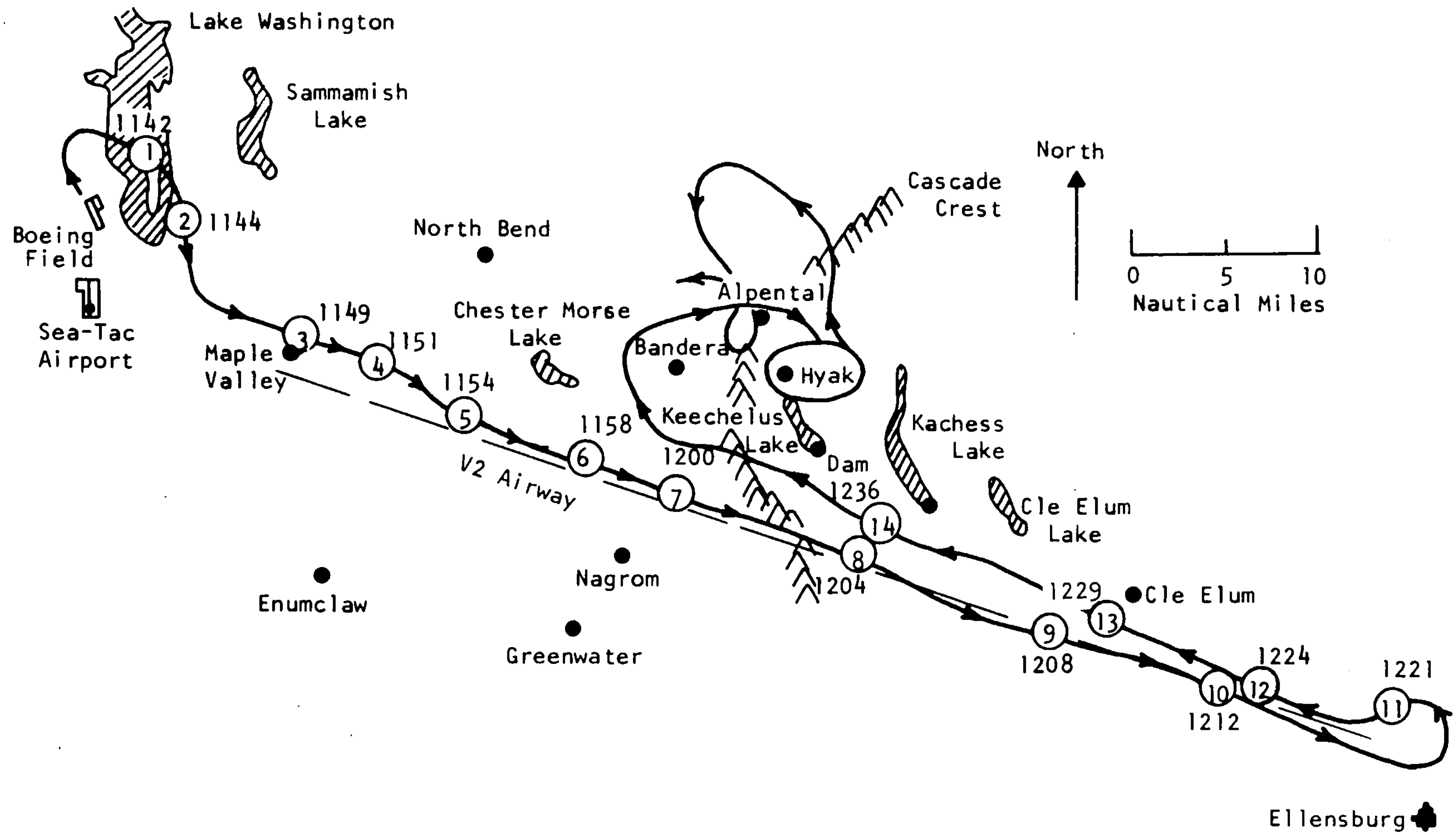

Fig. 5.33 Sketch of flight route from 1120 until 1312 PST on December 10, 1971. The symbol (1) refers to continuous cloud particle sampler runs. Four figure numbers give local time. Λ Cascade crest.

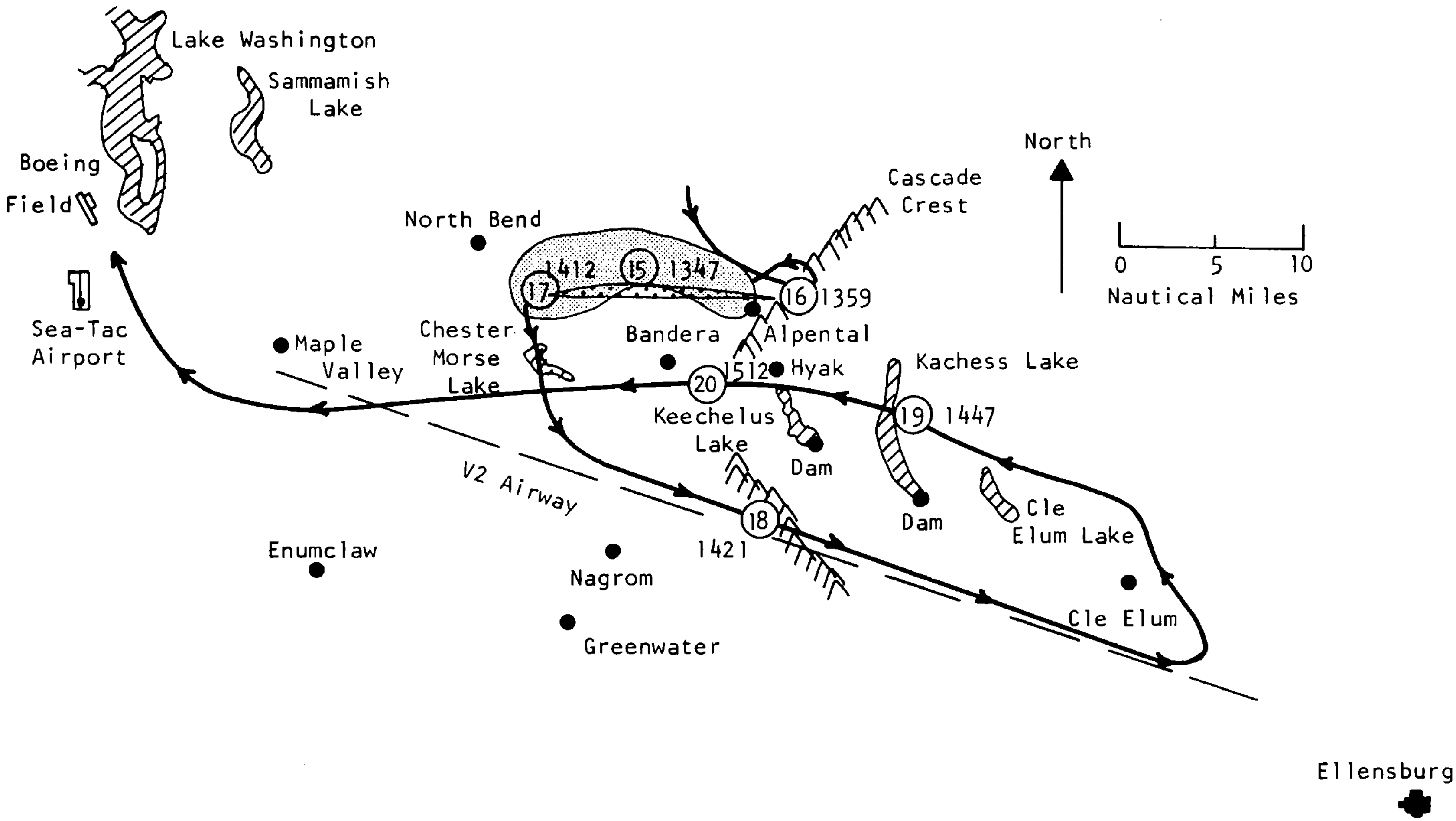

Fig. 5.34 Sketch of flight route (⟶) from 1312 until 1547 PST on December 10, 1971. The symbol (1) refers to continuous cloud particle sampler runs. Four figure numbers give local time. Prescribed seeding area. Actual seeded area. Λ Cascade Crest

calculated for these particles. However, the maximum observed fall distance for dry ice particles was approximately 2,000 ft.

Twenty-one ejection flares each containing 10 grams of AgI were expended at a rate of one every three minutes from 1312 until 1412 hours. The fall distance and burn rate for these flares are the same as for the 40-gram flares (see §5.1.2.2).

The initial seeded area encompassed approximately 40 square miles horizontally (Fig. 5.34). The vertical extent of the seeding varied from 10,100 to 9,300 ft. for the dry ice particles and from 9,900 to 6,300 ft. for the ejection flares.

Fukuta et al. (1970) calculated the ice nucleus production rate for dry ice in saturated air to be 8×10^{11} nuclei per gram. Using this production rate, the seeding rate, and the mean wind at 10,000 ft., calculations of turbulent diffusion of the ice nucleus concentrations were made according to the Pasquill-Gifford model. The diffusion pattern is identical to that shown in Fig. 5.10, however, the isopleths of nucleus concentrations would be reduced by a factor of 0.015, or approximately two orders of magnitude.

Similar calculations were made for the 10-gram AgI ejection flares. The results are similar to those shown in Fig. 5.11 except that the nucleus concentrations are reduced by a factor of 0.08, or approximately one order of magnitude.

In estimating the increase in seeded volume due to diffusion, the criteria established for the January 31, 1972, case of concentrations within the volume of greater than or equal to 10^3 nuclei per liter had to be relaxed. Instead the criteria of greater than or equal to 100 nuclei per liter was used and the increase in the seeded volume due to turbulent diffusion was calculated. The estimated seeded volume is shown in Figs. 5.35 and 5.36.

Seeding with 10-gram AgI ejection flares should have produced narrow columns of seeding material separated by three minutes in time or seven miles in distance.

5.2.3 Ice Crystal Trajectories

Predictions of ice crystal trajectories and comparisons of these trajectories with the seeded volume were made as described in §5.1.3. Tables 5.9 through 5.11 summarize the results of these analyses. It can be seen that it is likely that the seeding should have influenced the snow crystals falling at the Hyak and Alpental station. Seeding occurred north of the predicted trajectories of the ice crystals falling at Keechelus Dam and Kachess Dam,

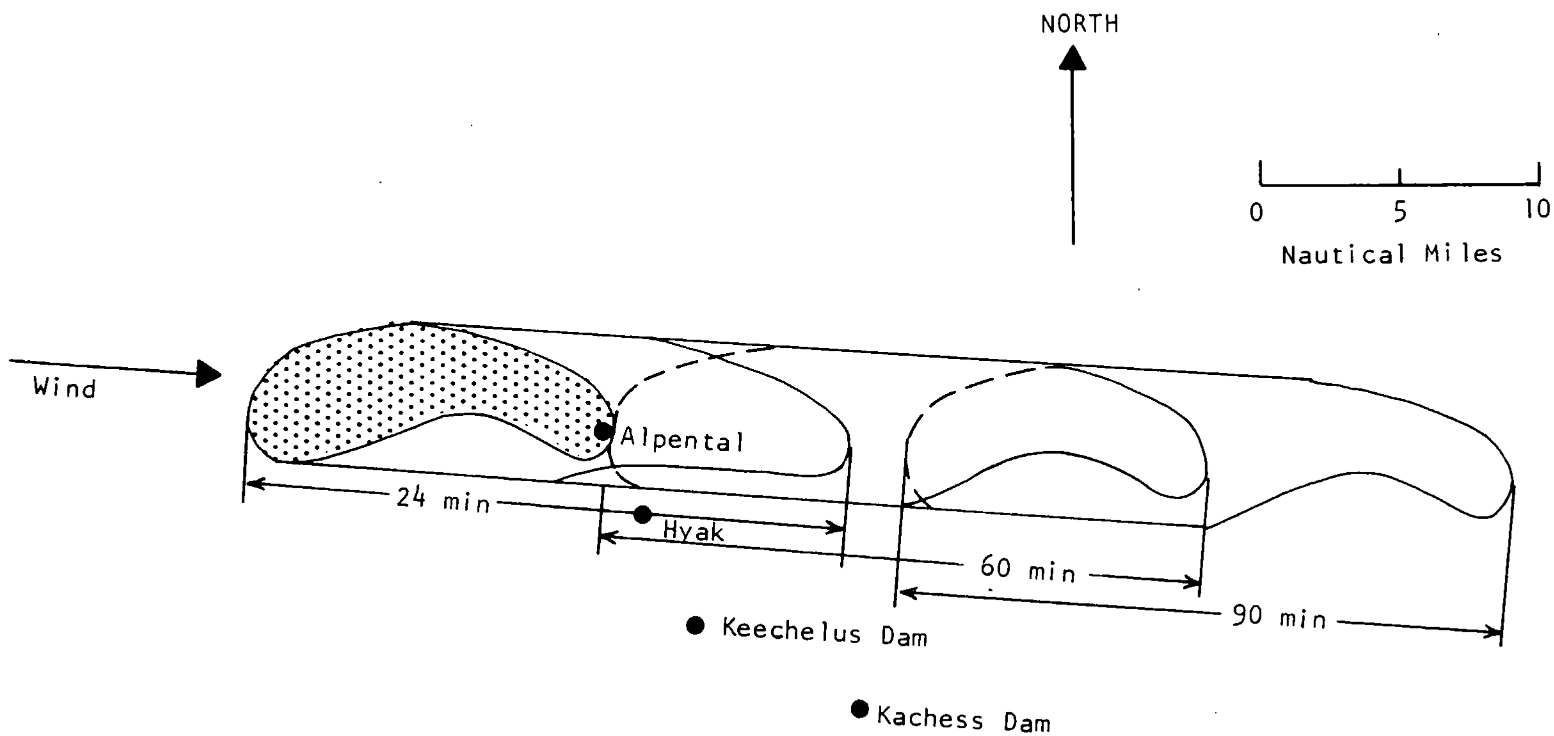

Fig. 5.35 Horizontal profile of increase in seeded region with time due to turbulent diffusion on December 10, 1971. Seeded region defined by elapsed time in minutes after seeding began. Initial seeded area.

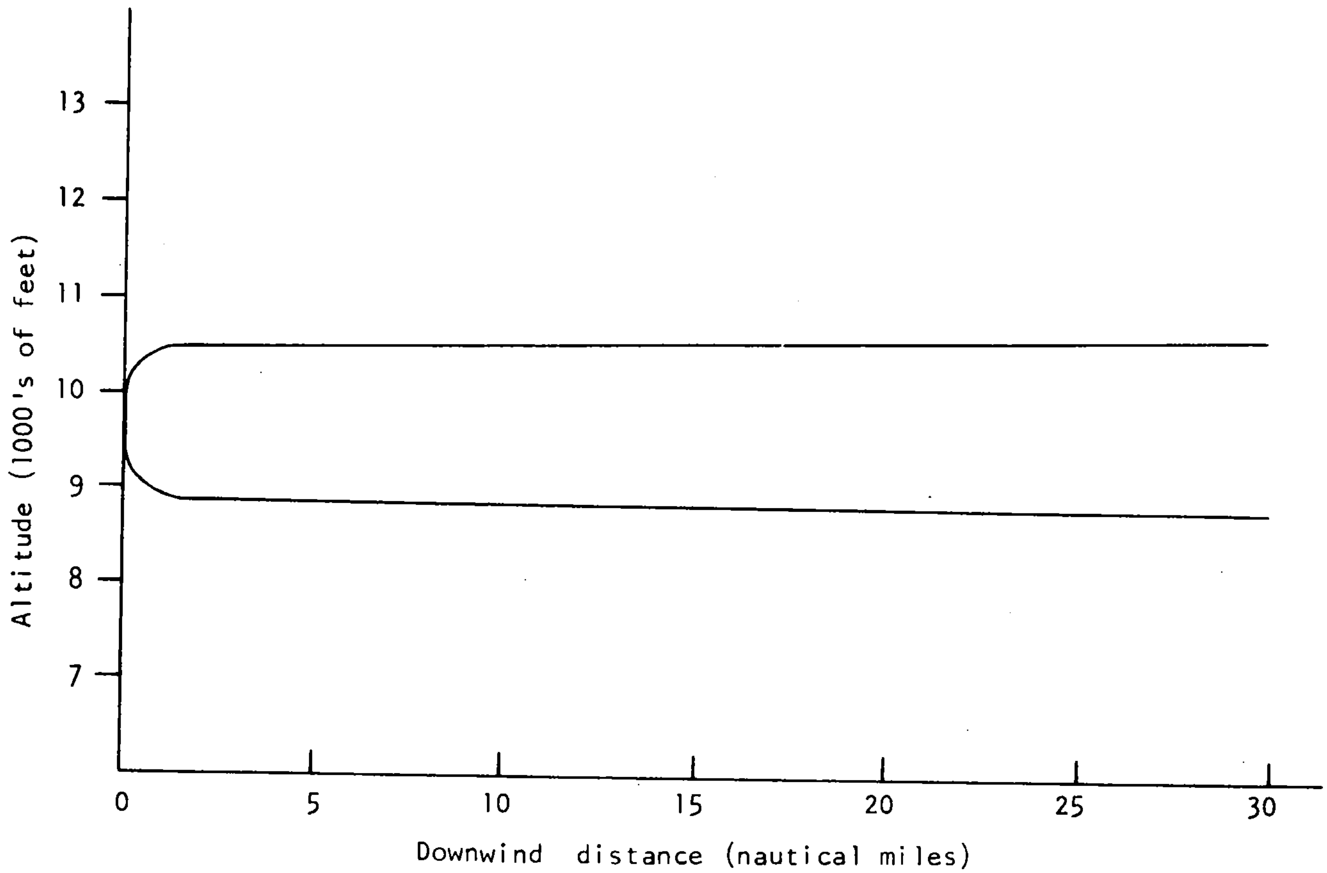

Fig. 5.36 Vertical profile of increase in seeded region due to diffusion on December 10, 1971.

TABLE 5.9

COMPARISON OF CRYSTAL TRAJECTORIES REACHING HYAK WITH SEEDED VOLUME

Crystal Type	Comparison of Trajectory with Seeded Volume		Qualitative Assessment of Seeding Effect	Time (PST) Seeding Effect Expected on Ground
	Horizontal	Vertical		
Assemblages of Plates	The last 40% of the trajectory of small rimed crystals, 25% of the small unrimed crystals and 60% of the small unrimed crystals coincided with the seeded area.	Dry ice and ejection flares seeded 4,000 ft. into the riming growth region.	Good chance	1320 - 1525
Graupel	Seeding occurred within one nautical mile of trajectory.	Dry ice seeded the diffusional growth region. Ejection flares seeded 3,500 ft. into riming region.	Fair chance	1320 - 1437
Stellars	Last 50% of trajectory of small crystals and 100% of large crystals coincided with seeded area.	Dry ice and ejection flares seeding the diffusional growth region of medium and large crystals. Ejection flares seeded 2,500 ft. into riming region.	Excellent chance	1320 - 1525
Columns	First 50% of trajectory coincided with seeded area.	Ejection flares seeded in the diffusional growth region.	Fair chance	Unknown
Plates	Last 50% of trajectory of small crystals and 100% of large crystals coincided with seeded area.	Dry ice and ejection flares seeded diffusional growth region of medium and large crystals. Ejection flares seeded 3,000 ft. into riming region.	Excellent chance	1320 - 1525

TABLE 5.9 (Cont.)

Crystal Type	Comparison of Trajectory with Seeded Volume		Qualitative Assessment of Seeding Effect	Time (PST) Seeding Effect Expected on Ground
	Horizontal	Vertical		
Bullets	Last 40% of trajectory of small crystals and 90% of large crystals coincided with seeded area.	Dry ice and ejection flares seeded from 2,000 to 4,000 ft. into riming region.	Good chance	1328 - 1502
Dendrites	Last 50% of trajectory of small crystals and 90% of large crystals coincided with seeded area.	Dry ice and ejection flares seeded diffusional growth region of the medium to large crystals. Ejection flares seeded 3,000 ft. into riming region.	Excellent chance	1320 - 1525
Aggregates	80% of trajectory of small crystals coincided with seeded area. Seeding occurred within one nautical mile of trajectory of large crystals.	Dry ice seeded the diffusional growth region. CO_2 and ejection flares seeded from 1,000 to 3,500 ft. into riming region.	Good chance	1315 - 1504

TABLE 5.10

COMPARISON OF CRYSTAL TRAJECTORIES REACHING ALPENTAL WITH SEEDED VOLUME

Crystal Type	Comparison of Trajectory with Seeded Volume		Qualitative Assessment of Seeding Effect	Time (PST) Seeding Effect Expected on Ground
	Horizontal	Vertical		
Assemblages of Plates	Last 25% of trajectory of small crystals and 60% of large crystals coincided with seeded area.	Ejection flares and dry ice seeded 3,500 ft. into the riming region.	Good chance	1401 - 1517
Graupel (0.1 cm diameter)	100% of trajectory coincided with seeded area.	Ejection flares seeded 3,000 ft. into riming region. Dry ice seeded in diffusional growth region.	Excellent chance	1324 - 1434
Dendrites	Last 50% of trajectory of small crystals and 100% of large crystals coincided with seeded area.	Dry ice and ejection flares seeded in diffusional growth region of medium to large crystals. Ejection flares seeded 2,500 ft. into riming region.	Excellent chance	1322 - 1517
Bullets	Last 50% of trajectory of small crystals and 100% of large crystals coincided with seeded area.	Dry ice and ejection flares seeded from 3,000 to 5,000 ft. into riming region.	Excellent chance	1317 - 1459
Columns	100% of trajectory coincided with seeded area.	Ejection flares seeded in upper 500 ft. of diffusional growth layer.	Fair chance	Unknown
Aggregates	90% of trajectory of small crystals and 100% of large crystals coincided with seeded area.	Dry ice seeded the diffusional growth region. Ejection flares seeded from 1,000 to 4,000 ft. into riming region.	Excellent chance	1316 - 1459
Plates	Last 40% of trajectory of small unrimed crystals, 60% of small rimed crystals, and 100% of large crystals coincided with seeded area.	Dry ice seeded the diffusional growth region of medium to large crystals. Ejection flares seeded 3.000 ft. into riming region.	Excellent chance	1322 - 1517

TABLE 5.11

COMPARISON OF CRYSTAL TRAJECTORIES REACHING KEECHELUS DAM WITH SEEDED VOLUME

Crystal Type	Comparison of Trajectory with Seeded Volume		Qualitative Assessment of Seeding Effect	Time (PST) Seeding Effect Expected on Ground
	Horizontal	Vertical		
Aggregates	Seeding occurred 3-1/2 nautical miles north of trajectory.	———	None	———
Bullets	Seeding occurred 3-1/2 nautical miles north of trajectory.	———	None	———
Sideplanes	Seeding occurred within one nautical mile of last 25% of trajectory of small unrimed crystals.	Dry ice and ejection flares seeded from 3,000 to 4,500 ft. into riming region.	Slight chance	1452 - 1641
Dendrites	Seeding occurred within one nautical mile of last 50% of trajectory of small unrimed crystals.	Ejection flares seeded 2,500 ft. into riming region.	Slight chance	1407 - 1530
Assemblages of Sectors	Seeding occurred within one nautical mile of 15% of trajectory of small unrimed crystals.	Ejection flares seeded 2,000 ft. into riming region.	Slight chance	1400 - 1528
Assemblages of Plates	Seeding occurred within one nautical mile of 15% of trajectory of small unrimed crystals.	Ejection flares seeded 2,000 ft. into riming region.	Slight chance	1400 - 1528
Columns	Seeding occurred 3-1/2 nautical miles north of trajectory.	———	None	———

however, there were indications that the area of effect of seeding was carried further south than shown in Fig. 5.35 and that it affected Keechelus Dam, Stampede Pass and Kachess Dam. Approximate time periods of the expected seeding effects are: Hyak (1315-1525), Alpental (1316-1517), Keechelus Dam (1400-1640), and Kachess Dam (1400-1640).

5.2.4 Airborne Observations

5.2.4.1 Cloud Particles and Visual Observations

Analysis of the data collected with the continuous particle sampler is presented in Table 5.12. The aircraft position during the individual runs is shown in Figs. 5.31 - 5.34.

Continuous particle sampler runs 1 and 2 were taken in the lower cloud deck during climb out from Boeing Field and indicate a high concentration of water drops. Run 3 was taken in clear air. Runs 4 through 10 were taken near 8,000 ft. along the V-2 airway. A transition from predominantly water drop to ice crystal clouds occurred as the aircraft progressed eastward across the Cascade Mountains. This phenomenon also occurred on January 31, 1972. Crystal types were both plate and columnar-like. Continuous particle sampler runs 11 through 14 were taken at a higher altitude, near 10,000 ft., as the aircraft proceeded westward toward the intended seeding orbit. These higher clouds were composed basically of plate-like crystals, irregular crystals and frozen drops. Columnar crystals were notably absent at the higher altitude. Continuous particle sampler run 15 was taken over the top of a decaying cumulus cloud. Run 16 was taken approximately two miles downwind from the seeded region and presumably in clear air. Run 17 was taken in the seeded region at the termination of seeding. Small plate-like crystals, irregular crystals, columns, and some small aggregates were observed. Run 18 was made seven miles south of the seeded region at an altitude of 8,000 ft. Both water drops and ice particles in the form of frozen drops, large aggregates, irregular crystals and plate-like crystals with riming, were observed. Runs 19 and 20 were taken three miles south and near the end of the maximum expected seeded region. Run 19 contained only low concentrations of plate-like and irregular crystals. Run 20 had similar crystals plus large columns and contained a relatively high concentration of water drops.

Based on the location of the continuous particle sampler runs relative to the predicted seeded volume and the cloud particle types observed, it can be stated that runs 18, 19 and 20 did not sample clouds in the artificially seeded region.

TABLE 5.12

SUMMARY OF CLOUD PARTICLES COLLECTED WITH CONTINUOUS

PARTICLE SAMPLER ON DECEMBER 10, 1971

(See Figs. 5.30-5.33 for position of continuous particle sampler run.)

Run No.	Water Drops		Ice Particles		Number Ratio of Water to Ice
	Diameter (μm)	Concentration (cm^{-3})	Type & Maximum Dimension (μm)	Concentration (cm^{-3})	
1	———	———	Some Ice (poor data)	———	———
2	20-50	9-18	(Poor data)	———	All drops.
3	(No data)	———	———	———	———
4	20-50	1.7-7	———	———	All drops.
5	10-40	0.15	Plate-like and irregular. Broken larger crystals. Possible stellar parts. 30-300 μm.	0.15-6.0 Decreasing during run	100:1
6	———	———	Some aggregates. Broken larger plate-like and irregular crystals. Some stellar parts. 30-300 μm.	0.15-0.8	All ice.
7	———	———	Frequent aggregates. Plate-like and irregular crystals. Possible needles. 30-150 μm.	1.5-6.0	All ice.
8	———	———	Frequent small aggregates. Plate-like and irregular crystals. 30-250 μm	3-11	All ice.
9	———	———	Small plate-like and irregular crystals. Some aggregates. A few short columns. 30-300 μm.	3-12	All ice.
10	———	———	A few aggregates. Plate-like and irregular crystals. Short columns. 30-250 μm.	0.8-6.5	All ice.

TABLE 5.12 (Cont.)

Run No.	Water Drops		Ice Particles		Number Ratio of Water to Ice
	Diameter (μm)	Concentration (cm^{-3})	Type & Maximum Dimension (μm)	Concentration (cm^{-3})	
11	———	———	Small rounded irregular crystals. Some small aggregates 30-200 μm.	0.3-1.4	All ice.
12	———	———	Some aggregates. Plate-like and irregular crystals.	1.5-7.5	All ice.
13	20-40	<0.13	Aggregates, irregular and plate-like crystals. A few frozen drops.	2.7-6.5	<1:1
14	———	———	Mainly frozen drops, some in groups. A few aggregates and irregular and hexagonal plates. 20-200 μm.	1.5-6.0	All ice.
15	30-60	0.16	———	———	All drops.
16	No data	———	———	———	———
17	20-80	0.1	Mainly small irregular and plate-like. Some columns. A few small aggregates. 20-250 μm	1.6-8.0	Nearly all ice.
18	20-70	1.7-14	Some frozen drops. Large aggregates, irregular and plate-like low density ice. A few stellar parts. Some riming.	3.5-8.5	1:3
19	———	———	Mainly plate-like and hexagonal plates. Some irregular crystals. 40-400 μm.	0.5-3.0	All ice.
20	10-30	5-12	Mainly plate-like and irregular. Some large columns. 40-500 μm.	0.08-0.5	1:50 to 10:1

Visual observations of optical phenomena observed from the aircraft are listed in Table 5.13. The cloud composition deduced from these observations correlates well with the continuous particle sampler data for simultaneous observations, and supplements the continuous particle sampler data at other times. Primarily ice crystal clouds are noted from 1215 through 1220 and mixed ice and water clouds from 1220 until 1250. At 1250 hours only water drop optical phenomena were observed. The aircraft at this time was between Chester Morse Lake and Bandera (Fig. 5.33) and near an altitude of 10,000 ft. The observations from 1329 through 1343 were taken in the seeded region. Predominantly ice particle phenomena were observed although water optics were observed at 1333. It should be noted that sub-suns observed in the seeded region became progressively more brilliant as the seeding progressed. Observations taken after seeding operations ceased indicated mixed water and ice clouds.

5.2.5 Ground Observations

Sky conditions were generally overcast at Hyak, Alpental, and Keechelus Dam. Cloud bases were estimated at 3,100 ft. above ground at Alpental, and Alpental top was obscured in fog. Cloud bases at Hyak were at ground level until 1200 hours and varied from 2,000 to 3,000 ft. above ground during the rest of the day. Cloud bases were estimated at 4,000 ft. above Keechelus Dam and broken sky conditions were reported on the 1400 observation. Moderate to light snow fell throughout the day at all stations.

5.2.5.1 Snow Crystal Analysis and Precipitation Rates

Analyses of snow crystals collected at the three ground stations and precipitation rate data from the optical snow rate sensor and snow bags are shown in Figs. 5.37 and 5.38.

Consider first the data for Alpental in light of the predicted period for the seeding effect (1316-1517). Ice crystal types prior to 1315 consisted primarily of lightly to densely rimed dendrites, radiating a[illegible]ages of dendrites, bullets, needles, double crystals, capped columns and aggregates. Similar crystals were observed from 1315 through 1515 with the following exceptions: columns instead of capped columns were observed; needles were not observed; plates and assemblages of plates, graupel, and graupel-like snow appeared. These crystals were moderate to densely rimed. After 1515 the crystal types observed were moderately rimed dendrites, radiating assemblages of dendrites, and aggregates. Snow rates from 1245 (i.e., prior to seeding) until 1445 were low relative to the rates before and after this period but a secondary maximum in the precipitation rate occurred from 1345

TABLE 5.13

VISUAL OBSERVATIONS OF WATER AND ICE OPTICAL PHENOMENA

OBSERVED BY FLIGHT SCIENTIST ON DECEMBER 10, 1971

Time (PST)	Optical Phenomena Observed	Cloud Composition Deduced From Optical Phenomena
1215	Sub-sun	Ice
1218	Sub-sun No optics around sun	Ice
1220	Sub-sun	Ice
1232	Sub-sun Water optics (faint and undefined)	Ice Water
1242	Sub-sun	Ice
1247	22^o halo	Water
1250	No low level ice optics Glory Cloud bow (faint)	——— Water Water
1329	Sub-sun (occasionally)	Ice
1333	Sub-sun (strong) Glory (occasionally)	Ice Water
1343	Sub-sun (brilliant)	Ice
1426	Sub-sun	Ice
1432	Ice optics (undefined)	Ice
1505	Corona	Water
1518	Parhelia	Ice

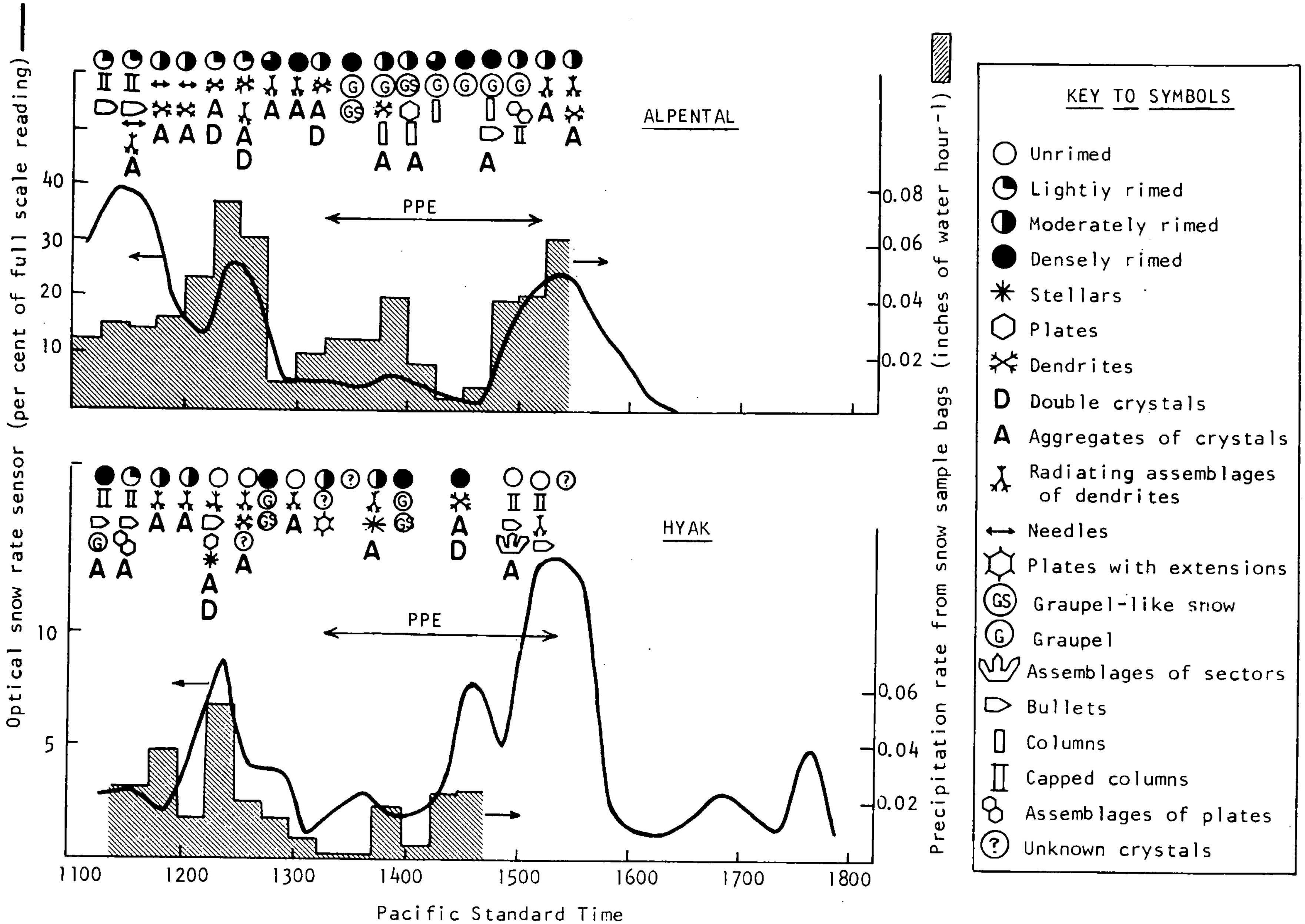

Fig. 5.37 Types of snow particles and precipitation rates at Alpental and Hyak on December 10, 1971. The predicted period of effect (PPE) of the artificial seeding at each ground station is noted.

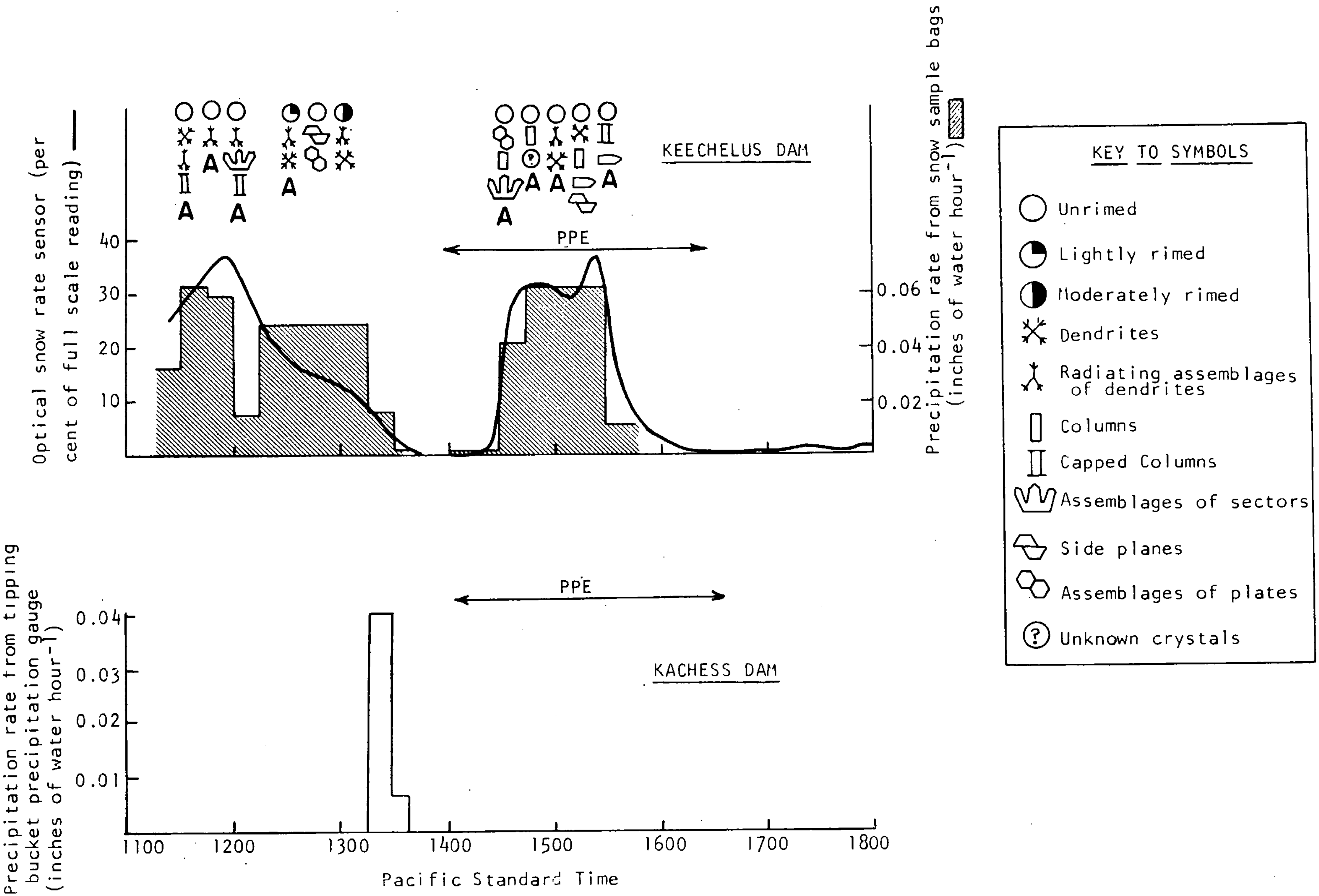

Fig. 5.38 Types of snow particles and precipitation rates at Keechelus Dam and Kachess Dam on December 10, 1971. The predicted period of effect (PPE) of the artificial seeding at each ground station is noted.

until 1400 which was in the predicted period of effect of seeding at Alpental (Fig. 5.37).

Crystal types observed at Hyak prior to 1315 consisted of capped columns, dendrites, radiating assemblages of dendrites, graupel, graupel-like snow, bullets, aggregates, plates, and assemblages of plates. The degree of riming of these crystals varied from unrimed to densely rimed. During the period of expected seeding effects (1315-1525), plates and assemblages of plates were not observed, however, plates with extensions, stellars, radiating assemblages of sectors, and double crystals were observed in addition to the other crystals observed earlier. A significant decrease in the precipitation rate also occurred at Hyak prior to seeding but there was an increase during the predicted period of effect (Fig. 5.37).

Crystal types observed at Keechelus Dam prior to seeding were moderately rimed to unrimed dendrites, radiating aseemblages of dendrites, radiating assemblages of sectors, side planes, assemblages of plates, aggregates and capped columns. If it is assumed that the seeded plume was carried a few miles further south than that shown in Fig. 5.35 (which is certainly within the margin of error of our calculations) the effects of seeding should have been observed at Keechelus Dam within the time period 1400 to 1640. During this period columns without caps and bullets were observed in addition to the previously mentioned crystals. The crystals collected on the ground during this period were unrimed. A significant increase in precipitation rate occurred at Keechelus Dam from 1315 until 1430 (Fig. 5.38)

Crystals were not collected at Kachess Dam, however, the only precipitation of the day fell at Kachess Dam between 1315 and 1340 which was about twenty minutes prior to the predicted period of effect (Fig. 5.38). An increase in precipitation also occurred at Stampede Pass between 1500 and 1600. However, stations upwind of the seeded area, for example Landsberg and Palmer (see Fig. 5.56), did not show any increases in precipitation during this period.

5.2.6 Summary of Effects Attributable to Seeding

5.2.6.1 Airborne Observations

Meager data were obtained from the continuous particle sampler in the seeded region, however, continuous particle sampler run 17 was within the seeded region and runs 19 and 20 were outside the seeded region but at the same altitude and in close proximity to run 17. In run 17 ice crystal concentrations as high as 8.0 cm^{-3} were measured and nearly all of the particles replicated were ice. In runs 19 and 20, on the other hand, lower ice crystal concentrations (3.0 and 0.5 cm^{-3}, respectively) were measured. Run 19 contained only ice crystals, however, run 20 had a high water-to-ice ratio. The maximum ice crystals size on run 17 was 250 μm while crystals up to 500 μm were observed on run 20 and 400 μm on run 19. From these observations it is apparent that the sample taken on run 17 was likely to have been affected by the artificial seeding.

The Flight Scientist observed progressively more brilliant sub-sun optical phenomena in the seeded region as discussed in §5.2.4.1. A sub-sun is produced by reflections from the basal faces of crystals, usually plates, which are oriented horizontally; the higher the concentration of ice crystals the more brilliant the sub-sun. Since brilliant sub-suns were observed in the seeded area it is concluded that they were due to seeding.

5.2.6.2 Ground Observations

Subtle changes in the habits of ice crystals collected at Alpental provide evidence that seeding affected the precipitation at this station. Needles and capped columns were observed prior to seeding while plates, assemblages of plates, and uncapped columns were observed during the seeding period (Fig. 5.37). Capped columns can grow at higher saturations than do uncapped columns and it can be seen from Table 5.10 that seeding occurred in the diffusional growth region of these crystals. The effect of seeding would be to reduce the water vapor content in the diffusional growth region thus causing the transition from capped to uncapped columns. The appearance of plates and assemblages of plates can be considered a direct effect of seeding. These crystal types were not observed either prior to or after the seeding period. From Table 5.10 it is apparent that seeding was favorable for development of these crystals. The degree of riming experienced by all of the crystals did not change significantly throughout the day, suggesting that seeding did not significantly affect the riming growth region. The appearance of graupel and graupel-like snow at Alpental during the seeding period only (Fig. 5.37) presents an interesting possible effect due to seeding on the occasion. As stated above, seeding most likely did affect the production of plates and columns and it can be conjectured that other crystal types were also affected (e.g., dendrites). Plates and columns tend not to aggregate but are subject to riming and the riming layer was apparently not significantly affected by seeding. Hence seeding in the diffusional growth layer produced a higher concentration of small, single crystals which may have subsequently fell through the riming layer and reached the ground as graupel.

The change in crystal habit observed at Hyak during the predicted period of effect of seeding was from plates and assemblages of plates to plates with extensions, double crystals, radiating assemblages of sectors and stellars to unrimed capped columns, bullets, and assemblages of sectors toward the end of the period of effect (Fig. 5.37). This indicates,as do some of the observations at Alpental, that the seeding probably did not glaciate all of the cloud.

Snow crystal data were not obtained at Keechelus Dam during the period 1315 to 1430 due to lack of snowfall. However, during the predicted period of effect of the seeding (allowing for a somewhat more southerly drift of the plume than that shown in Fig. 5.35) many different types of unrimed crystals appeared (Fig. 5.38).

Finally, at Alpental, Hyak, and Keechelus Dam there were significant increases in precipitation during the predicted period of effects of the seeding. Similar increases in preciptation did not occur at stations situated upwind of the seeded area.

It is concluded from these observations that on this occasion that the artificial seeding did not cause widespread glaciation of the clouds, particularly in the lower levels, although it probably caused some decrease in riming. The principal effect of the seeding appeared to be to cause significant increases in precipitation at the ground throughout our target area.

5.3 January 13, 1972

5.3.1 Synoptic Situation

The surface synoptic map for 1300 PST on January 13, 1972, (Fig. 5.39) shows a very weak pressure gradient over Washington State. There was an Arctic high pressure system to the northeast, a high to the southwest over the Pacific Ocean, a low pressure center far to the southeast and another low approaching from the northwest. Broken cloud extended over the Pacific Northwest. The clouds were generally stable with layers from 4,000 to 20,000 ft. The 850 mb map for 1600 PST shows cool air over the Cascade Mountains and slow warm advection. Aloft there was a tight gradient indicating a strong northwest flow from the Gulf of Alaska, through Washington State, to the South Central States. A time-cross section based on rawinsondes launched from Quillayute (on the Pacific coast of Washington) is shown in Fig. 5.40.

Precipitation over Washington was light and generally confined to the coast and the mountains. It was most likely the result of an onshore flow of

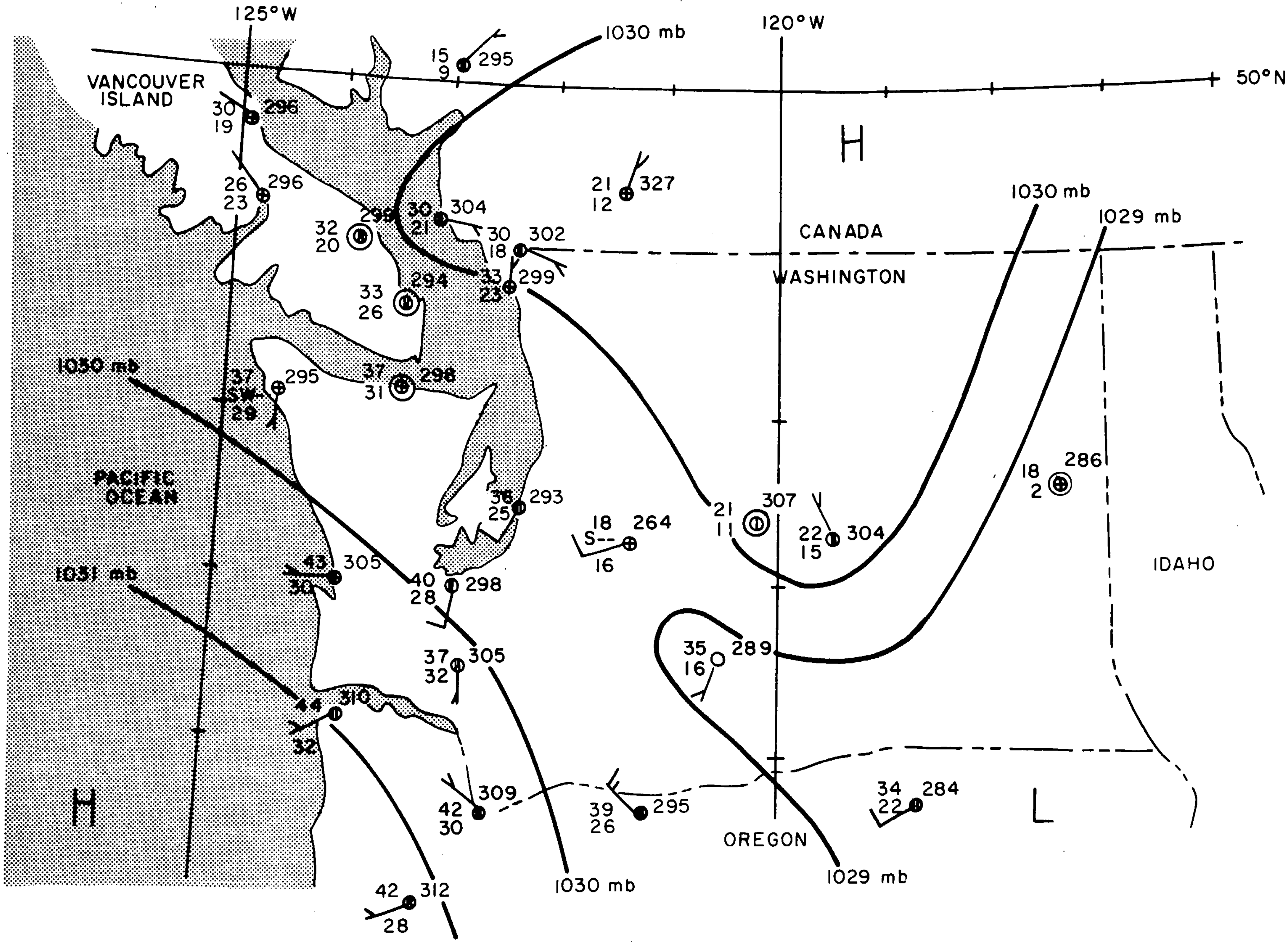

Fig. 5.39 Surface synoptic situation at 1300 PST on January 13, 1972.

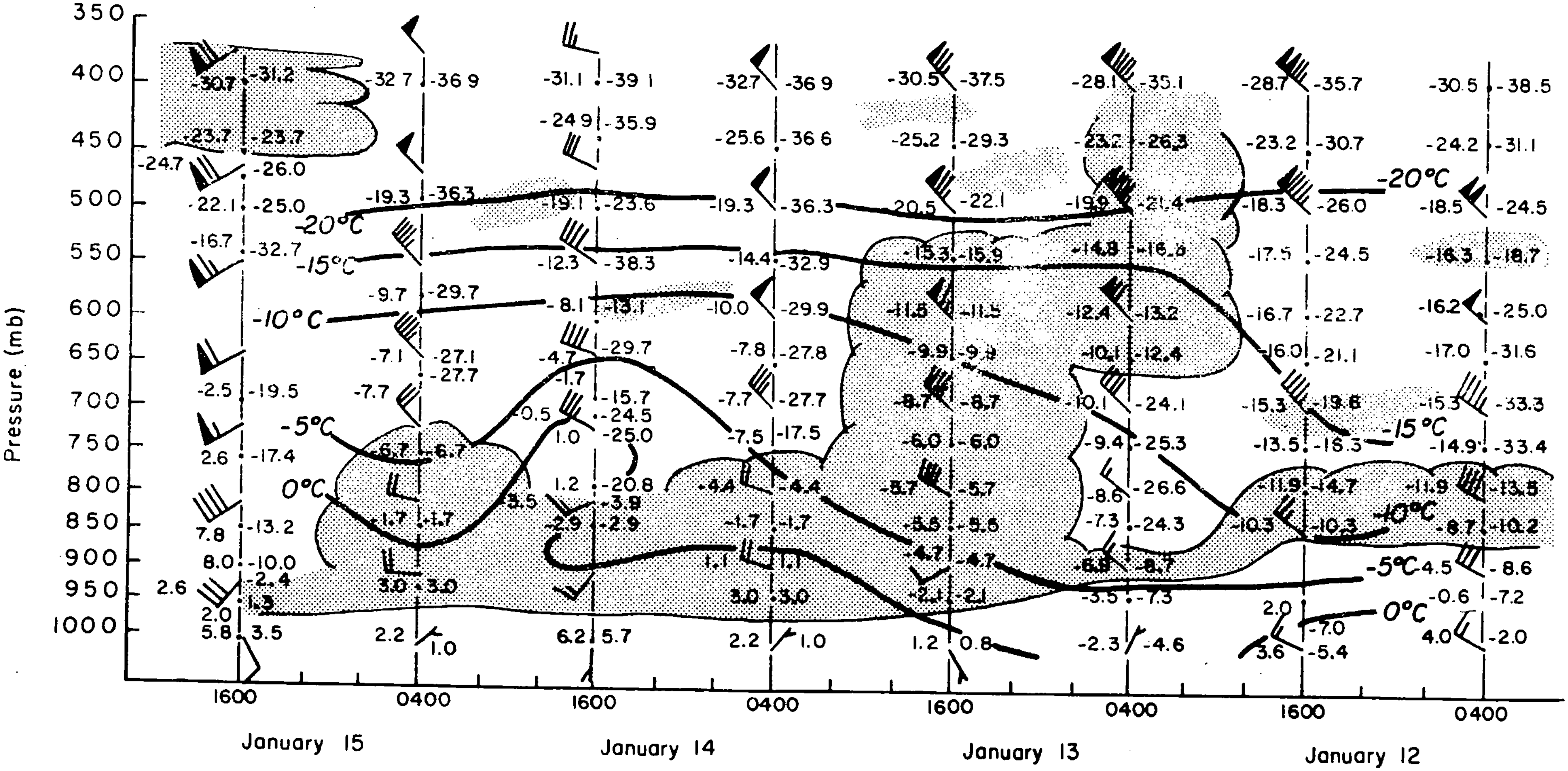

Fig. 5.40 Time cross-section for soundings at Quillayute between January 12-15, 1973.

moist air in the lower layers being lifted over the mountains by strong winds in the middle and upper layers to form orographic cloud and precipitation.

5.3.2 Airborne Observations

The period of the flight was from 1105 to 1432 PST; the flight route is shown in Fig. 5.41. During the first part of the flight (1120-1220) the cloud cover over the Cascades consisted of rather small broken cumulus and stratocumulus with tops up to about 7,500 ft. above MSL (Fig. 5.42). Later in the flight the cloud top rose to about 10,000 ft. and some lenticular clouds appeared at higher levels (Fig. 5.43a). The clouds below 7,500 ft. consisted mainly of supercooled droplets as evidenced by glories (Fig. 5.43b) and cloud bows, also the continuous particle sampler showed predominantly water droplets with a few rimed ice particles (Table 5.14). It should be noted however that temperatures were unusually low (-17°C at 8,500 ft. recorded from the aircraft and -4.6 to -6.7°C at the Alpental base station).

Artificial seeding was carried out from 1245 to 1313 in the area shown in Figs. 5.41 and 5.42 with the aircraft flying at 11,000 ft. Seeding was carried out with dry ice at a rate of 10 lb. per mile. Seeding with AgI ejection flares was also called for but, due to a malfunction, only two AgI 10-gm ejection flares were released during the seeding period (the AgI from these flares would have been dispersed between 9,000 and 6,000 ft.).

The clouds that were seeded were rather patchy, small cumulus. Optical phenomena due to ice crystals were produced in these clouds by the seeding. Following seeding the aircraft flew downwind where visual observations and the continuous particle sampler data showed the glaciated clouds to be drifting over our target area on the around (Table 5.14).

5.3.3 Ground Observations

Observations made at the ground stations are summarized in Fig. 5.44. During the sampling period, 1000-1600 PST, the snowfall rates were very low. However, an important change in crystal types and riming occurred at Keechelus Dam between 1300 and 1340 and this was accompanied by a slight increase in the snowfall rate. Calculations based on the mean wind speed between the ground and the height of the seeded clouds, give 1303 to 1340 for the expected period of effect due to seeding at Keechelus Dam! Before and after the period 1300-1340, moderately to densely rimed dendrites and graupel-like snow fell at Keechelus Dam. From 1300-1340, the snow crystals collected were large aggregates (up to 8 mm in diameter) of unrimed columns capped with stellars or plates, aggregates of unrimed stellars and a few dendrites. Also, the change

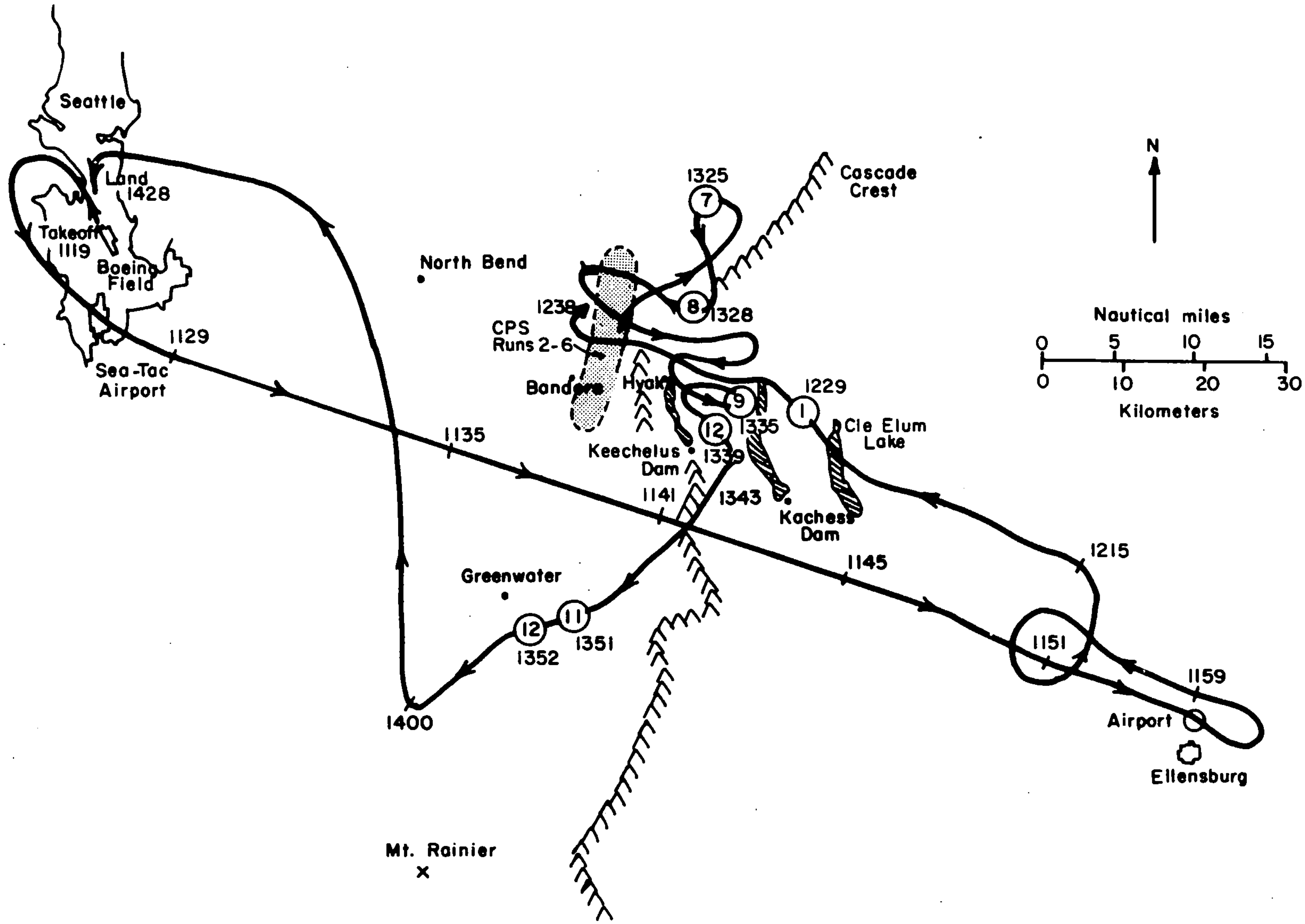

Fig. 5.41 Sketch of flight route (→) on January 13, 1972. The symbol (2) refers to Continuous Cloud Particle Sampler runs 2, etc. Four figure numbers give local time. ^Cascade Crest. ▒ Actual seeded area.

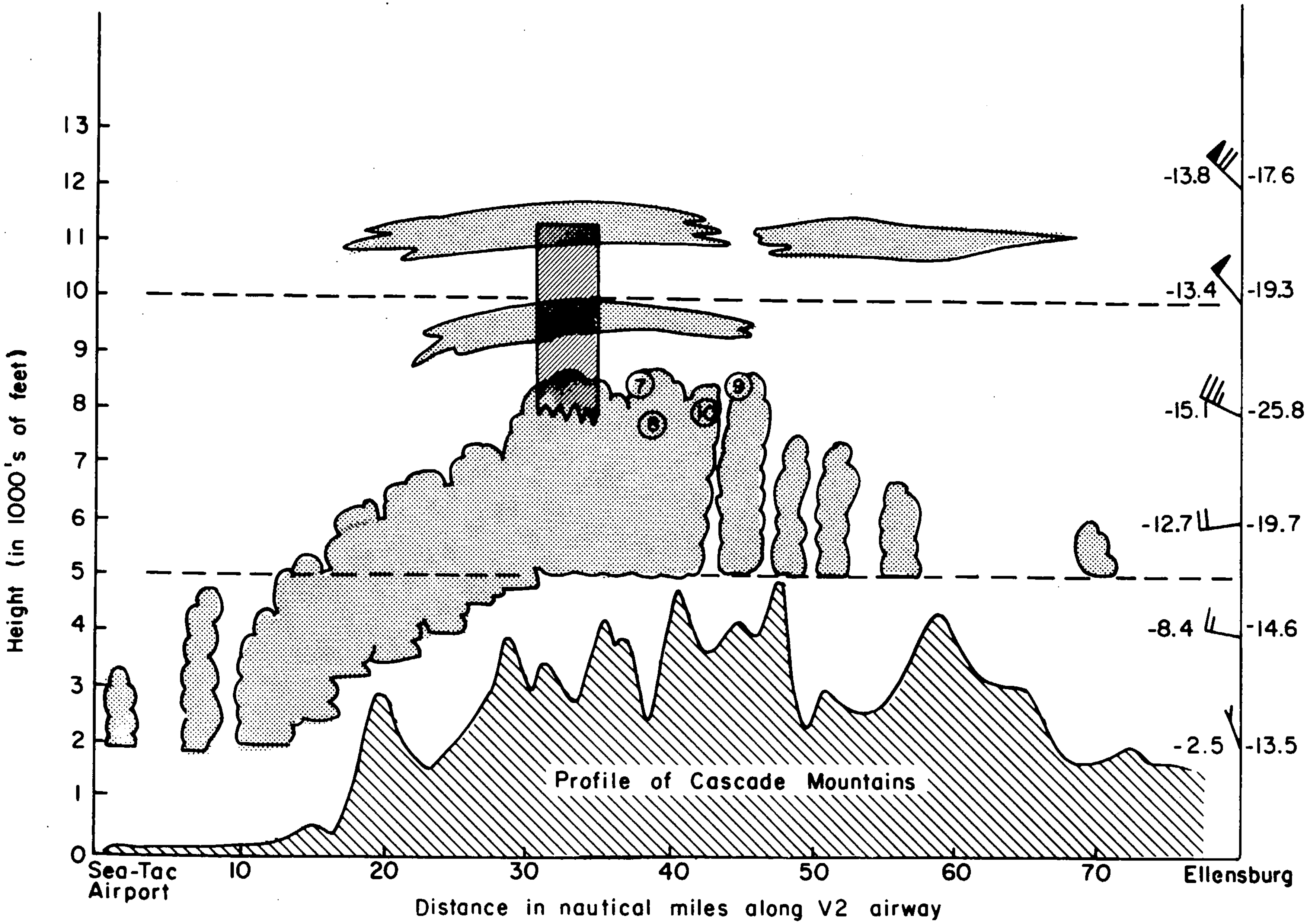

Fig. 5.42 Vertical cross-section from Seattle, Washington to Ellensburg, Washington, valid from 1200 to 1300 PST on January 13, 1972. Temperatures, dewpoints and winds are based on the 1249 PST rawinsonde from Greenwater (31 miles southeast of Sea-Tac Airport). Estimated area seeded by dry ice. (2) Continuous Particle Sampler runs taken after seeding.

(a)

(b)

Fig. 5.43 (a) Cloud conditions over western slopes of Cascade Mountains on January 13, 1972. Wave clouds can be seen over Mt. Rainier.

(b) Glory in unseeded clouds over Cascade Mountains on January 13, 1972.

TABLE 5.14

SUMMARY OF CLOUD PARTICLES COLLECTED WITH CONTINUOUS

PARTICLE SAMPLER ON JANUARY 13, 1972

(See Figs. 5.40 and 5.41 for position of each run.)

Run No.	Water Drops		Ice Particles		Number Ratio of Water to Ice
	Diameter (μm)	Concen- tration (cm^{-3})	Type & Maximum Dimension (μm)	Concen- tration (cm^{-3})	
1	———	———	No data	———	———
2	———	———	No data	———	———
3	15-50 Last part only.	0.4-2.2	———	———	All drops.
4	———	———	50-250. Plate-like ice.	0.07-1.5	All ice.
5	10-50 Mean < 20.	———	———	———	All drops.
6	8-15 First part only.	28-70	30-150. Irregular and plate-like.	0.07-0.7	100:1 at first, 1:5 later.
7	15-50 Many clear areas.	33-82	30-150. Frozen drops in groups. Some irregular and plate-like ice. Heavy riming.	0.3 - 1	100:1
8	30-50 Possibly frozen. Isolated.	<0.15	50-300. Plate-like ice, hexagonal plates, branched and sectored crystals.	0.16-1.6 Mean 0.8, higher later.	1:5, 1:50 later
9	15-40 Many clear areas.	19-45	50-300. Plate-like ice, some small aggregates.	0.15-0.75	>100:1
10	15-50 Last part only.	15-30	———	———	All drops.

TABLE 5.14 (cont.)

Run No.	Water Drops		Ice Particles		Number Ratio of Water to Ice
	Diameter (μm)	Concentration (cm^{-3})	Type & Maximum Dimension (μm)	Concentration (cm^{-3})	
11	15-25 Isolated drops to 50.	27-70	————	————	All drops.
12	15-70 Data on last part of run only.	25-42	————	————	All drops.

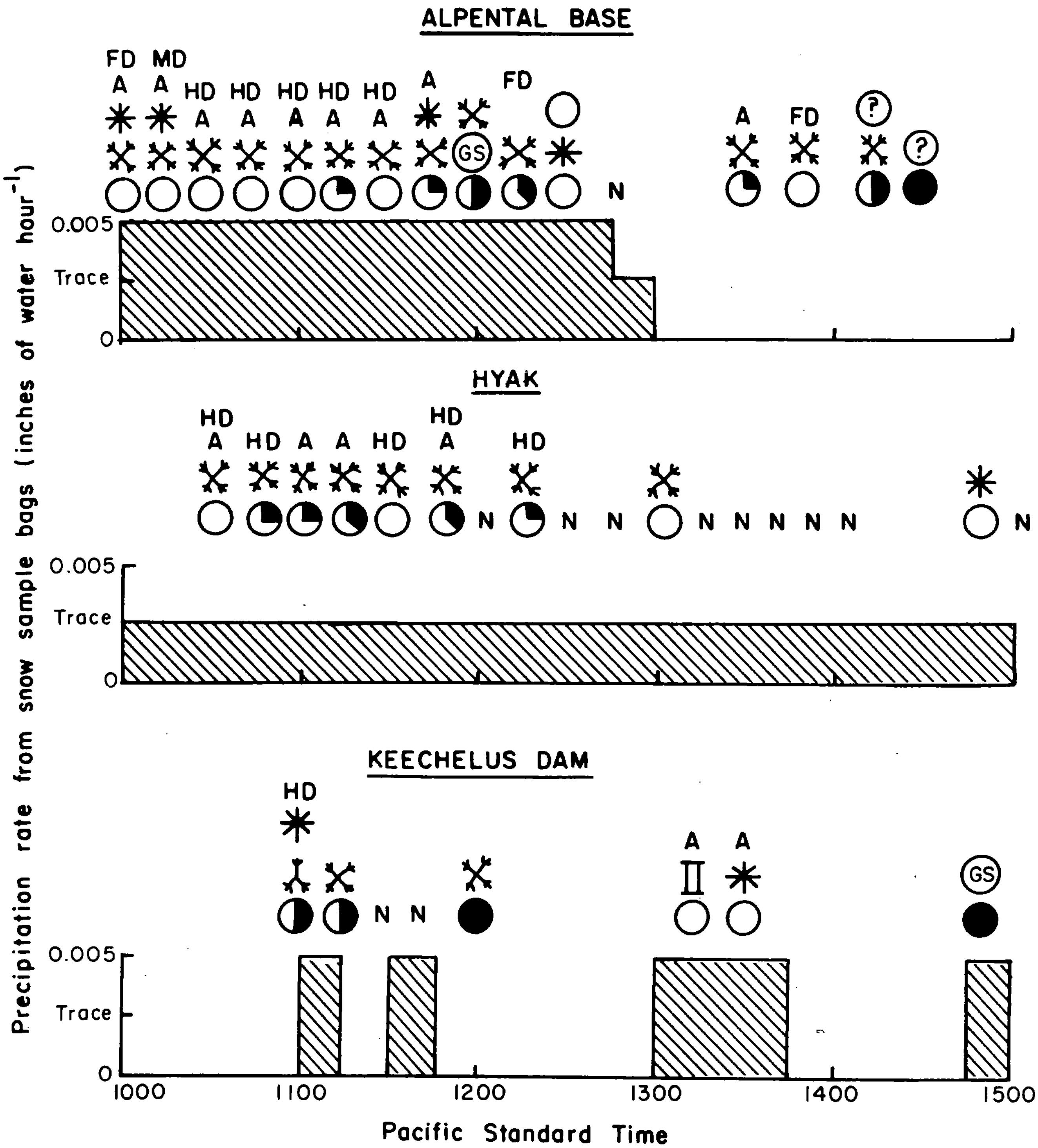

Fig. 5.44 Types of snow particles and precipitation rates at ground stations on January 13, 1972. See Table 4.1 for key to symbols.

from dendrites before seeding to stellars during the predicted period of effect (i.e., a change to crystals which grow at low supersaturations) confirms a seeding effect. At Hyak and Alpental the crystals were predominantly dendrites and they did not exhibit any appreciable changes which could be attributed to seeding (Fig. 5.44).

5.3.4 Ice Crystal Trajectories

Fig. 5.45 shows on a plain view of the target area the predicted trajectories of the aggregates which would have fallen at Alpental, Hyak and Keechelus Dam assuming average fall speeds of 0.5 and 1.5 m sec^{-1}. Fig. 5.46 shows cross-sections drawn from Fig. 5.45 of the projections of the trajectories on lines AB, CD, EF which pass through Keechelus Dam, Hyak and Alpental, respectively. The trajectories for Keechelus Dam should bracket the paths followed by the actual aggregates of unrimed stellars which were observed at that station. For Hyak and Alpental the trajectories indicate the paths which unrimed stellars would have followed if they had been observed at these two stations.

Also shown in Fig. 5.46 is the area that should have been affected by the continuous seeding with dry ice from the aircraft between 1245 to 1313. The lower limit of this area is taken as 8,000 ft., since our observations have shown that at a production rate of 10 lb. per mile the dry ice pellets do not survive for more than 3,000 ft. of fall.

It is clear from Fig. 5.46 that of the three ground stations, the snow crystals reaching Keechelus Dam had the best chance of being affected by the artificial seeding since stellar crystals produced in the seeded volume could have fallen out along trajectories which intersect the ground at Keechelus Dam.

5.3.5 Conclusions

Dry ice seeding at a rate of 10 lb. per mile was carried out west of the Cascade crest on January 13, 1972, under fairly stable orographic conditions. Airborne observations showed that the seeding caused glaciation of clouds over the target area. The location of the seeding was predetermined in order to affect precipitation in our small target area straddling the Cascade crest. Significant changes in precipitation attributable to the artificial seeding were not observed at Alpental or Hyak. A post-analysis of the region seeded and the likely trajectories of solid precipitation particles showed that seeding effects would not have been expected at these two stations. At Keechelus Dam dramatic changes occurred in crystal types and riming was

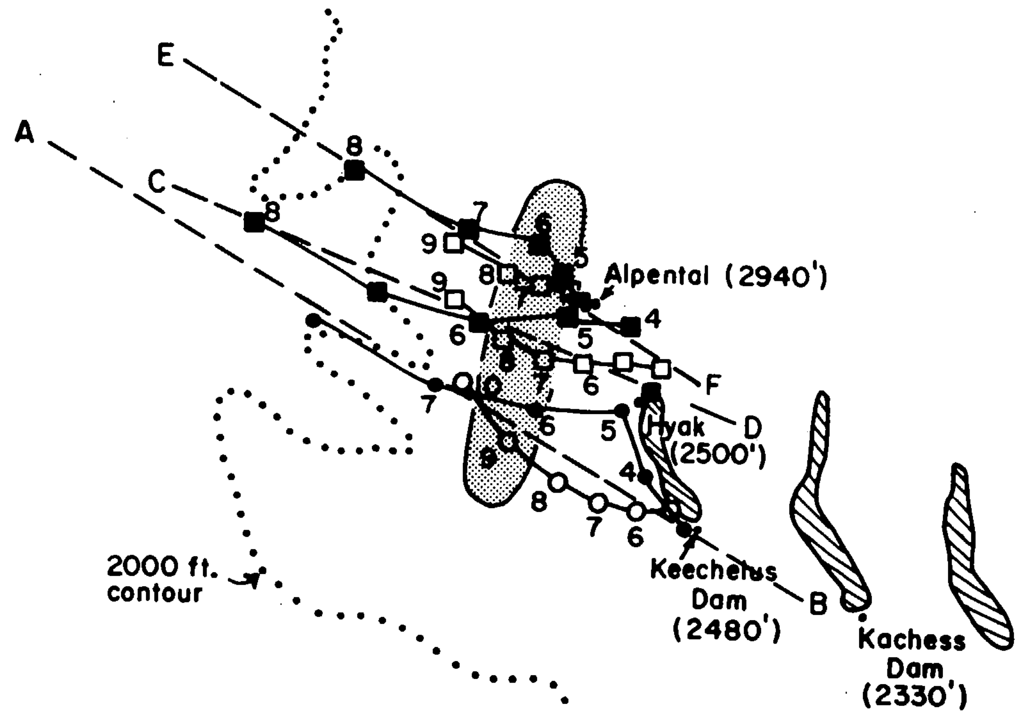

Fig. 5.45 Computed trajectories of precipitation particles which fell on the Cascade Mountains between 1300 and 1340 PST on January 13, 1972. Numbers against points give altitude of particle in thousands of feet. Path of slow aggregates of unrimed stellars. Path of fast aggregates of unrimed stellars. Path which slow aggregates of unrimed stellars would have taken if they had fallen. Path which fast aggregates of unrimed stellars would have taken if they had fallen. Seeding area.

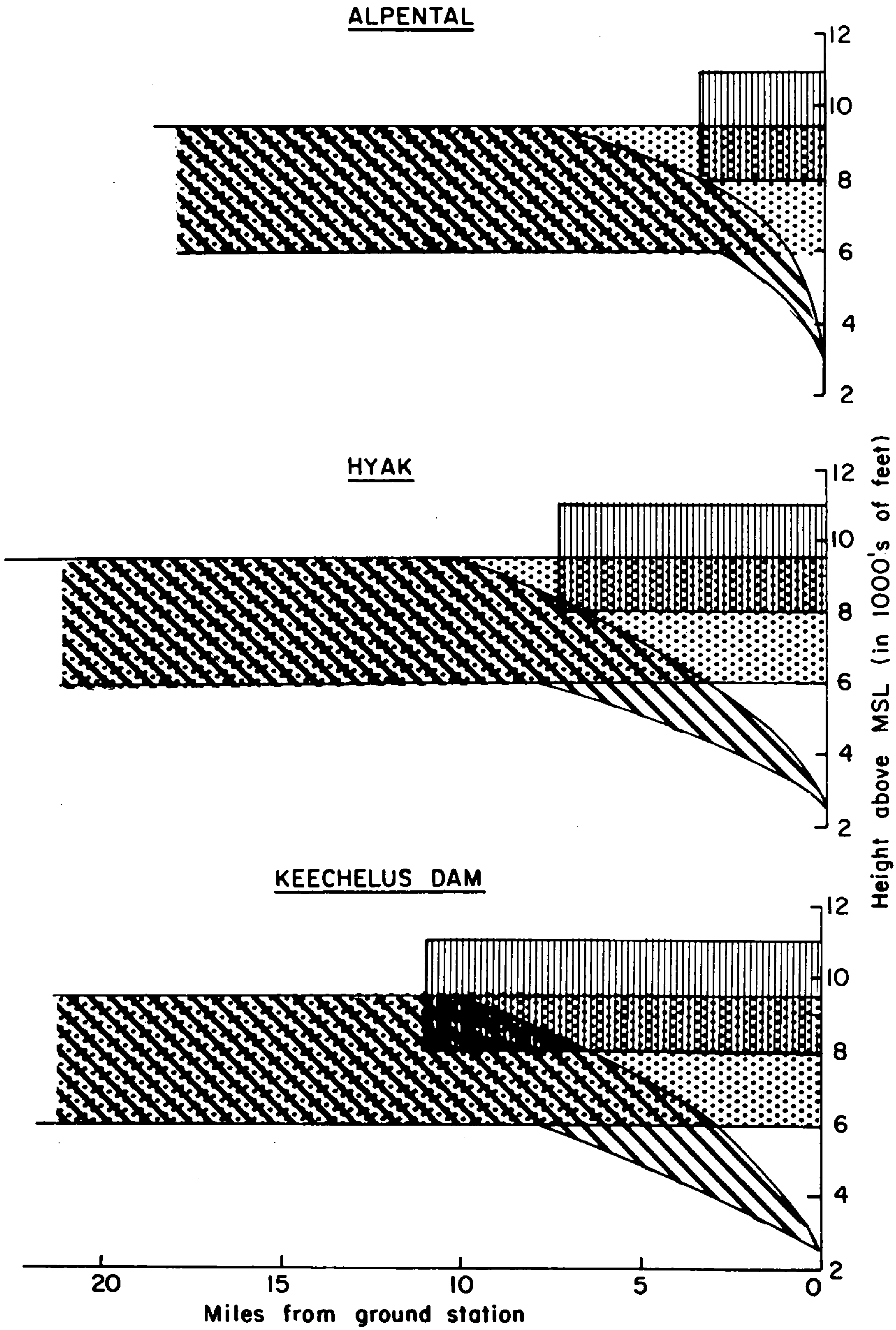

Fig. 5.46 Cross-sections of trajectories for aggregates of unrimed stellars over Cascade Mountains on January 13, 1972. Estimated area seeded with dry ice. Trajectories for aggregates of unrimed stellars. "Diffusional growth layer" for stellars.

eliminated from 1300 to 1340. This time period coincides almost exactly with that required for ice crystals produced by the seeding upwind to be carried to Keechelus Dam. Also, trajectory analysis shows that the types of crystals reaching Keechelus Dam during this period should have passed through part of the seeded area. Following the predicted period of effect due to seeding at Keechelus Dam, the snow crystals at Keechelus returned to normal (Fig. 5.44).

5.4 January 14, 1972

5.4.1 Synoptic Situation

The surface synoptic map for 1300 PST on January 14, 1972, is shown in Fig. 5.47 and a time cross-section from rawinsondes is contained in Fig. 5.40. A very weak pressure gradient existed over Washington State with a high pressure region to the east, a high to the west over the Pacific, with lows centered in the Gulf of Alaska and to the south of Washington. There was a low overcast over most of Western Washington, with thin layers of middle and upper cloud to the south and in the eastern part of the State. The 850 mb map showed a broad high pressure system over the Northwestern United States and out to the Pacific, with moderate westerly flow and slight warm advection. Aloft the pressure gradient indicated a west-north-westerly flow at about 40 knots.

Precipitation fell in the north of the State and on the western slopes of the mountains. It was produced mainly by moisture from the approaching frontal system, which was located off the British Columbia coast, as indicated in Fig. 5.40 by the strong warm advection in the middle layers over Quillayute. The precipitation was enhanced by orographic uplift due to the moderate northwesterly flow above 6,000 ft.

5.4.2 Airborne Observations

The flight route is shown in Fig. 5.48 and general cloud conditions encountered on the flight are indicated in Fig. 5.49. Cloud conditions were fairly stable throughout the period of the flight (1153-1443 PST) with some thickening occurring in the stratoform deck and stratocumulus later on in the flight. A strong inversion was present with minimum temperatures of -7 to -8°C at 8,500 ft. and temperatures of -2.1°C at 10,300 ft.

Prior to seeding, continuous particle sampler runs 2 and 3 were made at locations shown in Figs. 5.48 and 5.49. These showed that the clouds consisted entirely of water droplets from about 10 to 70 μm in diameter (mean diameter of about 50 μm, a few isolated up to 200 μm) in concentrations from 16 to 66 cm^{-3} (Table 5.15). These measurements were confirmed by observations of cloud bows [Fig. 5.50(a) and (b)].

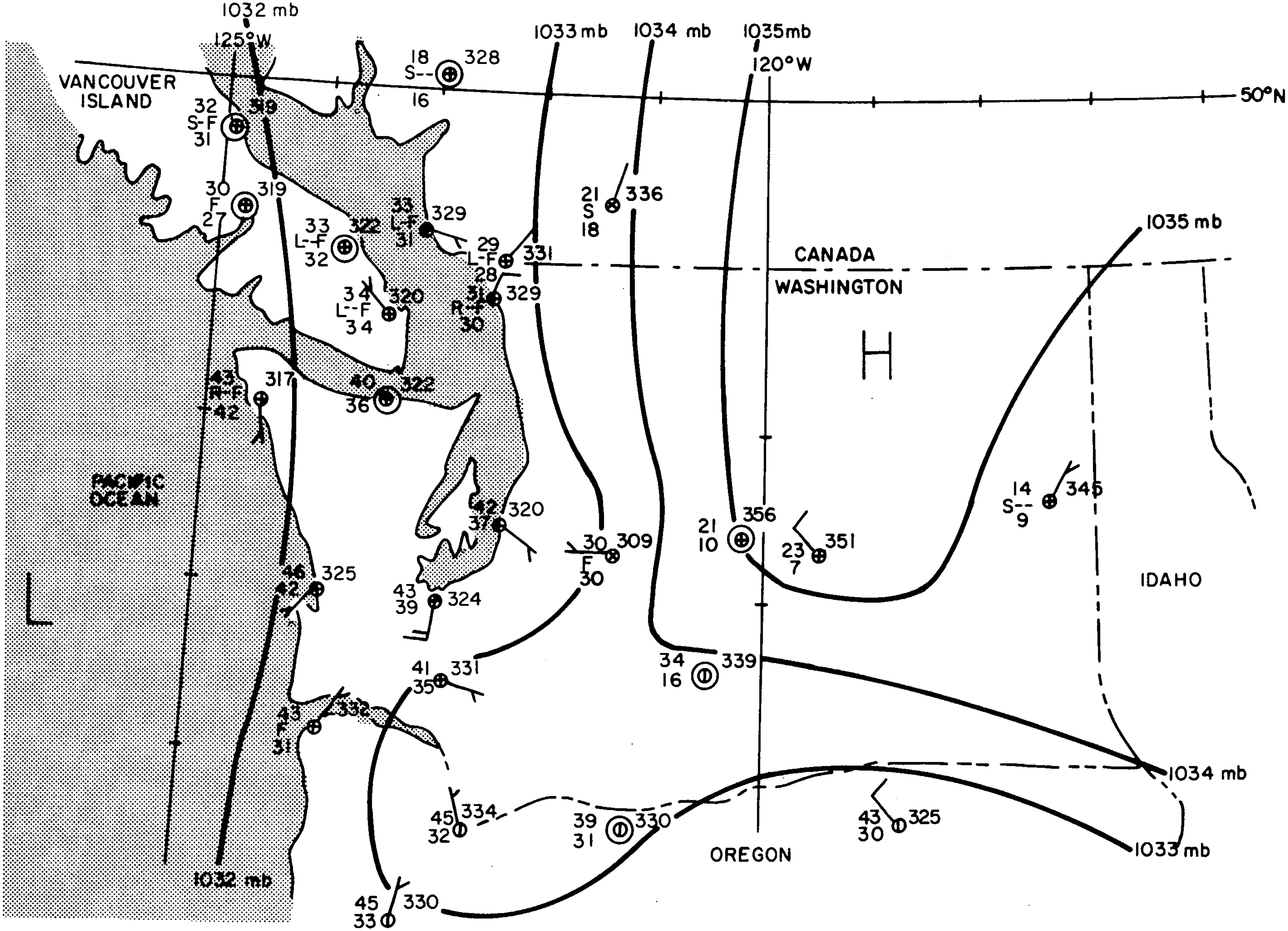

Fig. 5.47 Surface synoptic situation at 1300 PST on January 14, 1972.

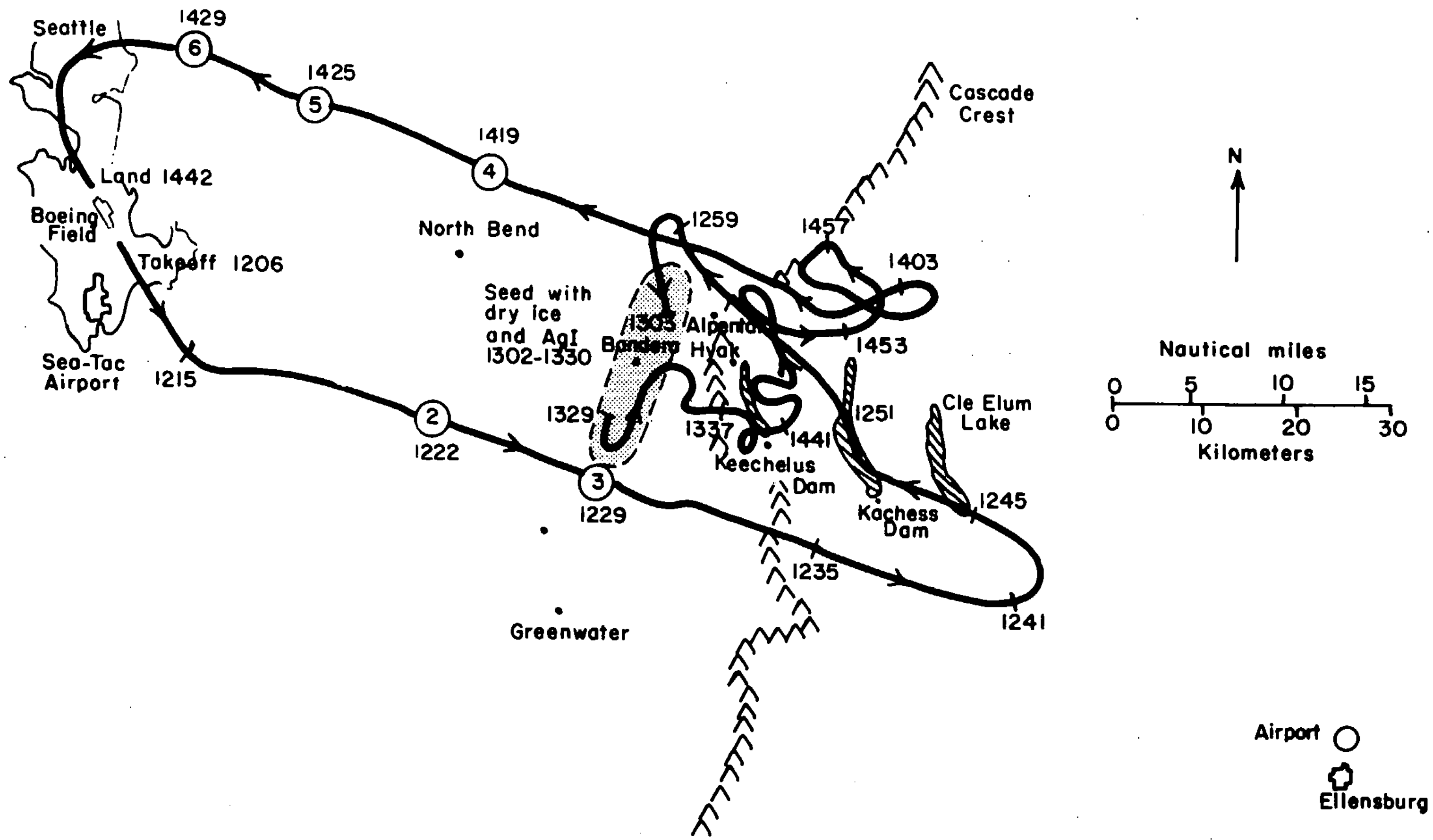

Fig. 5.48 Sketch of flight route (⟶) on January 14, 1972. The symbol (2) refers to Continuous Particle Sampler runs 2, etc. Four figure numbers give local time. ∧-Cascade Crest. ▒ Actual seeded area.

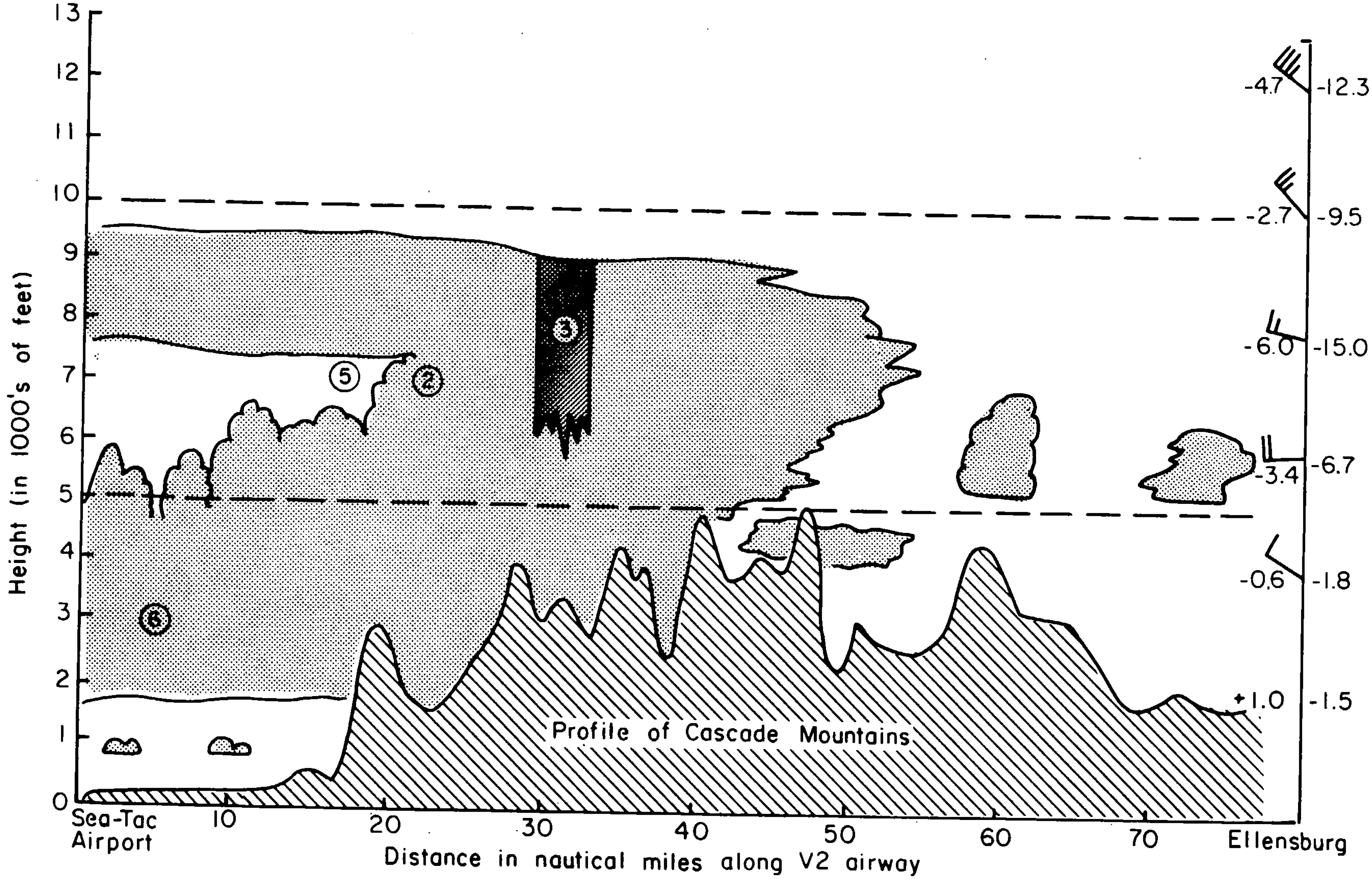

Fig. 5.49 Vertical cross-section from Seattle, Washington to Ellensburg, Washington, valid from 1220 to 1430 PST on January 14, 1972. The temperatures, dewpoints and winds are based on the 1252 PST rawinsonde from Greenwater (31 miles southeast of Sea-Tac Airport). Estimated area seeded by dry ice. (2) Continuous Particle Sampler runs.

TABLE 5.15

SUMMARY OF CLOUD PARTICLES COLLECTED WITH CONTINUOUS

PARTICLE SAMPLER ON JANUARY 14, 1972

(See Figs. 5.47 and 5.48 for position of each run.)

Run No.	Water Drops		Ice Particles		Number Ratio of Water to Ice
	Diameter (μm)	Concentration (cm^{-3})	Type & Maximum Dimension (μm)	Concentration (cm^{-3})	
1	———	———	No data.	———	———
2	15-70 Isolated drops to 200. Mean 50.	19-66 Some splashed larger drops.	———	———	All drops.
3	10-70 Isolated drops to 150. Mean 50.	16-66	———	———	All drops.
4	———	———	No data.	———	———
5	15-100 Splashed raindrops, with melting ice.	1.3-13	100-300. Rounded irregular melting ice in larger drops.	∿0.065	30:1
6	15-100	220-370	———	———	All drops.

Fig. 5.50 (facing page) Time sequence of photography showing effects of artificial seeding on January 14, 1972. (continued in Fig. 5.51)

(a) and (b) Prior to seeding, measurements and optical effects, such as the cloud bows shown here, showed that the region near the top of the stratoform cloud deck was composed of water droplets of nearly uniform size.

(c) The aircraft seeded from cloud top using both AgI and crushed "dry ice". As the seeding progressed the aircraft downwash and the shower of "dry ice" cut distinct furrows in the cloud top.

(d) The series of seeded strips of cloud quickly merged together and left large areas of the cloud top significantly more broken and uneven in appearance than the unseeded cloud. The first signs of partial glaciation are evident in the weak sub-sun and partial lower tangent arc seen in this photograph.

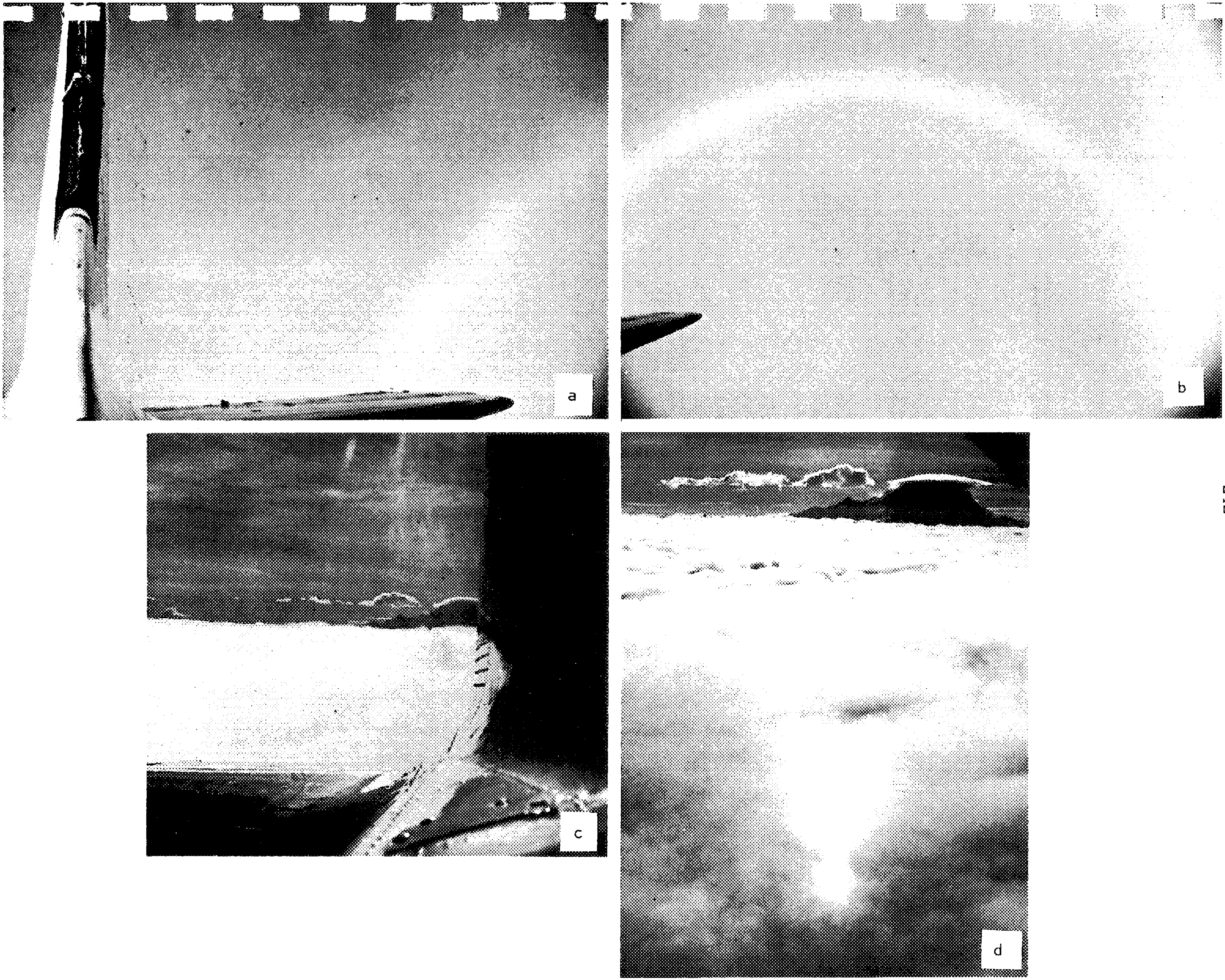
a
b
c
d

Artificial seeding was carried out between 1302 and 1329 PST as the aircraft flew just above cloud top (8,000-9,000 ft.) west of the Cascade crest (Fig. 5.48). Dry ice was dispersed at a rate of 10 lbs. per mile and 192 grams of AgI in pyrotechnic flares attached to the aircraft was burned at a rate of about 7 gm min^{-1} (three Colspan 64-gm end burning flares). Since the aircraft was flying in and out of the cloud top and as temperatures were fairly high, the dry ice was probably much more effective in causing the glaciation of the clouds which was observed following seeding.

During seeding the condensation trails produced by the dry ice pellets were clearly visible, as were vortex rolls produced by the aircraft. The region of cloud seeded by the dry ice was marked within a few minutes by a sharp trough in the upper layer of the cloud (Fig. 5.50c). As seeding progressed the tops of the stratocumulus clouds became more broken and uneven in appearance (Fig. 5.50d), but after ten to twenty minutes these ragged features smoothed out to produce a very uniform glaciated area which was quite distinct from the surrounding unseeded clouds [Fig. 5.51(a) and (b)]. Brilliant optical effects produced by ice crystals (e.g., columns) occurred in the seeded cloud [Fig. 5.51(c) and (d)]. By 1400 PST the clouds glaciated by seeding covered an area of about 400 km^2. As the seeded area drifted downwind the stratified droplet cloud reformed. Unfortunately, the main area of cloud affected by seeding was below the permissible flight level, therefore, the cloud particles could not be sampled with the continuous particle sampler.

5.4.3 Ground Observations

The snow crystal types and precipitation rates (where measured) on January 14 at Alpental Top, Alpental Base and Hyak are shown in Fig. 5.52. (At Keechelus Dam light rain fell between 0200 and 1800 PST, and at North Bend it was showery between 0001 and 1200 PST.) The direct effects of the artificial seeding upwind were predicted to affect Alpental between about 1315 and 1350. It can be seen from Fig. 5.52 that at Alpental Top the snow crystals changed from needles to columns at 1320 and then continued to fall until at least 1510 PST. Due to the fairly high temperatures the crystals were not replicated very well and it was not possible to deduce the degree of riming of the crystals after the transition in types at Alpental Top. Although melting obscured the crystals for some of the time at the lower elevation stations, there was no evidence that they underwent similar transitions to those observed at Alpental Top.

The maximum length of the columns which fell at Alpental Top between 1330 and 1400 PST was 0.5 mm. By comparison the size distribution of columns based

Fig. 5.51 (facing page) Time sequence of photographs showing effects of artificial seeding on January 14, 1972.

(a) and (b) As the intensity of the optical reflection and refraction phenomena increased, the contrast between the seeded and unseeded cloud also increased. In this photograph the seeded cloud is in the foreground.

(c) and (d) Within 20-30 minutes after seeding the rather ragged features of the cloud top smoothed out into a uniform and rather diffuse appearing glaciated cloud sheet. In this glaciated region the most intense and sharply defined optical effects were observed. These photographs show the lower tangent arc to the 22° halo, a portion of the 22° halo, a subsun and sub-parhelia. During this period the paranthelic arc was also observed.

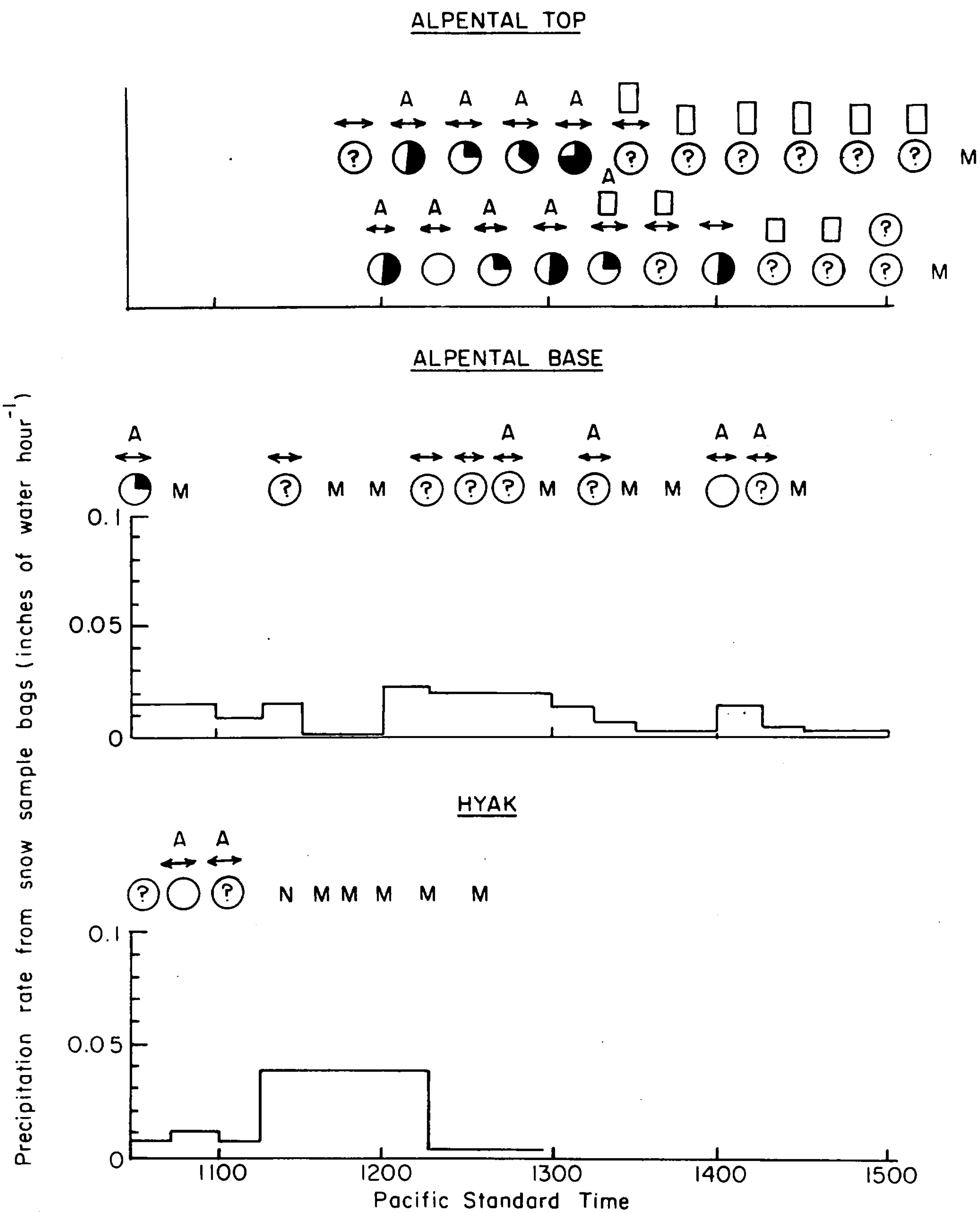

Fig. 5.52 Types of snow particles and precipitation rates at ground stations on January 14, 1972. See Table 4.1 for key to symbols.

on all data collected at Alpental Base during the winter of 1970-71 extended up to 1.5 mm in length.

5.4.4 Ice Crystal Trajectories

We have noted above that following artificial seeding needles were replaced by columns at Alpental Top. Trajectories for columns were computed assuming that their "diffusional growth layer" was similar to that for needles, except that the lower boundary of the layer was raised slightly since columns form only up to -5°C compared to -4°C for needles. The results are shown in Figs. 5.53 and 5.54. It is clear from these diagrams that seeding was carried out within the "diffusional growth layer" of the columns reaching Alpental Top. The effects of the heavy seeding in this layer was to cause glaciation and a reduction in humidity. This in turn would have resulted in needles being replaced by columns, the former grow only under water saturated conditions while the latter grow at sub-saturated conditions with respect to water.

5.4.5 Conclusions

Artificial seeding with dry ice and AgI pyrotechnics was carried out from the aircraft flying at cloud top west of the Cascade crest on January 14, 1972, under fairly stable orographic conditions. The effects of the seeding in glaciating large areas of cloud were clearly seen from the aircraft. Snow crystals falling at Alpental Top changed from needles to columns shortly after seeding. Trajectory analysis shows that this change could have been produced by the artificial seeding. Moreover, the observed transition in crystal types is that to be expected if the seeding resulted in glaciation of the clouds. Since seeding occurred from 1302 to 1320 and columns persisted at Alpental Top to at least 1510, some type of self-generating mechanism of the seeding effect is implied. Precipitation rates were not measured at Alpental Top but the rates at Alpental Base are shown in Fig. 5.52. It should be noted that Alpental was the only station in the mountains where precipitation was recorded after 1200 PST. It is quite likely that the precipitation at Alpental after about 1315 PST was produced by the artificial seeding. Unfortunately, temperatures were close to 0°C at Alpental Base and this prevented good observations of the crystal types and their degree of riming.

5.5 March 3, 1972

5.5.1 Synoptic Situation

At 1300 PST on March 3, 1972, a flat ridge of high pressure extended over the Pacific Northwest (Fig. 5.55). At 850 and 500 mb a short wave trough had passed through during the previous night with moderate cold advection (see

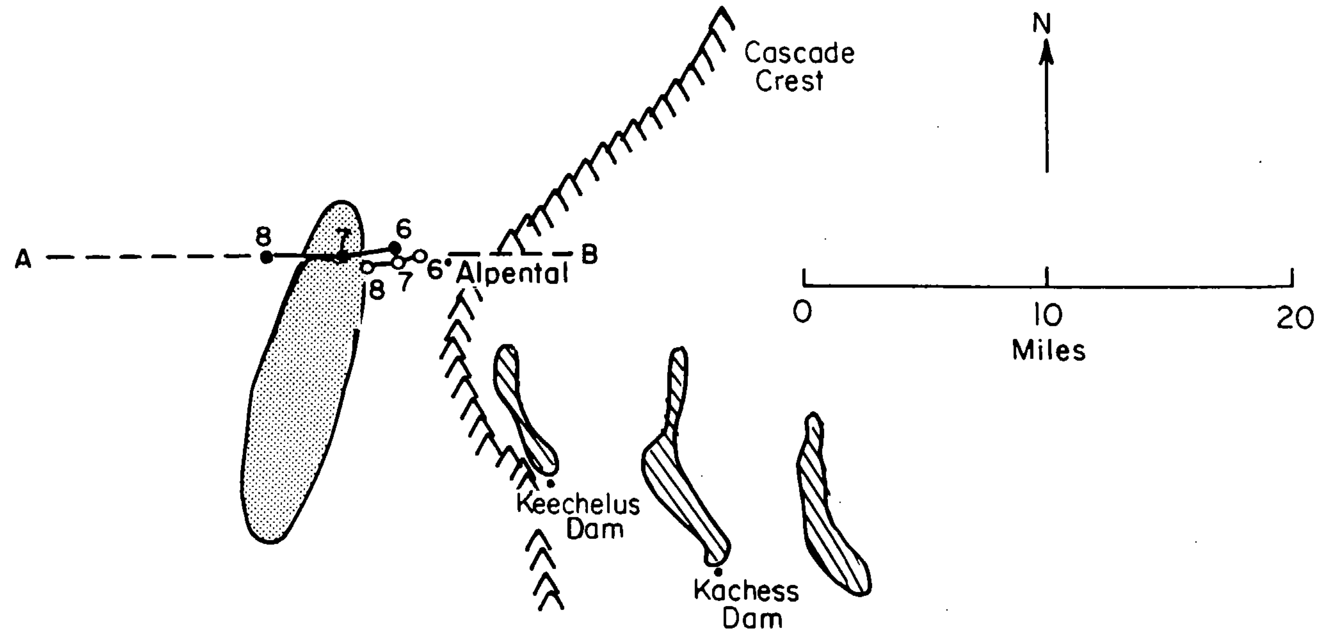

Fig. 5.53 Computed trajectories for slow (•——•) and fast (o——o) falling columns which fell on Alpental Top between 1410 and 1510 PST on January 14, 1972. Numbers against points give altitude of particles in thousands of feet. [shaded box] Seeded area.

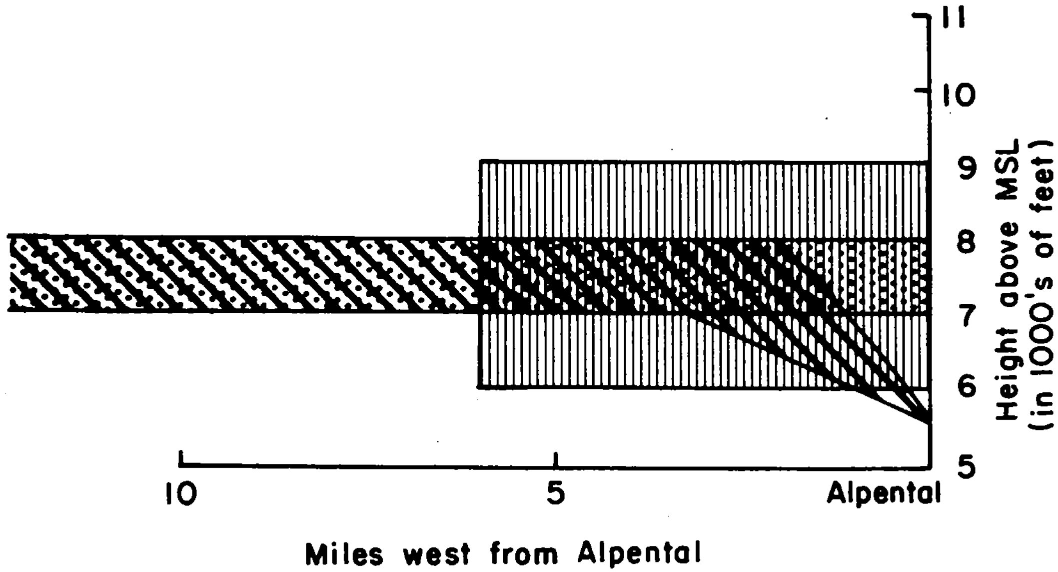

Fig. 5.54 Cross-section of trajectories along line AB in Fig. 5.53 for columns falling on Alpental Top between 1410 and 1510 PST on January 14, 1972. Estimated area seeded with dry ice. Trajectory of columns. Diffusional growth layer for columns.

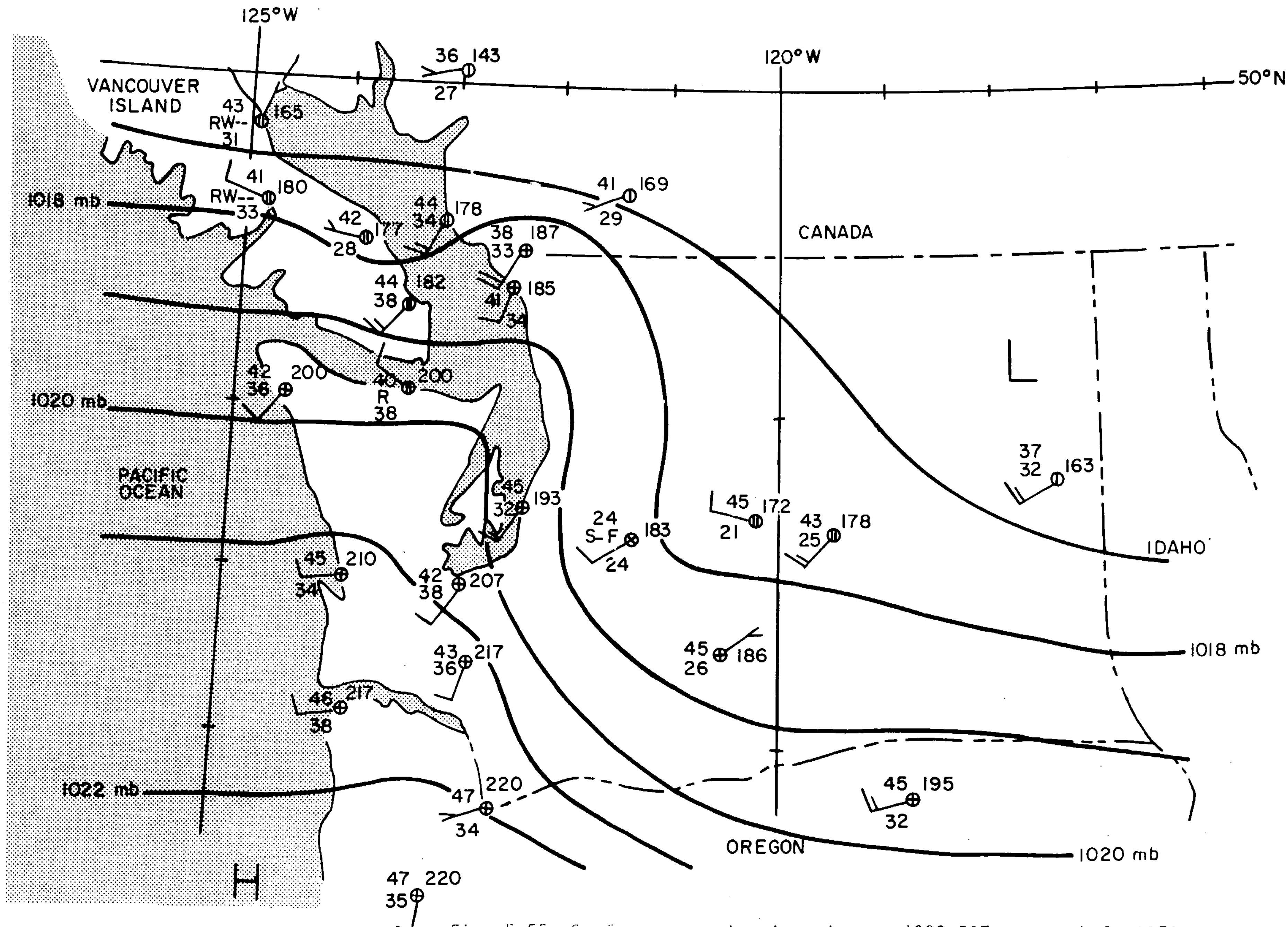

Fig. 5.55 Surface synoptic situation at 1300 PST on March 3, 1972.

Fig. 4.27). The main center of low pressure remained in the Gulf of Alaska. During the period of the aircraft flight (1100 to 1600 PST) the synoptic condition did not change significantly and the surface map for 1300 PST is representative of the general conditions. The onshore flow, with southwesterly winds, produced cloudy conditions in Western Washington and broken clouds east of the Cascade Mountains. The precipitation, except for widely scattered showers, was confined to the mountains.

5.5.2 Airborne Observations

The period of the flight was from 1126 to 1532 PST; the flight route is shown in Figs. 5.56 and 5.57. The lower clouds were cumuliform with stratified tops at about 8,000 ft. over the Puget Sound and 11,000 ft. over the Cascade crest (Fig. 5.58). On the first pass along airway V2 the lower clouds consisted primarily of water droplets with occasional rimed ice particles. Some ice appeared to be blowing out of the leeward edge of the clouds over the Cascade crest. Continuous particle sampler samples taken over the Cascade crest and prior to artificial seeding showed predominantly droplets with a few rimed ice crystals and frozen drops (Table 5.16).

Artificial seeding with AgI delay ejection flares was carried out from 1251 to 1440 PST in the regions just west of the Cascade crest shown in Fig. 5.56. Twenty-six 10 gm and two 40 gm AgI flares were released along the boundaries shown in Fig. 5.56. The aircraft was flying at 10,000 ft., therefore, the AgI was dispersed between 8,000 and 5,000 ft. above MSL. Continuous particle sampler runs 9-15, which were taken during the first period of seeding (1251 to 1404), showed that the clouds initially consisted almost entirely of water droplets (Table 5.6) but subsequently developed into ice. Between 1230 and 1330 cloud top decreased to about 10,000 ft. After 1410 the clouds appeared to be glaciated and the tops increased to about 11,000 ft. The crystals were predominantly irregular and hexagonal plates with a few stellars and broad-branched crystals. Continuous particle sampler samples taken downwind after seeding showed that the clouds over the target area on the ground were predominantly ice (except for continuous particle sampler run 23 which was in the most southerly position - Fig. 5.57). Continuous particle sampler run 24 that was taken near the center of the seeded area twenty-two minutes after the completion of seeding showed mainly ice (Table 5.16). Further west the cloud reverted to droplets (continuous particle sampler run 25).

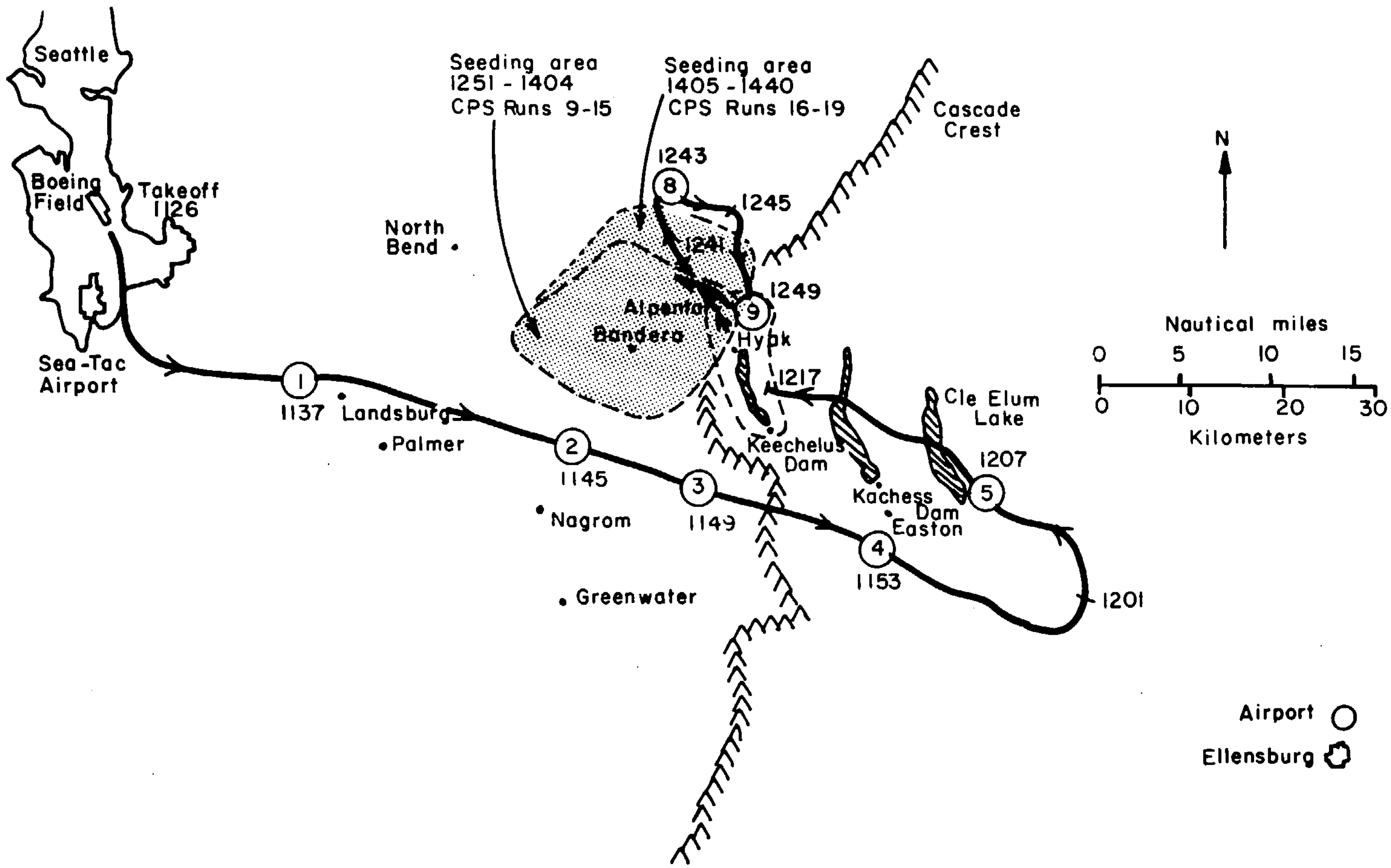

Fig. 5.56 Sketch of first part of flight route (⟶) on March 3, 1972. The symbol (2) refers to Continuous Particle Sampler run 2, etc. Four figure numbers give local time. /\-Cascade Crest. [shaded box] Actual seeded area.

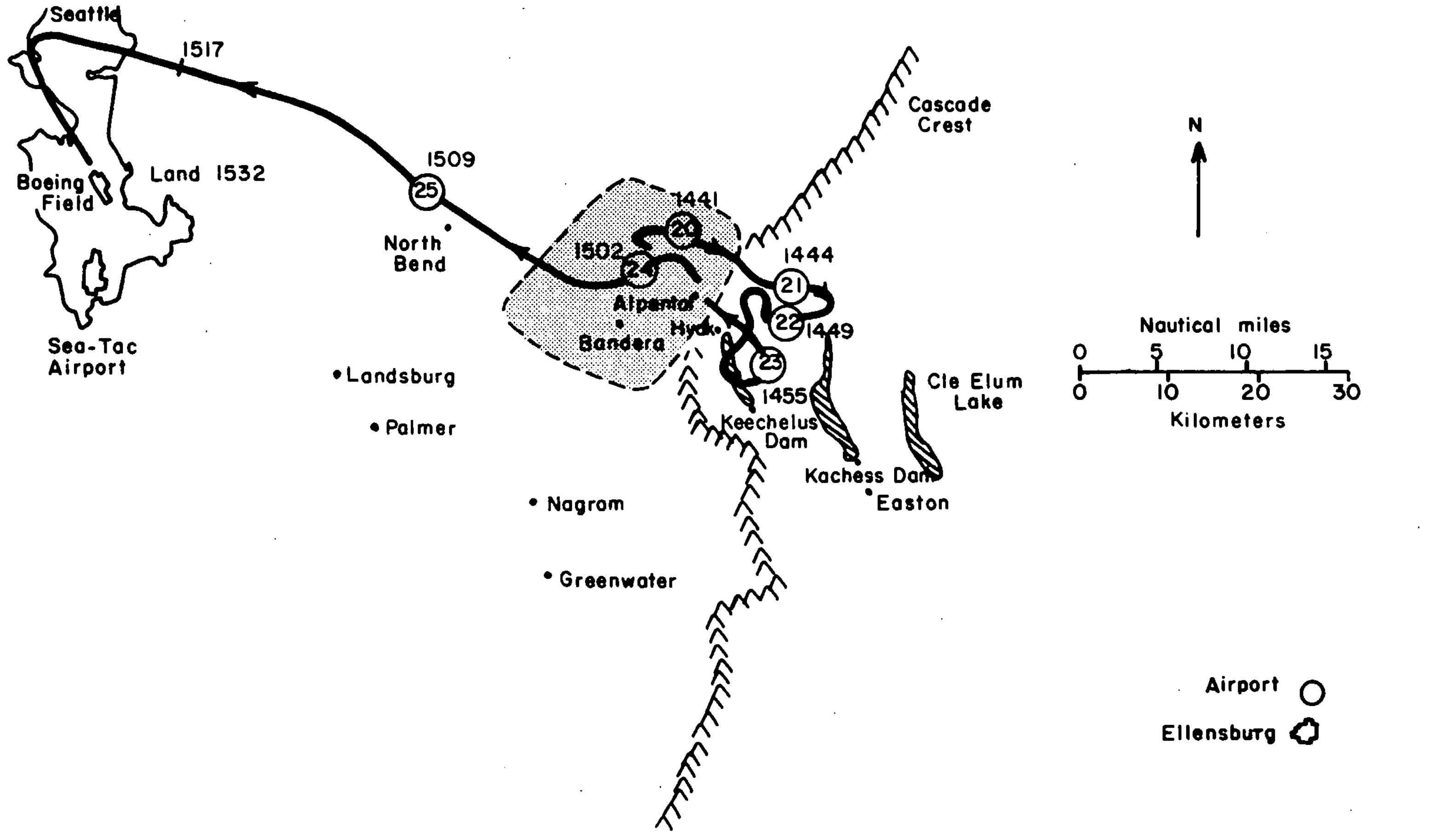

Fig. 5.57 Sketch of second part of flight route (→) on March 3, 1972. The symbol (2) refers to Continuous Particle Sampler run 2, etc. Four figure numbers give local time. ⋀ Cascade Crest. ▒ Actual seeded area.

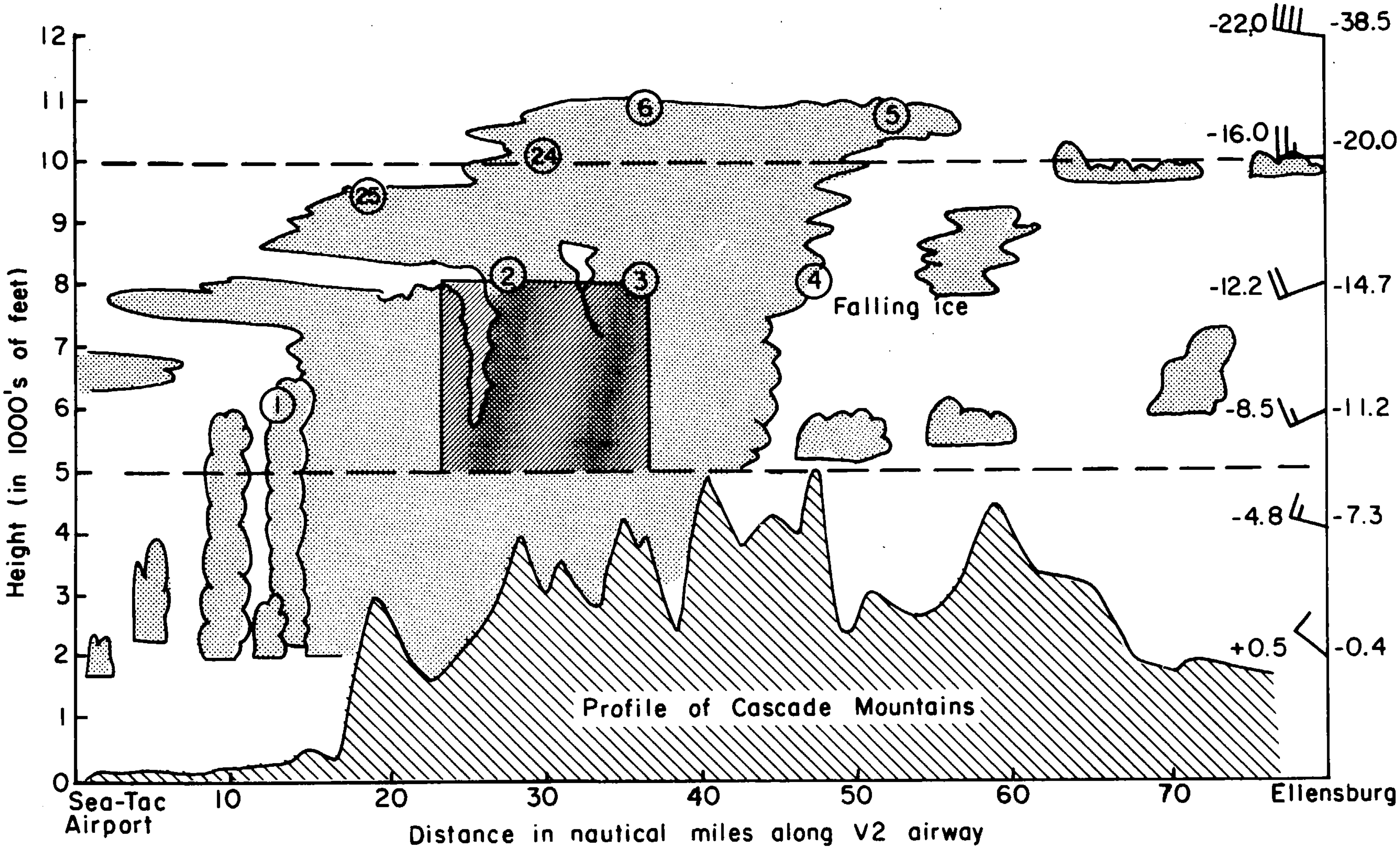

Fig. 5.58 Vertical cross-section from Seattle, Washington to Ellensburg, Washington, valid from 1130 to 1400 PST on March 3, 1972. Temperatures, dewpoints and winds are based on the 1258 PST rawinsonde from Greenwater, located 31 miles southeast of Sea-Tac Airport. Estimated area seeded by AgI. (1) Selected Continuous Particle Sampler runs.

TABLE 5.16

SUMMARY OF CLOUD PARTICLES COLLECTED WITH CONTINUOUS

PARTICLE SAMPLER ON MARCH 3, 1972

(See Figs. 5.56 and 5.57 for position of each run.)

Run No.	Water Drops		Ice Particles		Number Ratio of Water to Ice
	Diameter (μm)	Concentration (cm^{-3})	Type & Maximum Dimension (μm)	Concentration (cm^{-3})	
1	10-100	27-71	———	———	All drops.
2	20-50	4-26	100-200. Isolated irregular ice. One small rimed aggregate. Possible stellar parts.	<0.02	500:1
3	Mainly 20-30 Occasionally 100.	12-50	100-500. Irregular and columnar. Some plate-like. Slight to moderate riming.	0.08-0.8	80:1
4	15-40	3-14	60-500. Irregular and plate-like. Frozen drops. Moderate riming.	0.02-0.2	100:1
5	15-20 Mainly isolated to 60.	6.6-21	———	———	All drops.
6	10-50 Occasionally 70.	1.5-15 Patchy, some clear areas.	———	———	All drops.
7	10-60 Isolated to 120.	15-30	40-600. Irregular ice. Frozen drops, riming. Small rimed aggregates.	0.08-1.5	80:1 at first 10:1 later.
8	15-50 Occasionally to 70.	Up to 60. Mainly 7-30.	40-200. Occasional irregular ice. Some riming, and frozen drops.	<0.04	100:1
9	Mainly 30-40 at first. Later 15-70.	8-31	———	———	All drops.

TABLE 5.16 (cont.)

Run No.	Water Drops		Ice Particles		Number Ratio of Water to Ice
	Diameter (μm)	Concentration (cm^{-3})	Type & Maximum Dimension (μm)	Concentration (cm^{-3})	
10	15-60	9-26	40-150. A few irregular pieces of ice, two frozen drops.	<0.01	>1000:1
11	Mainly 20-30 occasionally to 50.	8-24	———	———	All drops.
12	15-40	13-35	———	———	All drops.
13	15-30 One patch of droplets only.	7-24	———	———	All drops.
14	Up to 40. 15-30 later. 10-20 at end.	4-23 Clear last part.	———	———	All drops.
15	10-40 Clear last half.	3-15	———	———	All drops.
16	15-50	4-20	50-150, irregular ice.	<0.01	Virtually all drops.
17	15-50	4-12	50-300. Irregular ice, with riming. Frozen drops, 1-800.	1.7-6	2:1
18	20-50	0.4-2.3	50-300. Plate-like and irregular. Some hexagonal plates.	0.8-3.8	1:2
19	20-60	0.1-0.4	50-700, mainly < 250. Irregular ice, hexagonal plates, broad-branched parts. Two stellars with plate-like extensions.	1.5-4.6	1:30
20	———	———	70-400, mainly < 200. Irregular plate-like, hexagonal plates and some columns.	0.3-1.4	All ice.

TABLE 5.16 (cont.)

Run No.	Water Drops		Ice Particles		Number Ratio of Water to Ice
	Diameter (μm)	Concentration (cm^{-3})	Type & Maximum Dimension (μm)	Concentration (cm^{-3})	
21	20-60	0.04-0.4	50-400. Irregular, irregular plate-like, and hexagonal plates.	0.16-1.6	1:5
22	30-80	0.02-0.2	80-350. Hexagonal plates and irregular ice.	0.14-1.4	1:10
23	15-25	25-100 Lower last part.	70-300. Plate-like, hexagonal plates and irregular.	0.16-0.8	50:1
24	20-70	0.14-1.4	70-600. Plate-like and hexagonal plates, 1-900 μm. A few frozen drops and aggregates. One stellar to 1300 μm. Some riming.	2.1-5	1:20
25	9-31	——	——	——	All drops.

5.5.3 Ground Observations

Precipitation rates, types of precipitation particles and their degrees of riming at three ground stations in the target area are shown in Fig. 5.59 (the crystal habits and riming at Alpental Top changed in a similar manner to those at Alpental Base). It can be seen that prior to about 1430 precipitation rates at all these stations were low and consisted of densely rimed dendrites, radiating assemblages of dendrites, graupel-like snow and graupel particles. From about 1430 to 1545 PST the precipitation rates increased sharply, the degree of riming decreased and additional crystal types appeared at the ground stations (aggregates, stellars, capped columns, assemblages of sectors, side planes and broad-branched crystals). Also during this period somewhat more crystals composed of two parallel plane plates separated by a frozen drop were collected than prior to 1430. At 1475 some very small plates (25-30 μm in diameter) were collected at Alpental Top. All of these changes indicate that the effects of the artificial seeding influenced the amounts and types of precipitation at the ground stations in the target area between about 1430 and 1545. After 1545 the precipitation rates decreased, riming increased again, and the new crystals which appeared between 1430 and 1545 disappeared. As we will see in §5.5.5, trajectory analysis shows that the direct effects of the upwind seeding should have been experienced at Hyak within the period 1310 to 1600 PST.

Snow samples collected at the ground at Alpental Base, Hyak and Keechelus Dam on March 3 were analyzed for their freezing nucleus concentrations. The results are shown in Figs. 5.60-5.62. It can be seen that increases in the concentrations of freezing nuclei were observed at all three ground stations during the period that seeding effects were expected.

5.5.4 Radar Observations

The radar measurements at Hyak began at 1020 PST on March 3 when the incoherent radar was turned on to survey the sky. At that time there was no precipitation at the radar station. At 1052 PST the Doppler radar was switched on and vertical probing began. At this time a few heavily rimed dendrites were falling at Hyak. Very light precipitation continued until 1200 PST when the incoherent radar was again used for a sky survey. Precipitation was observed at high altitude to the northwest. By 1207 PST the first weak signals were observed on the Doppler and the range gate was set out to 500 m. Particles with fall velocities from 1.5 to 2.0 m sec^{-1} were observed while heavily rimed stellars and graupel fell at the station. By

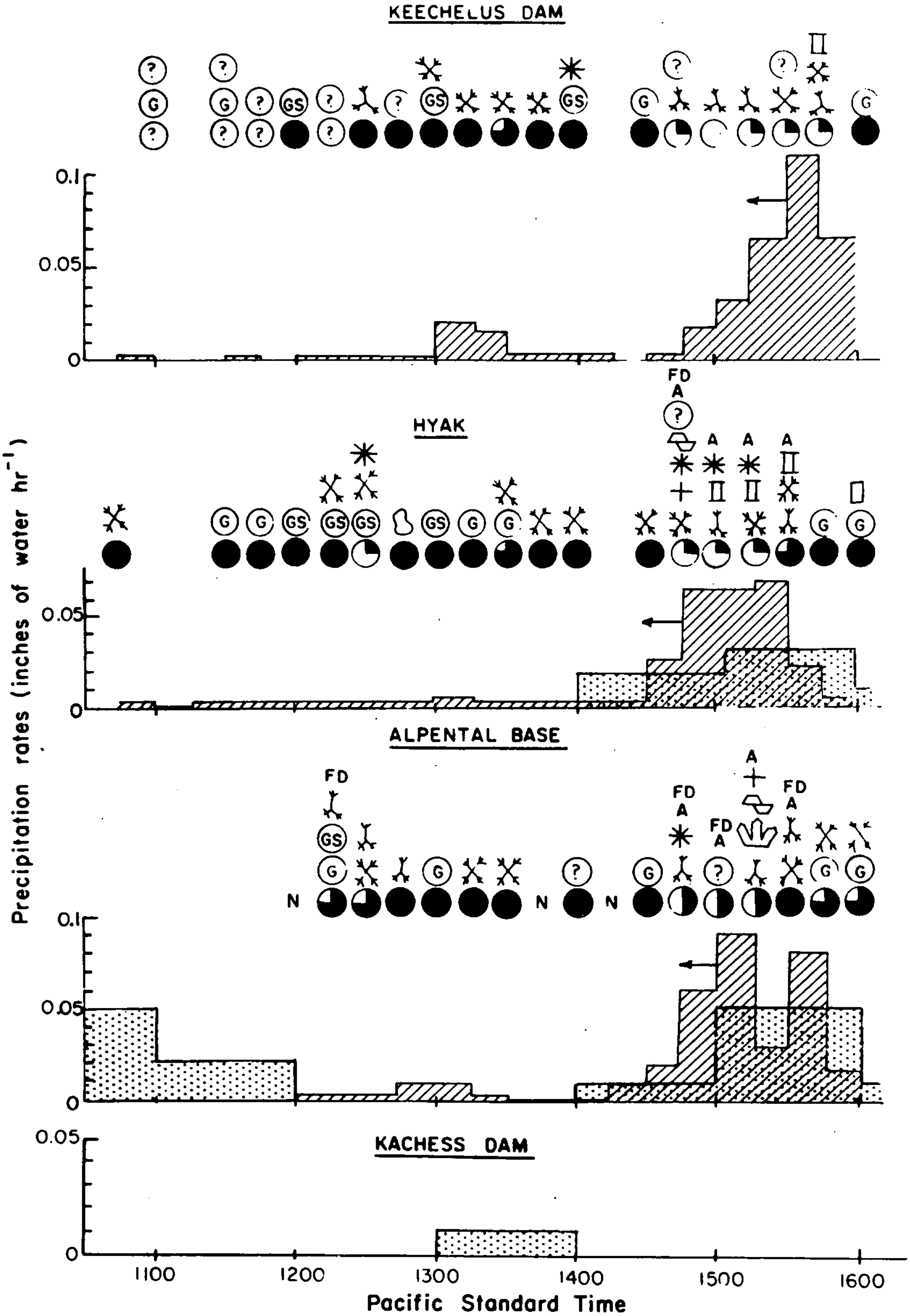

Fig. 5.59 Snow crystal types, riming and precipitation rates at three ground stations in target area on March 3, 1972. [hatched] Precipitation rates from snow bags. [stippled] Precipitation rates from weighing buckets.

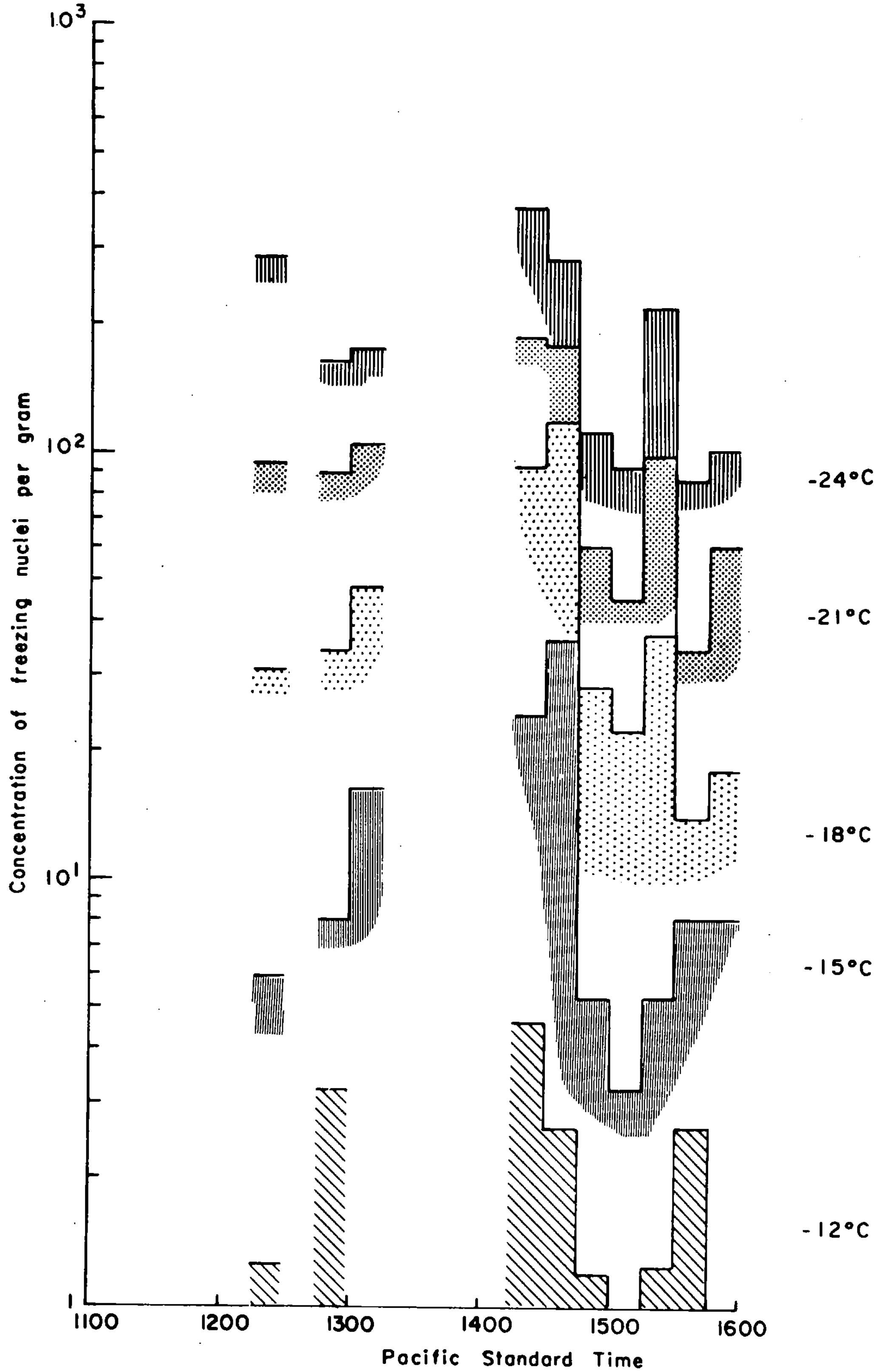

Fig. 5.60 Concentrations of freezing nuclei per gram of snow collected at Alpental Base on March 3, 1972.

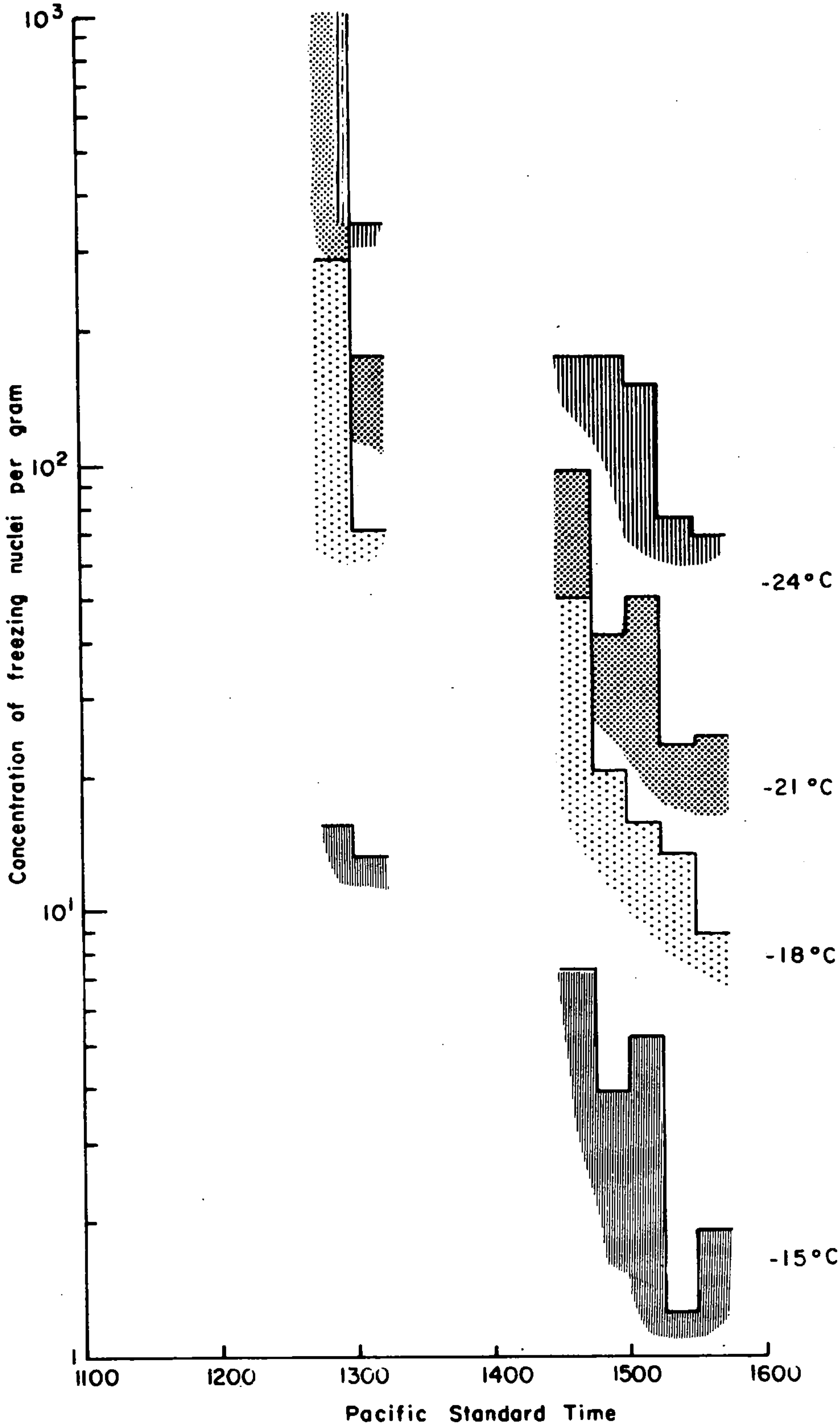

Fig. 5.61 Concentrations of freezing nuclei per gram of snow collected at Hyak on March 3, 1972.

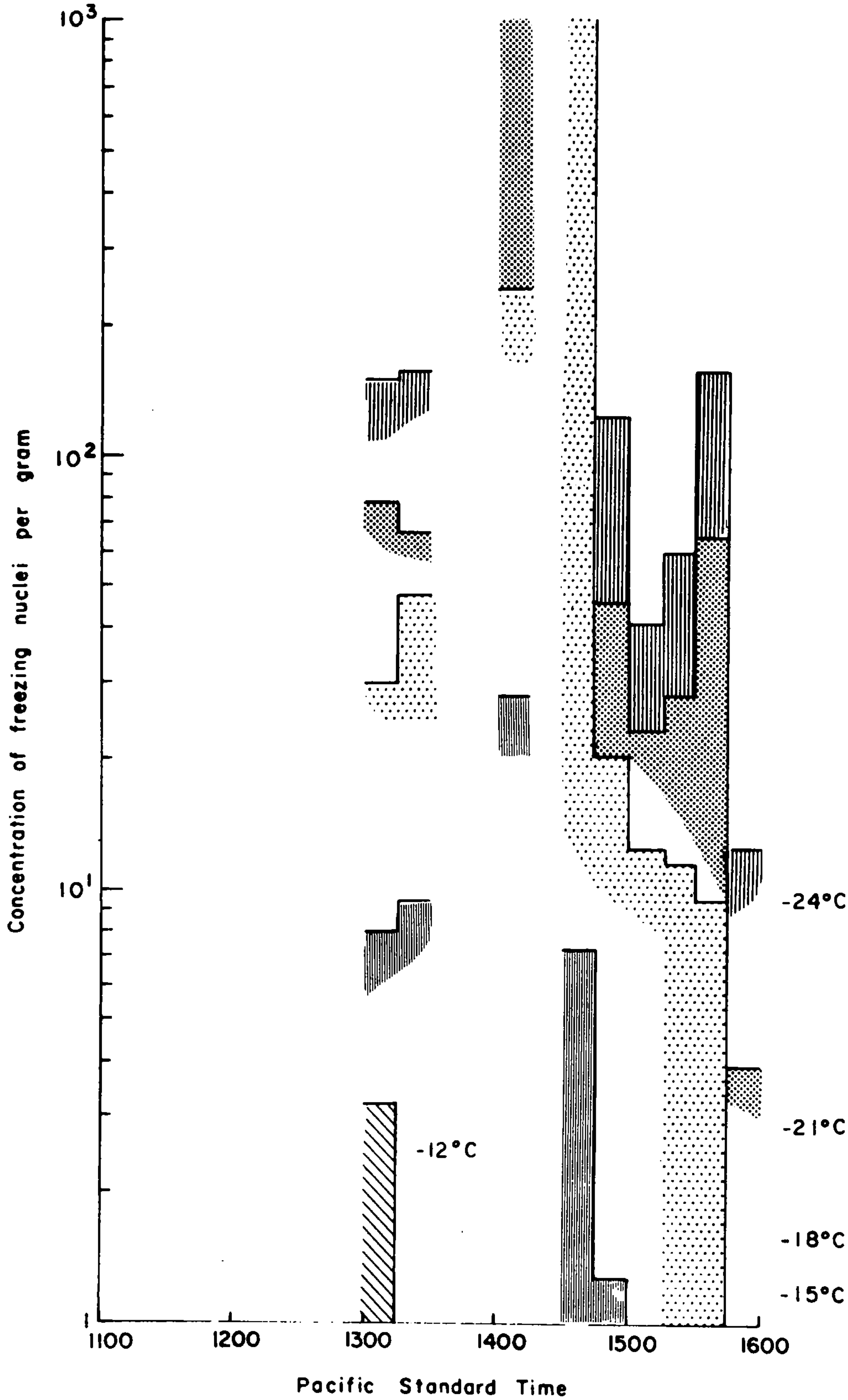

Fig. 5.62 Concentrations of freezing nuclei per gram of snow collected at Keechelus Dam on March 3, 1972.

1225 PST the average fall velocity had decreased substantially and lightly rimed stellars and dendrites predominated at ground level.

Subsequently, heavily rimed fast-falling crystals were observed at the station until 1430 PST. At 1315 and 1330 PST the Doppler measurements indicated that the average fall velocity fell below 1 m sec^{-1} for short time periods (see Fig. 5.63). At 1330 PST slide replicas of the precipitation particles reaching Hyak did indicate a slight decrease in riming which would have caused lower fall velocities (Fig. 5.59).

Starting at 1350 PST there was a steady increase in the average reflected power from the precipitation (Fig. 5.63). This marked the beginning of a rather unique event in our radar measurements to date. At 1415 PST the incoherent radar was turned on for another survey. Snow generating areas could be seen and widespread precipitation was observed. At 1420 PST heavily rimed columns and dendrites 1 mm in size were collected at the ground. The Doppler velocities appeared to be lower and the range gate was shifted to see if the velocities varied with height. However, there appeared to be little change with height at this time, indicating little growth over the range surveyed (1300 m). By 1448 PST the spectral characteristics had stabilized and appeared as a nearly single fall velocitiy of about 0.75 m sec^{-1} (Fig. 5.64). At about 1518 PST the range gate on the pulse Doppler was moved out to the region of snow generation which appeared to be between 1.8 and 1.95 km above the radar. By about 1540 PST the fall velocities had increased again (Fig. 5.64) and an observation of the generation layer showed that it had moved down to about 0.5 km above the ground. Conditions remained fairly stable until 1655 when the radar was switched off.

The marked shift to small fall velocities observed between about 1432 and 1529 PST (see Figs. 5.64 and 5.65) was accompanied by largely unrimed crystals reaching the ground at Hyak (see Fig. 5.59). It should be noted that the predicted effect of our overseeding is to reduce the riming and therefore the fall velocities of precipitaion particles, and that seeding was carried out from the aircraft situated about seven miles upwind of Hyak between 1251 and 1440 PST. The trajectory analysis described in the next section predicts that the time during which snowfall in our target area should have been affected by the artificial seeding should have occurred within the period 1310 to 1600 PST.

5.5.5 Ice Crystal Trajectories

Fig. 5.66 shows the diagrams used to estimate the period of possible effects of the artificial seeding at the ground station. Shown on a map of

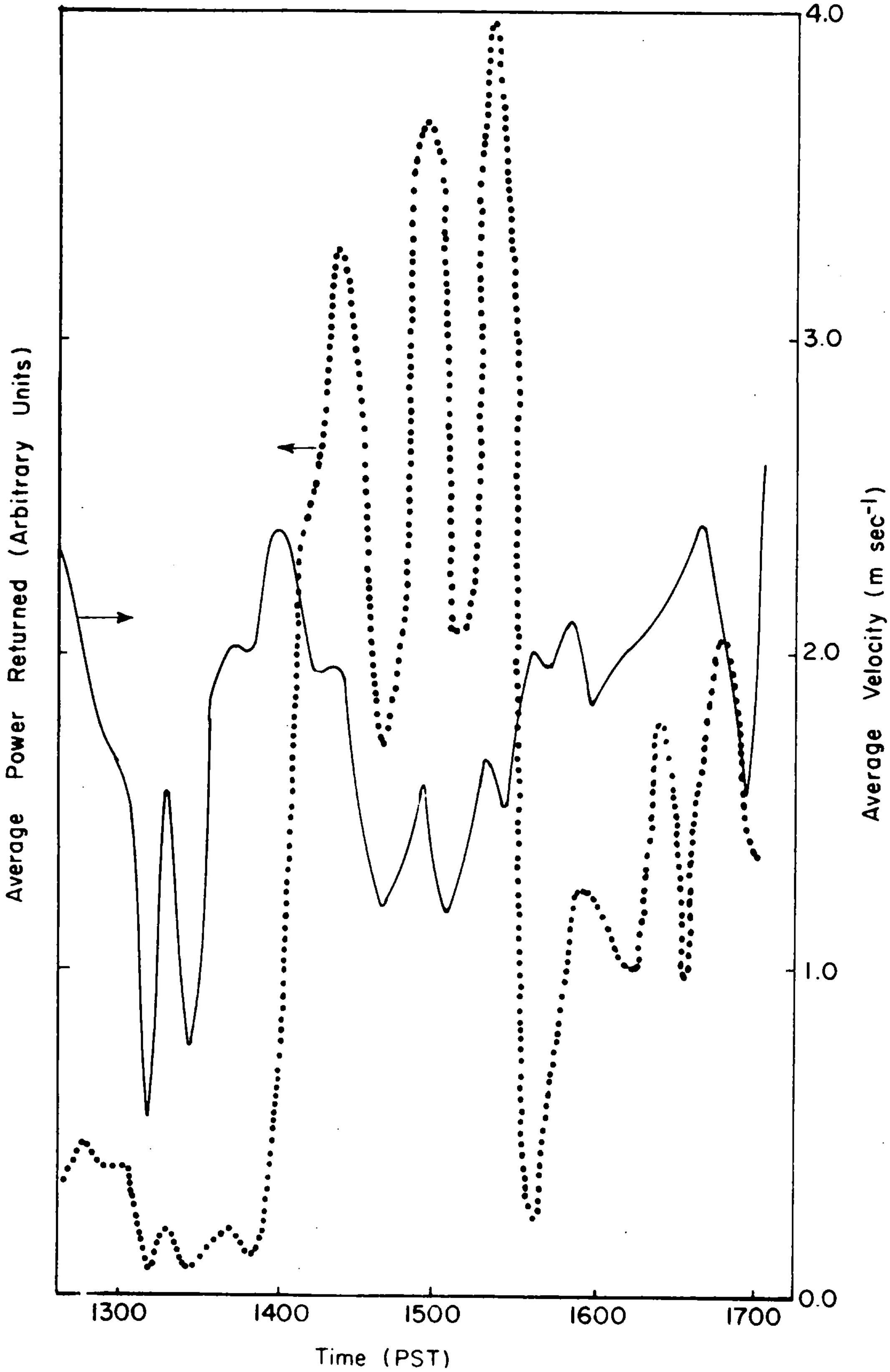

Fig. 5.63 Pulsed Doppler radar measurements of average velocity (———) and reflected power (•••••) of precipitation elements on March 3, 1972.

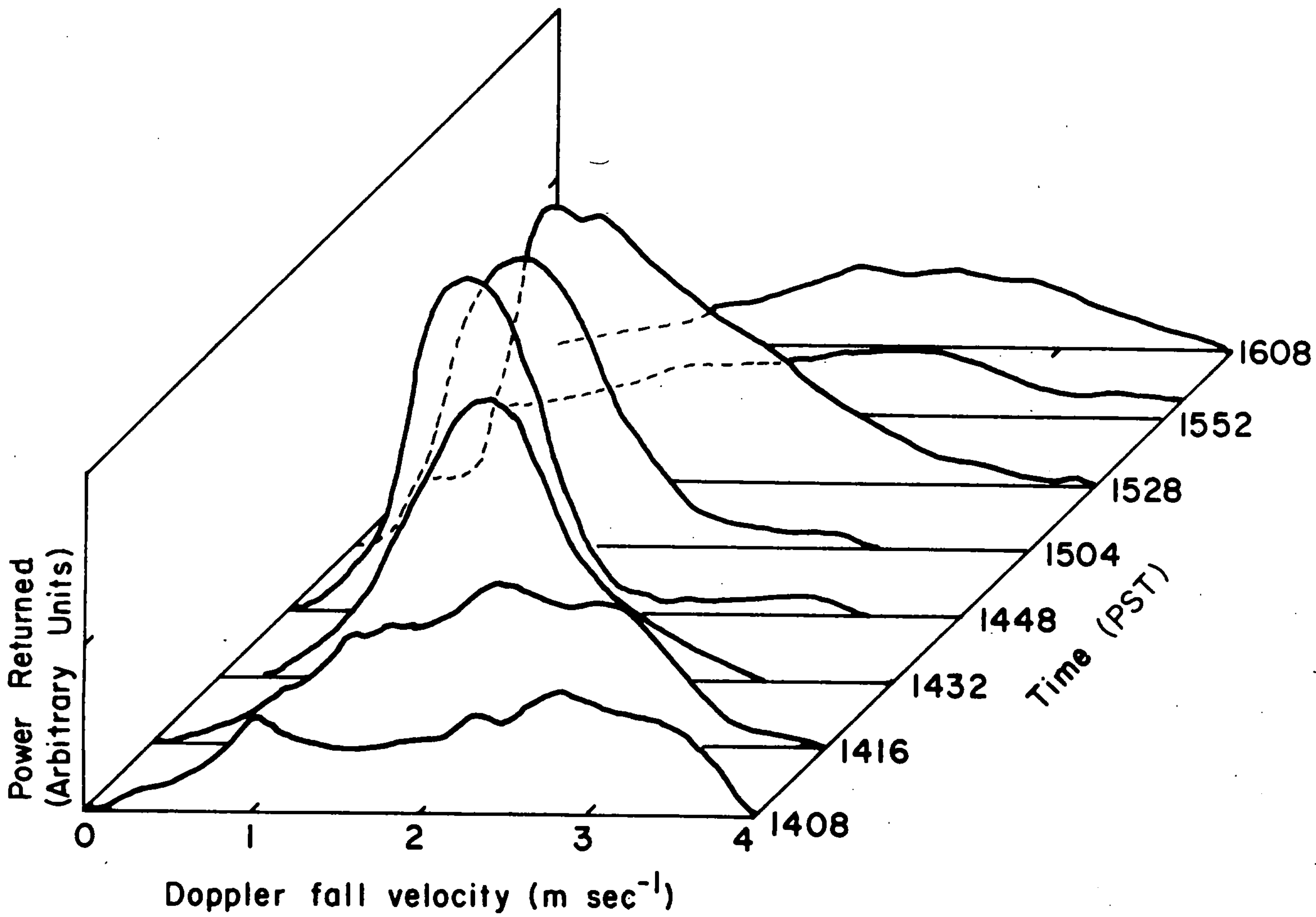

Fig. 5.64 3-D representation of Doppler radar velocity spectra of precipitation elements from 1408 to 1608 PST on March 3, 1972. The radar was located at Hyak and airborne seeding with AgI was carried out 7 miles upwind (west) of Hyak between 1251 and 1440 PST. Note the shift to smaller fall velocities between about 1432 and 1528 PST.

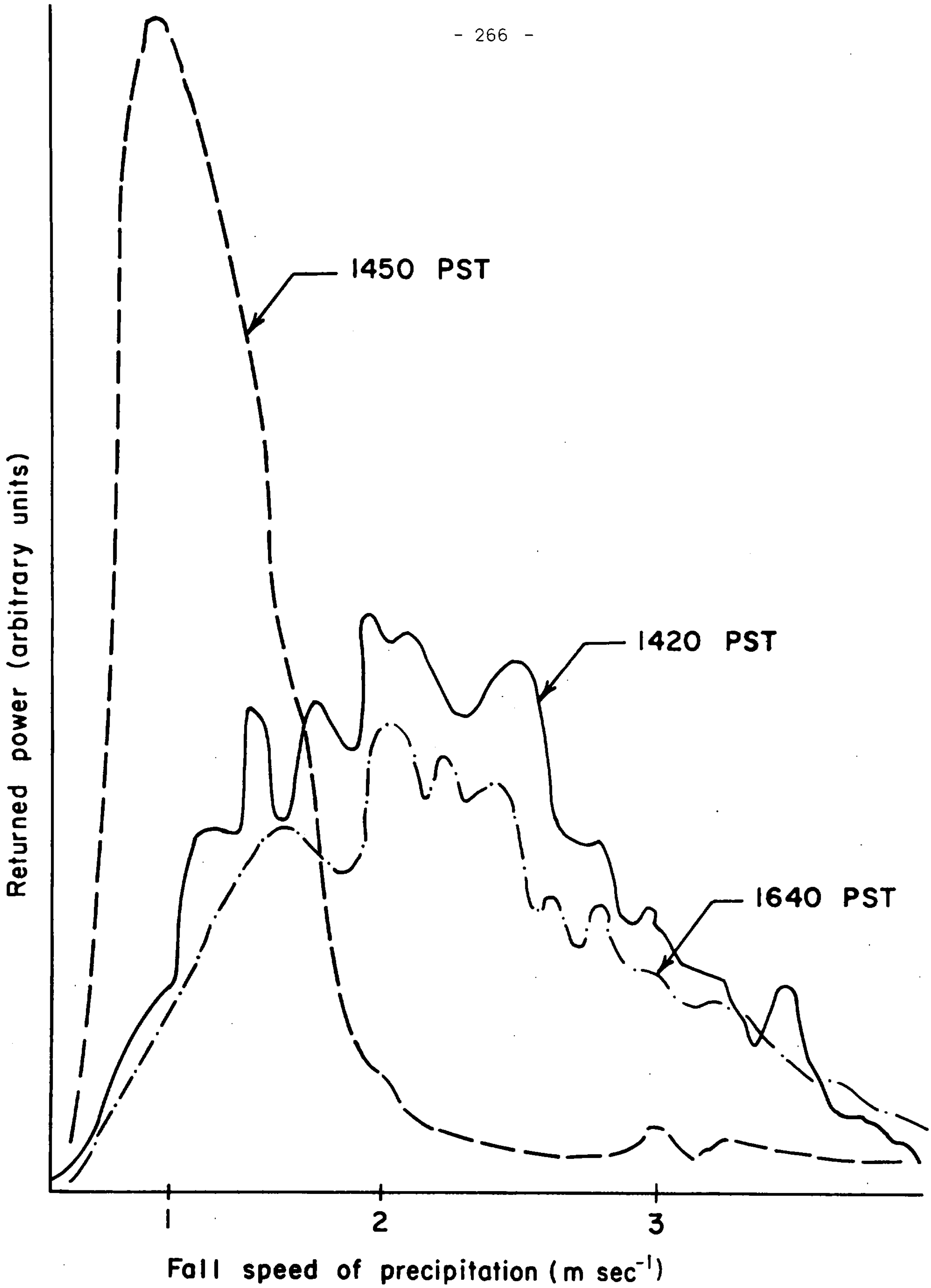

Fig. 5.65 Smoothed spectra of fall speeds of precipitation particles measured with Doppler radar on March 3, 1972 at Hyak.

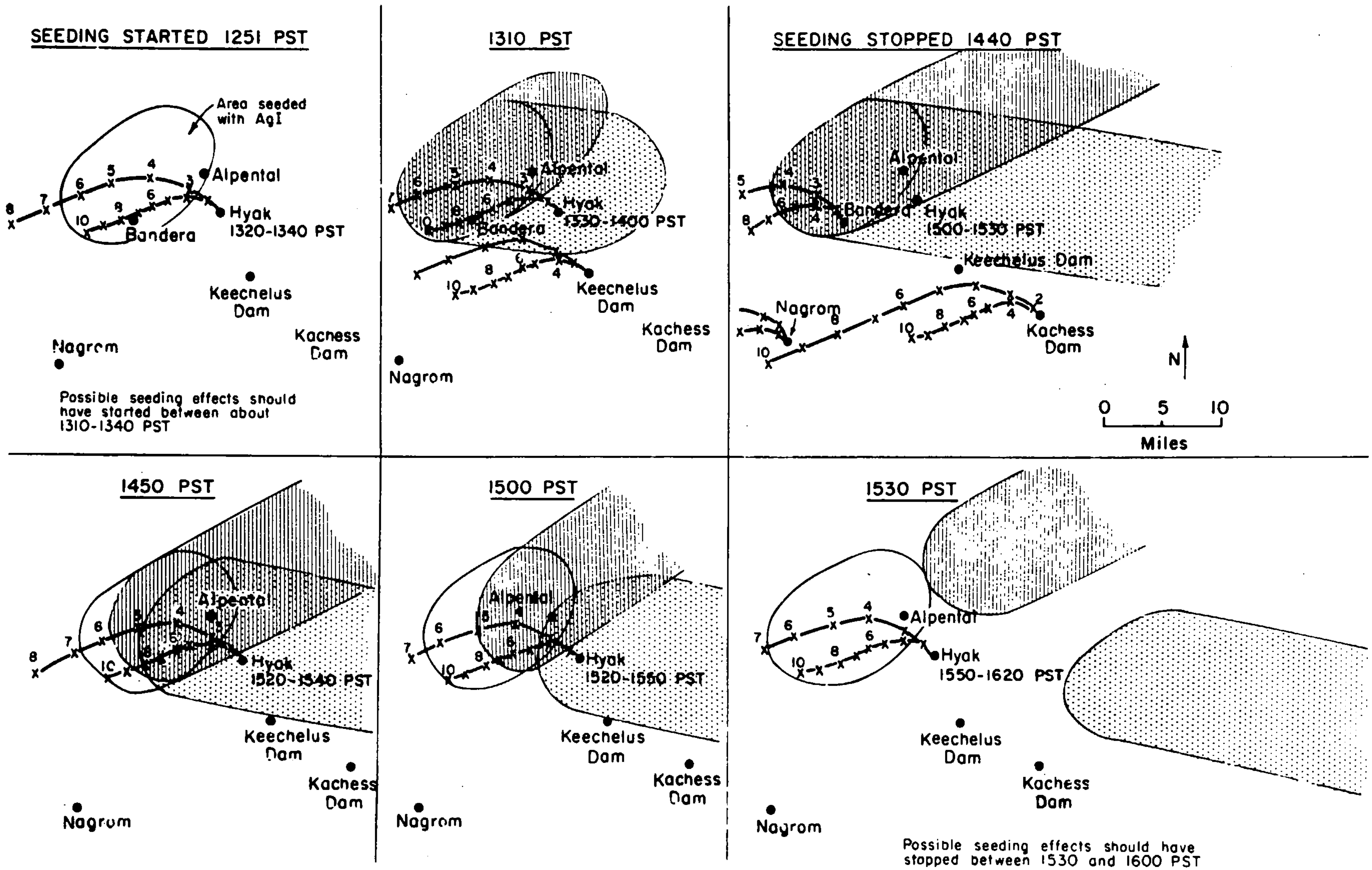

Fig. 5.66 Estimated positions of seeded plume at 10,000 (vertical hatching) and 4,000 feet (stippling) and trajectories of small and large aggregates reaching the ground on March 3, 1972. Numbers against trajectories give heights in 1000's of feet. Times written at Hyak give estimated period that crystals affected by seeding should have reached the ground at Hyak.

the target area are the estimated plume positions of the seeded material at 10,000 and 4,000 ft. (which bracket the region of cloud which was likely to have been affected by the AgI) for various times. The plumes are based on wind directions and lateral diffusion has not been included. Also shown are the computed trajectories for ice particles reaching the ground stations. The trajectories were computed in the manner described in §2.3 using fall speeds appropriate to the slowest and fastest of the aggregates which reached the ground stations from 1430 to 1530. It is clear that our three manned stations in the target area (Alpental, Hyak and Keechelus Dam) could have been affected by the seeding from about 1310 to 1600 PST. It was within this time period that the dramatic changes in precipitation rate, types of precipitation particles, degrees of riming (Fig. 5.59), freezing nucleus concentrations (Figs. 5.60-5.62), and fall speeds of the precipitation particles as measured by Doppler radar (Figs. 5.63-5.65) occurred.

5.5.6 Conclusions

Artificial seeding with AgI delay pyrotechnics was carried out from the aircraft flying upwind and just west of Alpental from 1251 to 1440 PST on March 3, 1972. Observations from the aircraft showed that the seeding glaciated the clouds. Computed ice particle trajectories indicate that snow particles reaching the ground at Alpental, Hyak and Keechelus Dam could have been affected by the seeding within the time period 1310 to 1600 PST. At these three stations sharp increases in precipitation occurred between about 1430 and 1545 PST, during the same period the degrees of riming of the precipitation particles decreased, new crystal types appeared (Fig. 5.59) and the concentrations of freezing nuclei in the snow decreased (Figs. 5.60-5.62). Radar measurements at Hyak showed that the Doppler velocities of the precipitation particles decreased dramatically between about 1432 and 1529. At Kachess Dam, where only precipitation rates were recorded, a similar sharp increase in the precipitation did not occur (Fig. 5.59) and it can be seen from Fig. 5.66 that the particles reaching this station were probably not affected by the AgI seeding. However, there was an increase in precipitation at Nagrom (Fig. 5.56) between about 1300 and 1700 PST, although this lies outside the predicted area of effect due to the seeding (Fig. 5.66). Landsburg, on the other hand, which is situated well upwind of the seeded area (Fig. 5.56), recorded no precipitation at all after 0900 on March 3.

It is possible that the observed changes in the intensity and nature of the snowfall between 1430 and 1545 PST observed at our ground stations on

March 3, 1972, were due in part to natural changes, since they seemed to cover a somewhat larger area in the mountains than we would have predicted to have been affected by the artificial seeding. However, there is little doubt from the evidence presented above that the artificial seeding did play a role in modifying the clouds and precipitation in the target area. Although seeding caused glaciation in some parts of the clouds and riming was reduced significantly, precipitation rates increased significantly at Alpental, Hyak and Keechelus Dam.

SECTION 6

OVERALL EVALUATION OF EFFECTS OF ARTIFICIAL SEEDING

In the previous section of this report, and in previous reports (Hobbs et al. 1970, 1971), we have evaluated from a physical point of view a number of individual case studies of artificial cloud seeding over the Cascade Mountains of Washington State. These have, for the most part, been cases in which a sequence of modifications to either the clouds or precipitation attributable to artificial seeding were documented. In many cases, however, clear-cut modifications attributable to seeding have not been observed. In these cases, the artificial seeding either did not produce appropriate modifications to several of the measured parameters which were greater than their natural variations or the effects of seeding did not change the clouds or precipitation within our small target area.

In this section the 23 seeding experiments carried out during the winter of 1971-72 are subjected to an overall analysis in an attempt to deduce those properties of clouds and precipitation over the Cascade Mountains which can be most reliably modified by seeding with artificial ice nuclei or "dry ice" and the conditions which are most conducive to controlled modification.

6.1 Airborne Observations

Table 6.1 lists the degrees to which effects attributable to artificial seeding were detected by five different techniques for all 23 occasions on which seeding was carried out in 1971-72. Table 6.2 shows the same information analyzed on a percentage basis considering only those cases where each detection technique was operationally possible. It can be seen from the last line in Table 6.2 that effects on the clouds due to artificial seeding were detected by one or more of the available techniques on 80 per cent of the 20 occasions on which the aircraft was able to fly in the seeded clouds. Possible verification was obtained on the remaining 20 per cent of occasions.

Changes in the habits of ice crystals or their concentrations was the most reliable technique for detecting seeding effects. Areas of the cloud affected by artificial seeding were frequently detected by their high concentrations of regular and generally small ice crystals which were often quite distinct from unseeded regions where the crystals were mainly irregular. The crystal habits observed after seeding generally agreed with the well-known ice crystal habit-temperature relationship (e.g., Magono and Lee, 1966). Some of the results are summarized in Table 6.3 which also includes data obtained in the winter of

TABLE 6.1

DEGREES TO WHICH VARIOUS OBSERVATIONAL TECHNIQUES AND MEASUREMENTS FROM

THE AIRCRAFT DETECTED EFFECTS ATTRIBUTABLE TO ARTIFICIAL SEEDING

Date	Sudden Change in or Appearance of Optical Effects due to Ice	Distinct Differences in Appearance of Clouds in and out of Seeded Track	Distinct Change in Ice Crystal Habits or Ice Concentrations Detected by Continuous Particle Sampler	Distinct Change in Ice Crystal Concentrations Detected by Optical Ice Particle Counter	Seeding Location and Drift of AgI Plume Detected by Mee Ice Nucleus Counter
Nov. 1, 1971	Could not fly in seeded area due to FAA restrictions.				
Nov. 8, 1971	?	X	?	?	Mee counter not installed.
Nov. 16, 1971	✓	✓	Could not descend to cloud level.		
Nov. 24, 1971	?	X	✓	?	Malfunction of Mee counter.
Nov. 29, 1971	✓	✓	?	X	Malfunction of Mee counter.
Dec. 2, 1971	?	X	Continuous Particle Sampler iced up before seeding.	?	X
Dec. 3, 1971	✓	?	✓	X	Mee counter not installed.
Dec. 9, 1971	X	X	X	✓	Mee counter not installed.
Dec. 10, 1971	✓	✓	X	?	Malfunction of Mee counter.

✓ = Positive verification of effects due to seeding
? = Possible verification of [illegible] to seeding
X = N[illegible]ification of eff[illegible] to seedi[illegible]

TABLE 6.1 (cont.)

Date	Sudden Change in or Appearance of Optical Effects due to Ice	Distinct Differences in Appearance of Clouds in and out of Seeded Track	Distinct Change in Ice Crystal Habits or Ice Concentrations Detected by Continuous Particle Sampler	Distinct Change in Ice Crystal Concentrations Detected by Optical Ice Particle Counter	Seeding Location and Drift of AgI Plume Detected by Mee Ice Nucleus Counter
Dec. 13, 1971	?	?	Malfunction of Continuous Particle Sampler	X	"Dry ice" seeding.
Dec. 15, 1971	√	√	√	?	"Dry ice" seeding.
Jan. 5, 1972	√	√	Malfunction of Continuous Particle Sampler	Optical Ice Crystal Counter failed	"Dry ice" seeding.
Jan. 7, 1972	X	X	Malfunction of Continuous Particle Sampler	√	Mee counter not installed.
Jan. 13, 1972	?	X	√	X	X
Jan. 14, 1972	√	√	Could not descend to cloud level.		
Jan. 17, 1972	Left seeded area due to heavy icing.				
Jan. 31, 1972	√	√	√	X	?
Feb. 14, 1972	?	√	√	√	X
Feb. 15, 1972	Left seeded area due to heavy icing.				
Feb. 22, 1972	√	√	?	√	"Dry ice" seeding.
Feb. 23, 1972	√	√	√	√	√

√ = Positive verification of effects due to seeding
? = Possible verification of effects due to seeding
X = No verification of effects due to seeding

TABLE 6.1 (cont.)

Date	Sudden Change in or Appearance of Optical Effects due to Ice	Distinct Differences in Appearance of Clouds in and out of Seeded Track	Distinct Change in Ice Crystal Habits or Ice Concentrations Detected by Continuous Particle Sampler	Distinct Change in Ice Crystal Concentrations Detected by Optical Ice Particle Counter	Seeding Location and Drift of AgI Plume Detected by Mee Ice Nucleus Counter
Mar. 2, 1972	X	?	?	?	X
Mar. 3, 1972	?	✓	✓	?	Air intake iced up.

✓ = Positive verification of effects due to seeding

? = Possible verification of effects due to seeding

X = No verification of effects due to seeding

TABLE 6.2

PERCENTAGE OF OCCASIONS ON WHICH VARIOUS DEGREES OF VERIFICATION OF EFFECTS DUE TO ARTIFICIAL SEEDING WERE OBTAINED BY AIRBORNE OBSERVATIONAL TECHNIQUES DURING 1971-72

Observational Technique	Positive Verification	Possible Verification	No Verification
Sudden change in or appearance of optical effects due to ice	Considers 20 of 23 seeded storms		
	50%	35%	15%
Distinct differences in appearance of clouds in and out of seeded track	Considers 20 of 23 seeded storms		
	55%	15%	35%
Distinct change in ice crystal habits or concentrations detected by continuous particle sampler	Considers 14 of 19 seeded storms; on 5 occasions the sampler was inoperative.†		
	57%	28%	15%
Distinct change in ice crystal concentrations detected by the U. of Washington optical ice particle counter	Considers 17 of 19 seeded storms; on 2 occasions counter malfunctioned.†		
	30%	40%	30%
Seeding location and drift of AgI plume detected by the Mee Industries ice nucleus counter	Considers 6 of 23 seeded storms; on 9 occasions the counter malfuntioned and on 4 occasions "dry ice" was the seeding agent.†		
	17%	17%	66%
Cases detected by one or more of above techniques	Considers 20 of 23 seeded storms		
	80%	20%	0%

†On 4 other occasions verification was not possible due to FAA restrictions on flight path.

TABLE 6.3

ICE CRYSTAL TYPES OBSERVED AFTER SEEDING

(1971-72 and 1972-73 data)

Date	Seeding Agent and Amount	Temperature at Seeding Level (°C)	Crystals Observed After Seeding
Dec. 3, 1971	Dry ice 5 lb $mile^{-1}$	-14	Hexagonal plates
Dec. 15, 1971	Dry ice 1.5 lb $mile^{-1}$	-17	Hexagonal plates, crystals with sector-like branches, broad-branched crystals, stellar germs
Jan. 31, 1972	AgI 1540 gm in 72 min.	-21	Short columns
Feb. 23, 1972	AgI 192 gm in 17 min.	-13	Hexagonal plates, stellars, crystals with sector-like branches, broad-branched crystals
Feb. 23, 1972	Dry ice 40 lb. in cumulus	-17	Hexagonal plates, stellars, crystals with sector-like branches
Feb. 23, 1972	Dry ice 2 lb $mile^{-1}$	-16	Hexagonal plates, stellar germs, crystals with sector-like branches
Nov. 21, 1972	Dry ice 1.2 lb $mile^{-1}$	- 5	Needles
Nov. 28, 1972	Dry ice 0.5 lb $mile^{-1}$	- 5	Needles or sheaths
Jan. 19, 1973	AgI 800 gm in 77 min. and Dry ice 2 lb $mile^{-1}$	-15	Stellars, hexagonal plates, crystals with sector-like branches, broad-branched crystals
Jan. 31, 1973	AgI 110 gm in 34 min.	-10	Hexagonal plates

TABLE 6.3 (cont.)

Date	Seeding Agent and Amount	Temperature at Seeding Level (°C)	Crystals Observed After Seeding
Mar. 5, 1973	Dry ice 20 lb. in cumulus	- 4	Needles or sheaths, long columns
Mar. 27, 1973	AgI 1500 gm in 59 min.	-15 to -18	Stellars, crystals with sector-like branches, hexagonal plates
Mar. 28, 1973	AgI 128 gm in 14 min.	-9 to -11	Short columns

1972-73. Plates, crystals with sector-likebranches, broad-branched crystals and stellars were collected most frequently following seeding at the -13 to -18°C levels. This indicates that the humidity was water saturation or below but generally not reduced to ice saturation at these temperatures. On January 31, 1972, short columns were collected after seeding with AgI at -21°C and short columns were also observed on March 28, 1972, when seeding was carried out at -9 to -11°C. These observations suggest that conditions may have been reduced to near ice saturation on these occasions so that nearly isometric crystals were produced. It should be noted that seeded clouds generally contain both glaciated areas and regions where supercooled droplets still dominate, consequently crystals of different growth habits are often found in close proximity.

Whenever possible sustained ice particle concentrations (as defined in §3.2.1) were determined from the continuous particle sampler for a period 30 minutes prior to seeding in clouds situated in the area to be seeded or within 5 to 10 miles of it. These were compared with the sustained ice particle concentrations measured during or up to 30 minutes after seeding. Data of this type were available for 13 seeded occasions from the 1971-72 season season. In Fig. 6.1 the ratio of the sustained ice particle concentration after seeding to that before seeding is plotted against the sustained ice particle concentration before seeding. Details of the seeding for each case are listed in Table 6.4. It can be seen from Fig. 6.1 that artificial seeding produced the largest increases in ice particle concentrations when the natural ice particle concentration was low. When the natural ice particle concentration exceeded about 2,000 per liter, artificial seeding did not cause significant increases in the concentrations of ice particles. These observations emphasize the importance of a detailed knowledge of the natural, background concentrations of ice particles in cloud seeding experiments (see §3.2).

To illustrate the dramatic changes in cloud structure which can take place following seeding, Fig. 6.2 shows measurements obtained on one occasion with the continuous particle sampler of the concentrations of water droplets and ice particles during and after seeding with AgI. It can be seen that toward the end of the period of seeding, and up to 24 miles downwind of seeding 30 minutes after seeding terminated, the clouds were glaciated. The temperature at the seeding level on this occasion (January 31, 1972) was -21°C which is much lower than is usual in the Cascade Mountains. The aircraft and ground observations made on this day have been discussed in detail in §5.1. Optical

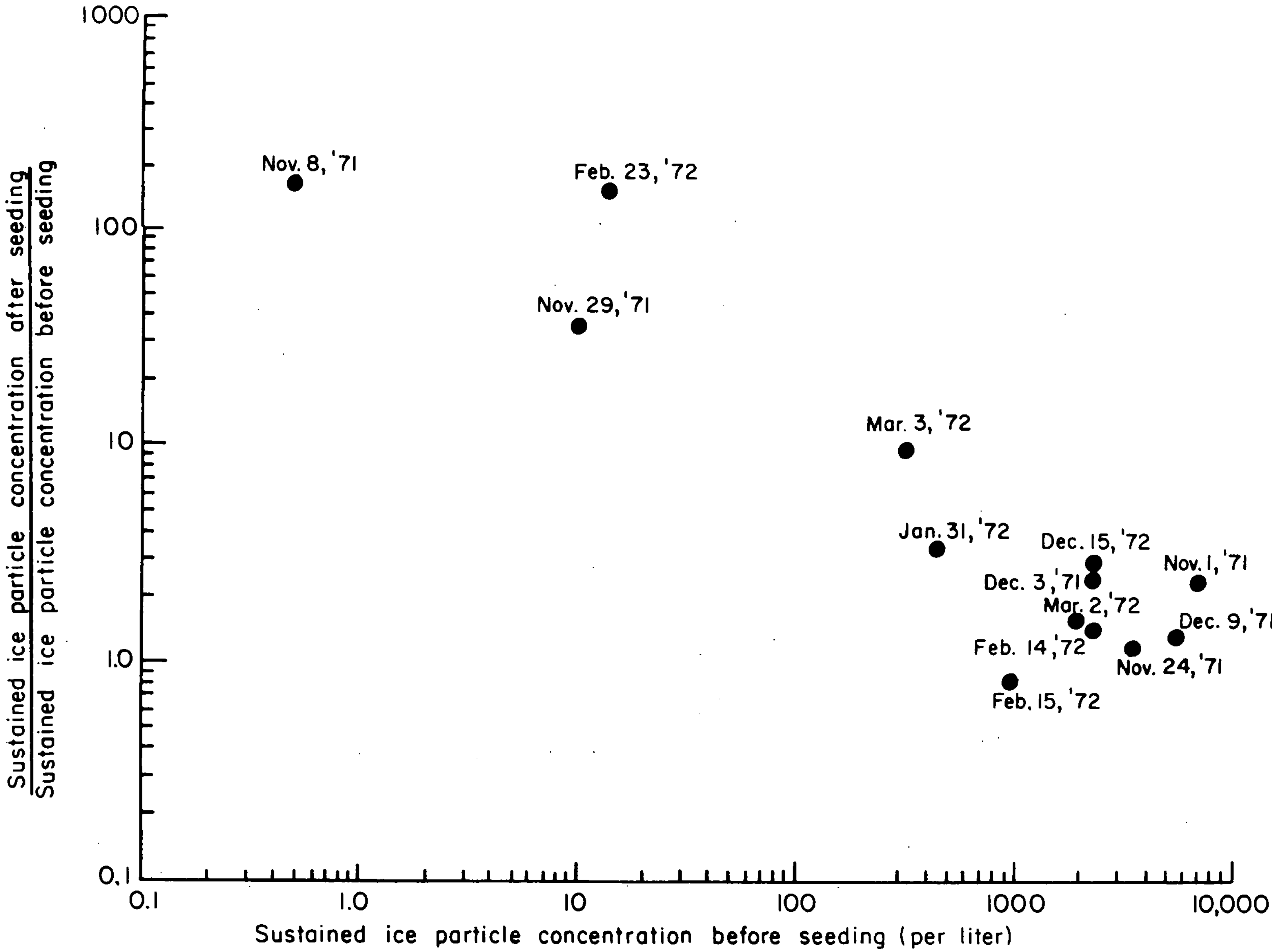

Fig. 6.1 Ratio of sustained ice particle concentration after seeding to that before seeding.

TABLE 6.4

EFFECT OF ARTIFICIAL SEEDING ON CONCENTRATIONS OF ICE PARTICLES

Date	Seeding Agent and Amount	Temperature at which crystals were sampled (°C)	Sustained ice particle concentrations before seeding ($liter^{-1}$)	Ratio of sustained ice particle concentration after seeding to that before seeding
Nov. 1, 1971	Dry ice 20 lb $mile^{-1}$	-15	7,000	2.3
Nov. 8, 1971	AgI 980 gm in 65 min.	- 8	0.5	2600
Nov. 24, 1971	Dry ice 1 lb $mile^{-1}$	-12	3,700	1.15
Nov. 29, 1971	Dry ice 1 lb $mile^{-1}$	- 7	10	35
Dec. 3, 1971	Dry ice 5 lb $mile^{-1}$	-14.5	2,400	2.4
Dec. 9, 1971	AgI 1040 gm in 75 min.	-12.5	5,700	1.3
Dec. 15, 1971	Dry ice 1.5 lb $mile^{-1}$	-16	2,500	2.8
Jan. 31, 1972	AgI 1540 gm in 72 min.	-20.5	450	3.3
Feb. 14, 1972	Dry ice 1 lb $mile^{-1}$	- 8.5	2,400	1.4
Feb. 15, 1972	Dry ice 4 lb $mile^{-1}$	- 6.0	1,000	0.8
Feb. 23, 1972	AgI 192 gm in 17 min.	-12	15	170
Mar. 2, 1972	AgI 1210 gm in 100 min.	-15	2,000	1.55
Mar. 3, 1972	AgI 340 gm in 110 min.	-17	400	9.4

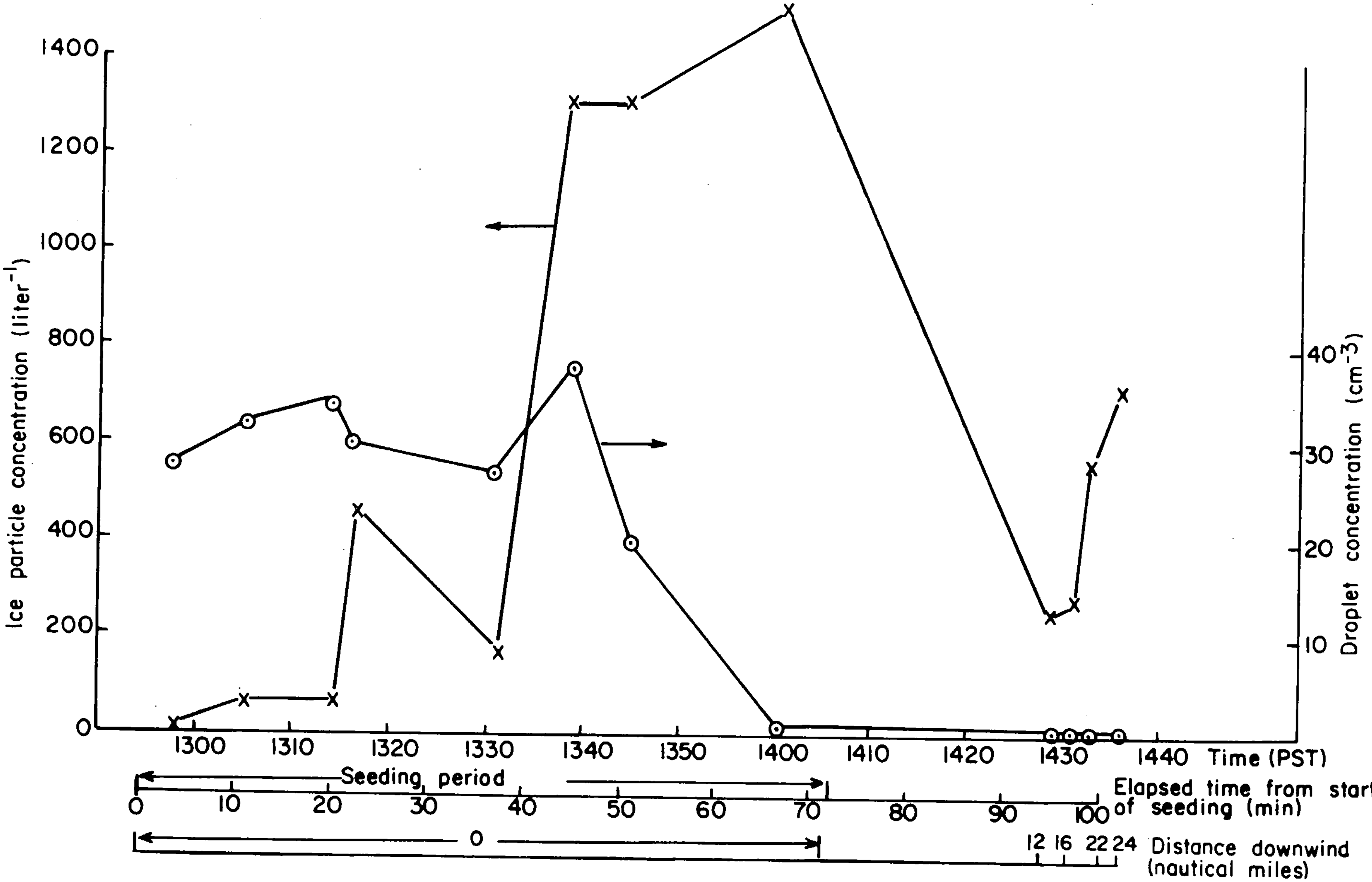

Fig. 6.2 Measured concentrations of cloud droplets (⊙) and ice particles (X) measured during and after seeding with 1590 gm of AgI on January 31, 1972.

phenomena and changes in the appearance of clouds provided valuable "remote probing" techniques for tracing the effects of artificial seeding on cloud structure (Table 6.2). Several examples have been given elsewhere in this report (see Figs. 5.21, 5.50 and 5.51) and these effects will be documented in a more quantitative manner in a future report.

The University of Washington optical ice particle counter functioned very well during the 1971-72 season and its real-time read out of ice particle concentrations was extremely valuable. However, as noted in §3.1.3, the present instrument only detects ice particles in excess of about 100 μm in size. This is probably the reason why positive verification of seeding effects was obtained for only 30 per cent of the seeded cases (Table 6.2). Work is now in progress to increase the sensitivity of the instrument.

While the Mee Industries ice nucleus counter is potentially a useful instrument for tracking AgI plumes, its use was rather severely restricted by operational problems. On the one occasion when it operated reliably the AgI plume was traced for about 10 miles in a 5 knot wind.

An example of a set of simultaneous measurements obtained with our optical ice particle counter and the Mee Industries ice nucleus counter as the aircraft flew in and out of a region of cloud previously seeded with AgI is shown in Fig. 6.3 where it can be seen that there was a good correlation between the two sets of measurements. The particles in cloud on this occasion are listed in Table 6.5.

6.2 Ground Observations

In evaluating the effects of seeding from data collected at our ground stations it is important to bear in mind that we are attempting to produce changes in precipitation within a very small, predetermined target area in the mountains by seeding the clouds upwind. The target area is essentially confined to a narrow strip following Interstate 90 extending from Alpental, situated just west of the Cascade crest, to Kachess Dam which is about 20 miles east of the Cascade crest (Fig. 1.4). Seeding is generally carried out at a location determined by the "simple" operational model described in §2.3, input data are the measurements from the rawinsonde launched from Greenwater, and observations of snow crystal types and winds at the ground stations in the mountains. The effects of seeding are evaluated by measuring and observing precipitation rates, snow crystal types, degrees of riming, freezing nucleus concentrations and the fall speeds of precipitation particles (by Doppler radar) in the target area. Changes attributable to seeding are required to occur within, or close to, the predicted period of effect (PPE) of seeding

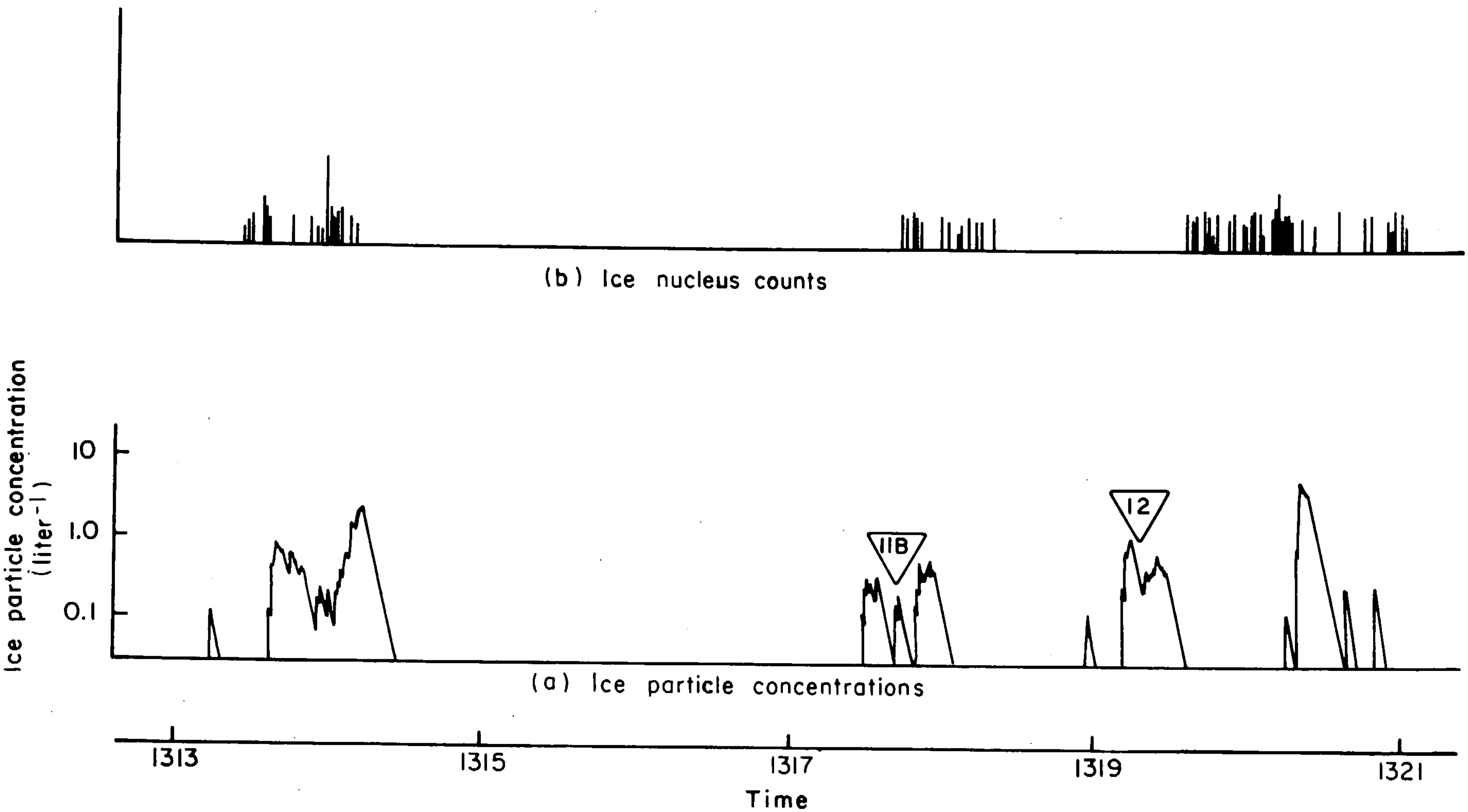

Fig. 6.3 Simultaneous ice nucleus counts (Mee Counter) and ice crystal concentrations detected by the University of Washington optical ice particle counter in a cloud seeded with AgI over the Cascade Mountains on February 23, 1972 (Flight 105). The numbers refer to the CPS run numbers in Table 6.5 .

TABLE 6.5

SUMMARY OF CLOUD PARTICLES COLLECTED WITH CONTINUOUS

PARTICLE SAMPLER ON FEBRUARY 23, 1972

(The relationship of each run to other data is indicated on Fig. 6.3.)

Run No.	Water Drops		Ice Particles		Number Ratio of Water to Ice
	Diameter (μm)	Concentration (cm^{-3})	Type & Maximum Dimension (μm)	Concentration (cm^{-3})	
11B	10-50	4-12 Mostly at beginning.	50-1300. Hexagonal plates, some in assemblages. 80-700 larger ones sectoring. Branched crystals >1000.	0.4-2	Mainly 20:1. Occasionally 1:5.
12	20-60	0.15-15 Occasional	50-700. Hexagonal plates to 350. Broken crystals to 700. Many small plate-like fragments.	0.4-6	1:4

suggested by the "simple" model and to return to the pre-seeded conditions after the PPE.

This technique for evaluating the effects of artificial seeding requires much more accuracy than, for example, seeding to change precipitation over a large watershed or within a target area the boundaries of which are defined in post-analysis. Therefore, it is not to be expected that on all, or even most, of the occasions the predicted effects of seeding will be observed in the target area. The obvious inadequacies of the "simple" model, or slight changes in the clouds or winds from those used as input data, will often cause errors in the targeting of the seeding effects to the ground. Instead, we must be content with a few detailed case studies (such as some of those presented in §5 of this report and in Hobbs et al., 1971) in which several physical parameters undergo sequential changes during the PPE of the type to be expected from seeding. Indeed, just one case study (such as that described in §5.1) in which a large number of different types of observations and measurements, both from the air and on the ground, verify the predicted effects of seeding, is sufficient to confirm the general efficacy of the approach.

In this section, however, rather than consider individual case studies, we give an overall analysis of the ground results obtained in seeded storms during the 1971-72 winter Cascade Project.

6.2.1 Effects of Artificial Seeding on Various Parameters

The storm days on which artificial seeding was carried out are divided into three groups according to whether the effects of the seeding at ground level were estimated to be "good," "fair" or "poor." A "good" effect indicates that a change occurred in several parameters within the predicted period of effect (PPE) which could be explained by the seeding. A "fair" effect is one in which changes were noted during the PPE but it was not clear that these were due to seeding. Those storm days on which either no changes occurred during the PPE, or changes occurred which could not be explained by the seeding, were classified as "poor."

In Table 6.6, 20 out of 23 storm days on which seeding was carried out are classified on this basis (insufficient ground data were obtained on the other three days to permit classification). On six days, the seeding effects were "good," on four they were "fair" and the remaining ten were "poor." Also listed in Table 6.6 are the conditions of various parameters on each day.

Some general conclusions emerge from the results shown in Table 6.6. First, on all of the days when "good" effects from seeding were observed, the

TABLE 6.6

CLASSIFICATION OF SEEDING EFFECTS BASED ON GROUND DATA

Date	Classification of Seeding Effect	Synoptic Description	10,000 Ft. Wind Direction (Deg)†	10,000 Ft. Wind Speed (m/sec)†	10,000 Ft. Moisture (gm/kg)†	Precipitation Rate‡ (inches of water/hr)	Riming§*	Typical Crystal Types§*	Aggregation	Variability: Precipitation Rate	Variability: Crystal Type	Duration of Seeding (hours and minutes)	Seeding Material	Seeding Rate	Degree of Glaciation of Clouds Before Seeding	Temperature at Seeding Level (°C)
Dec. 3, 1971	"Good"	Oro-graphic	155	4.8	1.7	<0.005			Low	High	Moderate	00:49	CO_2 AgI	5 lb/mile 10 gm/min	Low	-14
Dec. 10, 1971		Oro-graphic	277	11.1	1.3	0.02			High	High	Moderate	01:00	CO_2 AgI	5 lb/mile 3 gm/min	High	-17
Dec. 15, 1971		Oro-graphic	315	25.0	0.5	0.01			Moderate	Moderate	Low	00:48	CO_2	2 lb/mile	Low	-17
Jan. 13, 1972		Oro-graphic	323	26	1.6	Trace			Low	High	Low	00:48	CO_2 AgI	10 lb/mile 0.8 gm/min	Low	-13
Jan. 14, 1972		Oro-graphic	323	12	3.0	0.04			High	Moderate	Low	00:18	CO_2 AgI	10 lb/mile 11 gm/min	Low	- 8
Jan. 31, 1972		Oro-graphic	284	6.7	0.8	0.01			High	Low	Low	01:12	AgI	24 gm/min	Low	-21
Nov. 29, 1971	"Fair"	Post-frontal	323	7	1.8	<0.01			Moderate	Low		01:40	CO_2	1 lb/mile	Low	- 8.5
Dec. 13, 1971		Pre-frontal	306	19.5	2.6	0.03			High	Moderate	High	00:42	CO_2	2 lb/mile	Moderate	- 9
Feb. 22, 1972		Post-frontal	248	12.7	0.7	≈0						00:07	CO_2	2 lb/mile	Moderate	-11
Mar. 3, 1972		Oro-graphic	229	3	1.4	0.005			Low			01:49	AgI	3 gm/min	Low	-17
Nov. 1, 1971	"Poor"	Post-frontal	291	13	1.9	0.03			High	Moderate	Low	00:13	CO_2	17 lb/mile	High	-15
Nov. 8, 1971		Pre-frontal	228	16	3.3	≈0.			Low	High	Moderate	01:00	AgI	13.8 gm/min	Low	- 9
Nov. 24, 1971		Oro-graphic	246	11	2.1	0.1			Moderate	Moderate	Moderate	01:00	CO_2 AgI	1 lb/mile 13 gm/min	Moderate	
Dec. 2, 1971						Seeded in wrong location due to error										
Dec. 9, 1971		Post-frontal	283	26	1.4	0.03			Low	Moderate	Moderate	01:15	AgI	13 gm/min	High	-17
Jan. 5, 1972		Oro-graphic	302	26	1.1	0.02			High	High	Low	00:52	CO_2	5 lb/mile		- 7
Jan. 7, 1972		Post-frontal	249	24	1.6	0.05			Moderate	Moderate	Moderate	00:17	AgI CO_2	6 gm/min 10 lb/mile		-14
Jan. 17, 1972		Oro-graphic	260	32	1.0	0.01			Moderate	Low	Low	01:08	AgI	40 gm/min	High	-20
Feb. 14, 1972		Pre-frontal	272	17	3.0	0.1			High	Low	Low	01:24	CO_2	1 lb/mile 0.1 gm/min	High	- 8.5
Mar. 2, 1972		Oro-graphic	271	17	1.4	0.08			High	High	Moderate	01:40	AgI	12 gm/min	High	-15

†From Greenwater rawinsonde closest to time of seeding.

‡Average precipitation rate at Alpental Base during period of seeding.

§Typical of show crystal falling at Alpental Base during period of seeding.

*For Key see Table 4.1.

precipitation was due mainly to orographic uplift over the Cascade Mountains. This is probably due in part to orographic situations being simpler and more uniform than those associated with fronts, therefore, targeting of the seeding effects of the small target area on the ground is more accurate. However, we will see below, that orographic clouds are also associated with other conditions which are conducive to "good" seeding effects.

Fig. 6.4(a) shows the relationships between seeding effects, the average riming of the ice particles at the ground prior to seeding, and the degree of glaciation of the clouds before seeding as determined from the aircraft. It can be seen that out of the six days when "good" seeding effects were observed at the ground, five were days when the degree of glaciation of the clouds prior to seeding was "low." Also, five out of the seven days on which the seeding effects were "poor" had a "high" degree of glaciation prior to seeding. However, there was no clear correlation between seeding effects and the average degree of riming of the ice particles reaching the ground prior to seeding (there was also no correlation between the degree of glaciation of the clouds and the riming of the particles reaching the ground prior to seeding). This lack of correlation supports our previous suggestion (Hobbs et al., 1971, and §2.2.2 of present report) that the "diffusional growth layers" and "riming growth layers" of ice particles are largely independent of each other.

No correlation was found between seeding effects and the moisture content at 10,000 ft. However, there was a weak correlation between seeding effects and the speed of the wind at 10,000 ft. All days on which the seeding effects at ground level were judged to be "poor" had wind speeds in excess of 12 m sec^{-1} at 10,000 ft., while winds at this level on 66 per cent of the "fair" to "good" seeding days had wind speeds below 14 m sec^{-1}. However, the degree of glaciation of the clouds also tended to increase with increasing wind speed at 10,000 ft. and increasing the precipitation rate at the ground. It was also observed that the clouds tended to be highly glaciated prior to seeding when the wind at 10,000 ft. was between 250° and 300°; unglaciated to partially glaciated clouds occurred with winds from 150° to 330°. These correlations can be understood in general terms as follows. When the precipitation is formed under pre-frontal, post-frontal or strong orographic conditions, the wind speed is generally higher and from a more westerly direction than on days of weak orographic precipitation. The clouds that form in weak orographic conditions often consist of just a thin layer of stratus which may produce light precipitation. These clouds are less likely to be glaciated (and should

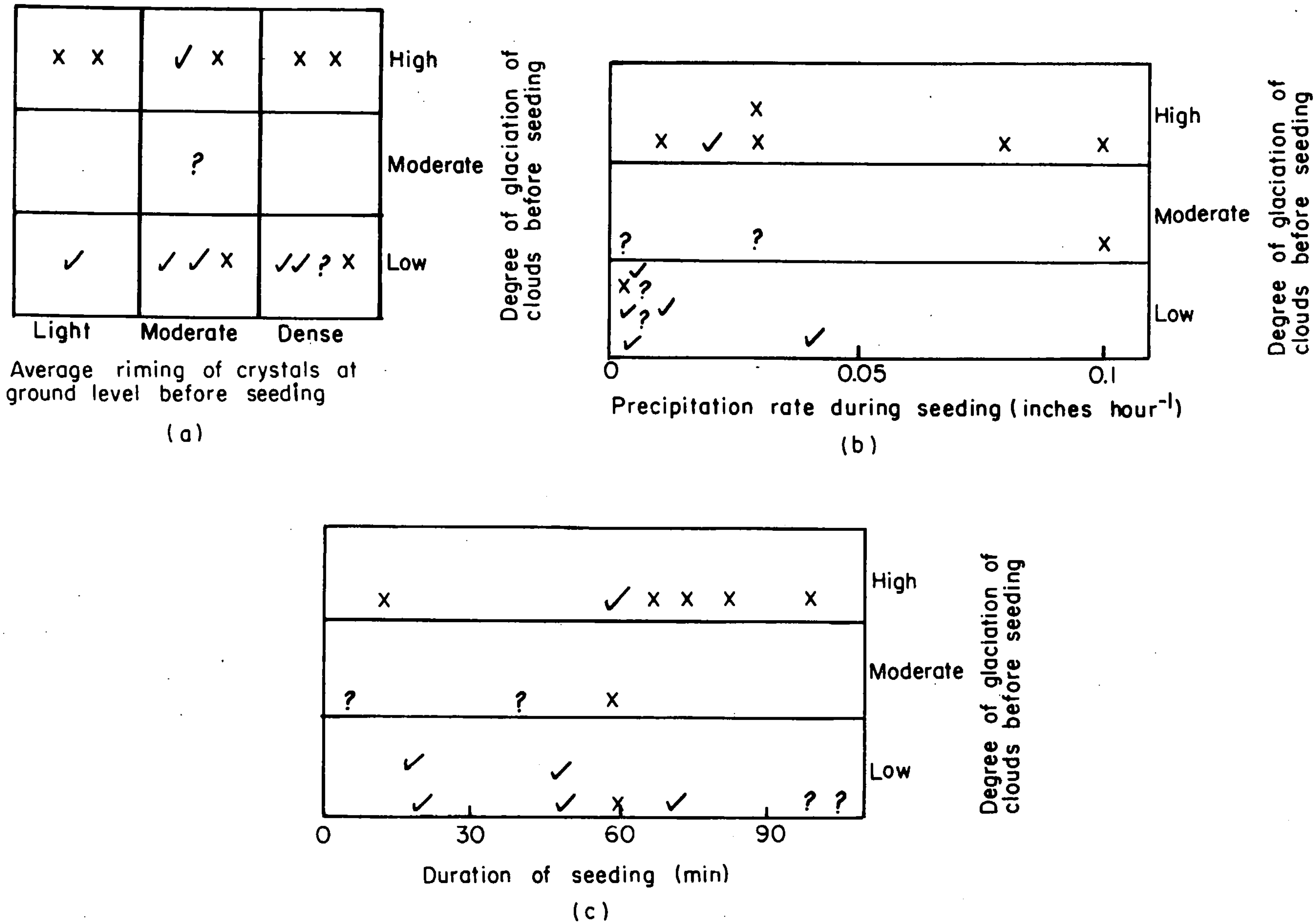

Fig. 6.4 Effects of various parameters of effects due to artificial seeding. ✓ ="good" seeding effect. ? = "fair" seeding effect. X = "poor" seeding effect.

therefore be more conducive to artificial modification) than the deeper clouds and more vigorous clouds associated with frontal activity or stronger orographic flow. Moreover, when the wind speeds are low, targeting of the seeding effects to to the small target area on the ground is easier, and with low natural precipitation rates the effects of artificial seeding may be more obvious. Fig. 6.4(b) shows this to be the case.

In Fig. 6.4(c) the seeding effect is compared with the duration of seeding but a correlation is not apparent.

The influences of seeding rates on seeding effects are shown in Fig. 6.5. Of the five occasions on which "good" seeding effects were observed when the clouds were low to moderately glaciated [Fig. 6.5(a) and (b)], three were seeded with both "dry ice" and silver iodide; for one of the remaining two "good" seeding effect cases, the temperature was comparatively low and a high seeding rate of silver iodide was used. For the clouds which were highly glaciated prior to seeding [Fig. 6.5(c) and (d)], only two out of six were seeded with both "dry ice" and silver iodide; of these two cases one gave a "poor" seeding effect, but seeding was at a very low rate and temperatures were high, and the other produced a "good" seeding effect with moderate seeding rates when the temperatures were also moderate. These results suggest that seeding with both "dry ice" and silver iodide might be more effective than seeding with either "dry ice" or silver iodide alone.

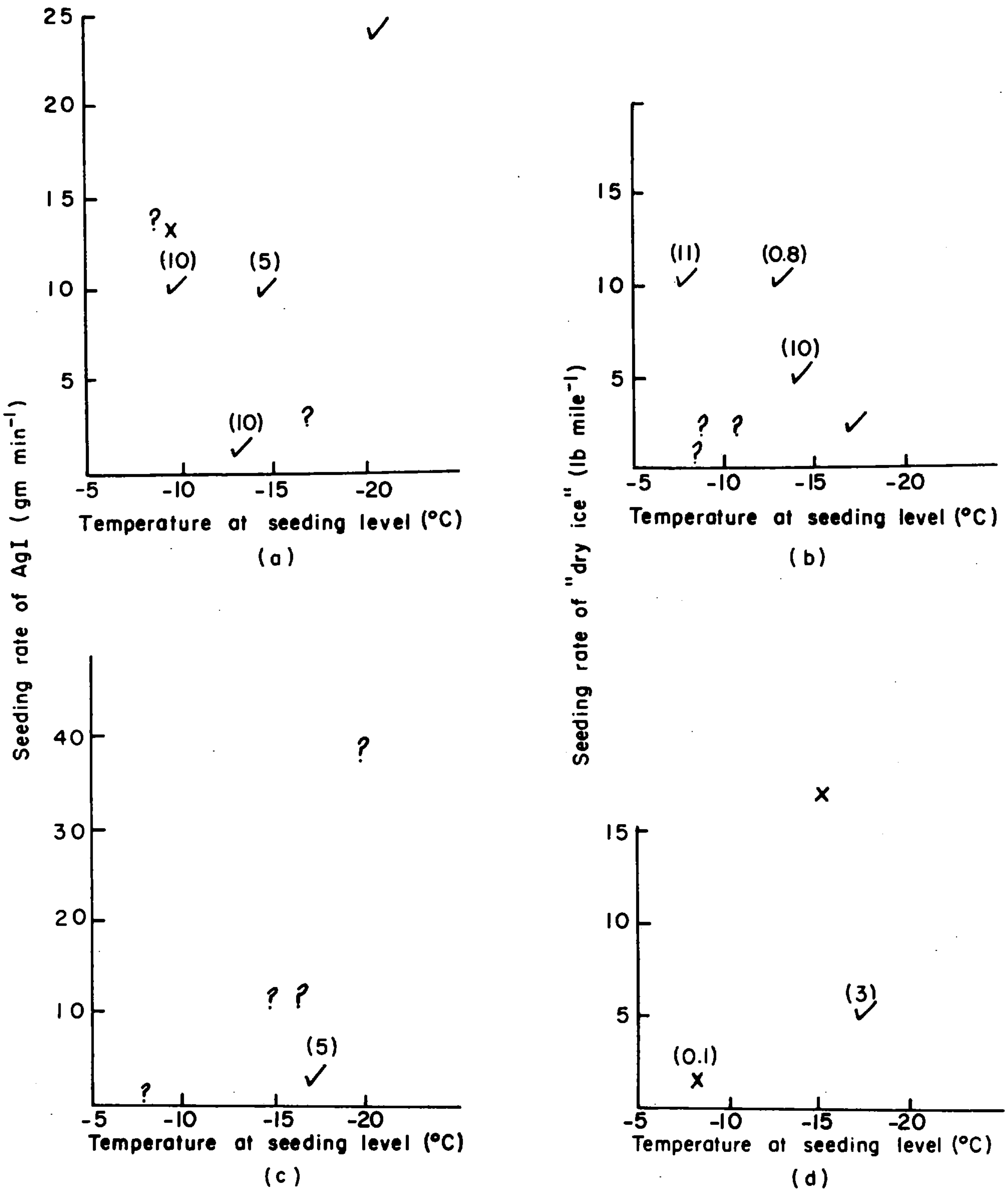

Fig. 6.5 Influence of artificial seeding rate on effects due to seeding. ✓ = "good" seeding effects. ? = "fair" seeding effects. X = "poor" seeding effects. (a) and (b) are for clouds which were low to moderately glaciated and (c) and (d) are for highly glaciated clouds. Numbers in brackets in (a) and (c) give simultaneous seeding rates of "dry ice" in lb mile^{-1}. Numbers in brackets in (b) and (d) give simultaneous seeding rate in gm min^{-1} of AgI.

REFERENCES

Abbott, C. E., J. E. Dye and J. D. Sartor, 1972. "An electrostatic cloud droplet probe." J. Appl. Meteor., 11, 1092-1100.

Auer, A. H., Jr., 1971. "Observations of ice crystal nucleation by droplet freezing in natural clouds." J. Atmos. Sci., 28, 285-290.

Auer, A. H., Jr., 1972. "Inferences about ice nucleation from ice crystal observations." J. Atmos. Sci., 29, 311-317.

Auer, A. H., Jr. and D. L. Veal, 1970. "The dimensions of ice crystals in natural clouds." J. Atmos. Sci., 27, 919-926.

Auer, A. H., Jr., D. L. Veal and J. D. Marwitz, 1969. "Observations of ice crystal and ice nuclei concentrations in stable cap clouds." J. Atmos. Sci., 26, 1342-1343.

Batchelor, G. K., 1950. "The application of the similarity theory of turbulence to atmospheric diffusion." Quart. J. Roy. Met. Soc., 76, 133-146.

Beals, G. A., 1971. "Guide to local diffusion of air pollutants." Air Weather Service, Tech. Rpt., 214.

Bentley, W. A., 1924. "Forty years study of snow crystals." Mon. Wea. Rev., 52, 530-532.

Brown, S. R., 1970. "Terminal velocities of ice crystals." Dept. of Atmos. Sci., Colorado State Univ., Atmos. Sci. Paper 170, 52 pp.

Burrows, D. A. and C. E. Robertson, 1969. "Comments on ice multiplication in clouds." J. Atmos. Sci., 26, 1340-1341.

Fukuta, N., W. A. Schmeling and L. F. Evans, 1971. "Experimental determination of ice nucleation by falling dry ice pellets." J. Appl. Meteor., 10, 1174-1179.

Hobbs, P. V., 1969. "Ice multiplication in clouds." J. Atmos. Sci., 26, 315-318.

Hobbs, P. V. and J. D. Locatelli, 1970. "Ice nucleus measurements at three sites in Western Washington." J. Atmos. Sci., 27, 90-100.

Hobbs, P. V., L. F. Radke, A. B. Fraser, J. D. Locatelli, C. E. Robertson, D. G. Atkinson, R. J. Farber, R. R. Weiss and R. C. Easter, 1971. "Studies of winter cyclonic storms over the Cascade Mountains (1970-71)." Contributions from the Cloud Physics Group, Research Report VI, University of Washington, 306 pp.

Koenig, L. R., 1963. "The glaciating behavior of small cumulonimbus clouds." J. Atmos. Sci., 20, 29-47.

Koenig, L. R., 1968. "Some observations suggesting ice multiplication in the atmosphere." J. Atmos. Sci., 25, 460-463.

Krasnovskaya, L. I., A. V. Levin and A. V. Tkachenko, 1971. "On the interpretation of experimental data on artificial cloud crystallization and evaluation of horizontal turbulent diffusion characteristics." Isv. Atmosph. and Oceanic Phys., 7, 302-308.

Langleben, M. P., 1954. "The terminal velocity of snowflakes." Quart. J. Roy. Met. Soc., 80, 174-181.

MacCready, P. B., Jr., 1964. "Standardization of Gustiness values from aircraft." J. Appl. Meteor., 3, 439-449.

Magono, C., 1954. "On the falling velocity of solid precipitation elements." Sci. Rpt. Yokohama Natl. Univ., Ser. 1, No. 3, 33-40.

Magono, C. and C. W. Lee, 1966. "Meteorological classification of natural snow crystals." J. Fac. Sci., Hokkaido Univ., Series VII, 2, 321-335.

Mossop, S. C., 1970. "Concentrations of ice crystals in clouds." Bull. Amer. Met. Soc., 51, 474-479.

Mossop, S. C., A. Ono and E. R. Wishart, 1970. "Ice particles in maritime clouds near Tasmania." Quart. J. Roy. Met. Soc., 96, 487-508.

Mossop, S. C., R. E. Ruskin and K. J. Heffernan, 1968. "Glaciation of a cumulus at approximately -4 C." J. Atmos. Sci., 25, 889-899.

Nakaya, U. and T. Terada, 1934. "Simultaneous observations of the mass, falling velocity and form of individual snow crystals." J. Fac. Sci., Hokkaido Univ., Series II, 1, 191-201.

Ono, A., 1969. "The shape and riming properties of ice crystals in natural clouds." J. Atmos. Sci., 26, 138-147.

Ostrowski, A., 1960. "Solution of Equations and Systems of Equations." New York, Academic Press.

Queney, P., 1947. "Theory of perturbations in stratified currents with application to airflow over mountain barriers." Univ. of Chicago Press, Misc. Rpt. No. 23.

Queney, P., 1948. "The problem of airflow over mountains: a summary of theoretical studies." Bull. Amer. Met. Soc., 29, 16-26.

Scorer, R. S., 1949. "Theory of waves in the lee of mountains." Quart. J. Roy. Met. Soc., 75, 41-56.

Stevenson, C. M., 1968. "An improved millipore filter technique for measuring the concentrations of freezing nuclei in the atmosphere." Quart. J. Roy. Met. Soc., 94, 35-43.

Tricker, R. A. R., 1970. "Introduction to Meteorological Optics." New York, American Elsevier Co., 285 pp.

Turner, D. B., 1969. "Workbook of atmospheric dispersion estimates." Nat. Air Pollution Control Admin., Cincinnati, Ohio.